International Study Group Progress Report

On Linear Collider Development

International Study Group

SLAC-Report-559
KEK Report 2000-7
April 2000

Table of Contents

5   X-band RF Power Sources   **149**

6   RF Pulse Compression and Distribution Systems   **177**

International Study Group

C. Adolphsen^a, M. Akemoto^f, R. Akre^a, S. Anami^f, V. Balakin^e, K.L. Bane^a, W. Barry^b, G. Bowden^a, D. Burke^a, R. Cassel^a, G. Caryotakis^a, .H. Chin ^{f}, J.E. Clendenin^a, E. Cook^c, J. Corlett^b, J. Cornuelle^a, J. DeLamare^a, A. Donaldson^a, E. Doyle^a, J. Eichner^a, P. Emma^a, K. Fant^a, .D. Farkas ^{a}, R. Fowkes^a, J. Frisch^a, S. Fukuda^f, . Funahashi ^{f}, S. Gold^a, J. Gronberg^c, S. Hawkins^c, H. Hayano^f, S. Hertzbach^d, . Higashi ^{f}, T. Higo^f, N. Hitomi^f, A. Honma^f, H. Horinaka^i, R.K. Jobe^a, R. Jones^a, E. Jongewaard^a, S. Kashiwagi^g, S. Kazakov^e, L. Keller^a, J. Klingmann^c, K. Ko^a, R. Koontz^a, T. Korhonen^f, T. Kotseroglou^a, A. Krasnykh^a, P. Krejcik^a, N. Kroll^a, K. Kubo^f, N. Kudoh^f, . Kurihara ^{f}, M. Kuriki^f, S. Kuroda^f, A. Larionov^e, R. Larsen^a, . Li ^{a}, G. Loew^a, R. Loewen^a, T. Markiewicz^a, T. Maruyama^a, S. Matsumoto^f, D.J. McCormick^a, B. McKee^a, B. Merritt^c, S. Michizono^f, K.K. Millage^a, R. Miller^a, M. Minty^a, A. Miyamoto^f, H. Mizuno^f, T. Naito^f, T. Nakanishi^h, H. Nakayama^f, . Namito ^{f}, C. Nantista^a, M. Neubauer^a, C. Ng^a, M. Nguyen^a, . Nosochkov ^{a}, K. Ohya^f, K. Oide^f, T. Okugi^f, S. Okumi^h, T. Omori^f, C. Pappas^a, J.M. Paterson^a, C. Pearson^a, R.M. Phillips^a, N. Phinney^{a,2}, T. Raubenheimer^{a,2}, J. Rifkin^a, A. Ringwall^a, M.C. Ross^a, R. Ruth^a, D.C. Schultz^a, J.C. Sheppard^a, K. Skarpass, VIII^a, D. Sprehn^a, G. Stupakov^a, . Sugimoto ^{f}, J. Sullivan^a, C. Suzuki^h, Toshikazu Suzuki^f, C. Takahashi^h, K. Takata^f, T. Takatomi^f, Seishi Takeda^f, F. Tamura^j, S. Tantawi^a, T. Tauchi^f, P. Tenenbaum^a, N. Terunuma^f, V.Teryaev^e, K. Thompson^a, K. Togawa^h, N. Toge^{f,1}, S. Tokumoto^f, H. Tsutsui^f, J.L. Turner^a, J. rakawa ^{f}, K. van Bibber^c, A. Vlieks^a, V. Vogel^e, K. Wada^i, J.W. Wang^a, J. . Wang ^{f}, . Watanabe ^{f}, P. Wilson^a, . Wilson ^{a}, M.D. Woodley^a, M. Woods^a, S. amaguchi ^{f}, H. amaoka ^{f}, K. okoya ^{f} and F. immermann ^{a,3}

^{a}St or i e r A eler tor e ter, St or iersit , li or i , SA

^{b} re e er ele tio l or tor, iersit o li or i , li or i , SA

^{c} re e ier ore tio l or tor, iersit o li or i , li or i , SA

[d] iersit o   ss   setts, A   erst,   ss   settts, SA

[e]   r I sttte o   le r P si s, Proti o, Rssi

[f] ig   erg A   eler tor Rese r   rg i tio   , s , I r i, p

[g] A   e Rese r I stitte o S ie e   gi eeri g, se   iersit, o o, p

[h] ep rt e t o P si s,   lt o S ie e,   go   iersit, go , p

[i] ep rt e t o P si s   le tro i s, ollege o   gi eeri g, s   Pre e tre   iersit, S   i,
p

[j] ep rt e t o P si s,   lt o S ie e,   iersit o   o o, o o, p

[1] Editor in chief.

[2] Editor.

[3] Now at CERN, Geneva, Switzerland.

Preface

A substantial consensus has grown among the international high energy physics community that an electron-positron linear collider is an essential compliment to the Large Hadron Collider now under construction at CERN. As recently stated by the International Committee on Future Accelerators (ICFA),

> I A re o e s o ti e igoros prsit o t e   eler tor rese r   eelop
> e t o   li e r olli er i t e e e erg r ge, it t e go l o   i g esig s o plete
> it reli le ost esti tes i   e e rs   e eliee t t   ele tro positro   olli er
> opti ie   or t e e p si s s ol   e ilt i   ti el   it i ter tio l p rti i
> p tio

The Directors of KEK and SLAC recognized the value and importance of international collaboration in the early stages of development of such a linear collider. In 1998 the Directors signed a Memorandum of nderstanding (MO) that established an International Collider Optimization Study Group (ISG) to enhance cooperation between the laboratories in the R&D and pre-design optimization needed for a collider. This ISG was charged to produce a Pre-Design Report within two years of the signing of the MO .

This document is a report on the activities of the ISG. It presents the progress that has been over the past several years. It also lists opportunities for continued collaboration on R&D toward an electron-positron linear collider that is able to satisfy the ICFA recommendation.

3

Acknowledgments

Memorial Foundation Bannpaku- aidan .

Many aspects of the R&D, particularly the fabrication and engineering design of re uired hardware components were not possible without contracts with the following industries:

Hitachi Corporation, Hitachi Shipbuilding Corporation, Ishikawajima Harima Heavy Industries Corporation, Mitsubishi Electric Corporation, Mitsubishi Heavy Industry, Nichicon Corporation, Nihon Chemicon Corporation, Nihon Koshuha Corporation, NKK Corporation, Sumitomo Heavy Industry Ltd., Toshiba Corporation, and Bechtel Nevada.

Their participation is greatly appreciated.

Introduction and Summary

Contents

1.1   The KEK-SLAC International Study Group (ISG)

1.1.1   Origin, Charge and Goals of ISG

The linear collider development effort worldwide has focused on the design of electron-positron colliders to explore the physics from the sub-TeV towards 1 TeV energy scale. Such a machine would complement the physics program of the LHC, scheduled to begin operation about 2005. In 1996-97, collaborations in the US and Japan presented designs for an electron-positron linear collider with an energy of 1 TeV in the center of mass and a luminosity of $1.0 \times 10^{34} \mathrm{cm}^{-2}\mathrm{s}^{-1}$. The US Next Linear Collider (NLC) was described in the Zeroth-order Design Report (ZDR) published in June, 1996[1]. The Japanese Linear Collider (JLC) was described in the JLC Design Study of April, 1997[2]. Both designs proposed an initial energy of 500 GeV with a luminosity over $5.0 \times 10^{33} \mathrm{cm}^{-2}\mathrm{s}^{-1}$, expandable to 1 TeV at a luminosity of $1.0 \times 10^{34} \mathrm{cm}^{-2}\mathrm{s}^{-1}$, with possible upgrade paths to reach 1.5 TeV.

Development of the technologies required for a TeV-scale linear collider has advanced substantially in recent years. Prototype RF components – klystrons, pulse compression systems, and accelerator structures – for such a collider are now being integrated into complete systems. Experiments with the Final Focus Test Beam (FFTB, Fig. 1.1) have demonstrated the ability to demagnify and instrument beams suitably for the collider. The FFTB was built at SLAC by a broad international collaboration led by SLAC and KEK. Commissioning of a full-scale damping ring is now underway at the Accelerator Test Facility (ATF, Fig. 1.2) at KEK. This too is being done by an international collaboration led by KEK and SLAC. Experiments with the ATF will provide the basis for the final design of the injector complex needed to prepare highly condensed beams for the linear collider.

In this context the directors of KEK and SLAC noted the importance of forming a formal collaboration between the two laboratories to pursue research and development for linear colliders. Thus in early 1998 the directors of KEK and SLAC signed a "Memorandum of Understanding (MOU) on International Linear Collider Optimization Study Group" for conducting certain pre-design optimization activities. The entire text of this MOU is reproduced in Appendix A of this report. The International Study Group (ISG) was asked to address the following specific issues:

1. Specification of objectives and performance requirements for the collider.

2. Identification of overall technical design strategies and options.

3. Identification of subsystem and component functional requirements and technical options and designs.

4. Description of civil engineering and infrastructure and models.

5. Manufacturing and industrial engineering to improve cost efficiency.

ISG Progress Report, April, 2000

6. Evaluation of possible construction techniques and schedules.

7. Remaining R&D items that need to continue.

It was intended that the ISG would be led jointly by KEK and SLAC, but it was expected to include substantial participation by other institutions from Japan and the United States as well as other nations. As the final product, the ISG was requested to produce a Pre-Design Report within two years of the signing of the MOU. The purpose of this document is to respond to this request and report on the progress that has been made by the ISG.
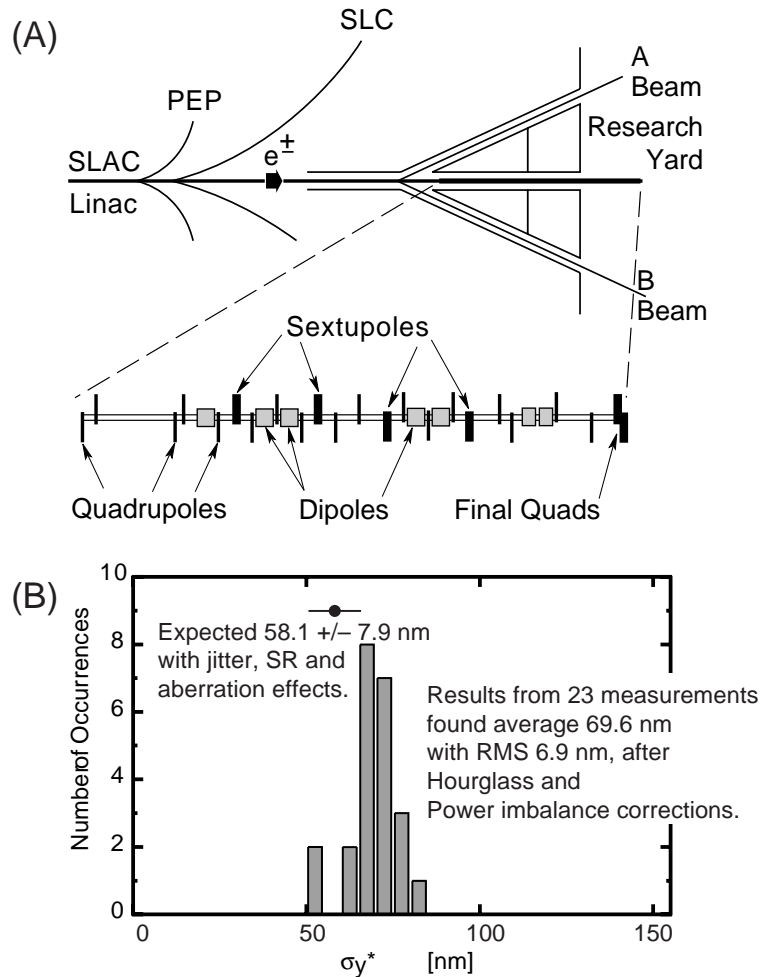
Figure 1.1: *(A) Schematic diagram of FFTB at SLAC, and (B) data that shows the distribution of measured vertical beam spot size at the focal point of FFTB.*
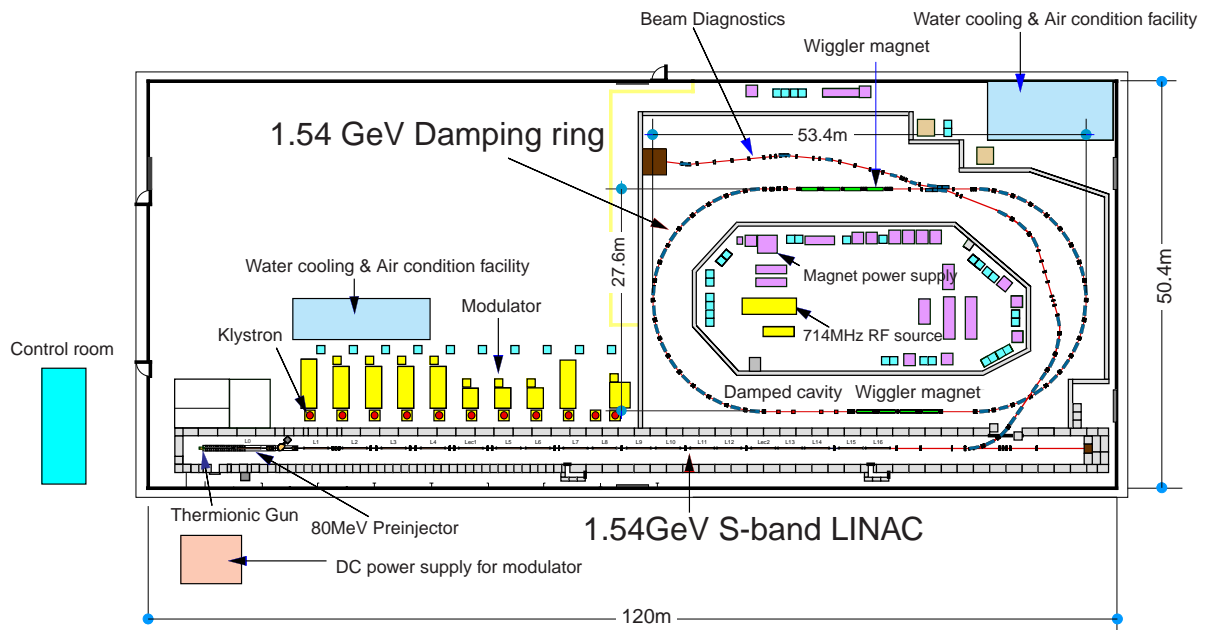
Figure 1.2: *Schematic plan view of ATF at KEK.*

1.1.2   Organization and Activities

The ISG has been organized to include a number of subgroups that work in various areas of accelerator study and technology development. The active working groups at the time of this report are given in Table 1.1

Each of these groups is co-led by people from KEK and SLAC. The chapters of this Report roughly match the working group structure.

Table 1.2 lists the major ISG meetings that have taken place up to the present time. Each major meeting was held approximately six months apart, with the host laboratory alternating between SLAC

WG1	Parameters and Accelerator Physics
WG2	Injectors
WG3	Main Linac Structures
WG4	Klystron Modulators
WG5	RF Modeling
WG6	Beam Delivery and Interaction Region

Table 1.1: *Active ISG working groups at the time of this report.*

and KEK. A major meeting, which lasted 4 to 5 days each, has been attended by typically 40 - 50 persons from the two labs and collaborators from other institutes. Details of the meeting agenda are reproduced in Appendix B of this Report.

Meeting	Date	Place
ISG1	January, 1998	SLAC
ISG2	July, 1998	KEK
ISG3	January, 1999	SLAC
ISG4	July, 1999	KEK
ISG5	February, 2000	SLAC

Table 1.2: *List of past ISG meetings.*

In addition, in many cases a major ISG meeting was preceded by a pre-ISG meeting where a limited number of physicists from SLAC and KEK met and laid out the meeting agenda and goals. Also, members of the ISG working groups have frequently traveled to each other's laboratory between the major meetings for detailed discussions, experiments and measurements.

The ISG has been an effective collaboration that has enhanced the efforts of both sides. Some of the major accomplishments of the ISG are described in the next section.

1.1.3   Summary of Accomplishments

The focus of the ISG work was on advancing the accelerator design and supporting technologies. This is a complex process which involves a close interaction between theoretical analysis of the collider design and R&D progress on hardware components. The sequence of efforts took place roughly in the following order:

- Optimization of the collider parameters and definition of system and subsystem requirements,

- Identification of design strategies and options,

- Development of specific technologies to achieve these requirements.

Development and testing of the required components, and R&D on manufacturing techniques have been important activities of the ISG. Experiments at the major test facilities such as the ATF at KEK and ASSET at SLAC have also played a significant role in the ISG studies.

Accelerator Parameters

As its first task, the ISG reviewed the highest level machine goals and parameters that had been previously presented in the two separate design studies, the JLC DS and the NLC ZDR. It was known when these studies were published that problems remained in each of these designs, and that

a re-optimization of the collider was possible. The ISG Parameters working group compared and discussed the two designs, and agreed on a common set of major parameters which were judged to be a considerable improvement on both earlier designs. A schematic diagram of the JLC/NLC is shown in Fig. 1.3, and the newly optimized parameters for the NLC/JLC are given in Tables 1.3 and 1.4.

	500 GeV			1 TeV		
	A	B	C	A	B	C
CMS Energy (GeV)	535	515	500	1046	1008	978
Luminosity w/ IP dilutions (10^{33})	7.7 (9.6)	7.0 (8.7)	6.0 (7.5)	15 (12.5)	13 (10.9)	11.6 (9.7)
Repetition Rate (Hz)		120 (150)			120 (100)	
Bunch Charge (10^{10})	0.75	0.95	1.1	0.75	0.95	1.1
Bunches/RF Pulse		95			95	
Bunch Separation (ns)		2.8			2.8	
Injected $\gamma\varepsilon_x/\gamma\varepsilon_y$ (10^{-8}m-rad)		300 / 3			300 / 3	
$\gamma\varepsilon_x$ at IP (10^{-8}m-rad)	400	450	500	400	450	500
$\gamma\varepsilon_y$ at IP (10^{-8}m-rad)	6	10	14	6	10	14
β_x/β_y at IP (mm)	10/0.10	12/0.12	13/0.20	10/0.125	12/0.15	14/0.20
σ_x/σ_y at IP (nm)	277/3.4	330/4.9	365/7.6	197/2.7	235/3.9	260/5.4
σ_z at IP (μm)	90	120	145	90	120	145
Υ (Beamstrahlung Param.)	0.14	0.11	0.09	0.38	0.30	0.25
Pinch Enhancement	1.41	1.36	1.50	1.41	1.46	1.5
Beamstrahlung δ_B (%)	4.5	4.0	3.6	10.9	10.3	9.7
# Photons per e^-/e^+	1.0	1.1	1.17	1.3	1.43	1.51

Table 1.3: *IP parameters for the NLC/JLC, reproduced from Chapter 2.*

One example of this optimization is the choice of the length of the RF pulse and bunch train. If the total amount of charge to be accelerated remains constant, adoption of a longer RF pulse with a longer bunch train reduces the total cost of the main linac. This is because the RF power required for the linacs remains roughly the same, while the number of RF source units decreases. The reduced beam loading associated with the longer bunch train also helps lower the power requirement. Of course, this means that the RF power sources and distribution systems must be able to handle longer RF pulses. The analysis by the ISG led to the decision to adopt a multi-bunch scheme with 95 bunches and a bunch spacing of 2.8 ns. The implied RF pulse length that the klystrons have to produce is 1.5 μs[1] This is a departure from both of the original NLC and JLC parameter sets, but it is considered to be a substantial improvement in the overall design. The expected luminosity is $(6 \sim 10) \times 10^{33}$ cm^{-2}s^{-1} at 500 GeV and $(10 \sim 13) \times 10^{33}$ cm^{-2}s^{-1} at 1 TeV operation.

There were extensive discussions on the choice of the accelerating structure and its basic parameters. A longer accelerating structure will relax the alignment and construction tolerances if the filling time for the structure is held constant because the wakefields are smaller. This is discussed in detail in

---

[1]Recent progress in the klystron development indicates that use of $\approx 3\mu$s pulses could be an even more attractive scenario.

	500 GeV			1 TeV		
	A	B	C	A	B	C
CMS Energy (GeV)	535	515	500	1046	1008	978
Repetition Rate (Hz)		120 (150)			120 (100)	
RF overhead (%)		8			8	
Average RF phase (deg.)	10.6	11.7	13.0	10.9	11.4	13.1
Linac Tolerances (μm)	16.1	15.2	14.6	13.1	11.7	11.9
Unloaded Gradient (MV/m)		72			72	
Effective Gradient† (MV/m)	59.7	56.7	54.5	59.7	56.7	54.5
Active Linac Length (km)		4.3			8.9	
Power/Beam (MW)	3.4 (5.1)	4.2 (6.3)	4.6 (6.9)	7.1 (5.9)	8.4 (7.0)	9.3 (7.8)
# of Structures per linac		2484			4968	
Structure Length (m)		1.8			1.8	
Structure Iris (a/λ)		0.18			0.18	
Structure Atten. (τ)		0.47			0.47	
Shunt Impedance (MΩ/m)		90			90	
Fill Time (ns)		103			103	
Q		7800			7800	
# of Klystrons per linac		1584			3312	
Klystron Peak Pwr. (MW)		75			75	
Klystron Pulse Length (μs)		1.5			1.5	
Pulse Method		4/4 DLDS			4/4 DLDS	
Pulse Comp. Gain (85% eff.)		3.4			3.4	
RF System Efficiency (%)		38			38	
Total AC Power (MW)		94 (141)			191 (160)	

Table 1.4: *Main linac parameters for the JLC/NLC, reproduced from Chapter 2.* † *Effective gradient includes RF overhead (8%) and average RF phase cos $\overline{\phi}_{rf}$.*
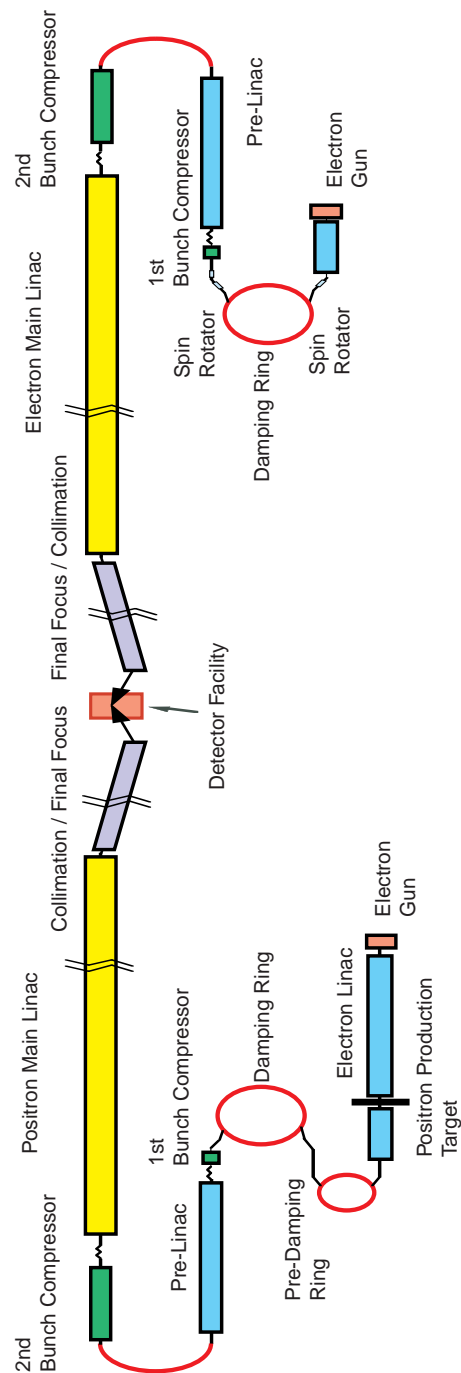
Figure 1.3: *Schematic diagram of JLC/NLC.*

Chapter 2. It is also expected that longer structures will reduce costs, since fewer structures will be needed as long as the same peak accelerating gradient can be maintained. However, this needs to be demonstrated as well as the feasibility of constructing longer structures. The choice of the aperture,

ISG Progress Report, April, 2000

normalized by the RF wavelength a/λ is another critical topic. As a result of the ISG discussions, a working decision was made to use a 1.8 m long accelerating structure with $a/\lambda \simeq 0.18$.

Other accomplishments include:

- Possible emittance dilution across the linear collider systems was estimated, resulting in a so-called "emittance budget". Possible ranges of operating parameters were also explored.

- A possible high-luminosity option was developed which would use a 1.4 ns bunch spacing while keeping the same bunch train length. The individual bunch charge would be decreased to maintain the total beam charge. To produce a lower vertical emittance, the damping ring would need to be aligned with higher accuracy (or possibly some other upgrade). In addition, the final focus system would need to produce a β_y^* of 0.08 mm.

- The feasibility of utilizing the low emittance beams for other applications such as nuclear physics, fixed target programs and FEL use was examined.

Specific details of the parameter analysis are discussed more completely in the following chapters of this report, but the agreement on this optimized parameter set fulfilled a very important goal of the ISG collaboration. It helped define the hardware systems to be designed jointly between SLAC and KEK. For the few hardware systems which were developed in parallel at SLAC and KEK, the common parameter set provided a measure by which one could assess the technical progress of both groups in an objective manner.

RF Systems

A major challenge at NLC/JLC is to provide the necessary acceleration to reach 0.5 TeV per beam in a cost effective and reliable manner. The main acceleration mechanism of the linear collider was chosen to be a conventional RF linac at 11.4 GHz (X-band). Because of the higher gradient achievable at X-band, the main linacs can be shorter and less expensive than with a lower RF frequency. Research and development of RF systems and components has been pursued vigorously by the ISG. Fig. 1.4 shows the shematics diagram of a generic RF system for linacs with room-temperature accelerating structures driven by high-power klystrons.

Klystron microwave amplifiers, driven by DC pulses from modulators, produce RF power with an AC phase that can be rapidly and accurately controlled. This control allows compression of the klystron pulses to high peak powers that are then used to create large accelerating fields in specially designed copper structures. ISG working groups were established to study all parts of the X-Band RF system.

One ISG working group has reviewed the design and construction techniques for modulators. Aside from maintenance and operation of existing test facilities, the present focus of the modulator R&D at both SLAC and KEK is on the feasibility of modulators based on semiconductor switching devices rather than thyratrons. Very encouraging early results indicate the future suitability of such technologies.
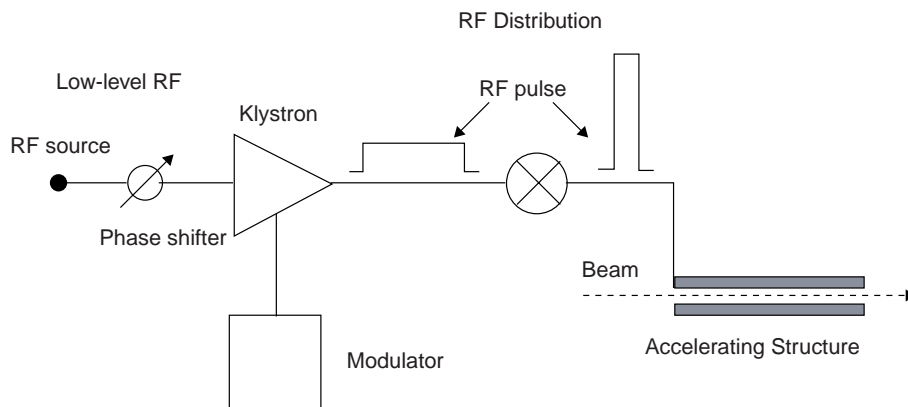
Figure 1.4: *Generic RF system for linacs with room-temperature accelerating structures driven by high-power klystrons.*

A large effort has been put into the development of X-band klystrons capable of producing the 75 MW, 1.5 μs RF pulses required for NLC/JLC. A sophisticated 2-dimensional (and 3-dimensional) modeling code has been introduced for the design and analysis of klystrons built at both KEK and SLAC. Active ongoing discussions in the ISG have reviewed the SLAC and KEK R&D programs and klystron design issues. The feasibility of solenoid-focused klystrons with these parameters has been
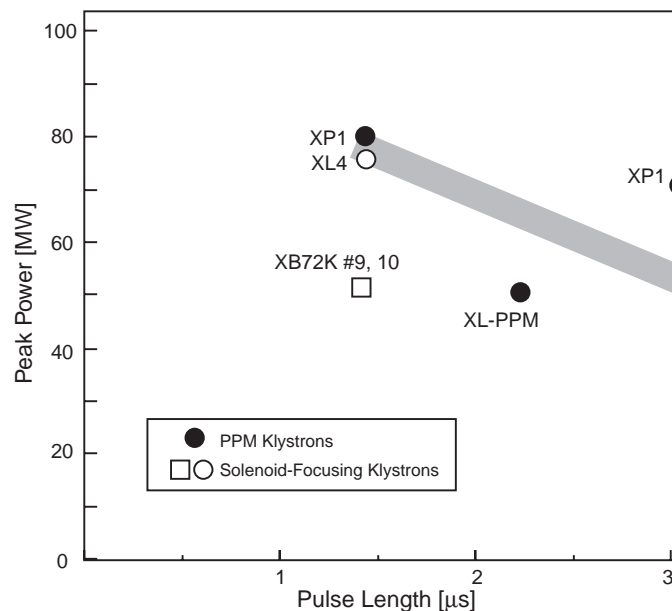
Figure 1.5: *Peak power and pulse length obtained from recent klystron prototypes built at SLAC and KEK. The gray bar indicates the performance goal for JLC/NLC. The XL4 (solenoid-focusing) and XP1 (PPM-focusing) models have cleared the goal.*

ISG Progress Report, April, 2000

well established experimentally, and recent effort has concentrated on the development of X-band klystrons with a PPM (periodic permanent magnet) stack for beam focusing. Following a successful 50 MW PPM klystron test in 1986, SLAC successfully operated the second prototype PPM klystron at $75 \sim 80$ MW with $1.5 \sim 3\mu s$ pulses. Fig. 1.5 shows the performance of recent klystron prototypes from SLAC and KEK.
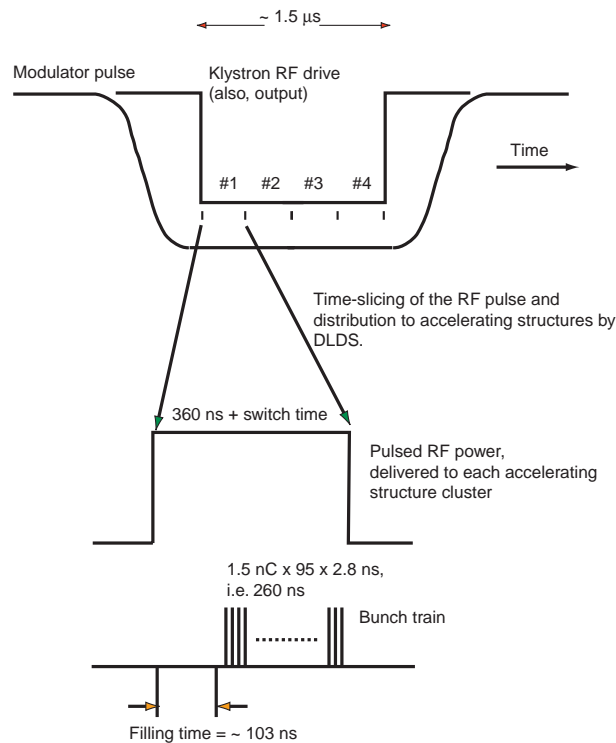
Figure 1.6: *Relationship of the 1.5 μs pulse from klystron, time-slicing of the pulse by the DLDS system, filling time and acceleration of the multi-bunch beam by each accelerating structure.*

Since the RF output from a single klystron is generally smaller in power yet longer in time than required to efficiently create accelerating fields in accelerating structures, some pulse compression (or, time-slicing of the combined RF pulses from several klystrons) is needed. The ISG chose to use 1.5 μs, 75 MW pulses from eight klystrons, combine them, and time-slice them into four pieces and distribute them to sets of accelerating structures spaced appropriately along the linacs. Fig. 1.6 shows the relationship of the pulse from the klystron, the time-slicing of the pulse, and the acceleration of a multi-bunch beam in the accelerating structure.

The Delay Line Distribution System (DLDS), which was originally conceived at KEK, was adopted by the ISG as the baseline scheme for distributing RF power to the accelerating structures. As shown in Fig. 1.7 the DLDS consists of a set of waveguide delay lines which are laid out to deliver time slices of klystron pulses to appropriate sets of accelerating structures. The delivery of the RF power is timed such that each structure has been filled with RF energy when the beam reaches it. This provides an efficient use of RF power with a reasonable quantity of components. Several DLDS design variants
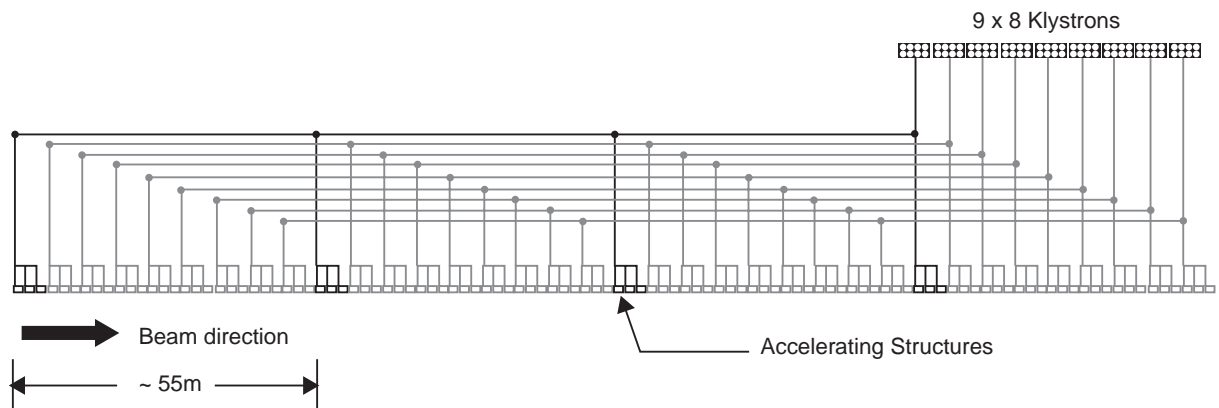
Figure 1.7: *Schematic diagram of the DLDS system for JLC/NLC. Nine ensembles of 8-klystron packages drive 108 accelerating structures which occupy approximately 220 m of the linac. This pattern is repeated along electron and positron main linacs.*
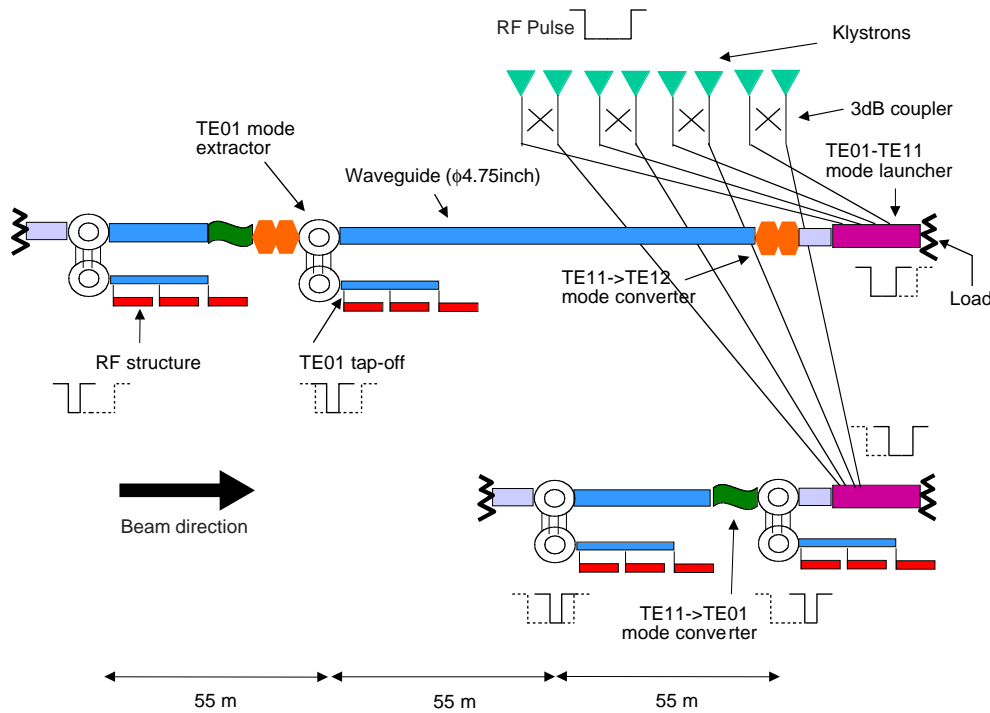
Figure 1.8: *A possible implementation of one of the "legs", in the DLDS, which corresponds to the highlighted portion within Fig. 1.7. This illustration shows the 2×2 scheme, where two delay lines are used to distribute RF pulses from a single 8-klystron pack. The required RF components, such as RF mode-launchers and mode-extractors are shown.*

ISG Progress Report, April, 2000

exist and other, different power distribution schemes are not yet totally excluded. A possible scheme, among several candidates, of an implementation of DLDS is shown in Fig. 1.8.

SLAC and KEK have jointly designed, fabricated, and tested a variety of prototype DLDS components. A major experiment has been carried out in the ATF injector tunnel to show that independent RF modes can be transported over 50 meters of DLDS waveguide with good efficiency and purity. This test provides confidence that the DLDS concept is a viable and highly efficient method for delivering X-band RF power to accelerating structures.
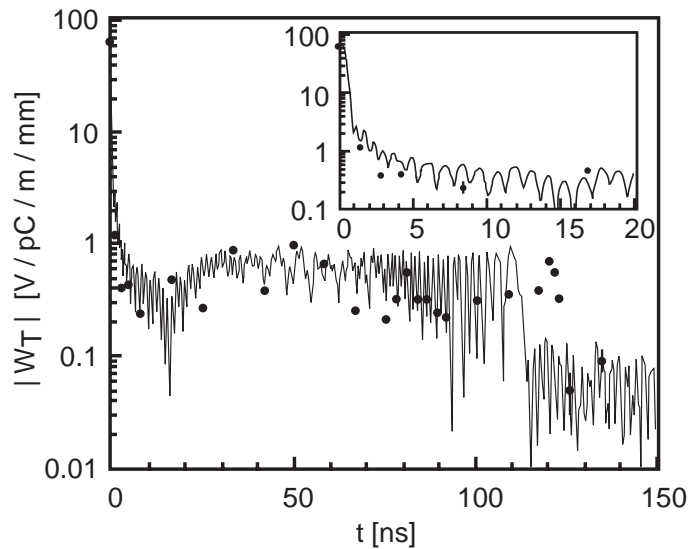
Figure 1.9: *Vertical wakefield amplitude measurements (data points) and predictions (solid line) from beam testing of the DDS1 prototype of the Damped-Detuned accelerating structure. The insert shows an expanded view of the first 20 ns. At NLC/JLC, reduction of transverse wakefield of ~ 1 V/pc/m/mm or below is required. This data shows that DDS1 clearly satisfies this requirement.*

The accelerating structure is a key element in achieving the beam parameters needed in the JLC/NLC, and the ISG has worked extensively on design and manufacture of the precise structures required for the collider. This effort has made significant progress. The damped and detuned structure (DDS) design, which has been pursued by SLAC, was adopted as the baseline design for the accelerating structure. KEK has taken the lead in developing manufacturing processes aimed at achieving the precision and accuracy required by the X-Band frequency choice. A series of beam experiments have proven that the DDS design is effective in suppressing wakefields, and that the structures can be manufactured with accuracy several times better than the tolerances set by the design. A series of measurements made with the SLAC linac have demonstrated this remarkable success. (See Fig. 1.9.) An advanced version of DDS has been developed which utilizes rounded cavity corners for improved shunt impedance and higher Q. The first prototype of this rounded DDS (RDDS1) has been manufactured at KEK, and is scheduled to be tested with beam at SLAC later in 2000. Fig. 1.10 shows a schematic design of a copper disk for RDDS1.
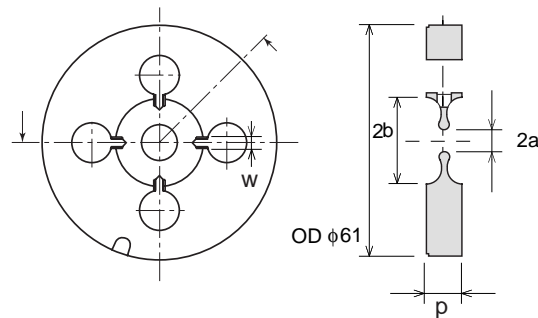
Figure 1.10: *Schematic design view of a copper disk fabricated for building an RDDS structure prototype.*
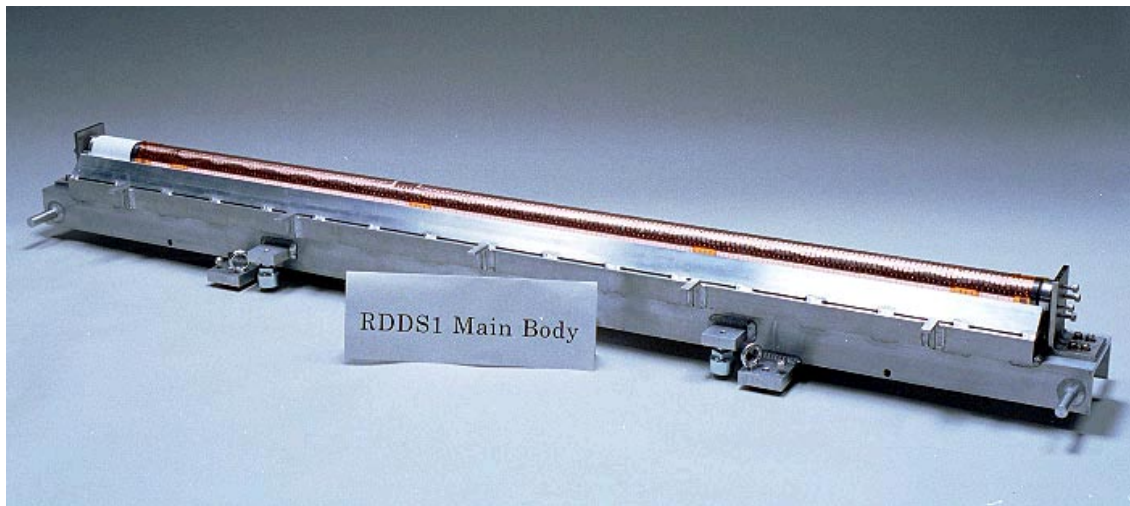
Figure 1.11: *Completed RDDS1 disk stack.*

In summary, the ISG group considers that X-band technology with realistic peak power specifications can be deemed 'sufficiently realistic, reliable, and affordable' for a construction start in the 2000s.

Other Studies

The ISG has also carried out a number of important studies of the injector and beam delivery systems for the NLC/JLC. The Injectors Working Group has made comparative evaluations of designs and options for creation and preparation of the beams for the collider. Much of this conceptual work has been done in the context of ATF experimental program at KEK, and with input from experience with the SLC at SLAC. More complete discussions of this work is found later in this report, and in a separate report from the ATF Collaboration[3].

The Beam Delivery/Interaction Region Working Group has made particularly important comparisons

of calculations of machine-induced detector backgrounds and have worked on design and study of instrumentation that will be important aids in tuning the collider. Work done by this group has resolved a number of previous discrepancies in calculations of backgrounds, and has led to shared confidence that these backgrounds are well understood and can be controlled. These were important goals for the ISG.

1.2   Conclusions and Opportunities for Further Collaboration

Taken together, the work of KEK and SLAC scientists and engineers in the ISG Collaboration has provided a critical foundation for the next steps in the development of a coherent collider design and sharpened the focus of R&D plans.

It is our assessment that the feasibility of a linear collider, based on X-band technology, has been substantially solidified through the activities of the ISG. It is also our belief that the ISG collaboration has been extremely effective in accelerating technological progress in these areas over the past two years. We consider that X-band technology with realistic peak power specifications can be deemed 'sufficiently realistic, reliable, and affordable' for a construction start in the 2000s. Nonetheless, the R&D work for JLC/NLC cannot yet be considered complete at this stage. Some of the major opportunities for further collaboration are listed below:

1. Development of an electron gun, in particular a polarized electron gun, and buncher systems with the NLC/JLC specifications at ATF or elsewhere.

2. Solid establishment of production and handling techniques for low emittance beams at ATF in multi-bunch conditions.

3. Continued critical reviews and eventual unification of the injector systems designs for JLC and NLC to accelerate progress on detailed designs of the subsystems.

4. Experimental reconfirmation of basic material science data required for operation of the positron production target and beam collimation systems.

5. Firm establishment of klystron modulator technologies based on high power semiconductor switching devices.

6. Long-term testing of high power X-band klystrons and studies on mass manufacturability.

7. Complete design of the accelerating structure and studies on its mass manufacturability.

8. "String testing" of a complete unit of the X-band RF system which consists of modulators, 8 klystrons, a full-scale DLDS and 12 (or more) accelerating structures.

9. Reexamination of numerous topics concerning the standard hardware components such as power supplies, magnets, monitors, vacuum, cooling and control systems hardware.

10. Further optimization of the beam optics designs of the final focus and beam dump. Full engineering studies of the construction of the interaction region.

Many of the topics above can be pursued by the existing ISG working groups. However, some may call for reconsideration of the framework of the collaboration or its scale, and possible involvement by new participants. This is because of the increased budget, time, manpower and management resources

required. We hereby submit this Report in the hope that it provides the laboratory and community leaders with the necessary information to evaluate these long range issues.

References for Chapter 1

[1] "Zeroth-Order Design Report for the Next Linear Collider," LBNL-PUB-5424, also SLAC Report 474 or UCRL-ID-124161, May 1996.

[2] "JLC Design Study, KEK Report 97-1," April, 1997.

[3] "ATF, Accelerator Test Facility: Study Report JFY 1996-1999," in preparation, April, 2000.

Authors of Chapter 1

- David Burke

- Nobu Toge

CHAPTER **2**

Accelerator Parameters

Contents

2.1 Introduction

The luminosity of a colliding beam facility is given by

$$\mathcal{L} = \frac{n f N^+ N^-}{4\pi\sigma_x\sigma_y} H_D \qquad (2.1)$$

where $\mathcal{L}$ is the luminosity, n is the number of bunches, f is the repetition rate, $N^{+/-}$ is the number of positrons/electrons per bunch, $\sigma_{x/y}$ is the horizontal/vertical beam size, and H_D is the disruption enhancement.

Unlike a conventional storage ring where the bunches collide many thousands of times per second, the AC and RF power sources of a linear collider limit the repetition rate to a few hundred hertz. To reach high luminosity, it is necessary to collide long trains of bunches and focus them to a very small beam size at the interaction point (IP). The most difficult challenges are: to produce low emittance beams; accelerate them without excessive emittance dilution; and focus them to the tiny size required. This determines the basic components of the linear collider which include electron and positron sources to generate a multi-bunch high-current beam, damping rings to produce ultra-low emittance beams, bunch compressors to reduce the bunch length, main linacs to accelerate the beams to full energy efficiently while preserving the low emittance, and the final transport line to focus and collide the nanometer scale beams.

The primary task of Working Group 1 (WG1) was to compare the different NLC and JLC designs and produce a common optimized parameter set to serve as a basis for further R&D efforts. The emphasis was on the configuration of the main linac RF systems so these parameters could serve as input to the other working groups. A common emittance budget was also determined which could be used for simulation studies and tolerance calculations. The JLC and NLC efforts specified different optics designs for many individual areas such as the damping rings or final focus. No attempt was made to choose between these options at this point since both designs appeared to meet the essential requirements. Brief comparisons between the injector and final focus systems can be found in Chapters 3 and 8; a more detailed comparison will be made as part of preparation of a final design report.

In the next section, we will describe the NLC/JLC parameters. We will start with a review of the JLC DS [1] and NLC ZDR [2] designs as they existed before the ISG study, then discuss details of the parameter optimization and the resulting parameter set, and finish with a discussion of possible high luminosity parameters which should be attainable with the designs presented. We will discuss some of the beam dynamics issues in the injectors, main linacs, and beam delivery systems that are relevant to the parameter determination and have been investigated as part of the ISG process in WG1. Finally, we will discuss possible high-luminosity options and use as JLC/NLC for other applications such as FEL.

2.2   JLC and NLC design status before ISG

	500 GeV		1 TeV	
	JLC 3-97	NLC 6-96	JLC 3-97	NLC 6-96
Luminosity w/ IP dilutions (10^{33})	8.3	5.3	17	11
Repetition Rate (Hz)	150	180	150	120
Bunch Charge (10^{10})	0.70	0.75	0.70	1.10
Bunches/RF Pulse	85	90	85	75
Bunch Separation (ns)	1.4		1.4	
Injected $\gamma\varepsilon_x/\gamma\varepsilon_y$ (10^{-8}m-rad)	300 / 3		300 / 3	
$\gamma\varepsilon_x$ at IP (10^{-8}m-rad)	330	430	330	520
$\gamma\varepsilon_y$ at IP (10^{-8}m-rad)	4.8	13	4.8	17
β_x/β_y at IP (mm)	10/0.100	10/0.150	10/0.100	12/0.150
σ_x/σ_y at IP (nm)	260/3.1	294/6.3	184/2.3	250/5.1
σ_z at IP (μm)	90	125	90	150
Υ (Beamstrahlung Param.)	0.10	0.09	0.30	0.30
Pinch Enhancement	1.4	1.4	1.4	1.4
Beamstrahlung δ_B (%)	4.4	3.2	9.9	12.6
# Photons per e^-/e^+	1.1	1.0	1.4	1.8

Table 2.1: *JLC 3-97 and NLC ZDR (6-96) IP parameters*

The JLC and NLC as described in JLC Design Study (DS) and the NLC Zeroth-Order Design Report (ZDR) were similar designs based on X-band RF technology. Detailed parameters at the IP for the nominal 500 GeV and 1 TeV center-of-mass (cms) designs are listed in Table 2.1 while the corresponding main linac parameters are listed in Table 2.2. The designs had similar bunch trains, IP parameters, and linac systems. The principal differences were related to technical choices in the linac design and are summarized below:

- The JLC specified 1.3m detuned structures (DS) as compared to 1.8m damped-detuned structures (DDS) in the NLC design. This difference was based on two issues. First, the DDS-type structure, at the time of the design studies, was a brand new concept that was significantly more complicated than the DS-type structure. It had just been tested by SLAC and thus personnel at KEK were justifiably concerned about the feasibility of the approach. Second, it was clearly more difficult to construct the longer 1.8m structures while meeting the desired tolerances on the structure straightness. In fact, two structures had just been constructed at SLAC with significant misalignments along their length.

- The JLC relied on the more efficient Delay Line Distribution System (DLDS) pulse compression with a factor of 3 power gain. NLC specified the SLED-II pulse compression system with roughly

	500 GeV		1 TeV	
	JLC 3-97	NLC 6-96	JLC 3-97	NLC 6-96
RF overhead (%)	0	8	0	8
Average RF phase (deg.)	17	15.0	17	8
Unloaded Gradient (MV/m)	73	50	73	85
Effective Gradient† (MV/m)	56	29	56	55
Active Linac Length (km)	4.3	8.2	8.8	8.8
# of Structures per linac	3294	4528	6727	4908
Structure Length (m)	1.31	1.80	1.31	1.80
Structure Iris (a/λ)	0.166	0.180	0.166	0.180
Structure Atten. (τ)	0.61	0.53	0.61	0.53
Fill Time (ns)	106	100	106	100
# of Klystrons per linac	2196	2264	4485	4908
Klystron Peak Pwr. (MW)	67	50	67	75
Klystron Pulse Length (μs)	0.75	1.5	0.75	1.1
Pulse Method	4/3 DLDS	SLED-II	4/3 DLDS	BPC
Pulse Comp. Gain	3.0	3.6	3.0	3.5
RF System Efficiency (%)	28	28	28	38
Total AC Power (MW)	114	121	234	193

Table 2.2: *JLC 3-97 and NLC ZDR (6-96) main linac parameters. † Effective gradient includes RF overhead and average RF phase $\cos \overline{\phi}_{rf}$.*

a factor of 4 power gain but significant inefficiencies. Here, the issues were reversed in that the SLED-II pulse compression system had been tested at the NLCTA while the DLDS, proposed at KEK, was a brand new concept that promised better performance but was not yet well understood. However, the NLC ZDR recognized that the pulse compression system would have to be upgraded to operate efficiently at 1 TeV.

- The JLC design assumed that the 500 GeV cms initial stage and the 1 TeV upgrade would use the same RF system and that the linacs for the 500 GeV cms case were simply half as long as those for 1 TeV. The NLC assumed that reaching 1 Tev would require an upgrade to the RF system that increased the gradient and specified linacs that were similar in length for both 500 GeV and 1 TeV cms.

- The JLC design assumed smaller emittance dilutions through the linac which then led to smaller IP spot sizes and a higher luminosity. The NLC assumed over twice as much dilution would occur between the damping ring and the IP.

- Finally, the JLC expected 20% beam loading in the main linac. The NLC design called for over 30% beam loading plus an additional 8% overhead on the RF system. This choice is related to a number of the issues above. In particular, with the longer DDS structures which have higher group velocity and larger apertures, the wakefields in the NLC structures were significantly smaller which allowed higher beam currents for similar tolerances. Second, larger beam currents were required to maintain the luminosity with the larger emittance dilutions and spot sizes that were assumed in the NLC design. Finally, the additional RF overhead was assumed to account for RF feedback, a certain number of power sources that were off for maintenance, and some flexibility in the choices of the RF phases.

As already stated, many of these differences were historical and can be understood as such. For example, the NLC was based on the SLED-II pulse compression system which was being tested at the NLC Test Accelerator (NLCTA) even though it was known that the performance was not really satisfactory and that some upgrade would be needed to attain the 1 TeV parameters. Similarly, the JLC design was based on a purely detuned structure that was relatively short because the physicists at KEK did not have experience with longer structures or with the DDS scheme even though it promised better performance. Similarly, the NLC had chosen relatively conservative parameters with large emittance dilutions that were based on some of the initial operating experience with the SLC.

2.3   Technology Choices for NLC/JLC Design

In recent years, there have been a number of technical developments that would be advantageous for both the JLC and NLC designs. This includes the proposal for the highly efficient DLDS pulse compression system at KEK, the development of the concept of more efficient Rounded DDS (RDDS)

structures at SLAC (see Chapter 7 for more details), and an improved understanding of the SLC operation and emittance preservation. Finally, with the successful development of the 50 MW Periodic-Permanent Magnet (PPM) klystron at SLAC, it was felt that the NLC upgrade concept was overly conservative and it would be quite reasonable to assume a higher power RF system at the onset (see Chapter 5).

Thus, the following parameter sets are based on RDDS accelerator structures which are powered by 75MW klystrons with a pulse length of roughly 1.5μs and a DLDS pulse compression system that compresses the RF pulse by a factor of four (see Chapter 6). The assumed efficiencies are 75% for the modulator, 60% for the klystrons, and 85% for the pulse compression system.

These decisions will be re-evaluated in the future as further R&D is completed on the RF components. For example, since the quantity for comparison is the energy per RF pulse, an RF power source with a larger peak power and comparably shorter pulse length, as previously proposed at KEK, would utilize a simpler pulse compression system although it might require a more difficult modulator. Alternately, given the recent successful operation of a Periodic Permanent Magnet klystron at 75 MW and 3μs, we might consider doubling the pulse compression and reducing the number of RF sources by a factor of two.

2.4 Parameter Optimization

There have been many optimization studies of the RF parameters to maximize the RF-to-beam efficiency; these issues are discussed in Refs. [3, 4, 5, 6]. In general, in a linear collider, one can rewrite the luminosity equation Eq. (2.1) as

$$\mathcal{L} \propto \frac{P_{ac}\eta_{ac}\eta_{rf}}{E_{cms}}\sqrt{\frac{\delta_B}{\epsilon_y}}H_D \tag{2.2}$$

where P_{ac} is the AC power required to operate the collider, η_{ac} is the efficiency of the RF generation system from the AC power, η_{rf} is the RF-to-beam transfer efficiency, E_{cms} is the center-of-mass (cms) energy, δ_B is the average energy loss due to beamstrahlung, ϵ_y is the vertical emittance, and H_D is the luminosity enhancement which is typically $1.3 \sim 1.5$ with 'flat' beams. There are actually relatively few free parameters in this equation and one can show that, when limitations imposed by the beam dynamics are included, the parameters are tightly constrained [6].

Unfortunately, these previous studies allow one to understand the parameter scaling but they are not sufficiently complete to allow detailed optimization of the parameters. Instead our technique for the JLC/NLC collider was to utilize a linear collider optimization program LCOPT [7] written by K. Yokoya. This program calculates the RF system parameters, the wakefields and alignment tolerances, and the IP parameters in a self-consistent manner. Further we modified the LCOPT code to correctly

model the RDDS accelerating structures and include the cost information that was compiled for the NLC ZDR design.

In performing the optimization, we studied the length of the bunch train, considered the accelerating structure length, and studied the accelerating structure aperture. Finally, we considered variations in the acceleration gradient that were consistent with the possible permutations of the RF system. During the optimization process, the charge per bunch, the bunch train length, the bunch length, and the beta functions at the IP were varied. The luminosity at the IP, the average energy loss due to beamstrahlung, and the average RF phase (which is necessary to compensate the longitudinal wakefield) were constrained and the capital cost and AC power requirements of the collider linacs were minimized. The capital cost, which is plotted in arbitrary units, is based on the estimates made for the NLC ZDR design using US accounting rules. These costs include the estimated cost for the following linac RF components: modulators, klystrons, pulse compression and associated vacuum systems, and the low level RF. It also includes the linac beamline components, i.e. the magnets, accelerating structures, supports, remote movers, and the vacuum systems, and the conventional facilities, i.e. the linac tunnel, cooling water, and electrical power. In a linac system, the cost tends to be optimized when the costs that are proportional to the total RF power are equal to the costs that are proportional to the beamline length. It is thought that these NLC ZDR cost values provide a guide for the cost optimization of a collider. However, a similar procedure must be performed in the future using a Japanese cost model to verify that the results are similar. In the following sections, we describe the results of these different optimizations and present the current parameter sets.

2.4.1 Bunch Spacing and Train Length

There is a significant cost savings associated with reducing the average current in the accelerator and lengthening the bunch train. This reduces the beam loading, thereby reducing the required peak RF power, while requiring a longer RF pulse length which, if it can delivered, reduces some of the inefficiencies in the modulators. However, if the average current is reduced too much, the RF-to-beam efficiency begins to drop, causing the linac costs to rise again. This is illustrated in Fig. 2.1, where the linac cost is plotted against the time between bunches Δ_B while holding the charge per bunch and number of bunches constant at 1×10^{10} and 90, respectively. In the NLC/JLC design, the required number of RF power units was reduced by roughly 30% by going from a bunch spacing of 1.4 ns to 2.8 ns which resulted in a 15% cost savings; 1.4ns corresponds to 16 RF buckets at 11.424 GHz while 2.8 ns is 32 RF buckets.

Although there do not appear to be hard limits on the bunch train length, the damping rings become more costly and difficult (the damping ring costs are not included in LCOPT) and the RF pulse compression system becomes larger. In addition, potential limitations such as RF breakdown limits are not fully understood at this time. However, based on the NLC cost model, there do not appear to be significant gains for a bunch spacing larger than 2.8 ns, since the reduction in the number of klystrons is offset by the increase in the DLDS system. Thus, in the following studies, we have assumed a bunch length of roughly 250 ns which corresponds to about 90 bunches spaced by 2.8 ns. However, we also believe that it is desirable to maintain the option of operating with twice as many
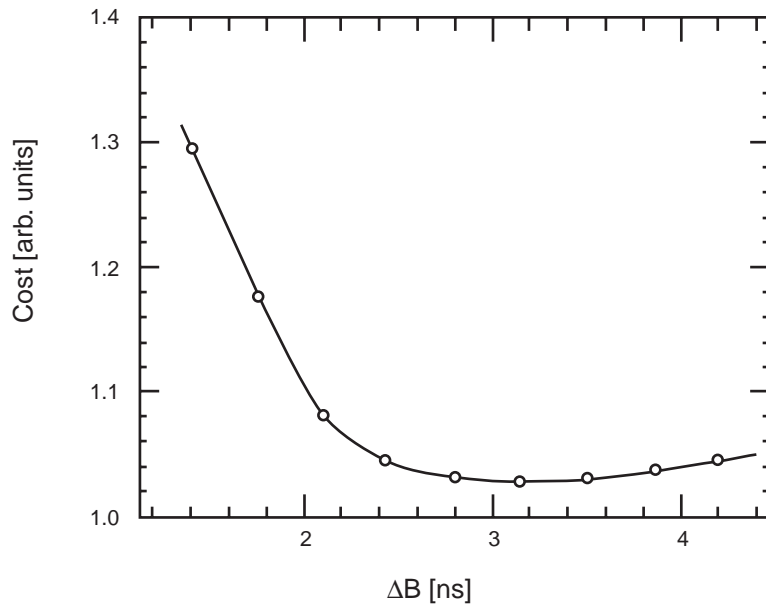
Figure 2.1: *Linac cost versus bunch spacing assuming a train of 90 bunches with a charge of* 1×10^{10}.

bunches at the 1.4 ns bunch spacing and lower bunch currents. This should reduce the emittance dilution due to short-range wakefields and the backgrounds due to beamstrahlung although it would increase the effects of the long-range wakefields. In addition, the 1.4 ns bunch spacing allows for the possibility of much higher luminosity as is discussed in Section 2.6.

Finally, the studies indicate that, with roughly 90 bunches per train, the primary cost benefit arises when increasing the bunch spacing from 1.4 to 2.1 ns with little further savings at 2.8 ns or beyond. In the future, this 2.1 ns bunch spacing should be reconsidered since it will decrease the length of the DLDS delay lines and simplify the damping rings. In addition, it may allow for further pulse compression (5x rather than 4x), reducing the number of klystrons and modulators at the cost of increasing the pulse compression complexity. Unfortunately, with the RF pulse compression systems considered, it not easy to change the compressed RF pulse length or the corresponding bunch train length after construction of the linacs. Thus, we should evaluate the possibility of higher pulse compression well before construction begins.

2.4.2   Accelerating Structure Length

Next, we studied the effect of the accelerating structure length. Longer structures are thought to have the following advantages: (1) the higher group velocity (for the same fill time) implies smaller wakefields and reduced alignment and construction tolerances, (2) longer structures have smaller transverse mode separation and thereby smaller long-range transverse wakefields, which reduces the need to interleave a number of structure types to reduce the long range wakefield, and (3) longer

structures are thought to lead to less total cost for the same accelerating gradient, because much of the cost is associated with the structure ends.

In Fig. 2.2, the linac cost, structure-to-structure alignment tolerances, and optimal average iris radius are plotted versus the accelerating structure length. Because the optimal attenuation parameter is roughly constant, the iris radii increase as the structure length increases to maintain a constant structure fill time. At the same time, the alignment tolerances increase rapidly with iris radii because the transverse wakefield is decreasing in strength. However, longer structures are also likely to be harder to construct and further R&D is needed to see if the construction is possible. At this time, a 1.8 meter structure DDS3 has been constructed at KEK which achieved roughly a factor of two better alignment than the $\pm 20\mu$m (or 12μm rms) required for JLC/NLC (see Chapter 7 for further discussion of the DDS3 structure).
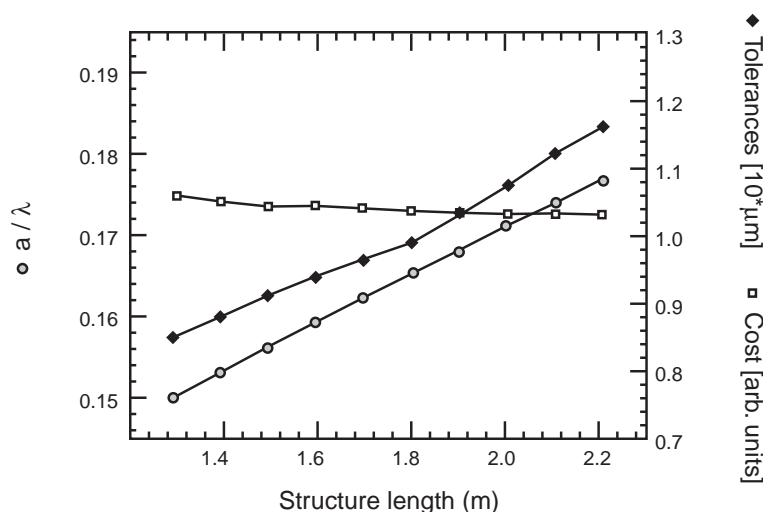
Figure 2.2: *Variation of optimal average iris radius (a/λ), alignment tolerances, and linac cost with structure length.*

In the subsequent discussions, a 1.8 meter long structure will be assumed. At this time, we believe that such long structures are manageable and thus represent both a cost savings and more relaxed alignment tolerances. This assumption should be revisited in the future after further experience in structure construction.

2.4.3   Iris Radius

The choice of the iris radius and thereby the structure fill time is a balance between the RF-to-beam efficiency and relaxed tolerances, which as described earlier, ease with increased group velocity. The variation of the AC power and cost versus the iris radius divided by the RF wavelength (a/λ) is shown in Fig. 2.3 while the structure-to-structure alignment tolerances and linac length are plotted in Fig. 2.4. Finally, the dependence of the bunch charge and the number of bunches per train is illustrated

in Fig. 2.5. For the assumed constant RF pulse length, the bunch train length decreases while the charge per bunch increases to maintain the luminosity. This is because the accelerating structure fill time increases as the iris radius decreases.
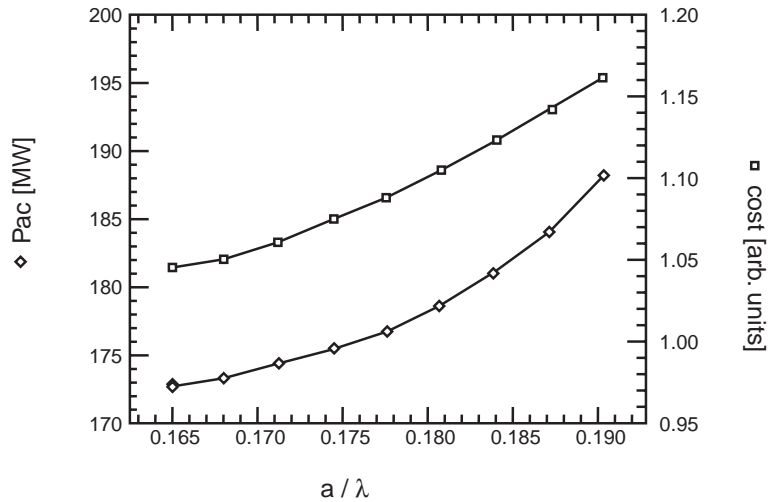
Figure 2.3: *Linac cost and AC power requirements for both linacs versus the average iris radius* (a/λ).

Moreover, the additional RF overhead required for BNS damping is not included in the above calculations. At $a/\lambda = 0.18$, roughly 3% additional overhead is required to generate and then remove the energy spread needed for BNS damping. This increases to roughly 5% at $a/\lambda = 0.165$ and thus the cost and AC power variation shown in Fig. 2.3 actually overestimates the increase in the cost and power significantly.

With our parameters, the RF efficiency is maximized at an $a/\lambda \approx 0.165$; notice the optimized value in Fig. 2.2. However, close to the peak, the dependence is rather weak and thus we have chosen an $a/\lambda = 0.18$ and a fill time of 104 ns. In this case, the required RF power and the linac costs are approximately 2% more than at the optimum, BUT the alignment tolerances are roughly 50% looser.
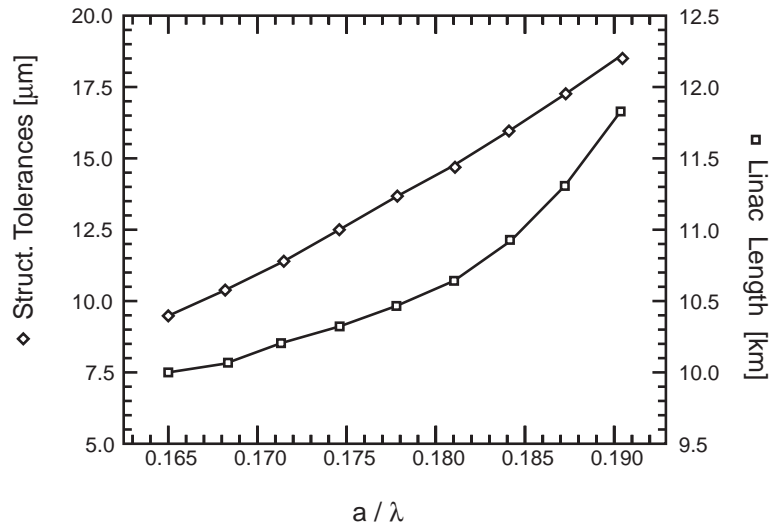
Figure 2.4: *Structure-to-structure alignment tolerances and length per 500 GeV linac versus the average iris radius* (a/λ).
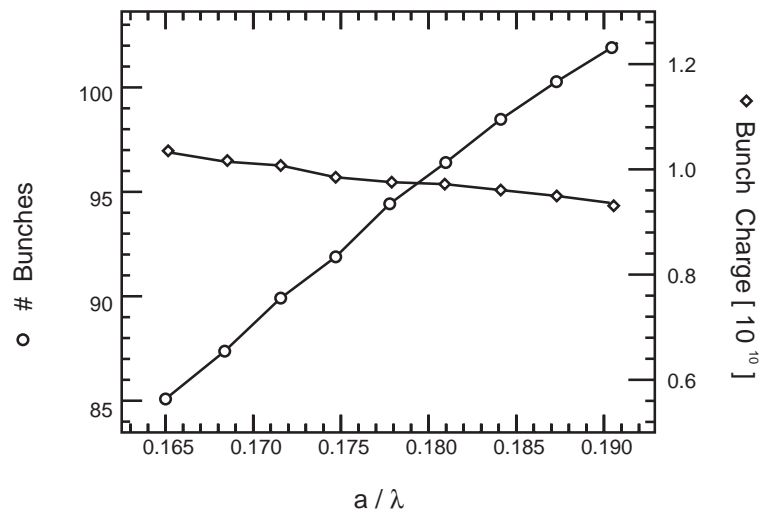
Figure 2.5: *Number of bunches per train and bunch charge versus the average iris radius* (a/λ).

2.4.4   Acceleration Gradient

Finally, we considered variations in the acceleration gradient that are consistent with our RF system, i.e. 75 MW klystrons with a $1.5\,\mu s$ pulse, and a factor of 4 compression using DLDS. As described in Chapter 6, the DLDS pulse compression system takes power from a number of klystrons and then divides the pulse in time and directs it to different groups of accelerator sections. To achieve a factor of four compression, the RF power from four or eight klystrons is directed to four groups of structures.

We considered four different configurations of the DLDS system. In all cases, we assumed that the system was powered with eight 75 MW klystrons but the RF power from each of the four feeds was used to power 2, 3, 4, and 6 accelerator sections, respectively. Strictly, the spacing between feeds and thus the RF pulse would also have to change with the number of structures per feed however, for this study, we ignored the RF pulse length variation to provide a more reasonable comparison. The results are illustrated in Fig. 2.6 where we have plotted the total AC power, the linac cost, the length per linac, and the structure-to-structure alignment tolerances versus the number of 1.8 meter structures that are powered from each DLDS feed.
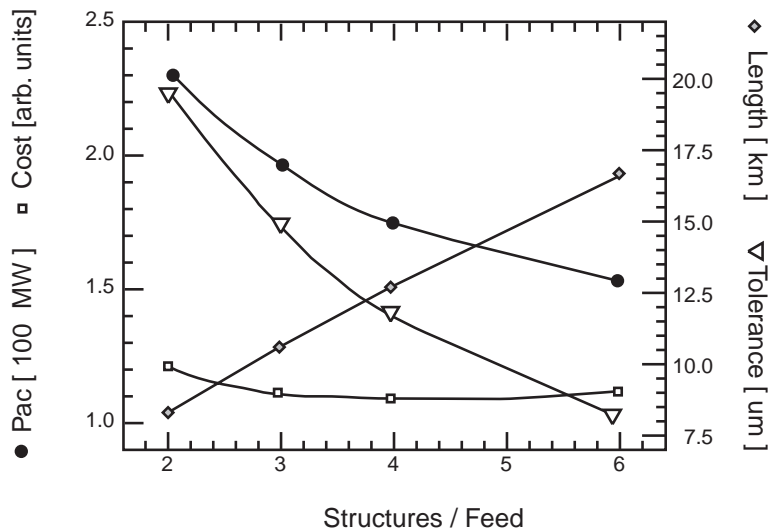
Figure 2.6: *Linac length, linac cost, alignment tolerances, and AC power requirements versus the number of structures per DLDS feed; the nominal case with 3 structures per feed corresponds to an unloaded gradient of 72 MV/m while 2 structures per feed and 6 structures per feed correspond to 88 and 51 MV/m, respectively.*

The linac cost is relatively flat as a function of the gradient however the tolerances tend to become tighter as the gradient decreases. This arises because the linac is longer and because the bunch must be lengthened to compensate for the short-range longitudinal wakefield. For these reasons, we have assumed 3 structures per feed with each structure receiving 170 MW of RF power which is at the high gradient side of the cost minimum.

2.5   Parameters for 500 GeV and 1 TeV cms

After studying the different hardware choices, we were able to calculate optimized parameters for the NLC/JLC at the nominal cms energies of 500 GeV and 1 TeV. The IP parameters are listed in Table 2.3 while the linac parameters are listed in Table 2.4. The collider is assumed to be based on:

- 75 MW klystrons with a $1.5\,\mu$s RF pulse

- DLDS pulse compression by a factor of four

- 1.8 meter RDDS structures with $a/\lambda = 0.18$

- 8% RF overhead for energy feedback, repair, and BNS damping

- Emittance dilutions which are between those in the JLC DS and the NLC ZDR designs as described in Section 2.2

With these choices, we have calculated three sets of parameters at each nominal center-of-mass energy to describe an operating range. Over this range, the luminosity is roughly constant but the bunch charge, length, emittance dilution, and IP focusing vary significantly. In addition, the cms energy varies because the beam loaded gradient depends on the average current that is accelerated. This operating range is defined to ensure operational flexibility of the collider complex. The hardware specifications are set by the most difficult requirements over the entire range. The SLC was initially envisioned to operate at significantly higher beam currents and larger spot sizes than were ultimately found to be optimal.

Finally, the nominal parameters are calculated for 120 Hz operation. However, values are also listed in parentheses which are calculated at 150 Hz and 100 Hz for the 500 GeV and 1 TeV parameters, respectively. The repetition rate considerations are discussed later.

	500 GeV			1 TeV		
	A	B	C	A	B	C
CMS Energy (GeV)	535	515	500	1046	1008	978
Luminosity w/ IP dilutions (10^{33})	7.7 (9.6)	7.0 (8.7)	6.0 (7.5)	15 (12.5)	13 (10.9)	11.6 (9.7)
Repetition Rate (Hz)		120 (150)			120 (100)	
Bunch Charge (10^{10})	0.75	0.95	1.1	0.75	0.95	1.1
Bunches/RF Pulse		95			95	
Bunch Separation (ns)		2.8			2.8	
Injected $\gamma\varepsilon_x/\gamma\varepsilon_y$ (10^{-8}m-rad)		300 / 3			300 / 3	
$\gamma\varepsilon_x$ at IP (10^{-8}m-rad)	400	450	500	400	450	500
$\gamma\varepsilon_y$ at IP (10^{-8}m-rad)	6	10	14	6	10	14
β_x/β_y at IP (mm)	10/0.10	12/0.12	13/0.20	10/0.125	12/0.15	14/0.20
σ_x/σ_y at IP (nm)	277/3.4	330/4.9	365/7.6	197/2.7	235/3.9	260/5.4
σ_z at IP (μm)	90	120	145	90	120	145
Υ (Beamstrahlung Param.)	0.14	0.11	0.09	0.38	0.30	0.25
Pinch Enhancement	1.41	1.36	1.50	1.41	1.46	1.5
Beamstrahlung δ_B (%)	4.5	4.0	3.6	10.9	10.3	9.7
# Photons per e^-/e^+	1.0	1.1	1.17	1.3	1.43	1.51

Table 2.3: *IP parameters for the JLC/NLC*

	500 GeV			1 TeV		
	A	B	C	A	B	C
CMS Energy (GeV)	535	515	500	1046	1008	978
Repetition Rate (Hz)		120 (150)			120 (100)	
RF overhead (%)		8			8	
Average RF phase (deg.)	10.6	11.7	13.0	10.9	11.4	13.1
Linac Tolerances (μm)	16.1	15.2	14.6	13.1	11.7	11.9
Unloaded Gradient (MV/m)		72			72	
Effective Gradient† (MV/m)	59.7	56.7	54.5	59.7	56.7	54.5
Active Linac Length (km)		4.3			8.9	
Power/Beam (MW)	3.4 (5.1)	4.2 (6.3)	4.6 (6.9)	7.1 (5.9)	8.4 (7.0)	9.3 (7.8)
# of Structures per linac		2484			4968	
Structure Length (m)		1.8			1.8	
Structure Iris (a/λ)		0.18			0.18	
Structure Atten. (τ)		0.47			0.47	
Shunt Impedance (MΩ/m)		90			90	
Fill Time (ns)		103			103	
Q		7800			7800	
# of Klystrons per linac		1584			3312	
Klystron Peak Pwr. (MW)		75			75	
Klystron Pulse Length (μs)		1.5			1.5	
Pulse Method		4/4 DLDS			4/4 DLDS	
Pulse Comp. Gain (85% eff.)		3.4			3.4	
RF System Efficiency (%)		38			38	
Total AC Power (MW)		94 (141)			191 (160)	

Table 2.4: *Main linac parameters for the NLC/JLC.* † *Effective gradient includes RF overhead (8%) and average RF phase* $\cos \overline{\phi}_{rf}$.

2.5.1 Emittance Budgets and Tolerances

The parameter sets listed above are based on an emittance budget as described in Table 2.5. This budget is tighter than that in the NLC ZDR but looser than that in the JLC DS. We believe that the budget is conservative in that we do not assume the use of direct emittance minimization techniques similar to those utilized very successfully in the SLC. While such techniques may eventually be used, they can be time consuming to implement and likely will not be available until the collider operation is relatively mature.

The tolerances listed in Table 2.5 are those on the accelerating structure-to-structure alignment due to the short-range transverse wakefields assuming that 60% of the emittance budget for the linac is allocated to this single source, e.g. 78% dilution in cases B. This is the most important source of emittance dilution although it is also the source most easily corrected using the direct emittance correction techniques mentioned above. Clearly, these tolerances must be attained using beam-based alignment techniques such as those described in Section 3.2.

Presently, the same budget is allocated to both the 500 GeV and the 1 TeV cms parameter sets. It should be noted that although the listed tolerances are looser in the 500 GeV cases, the components must be designed and constructed to attain the 1 TeV tolerances. However, the looser tolerances at 500 GeV will allow for rapid commissioning while optimizing the beam-based alignment techniques. Finally, because the dilution depends upon the beam charge, the tolerances are comparable for the low and high charge cases even though the budgets are significantly tighter in the low charge cases. However, with the tighter budgets, there is little allowance for other sources of dilution such as betatron coupling or dispersive errors.

	A	B	C
$\gamma\epsilon_x/\gamma\epsilon_y$ from DR $[10^{-8}]$		300 / 3	
$\Delta\epsilon_x/\Delta\epsilon_y$ in source (10 GeV) [%]	0 / 0	20 / 50	40 / 80
$\Delta\epsilon_x/\Delta\epsilon_y$ in linacs [%]	20 / 60	20 / 130	30 / 200
$\Delta\epsilon_x/\Delta\epsilon_y$ in beam delivery [%]	10 / 40	20 / 50	30 / 80
$\gamma\epsilon_x/\gamma\epsilon_y$ at IP $[10^{-8}]$	400 / 6	500 / 10	600 / 14

Table 2.5: *Proposed Emittance Budgets for JLC/NLC.*

2.5.2 Repetition Rate Considerations

The repetition rate was chosen to be a multiple of the AC line frequency. In the US, this is 60 Hz while in Japan it is either 50 or 60 Hz, depending on the region. We have studied the possibility of operation between 60 Hz and 180 Hz. At 60 Hz, the bunch train would be twice as long which allows for slightly more efficient operation. However the modulators and klystrons would have to generate RF pulses with twice as much energy per pulse and this could increase the cost of those systems significantly. At 180 Hz, the opposite holds; here, the bunch train length is decreased for the same luminosity and

the RF-to-beam efficiency decreases. In our cost model for the linacs, this results in roughly the same cost as for 120 Hz operation. However, the cost model does not include the increased damping ring costs due to the fact that the train length is shorter with respect to the 60ns allocated for the rise and fall times of the injection/extraction kicker.

For these reasons, we have listed parameters at 120 Hz and, in parentheses, listed reasonable alternate repetition rates which are multiples of the 50 Hz that might be desirable in certain regions of Japan.

2.5.3   500 GeV to 1 TeV Upgrade Path

The collider would initially be constructed with components to operate at a cms energy of 500 GeV. The RF modules would be identical to those needed for 1 TeV operation but only the first half of the linac RF would be installed and the remainder of the linac tunnel would be completed with vacuum spool pieces. All linac quadrupoles would be installed and those at the end of the linac would be operated at half strength to maintain the optics. Finally, to upgrade the beam energy, additional RF modules would have to be installed.

In specifying the parameters for the 500 GeV case, we have chosen to assume the same IP beta functions as at 1 TeV. These would be easily attained by the final focus at the lower beam energy although, assuming the same normalized emittances, the final focus apertures will have to be larger than for 1 TeV cms. With these relatively large beta functions, the charge requirements are almost identical to those at 1 TeV. In the future, we will study the option of using lower IP beta functions to reduce the beam charge and thereby ease the beam loading and alignment tolerances for the 500 GeV parameters. The relaxed beam tolerances would simplify the commissioning procedure.

2.6   Possible Higher Luminosity Scenarios

In this section, we discuss the possibility of operating NLC/JLC at higher luminosity than that quoted in Table 2.3. The three parameter sets **A**, **B**, and **C** in Table 2.3 are proposed to provide flexibility in the machine operation. Once the machine is well tuned so that any of these operating conditions can be met, there will be a possibility to further increase the luminosity, in particular in the low energy region, with additional effort. Table 2.6 shows two examples of higher-luminosity operation at E_{CM}=500 GeV:**X** is moderate and **Y** is more challenging. The basic assumption is that all of the systems (in particular, the sub-harmonic buncher) can accept a bunch spacing of 1.4ns. This means the lowest RF frequency in the system is 714 MHz.

The changes from **A** to **X** are:

- Halve the bunch spacing from 2.8ns to 1.4ns and double the number of bunches to 190, keeping

the train length constant.

- Decrease the bunch charge from 0.75×10^{10} to 0.55×10^{10} so that the total train charge is the same as in **C**.

- Decrease $\gamma\epsilon_y$ from the DRs to 2×10^{-8}m by improving the alignment.

- Maintain the same relative emittance increase in the linac with smaller absolute dilution.

- Improve the Final Focus for smaller $\beta^\star$s.

With **X** the structure alignment tolerance is slightly looser than in **A** because of the reduced bunch charge but the quadrupole alignment and long range beam breakup (BBU) tolerances will be a little tighter. **Y** further assumes an increase in the bunch charge to 0.70×10^{10} so that the train charge is larger than in **C** by a factor of 1.27. The major problem with the increased charge is the heavier beam loading which reduces the effective gradient. This either requires additional RF power (more structures or more klystron power) or reduces the final energy achievable.

		X	Y
Luminosity $/\mathcal{L}_A$		1.80	2.90
Nominal Lum. $/\mathcal{L}_{0,A}$		1.77	2.87
Bunch Population	10^{10}	0.55	0.70
No. of bunches/pulse		190	190
Bunch separation	ns	1.4	1.4
Linac length/beam[7]	km	5.54	5.97
AC power (2 linacs)	MW	126	136
Beam power/beam	MW	6.28	7.99
Loaded gradient[4]	MV/m	54.2	50.2
Bunch length σ_z	μm	80	80
$\gamma\epsilon_x$ (DR exit)	10^{-6}m	3	3
$\gamma\epsilon_y$ (DR exit)	10^{-6}m	0.02	0.02
$\gamma\epsilon_x$ (IP)	10^{-6}m	4	4
$\gamma\epsilon_y$ (IP)	10^{-6}m	0.04	0.04
Cavity align. tol.[6]	μm	18	14
β_x^*	mm	7	7
β_y^*	mm	0.08	0.08
IP beam size σ_x^*	nm	239	239
σ_y^*	nm	2.57	2.57
Diagonal angle σ_x^*/σ_z	mrad	2.99	2.99
Disruption param D_x		0.088	0.112
D_y		8.16	10.4
Pinch enh. H_D[5]		1.36	1.41
Υ_{ave}		0.127	0.163
δ_{BS}	%	3.52	5.27
n_γ		0.89	1.12

Table 2.6: *Parameters[1] for the high luminosity option for 500 GeV center-of-mass energy.*

1) E_{CM} is adjusted exactly to 500GeV in contrast to the three paratemer sets A, B, and C.

2.7 Beam Dynamics Issues with Injectors

The Linear Collider Injector System is designed to produce low emittance, $8 \sim 10$ GeV electron and positron beams at $100 \sim 150$ Hz for injection into the main linacs. Each beam consists of a train of 95 bunches spaced by 2.8 ns; each bunch has a population of up to 1.15×10^{10} particles. At injection into the main linacs, the horizontal and vertical emittances are specified to be $\gamma\epsilon_x = 3 \times 10^{-6}$ m-rad and $\gamma\epsilon_y = 3 \times 10^{-8}$ m-rad and the bunch length between $90 \sim 150 \,\mu$m. Electron polarization of greater than 80% is required. The need for low technical risk, reliable injector subsystems is a major consideration in the design effort.

In the JLC and NLC Injector Systems, the electron and positron beams are generated in separate accelerator complexes, likely, located at the entrances to the two main linacs. Each injector complex consists of a source system, a damping ring complex, and a prelinac and bunch length compression system. Although many aspects of the injector systems have been prototyped in the SLC at SLAC and with the ATF at KEK, there are significant additional challenges in the full LC designs. The JLC and NLC design concepts are summarized in Chapter 3 along with results from the ATF test facility at KEK. In this section, we will review a few of the issues that have a direct impact on or are directly impacted by our parameter choices.

- The long high intensity bunch train creates difficulties for both the electron and positron sources.

  - The present generation of semiconductor photocathodes used for the polarized electron gun exhibit a saturation effect which limits the total current that can be extracted. An intensive R&D effort to develop satisfactory cathodes is underway at Nagoya University, KEK, and SLAC.

  - For the positron target, the instantaneous energy deposition from the full bunch train may exceed the damage threshold of the target material. This problem is being addressed by an active program of simulations and materials studies.

  - The high average current also introduces significant beam loading in the bunchers, boosters and prelinacs, where phase manipulations in the bunchers and a combination of ΔF and ΔT compensation in the accelerating structures are used to produce a beam of the required uniformity and stability.

- One of the differences between the JLC and NLC injection systems is the emittance and the yield from the positron sources. In the NLC design, it is assumed that the positron yield will be relatively low and thus the acceptance must be large to capture as many e^+ as possible; for these reasons, the NLC uses an L-band accelerator after the positron target. The JLC design assumes a higher positron yield, in part, due to a higher energy electron beam incident on the positron target (10 GeV versus 6.2 GeV), and thus needs to capture a smaller positron beam emittance making an S-band linac after the positron target feasible. These differences also impact the pre-

damping ring design which must accept the undamped positron beam while providing sufficient damping so that later the beams can be fully damped in the main damping ring.

- The length of the bunch train as well as the collider repetition rate and the emittances from the particle sources directly impact the damping ring design. The rings must produce the fully damped bunch trains at the desired repetition rate. As any of the above parameters increase, the design of the rings become more difficult.

- The present JLC/NLC parameters specify a bunch spacing of 2.8 ns while preserving the option to also operate with 1.4 ns spacing. This restricts the minimum RF frequency used for the bunchers and damping rings to 714 MHz even though it would be easier to construct the RF systems at the lower 357 MHz.

- Finally, the desired bunch length and peak current impact the bunch compressor systems. Shorter bunches require more sophisticated systems. In addition, higher peak currents may introduce significant emittance degradation due to coherent synchrotron radiation; this is calculated to be a small effect in the present parameters.

2.8   Beam Dynamics Issues with Main Linacs

The X-band main linacs are required to accelerate trains of bunches from 10 GeV to 500 GeV, to produce a beam at 500 GeV whose energy spread is small compared to the bandwidth of the beam delivery system, and to transport the beam without excessive emittance dilution. One of the other focuses of Working Group 1 has been to study the alignment and construction tolerances in the main linacs.

The strong sensitivity of linac performance to alignment has several implications for construction of the RF structures and their supports. In addition to excellent structure straightness, the structures must be installed on supports which will preserve that straightness for the life of the facility. Since a 1.8 meter copper structure can distort at the micron level due to thermal changes, the temperature of the structures must be maintained at the level of one degree Centigrade during beam operations.

In addition to construction and installation, the tight alignment tolerances impact the operation of the main linac. In order to achieve acceptable alignment of the quadrupoles and structures, we have found that remote-controlled precision translation stages are needed for the magnets (with horizontal and vertical degrees of freedom) and the structure girders (with horizontal and vertical degrees of freedom at either end). The girder stages must be capable of one micron steps, while the step size required for the quadrupole stages is on the order of 100 nm. The optimal position of each magnet and girder is determined by measuring the beam position in each quadrupole and at either end of each structure; typically, this must be done with micron precision. Finally, it is necessary to know the offset between the magnetic center of each magnet and the electrical center of the associated beam

position monitor at the level of 1-2 microns; this we intend to determine via changing the strength of each quadrupole in turn and observing the downstream deflection to measure the beam-quadrupole offsets, and thus computing the quadrupole-monitor offsets by subtracting the monitor readings with all quadrupoles at design values.

In the following, we will describe some of the issues that were addressed by Working Group 1 (WG1). First, we discuss the detailed layout of the linacs. Next, we describe the wakefield calculations that form the basis of the tolerance estimates. This is followed by a discussion of the beam-based alignment techniques that are needed because of the tight alignment tolerances. Finally, we describe a number of the alignment tolerances that are important to preserve the high beam quality.

2.8.1   Linac Layout

The main linacs consist of a FODO quadrupole lattice interspersed with accelerating structures. The present JLC design calls for RF girders consisting of two accelerating structures while the present NLC design specifies RF girders with 3 accelerating structures per girder. At the low energy end of the linac, the quadrupoles are spaced by one RF girder and, then as the beam is accelerated, the spacing is increased by an integral number of RF girders—in the JLC design, the spacing goes from 1 2-structure RF girder to 6 RF girders at 500 GeV end [8] while in the NLC design, the spacing increases from 1 3-structure RF girder to 3 RF girders at the high energy end [9]. In both designs, the total focusing and the total number of quadrupoles is similar although the focusing is stronger at the low energy end of the JLC design because of the more closely spaced magnets and stronger at the end of the NLC design.

There are advantages and disadvantages of both girder lengths. At this time, the plan is to direct the 600 MW from the DLDS system into three accelerators structures—it may simplify the layout to have the three structures on a single girder. However, the weaker focusing due to the larger quadrupole spacing at the low energy end of the linac implies slightly tighter tolerances. In addition, there is some concern that the alignment of the three structure girders may be more difficult—see Tolerance Calculations. There has been a preliminary comparison of the differences [9], however these topics require further investigation.

Finally, there are two or three "diagnostic stations" located along the length of the NLC linac design. These stations provide emittance and energy diagnostics to allow verification of the beam properties. The stations are located at the transitions from one quadrupole spacing to the next. At this time, there is some question about the required spacing of these diagnostic stations. While recognizing the issue, JLC design has not yet determined where and how to implement these stations.

2.8.2   Wakefield Calculations

The detailed calculation of the short-range and long-range wakefields has been a topic of close collaboration for many years—long preceding the start of the ISG. Presently the short-range wakefields are

calculated using a modal representation and a high frequency roll-off assumed for a periodic structure. Over the last few years, a couple of relatively simple parameterizations have been developed that can be used to accurately estimate the wakefields [10, 11, 12].

Precise knowledge of the short-range wakefields is very important to be able to accurately estimate the tolerances and the difficulty of emittance preservation; most alignment tolerances are driven by the short-range wakefields. At this time, all members of the collaboration are comfortable with our present calculations.

Calculation of the long-range wakefields is in some sense more difficult because the long-time behavior of the wakefield depends on the detailed coupling among the cells of the structure and the coupling to the damping manifolds that reduce the Q's of the dipole modes from roughly 7000 to 1000. The calculations are further complicated because every cell of the 206 cells in each structure are different. The present approach uses sophisticated 3-D modeling to calculate the parameters of a number of the cells in the structure. Parameters for the other cells are then calculated by interpolation. These results are then input into a 2-band circuit model which is used to calculate the long-range transverse wakefield. Presently, we feel that this model should yield very accurate predictions of the long-range wakefield and these wakefields are being used in our simulations [13, 14].

The long-range wakefield calculations have been compared with measurements in the ASSET test facility at SLAC. In general, the agreement had been quite good. However, the amount and extent of available information on fabrication errors of the R&D structures tested to date are somewhat limited. Consequently, fully detailed comparison is difficult. This will be remedied with the RDDS1 accelerating structure that was assembled by KEK and SLAC, and should be tested in the ASSET facility in the spring of 2000. The long-range wakefield calculations as well as the ASSET measurements and the accelerating structure construction are discussed in greater detail in Chapter 7 of this document.

2.8.3   Beam-Based Alignment Techniques

As discussed above, the alignment of the main linac quadrupoles and RF structures to the beam will be supported by a high-precision beam position monitor captured in the bore of each quadrupole, high-precision monitoring of the beam position in two or three locations in each RF structure, and remote-controlled translation stages for each quadrupole and either end of each girder. The beam position monitors in the quadrupoles have similar performance requirements as those constructed for the Final Focus Test Beam [15] while the structure RF BPMs have been successfully tested in the ASSET facility at SLAC [14]. Considerable effort has been devoted to development of algorithms which convert the position readings of the BPMs into motion commands for the translation stages, since the quality of the linac alignment translates directly into the quality of the extracted beam. The required qualities of the alignment algorithm are the following:

- The alignment of the linac must be accomplished in a time short compared to the time required for ground motion to distort the alignment

- The alignment algorithm must be compatible with high-luminosity operation, since the afore-

mentioned ground motion effects will probably require repetition of alignment several times per day

- The algorithm must be properly interfaced with steering feedbacks in the linac and the beam delivery regions of the accelerator

- The algorithm must generate solutions which do not drive the translation stages past their limits

- The algorithm must limit emittance dilution due to single-bunch effects to a small fraction of the emittance budget.

A number of algorithms have been examined for the main linac, using both the JLC lattice [8] and the NLC lattice [16, 18]. While several algorithms appear to achieve the goals listed above, none has at this time been fully tested in simulation.

2.8.4 Main Linac Tolerances

The X-band main linacs are required to accelerate trains of bunches to 500 GeV, and to transport the beam without unacceptable dilution of the emittances (particularly the extremely small vertical emittance). It is this last constraint which results in the most difficult tolerances in the main linac: RF structure and RF girder alignment, quadrupole alignment, and RF structure straightness.

The phenomenon which drives main linac emittance dilution is the strong transverse wakefield generated by the X-band RF structure. The wakefield introduces the following difficulties:

- The short-range wakefield causes the tail of a bunch to be deflected relative to the head when the bunch is offset from the center of the RF structure, which directly increases the emittance.

- The short-range wakefield causes any initial betatron oscillation to increase as the beam travels down the linac, resulting in jitter amplification and direct emittance dilution (due to the head-tail effect described above). In order to mitigate this effect, the linac RF is phased to reduce the energy of the tail relative to the head; this effect combines with the chromaticity of the quadrupoles to provide BNS Damping of the jitter amplification. However, this causes the beam energy spread in the linac to be relatively large, which in turn causes emittance dilution due to dispersion when the bunch is offset from the center of the quadrupoles in the linac.

- The deflecting wakefields in the RF structure persist after the generating bunch has departed, and cause the centroids of the subsequent bunches in the same train to be deflected relative to the leading bunch. These long-range wakefields cause the total emittance of a bunch train to be enlarged even if the single-bunch emittances are preserved. The long-range wakefields are damped through a combination of damping and detuning (see above); however the higher-order mode detuning is only effective if the electron beam is offset from the center of each cell in a given RF structure by the same distance, and therefore control of the long-range transverse wakefield places additional tolerances on the straightness of each RF structure, as well as the relative angle of the beam through the structure.

In addition to the alignment tolerances listed above, which are related to emittance preservation, there are tolerances on systematic and random errors in klystron phases and amplitudes; these tolerances are determined by the stability requirements of the end-of-linac energy, set by the demands of the detector, and the acceptable end-of-linac energy spread, which is set by the narrow bandwidth of the final focus. The tolerance on the optical match between the beam and the linac lattice is set by the degree of filmentation in the linac; for a fully filamented beam a 25% optical betatron mismatch will cause 6% emittance dilution. Finally, there are a variety of second-order effects: for example, misalignments coupled with errors in RF phase or amplitude can potentially produce an emittance dilution which is larger than that obtained with misalignments of an optically perfect system. Such combinations of errors have the potential to further tighten the linac's tolerances.

The sensitivity of the main linac to various errors and misalignments can generally be calculated analytically. These calculations are confirmed through the use of simulation programs which perform tracking of the electron beam in the presence of errors, misalignments, wakefields, etc. The main program used at SLAC for linear accelerator simulation is LIAR (Linear Accelerator Research program); the main program used at KEK for this purpose is SAD (Strategic Accelerator Design)[17]. The algorithms used in the two programs have not yet been directly cross-checked with a common beamline and set of assumptions about its errors; this is planned for the near future. However, SAD simulations of the JLC linac and LIAR simulations of the NLC linac produce quantitatively similar results. For example, allowing a 3% "overhead" in installed RF voltages produces acceptable stability against incoming beam jitter (via the aforementioned BNS damping mechanism) in both linac designs. The following sensitivities to errors and misalignments have been studied for the 1 TeV CM main linac, assuming a normalized vertical emittance of 3×10^{-8} meter-radians on injection into the main linac:

- Random, uncorrelated RF structure-to-structure misalignments: 12 microns results in 78% dilution of the single-bunch emittance

- Static offsets between quadrupole centers and BPM centers: 2 microns results in 35% dilution of the single-bunch emittance [8]

- RF structure bowing: a total bow of 60 microns over the 1.8 meter length results in 13% dilution of the single-bunch emittance [19]

- RF structure angle with respect to the beam trajectory: a slope of 80 microradians results in 13% dilution of the multi-bunch emittance [19]

- Uncorrelated misalignments of the cells within an RF structure: 8 microns results in 13% dilution of the multi-bunch emittance [20]

- Misalignments of RF structure cells with respect to nearest-neighbor cells (random-walk misalignments): 3.4 microns results in 13% dilution of the multi-bunch emittance [20]

- Random phase errors in which all 12 structures on an 8 klystron power unit have the same phase: 10 degrees of rms phase jitter results in 1.5% average energy loss and 0.35% rms energy jitter error [8, 21]

ISG Progress Report, April, 2000

- Systematic phase error for the main linac (or injection-time error): an error of 1 degree of X-band results in a 0.3% final energy error and a 0.15% rms final energy spread

- Random amplitude errors in which all 12 structures on a power unit have the same amplitude error: 6% rms amplitude jitter results in 0.27% rms energy jitter [8, 21]

- Systematic amplitude error for the main linac: a systematic error of 1% in RF amplitude results in a 1% error in final beam energy

- Quadrupole magnet rotation errors: 300 microradian rms rotation errors result in 5% vertical emittance increase.

In addition to the sensitivities studied above, we have considered the second- order effects of RF errors combined with misalignments, and in general the additional emittance dilution incurred is small. For this reason we expect that the sensitivity to model errors in the main linac will also be small, although no systematic study of same has yet been performed.

Further studies and calculations of main linac sensitivities and tolerances include:

- A careful comparative study of a linac with 2 RF structures per girder versus using 3 RF structures per girder.

- A study of the use of orbit bumps in the linac to perform global emittance correction; in principle such bumps could ease some of the linac alignment tolerances.

- Recharacterization of the linac sensitivities to misalignments and errors as tolerances on each class of error, in which the relative difficulty of correction or prevention of errors is taken into account.

- A full simulation of the main linac with all of the tolerances as specified and all correction algorithms operating, to ensure that unforeseen higher-order effects are properly taken into account.

2.9 Beam Dynamics Issues with Beam Delivery

The role of the beam delivery system is to transform the beam which is extracted from the main linac into a beam which is acceptable to the detector. In practice, this means that the beam delivery system must:

- Remove the particles at large amplitudes which would cause unacceptable detector backgrounds,

- Focus the beam to the very small sizes listed in Table 2.3,

- Provide the IP crossing angle via a set of achromatic arcs, such that the linacs may be constructed in a single straight line,

- Allow a transverse and a longitudinal offset between two IR halls,

- Provide a variety of beam diagnostic and correction systems prior to the collision point.

2.9.1   Beam Delivery System Parameters

The principal beam delivery system parameters are: the IP betatron functions ($\beta^*_{x,y}$), the free length from the last quadrupole to the IP (L^*), the crossing angle, the bandwidth (energy range over which a given collection of magnet settings will produce adequate luminosity), the collimation depth, the collimation efficiency, and the system length.

IP Beta Functions

All linear collider designs presently under consideration experience *disruption*, which is the focusing of each beam by the opposing beam (a very intense form of beam-beam tune shift). Disruption has the positive effect of increasing the luminosity by decreasing the effective beam size at the IP, but also has several negative effects: it increases the angular divergence and energy spread of the outgoing beams (making them more difficult to transport to their dumps), causes a burst of photons from the focusing ("beamstrahlung") which must also be transported safely out of the detector, and causes the production of low-energy e^+e^- pairs which result in detector backgrounds. Since the severity of the disruption is proportional to the rms distance of particles in one beam from the center of the other, and since the horizontal emittance is much larger than the vertical due to the planarity of the damping rings, the value β^*_x is kept relatively large (typically 2 orders of magnitude larger than the β^*_y) in order to maintain disruption at acceptable levels. For the parameters in Table 2.3, the luminosity is increased by 40% to 50% over the geometric luminosity and the energy spread is increased to 10% at 1 TeV CM by the disruption and beamstrahlung. Under these conditions, beam loss in the extraction line for the 1 TeV CM case is approximately 500 watts, due primarily to overbent and over-focused particles in the low-energy tail. Increasing the disruption would lead to dramatically increased losses in the extraction line, which are not believed to be tolerable.

The disruption effect is relatively insensitive to β^*_y, so in principle the value of β^*_y should be set as low as possible. However, there are several practical limitations on β^*_y:

- If the value of β^*_y is smaller than the rms bunch length σ_z, the luminosity and disruption are both reduced due to the "hourglass effect"

- Small values of β^*_y will cause the vertical IP divergence, $\theta^*_y \equiv \sqrt{\epsilon_y/\beta^*_y}$, to be increased, which in turn increases the beam size in all final focus magnets; the acceptable range of magnet lengths and apertures limits acceptable values of β^*_y

- Small values of β_y^* require a stronger final doublet to produce the required demagnification; this in turn causes more chromaticity, which requires more chromatic correction; increased chromatic correction can be achieved only by increasing the bend strength in the final focus (which dilutes the horizontal emittance), increasing the length of the final focus, or decreasing the bandwidth of the final focus (by strengthening the sextupole magnets used for chromatic correction)

- Synchrotron radiation losses in the final doublet itself result in dilution of the IP beam size; consequently, a linear collider with a given final focus design and vertical emittance has a minimum beam size which can be achieved (this size is called the "Oide Limit," and the effect is known as the "Oide Effect"[22]).

Consideration of these limitations led to the choice of $\beta_x^* \approx 10$ mm and $\beta_y^* \approx 125$ μm.

Free Length

The chromaticity of a final doublet system increases with the field-free length between the final quadrupole and the focal point (L^*). Since chromaticity correction is costly in either horizontal emittance growth, final focus bandwidth, or total system length, the value of L^* must be kept as small as possible. For value of L^* smaller than 2 meters, however, it was found that the improvement in final focus performance was marginal, since the effects of synchrotron radiation come into play more strongly for shorter L^*. In addition, extraction of spent beams is simplified by a larger L^*, and larger L^* also permits more of the detector to be installed in the space between final quadrupoles. For these reasons, an L^* of 2.0 meters was selected.

Crossing Angle

The principal purpose of the IP crossing angle is to eliminate "parasitic" beam crossings in the long bunch train, ensuring that each bunch collides with one and only one opposing bunch, and that the collision occurs at the interaction point. The crossing angle also assists in the extraction of the spent, disrupted beams since it prevents the spent beams from exiting down the small aperture used by the opposite beam for entry, and it protects the detector from muons generated in the upstream collimation system and synchrotron photons generated by the quadrupoles in the linac. All of these functions are optimized by a larger crossing angle, but there are several limitations. First, if the crossing angle becomes comparable to the diagonal angle of the beam ($\sigma_x/\sigma_z \sim$ few mrad) the luminosity is degraded unless a crab-cavity is used to realign the beams at collision point; the feasibility of the crab-cavities has not been experimentally verified. Second, as the crossing angle becomes large ($20 \sim 40$ mrad), the deflections and analomous dispersion that arise from passing through the IP solenoid at an angle become more difficult to correct.

Both the JLC and NLC designs make use of a large achromatic arc following the collimation section to eliminate muons and other debris (8 mrad for JLC versus 10 mrad for NLC); the JLC design then has a reverse bend of 4 mrad in the final focus, for a net crossing angle of 8 mrad. The NLC final

focus has very little net bending, resulting in a net crossing angle of 20 mrad. In the NLC, the effects of the solenoid and crossing angle result in a 1.5% reduction in luminosity at 1 TeV ECM, primarily due to synchrotron emission in the solenoid; the effective horizontal beam size is reduced through use of a crab cavity in the final transformer. Thus, the JLC design does not need crab-cavities but has a tighter and therefore more difficult extraction of the disrupted beam, while the NLC design has crab cavities with the extremely tight phase tolerances.

Bandwidth

The total energy range over which the final focus must provide the required demagnification without retuning is set by the expected energy spread and energy jitter of the beams produced by the linac. The linac energy spread is determined by how much accelerating voltage is afforded to cancel out the BNS damping energy spread at the end of the linac, and the energy jitter is set by the RF jitter tolerances in the linac. For the present main linac design, the total final focus bandwidth must be no smaller than 1%. As discussed above, this decision sets limits on the chromatic aberrations which are permitted in the final focus, which in turn constrains the design of the chromatic correction system and the selection of IP parameters.

It is worth noting that increasing the charge per bunch will increase the beam loading; therefore, operation at full energy with a larger charge than shown in Table 2.3 implies a larger post-linac energy spread than is presently foreseen in the design. This will in turn require a larger final focus bandwidth than the present parameters demand.

Collimation Depth

The collimation depth is set primarily by synchrotron radiation emission within the final doublet. Ray traces in the NLC design have shown that particles which are more than 40 σ_y or 8 σ_x from the beam center will produce radiation in the final quadrupole which will cause unacceptable backgrounds in the detector. Consequently, the collimation system must remove all particles which are at or beyond these limits; the requirements are similar in the JLC design.

The collimation depth in energy is determined by the energy acceptance of the final focus (energies over which beams are transported safely to the dump, as opposed to the bandwidth, which is the energy range which produces luminosity). Early estimates indicated that ±4% off-energy particles would be transported safely to the main dumps, but more recent studies indicate that the energy acceptance may be narrower than this.

Collimation Efficiency

The collimation efficiency is a measure of what fraction of particles which are at amplitudes larger than the collimation limits remain in the beam after the main collimation system. Imperfect collimation efficiency can be due to scattering off of collimator jaws rather than stopping, or imperfect phase

coverage of the collimator jaws. Large-amplitude particles which escape the main collimation system must be collimated in the final focus; the more efficient the main collimation system design, the simpler the final focus collimation system can be.

An additional category of particles to be collimated in the final focus is particles which are scattered out of the beam core to large amplitudes in the beamline between main collimation and final focus. This scattering is due to Coulomb scattering off of the residual gas in the vacuum chamber, and also scattering off of thermal photons. Estimates indicate that 10^3 to 10^4 particles per bunch train will scatter from the core into the halo between the main collimation system and the final focus. Therefore, if the halo which is collimated in the main collimation system is expected to remove 10^9 particles per bunch train, a collimation efficiency which permits 1 particle out of 10^6 to rescatter into the beam is adequate for this design.

2.9.2   Comparison of JLC and NLC Beam Delivery Systems

In general the beam delivery systems of the JLC and NLC are quite similar. This is not unexpected, as the requirements, shown in Table 2.3, are identical. However, the systems differ in several particulars:

- The JLC collimation system uses strong sextupole magnets to increase the size of the beam "halo" (the particles with large amplitudes) by a larger factor than the beam "core" (the particles with small amplitudes) is increased; the NLC system uses conventional optics (quadrupoles only) to make the halo large enough to collimate. In principle the sextupole magnets of the JLC system can simplify collimation, as the halo is more diffuse and far from the core at the collimator location.

- The JLC and NLC beam delivery arcs are similar in total angle (8 mrad for the former versus 10 mrad for the latter); however the JLC final focus then has a reverse-bending angle of 4 mrad, making the total crossing angle 8 mrad, while the NLC crossing angle is 20 mrad total. The NLC crossing angle requires a crab cavity near the IP to achieve acceptable luminosity, which the JLC angle does not; however the small JLC crossing angle makes extraction of the disrupted beam from the detector more difficult.

- The NLC final focus uses the basic optics of the Final Focus Test Beam, in which the dispersion function is equal at the two sextupoles of each chromatic correction section, while the JLC uses an asymmetric-dispersion scheme. The NLC system uses a special set of sextupoles for bandwidth optimization, which are absent in the JLC system.

- The NLC final doublet includes both electromagnets and a permanent magnet embedded in the detector; the JLC design uses electromagnets for all doublet components. The NLC system has the advantage of a smaller, lighter magnet inside the detector which does not require cooling and thus can be made more stable against vibration, while the JLC design is easier to operate because all of the magnets can be scaled in strength. The combination of the JLC final doublet magnet and its small crossing angle also presents problems in extracting the disrupted beam and its halo of beamstrahlung photons.

The primary work to be done on the beam delivery system in the context of the SLAC/KEK collaboration is a detailed study of the benefits and liabilities of each system (ease of tuning, tolerances, bandwidth, machine protection, construction difficulties, etc.). Once that is complete a composite system design is possible, which utilizes the best features of each of the present ones. For example, a final focus system which combines the JLC's asymmetric dispersion and the NLC's bandwidth sextupoles could potentially achieve a high bandwidth in a relatively short system.

2.10   Applications of the Linear Collider Facility

2.10.1   Introduction

While the primary purpose of both the JLC and NLC linear collider projects lie in studies of high energy physics in the sub-TeV to TeV energy ranges, the availability of ultra-low emittance, high energy electron and positron beams could provide opportunities for research in other branches of science:

1. Low-emittance, short bunches of electrons at high energies, with suitably low energy spread, could be potentially used to produce FEL photons.

2. Low-emittance, high energy electron and positron beams extracted at various portions of the linear collider facility could be used for fixed-target experiments using either the incident particle beam or creating high energy photons for either high energy or nuclear physics. It should be noted that although the beam parameters may not always necessarily satisfy the excitation conditions of FEL emission, the beams can be still used to produce high energy photons.

In this section, we summarize briefly some considerations and issues concerning these applications at JLC/NLC. While these studies are at a rather preliminary stage, it is hoped that they provide useful material for discussion during future development of linear collider designs.

2.10.2   General Discussions on FEL Excitation

It has been known for some time that a high power, x-ray FEL based on SASE (self amplified spontaneous emission) might be included in electron-positron linear collider facilities. The high quality electron beam (lower emittance, shorter bunch, higher energy compared with existing electron accelerators) is very attractive for use as an FEL source. For example, the design study for the TESLA collider [23] has an extensive discussion on this possibility.

Unfortunately however, the characteristics of the electron beam from the damping ring of NLC/JLC, is not adequate for exciting FEL as is, depending on the desired wavelength of FEL photons. A critical condition for FEL excitation is that the spread in the longitudinal velocities of particles within a bunch be kept small. This velocity spread arises from the energy spread and betatron oscillations of the particles. For a given energy spread and transverse emittance, one can choose the betatron focusing parameters in the undulator section to balance the two effects and this determines the minimum wavelength of FEL excitation.
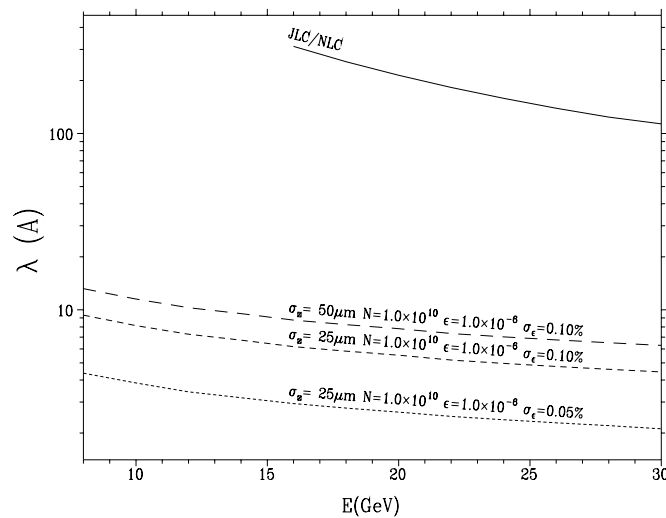

Figure 2.7: *Minimum FEL wavelength as a function of the beam energy.*

Fig. 2.7 shows the expected minimum wavelength as a function of the energy for JLC/NLC and other electron beams.[1] The curve at the top is that for the collider parameters of NLC/JLC in the X-band main linac. The expected wavelength is generally larger than 100 Angstrom, and is not very promising for prospective users of shorter wavelength photons.

It has been thought that the damping ring and/or the high quality positron beam, which would be part of a linear collider such as JLC/NLC, was an advantage. However, these two points do not help for an FEL; the horizontal emittance determines the FEL performance and positrons are not needed. RF guns with recent technologies are expected to provide better parameters for FEL operation. In the following we will consider electron beams from an RF gun without using the damping rings.

Fig. 2.7 also shows three other curves for different beam parameters. From this we see that, for an FEL with $\lambda \sim 10$ angstrom, the beam should have a bunch length $\lesssim 50\mu$m and an rms energy spread $\lesssim 0.1\%$. An improved RF gun is expected to give a normalized transverse emittance of 1×10^{-6}m·rad and a bunch length of a few picoseconds at a bunch intensity $\sim 10^{10}$. To accelerate this beam and to make the bunch length shorter, we can make use of the S-band linac and the second bunch compressor.

---

[1]This figure is based on a simple, optimistic calculation for the sake of an order-of-magnitude discussion. The calculation does not include effects such as the diffusion due to incoherent synchrotron radiation, interruption of undulator fields by focusing magnets, etc.

The designs of these systems are originally optimized for collider operation. However, they can be used for an FEL, if some care is taken, particularly with the control of the energy spread and the coherent synchrotron radiation.

To obtain a wavelength as short as possible, we need to accelerate beyond the energy of the S-band prelinac which is set at $8 \sim 10$ GeV. In using the first portion of the X-band main linac for an FEL, the primary issue is the energy spread due to the longitudinal short-range wakefield. This is a correlated energy spread. However, since the bunch length is much shorter than for standard collider operation, it is very difficult to do the energy compensation using off-crest acceleration.

On the other hand, the transverse dynamics in the X-band linac are not an issue because the bunch length is shorter and the vertical emittance for the FEL is much larger than for collider operation. Using C-band instead of X-band will make the energy spread problem slightly (about factor of 1.5) better. This is because of the smaller wakefield. However, the improvement is not drastic, because the off-crest compensation is even harder.

2.10.3   Possible Implementations of the FEL Subsystems at NLC/JLC

As a simple starting point for a possible FEL design, we begin with the parameters of the LCLS [24] (Linear Coherent Light Source) x-ray FEL, now being planned at SLAC. Table 2.7 shows LCLS-type parameters. Some of the fundamental requirements on the electron beam density for FEL applications are quite different from those at JLC/NLC.

As noted the phase space density of the NLC/JLC beam is not matched to that needed by an FEL. Thus, to add an FEL to the facility, there must be some method of creating the required phase space. This might be achieved by a few modifications to the bunch compressor systems as well as the use of an RF photoinjector gun at the entrance to the 2-GeV booster linac. Possible operational scenarios include:

1. Introduce an additional S-band linac at the end of the prelinac and add a new bunch compressor. This becomes very similar to the LCLS design. It shares much of the JLC/NLC infrastructure.

2. Add a parallel X-band linac adjacent to the main linac and run the injector linacs at a higher repetition rate.

3. Use the main X-band linac in dedicated FEL operational mode. This reduces the luminosity delivered for high energy physics or requires operating the low energy portion of the collider at a higher rate.

Each of the schemes would be very similar through the beginning of the second bunch compressor. The first scenario could be designed as nearly a straightforward copy of the LCLS. Since the S-band injector linacs have relatively long filling times, the FEL beam can be accelerated on the trailing edge of the RF pulses and, at the end of these injector linacs, it would then be injected into a dedicated linac for the FEL. The second and third scenarios are similar in that the injector linacs would accelerate

Electron energy [GeV]	14.3
FEL x-ray radiation wavelength [A]	1.5
Repetition rate [Hz]	120
Bunch charge [nC]	1.0
Normalized emittance in undulator (rms)[mm-mrad]	1.5
Peak current required [kA]	3.4
Energy spread (rms, uncorrelated) [%]	0.02
Energy spread (rms, correlated) [%]	<0.1
Bunch length (rms) [μm]	24
Length of undulator [m]	112
Undulator period [cm]	3
Number of undulator periods	3328
Undulator peak field [T]	1.32
Undulator gap [mm]	6
Undulator parameter	3.71
FEL parameter	4.7×10^{-4}
Field gain length [m]	11.7
Saturation peak power [GW]	9
Peak brightness [photons/s/mm^2/mrad^2/0.1%]	10^{33}
Average brightness (single-bunch)	4×10^{22}

Table 2.7: *Parameters for the proposed Linac Coherent Light Source at SLAC*

the FEL beam through the second bunch compressor. At this point, the FEL beam would be injected into a dedicated FEL X-band linac which is only a few hundred meters in length. The last scenario is distinct in that it would use the main X-band linac which would either operate at a higher repetition rate or with reduced rate to the high energy IP. These three options are illustrated schematically in Fig. 2.8 and the last scenario is described in some detail below.
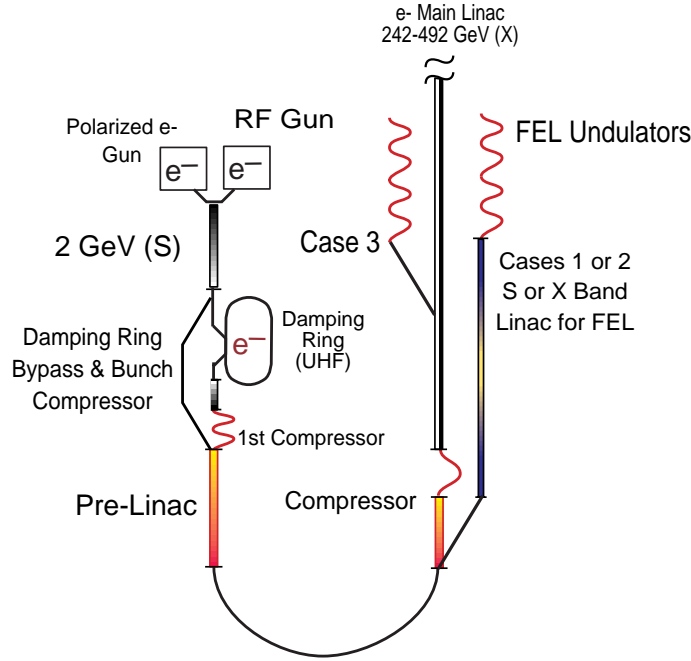

Figure 2.8: *Schematic of NLC/JLC injector with modification for an FEL. The additional components are listed in bold type and denoted as cases 1–3.*

An RF photo-injector gun is used at the beginning of the 2-GeV S-band booster linac. Each bunch contains a charge of 1 nC with an rms bunch length of 800 μm (2.7 psec). The transverse normalized emittance (equal in x and y) required from the gun is 1 μm. The bunch is accelerated to 2 GeV in the booster-linac at 20° off crest of the RF. A new 2.8 m long chicane in the damping ring bypass line is used to compress the bunch to 360 μm rms with the chicane having an R_{56} =30 mm. The JLC/NLC BC1 wiggler is not used for the FEL beam, since the main damping ring is bypassed in the FEL mode. The bunch is then accelerated in the 6 GeV S-band prelinac and turned around in the BC2 arc. The prelinac phase is set to 6° off crest to minimize the energy spread in the arc ($<0.05\%$ rms). With this small energy spread the arc does very little to the bunch length. At this point, the FEL beam could be separated into a dedicated beamline with an additional bunch compressor, and subsequently accelerated as outlined for the first two scenarios. The rest of this description is specific only to the third scenario listed above.

After the arc, the bunch is decelerated in the BC2 X-band section (from 8 GeV to 7.2 GeV) by running at an amplitude of 60 MV/m and a phase of 140°. This decelerates the beam slightly and introduces a nearly linear energy-time correlation for compression. It also helps to compensate the non-linear

effects of the next chicane. The voltage required in the X-band section is 65% more than for the nominal collider mode compression. This requires a length of $\sim$18 meters, or ten 1.8-meter sections, rather than the six sections required for the collider compression. Possibly the four additional sections can be powered for the FEL and switched off for the collider.

The bunch then enters the nominal NLC/JLC BC2 chicane where $R_{56} = 43$ mm and the bunch length is reduced to $24\,\mu$m rms. The energy spread is still fairly large here (0.86% rms) but is also highly correlated along the bunch. The next 110 meters of main X-band linac accelerates the beam to 14.3 GeV while the longitudinal wakefield reduces the correlated energy spread. A higher energy is also possible if the increased wakefield in the longer linac can be compensated in some manner. The final energy spread (0.18% rms) and bunch length (23 μm rms) are shown in Fig. 2.9. Note that the energy spread of the beam core is $\sim$0.06% rms. The full rms of 0.18% is exaggerated by the weakly populated energy tails. The temporal distribution along the short bunch is not very flat. It has peaks which may exceed 10 kA. Most of the bunch should saturate ($>$3.4 kA), but the shape might be improved by more careful optimization of the whole system.
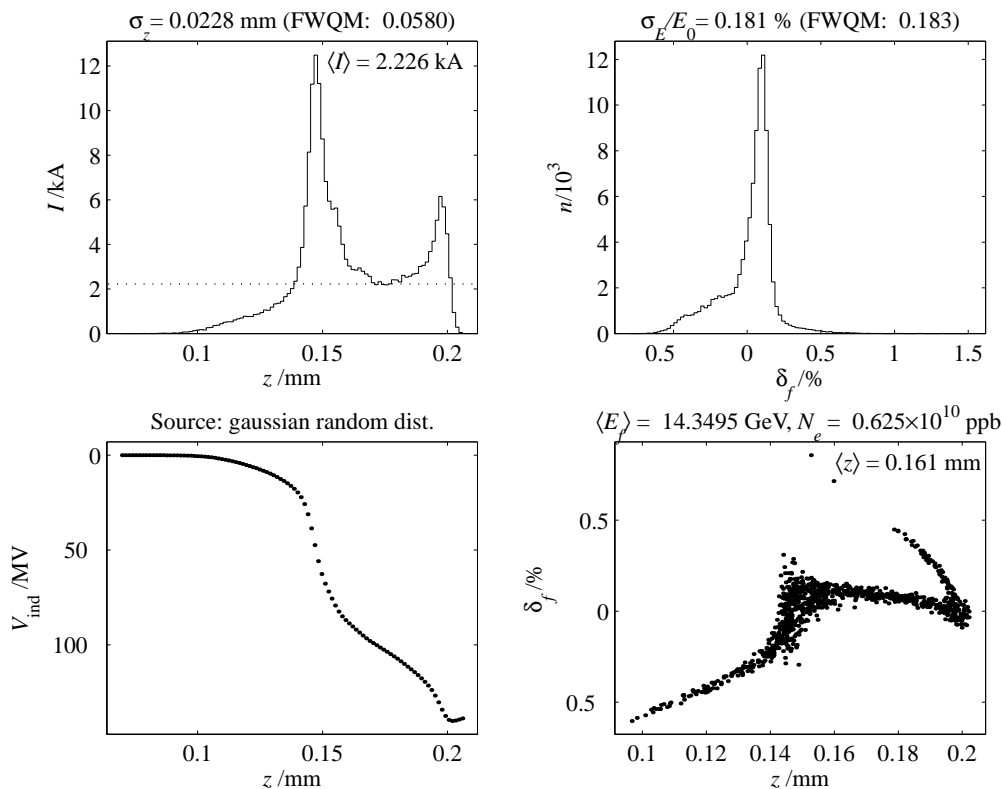

Figure 2.9: *Temporal distribution (top-left), energy distribution (top-right), beam-induced voltage (lower-left), and longitudinal phase space (lower-right) at 14.3 GeV after 110-meters of X-band main linac.*

The primary considerations with these scenarios are:

- An additional compressor is needed in the damping ring bypass line.

- The RF gun must be installed and operated.

- The prelinac must be operated in a parasitic mode.

- The RF voltage in the BC2 X-band section must be increased for the 3rd scenario.

These issues need to be studied in some detail to determine the best scenario. The smaller horizontal emittance required for the FEL is also a potential issue as there many be difficulties with emittance preservation in, for example, the BC2 arc with synchrotron radiation.

2.10.4   Use of Extracted Beams

The high energy beams generated by the main accelerators would likely have a number of uses other than the primary physics experiments. For example, it is almost certain that a facility would be needed for generating very low current test beams with close to the full beam energy. These could be generated by capturing some of the beam energy tail and redirecting it to an alternate location. The best location for these test beams will have to be considered in detail. There are also important machine and personnel protection issues involved which will have to be examined.

In addition, the high energy beam from the JLC/NLC can be used to generate very high intensity gamma rays for nuclear physics and other applications. We assume that at these energies, there will only be incoherent emission. For example, gamma rays of energies from 2 to 50 MeV can be produced with electron beams of energies from 50 to 250 GeV. This would require an undulator with a 100 m length, 1 cm period, $K = 0.5$ and a 4mm gap, which is considered feasible. The number of photons produced would be roughly 2×10^{11} per bunch, or 2×10^{13} per train. For the 250 GeV case, this corresponds to an average power of $\sim$75KW in the gamma beam. The output of the undulator can be collimated to produce a narrow spectrum (limited by the 0.3% energy spread of the electron beam). There will be $\sim 10^{10}$ gammas per pulse ($\sim 10^{14}$ per second) in this energy width in a $\sim$500 micron beam with a sub microradian divergence angle. The gamma ray pulses will also have a sub-picosecond time structure which may be useful for some experiments.

There are many possible uses of such a photon beam. One example which might attract special attention would be to use an undulator of this type at an energy of 150 GeV or higher to provide sufficient gammas for conversion to polarized positrons for a NLC/JLC polarized positron source. A practical problem, however, is it would be difficult to transmit the main NLC beam through the undulator without degradation of the energy spread and emittance. Instead, several alternatives are possible:

- Use a pulsed magnet to divert some of the bunch trains into the undulator. This is simple, but it decreases the average luminosity for high energy physics.

- Use a fast kicker to divert some of the bunches within a bunch train. This provides 120Hz photons at a small loss in luminosity.

ISG Progress Report, April, 2000

- Operate the front of the machine (150 GeV) at 240 Hz with an RF gun. This would allow use of the system for polarized positron production, but requires 240 Hz operation of part of the Main Linac.

For any of these schemes, the undulator could be located in the main Linac tunnel.

The primary beam could also be used for fixed target experiments. It would have five times more energy and two times higher average current compared to the highest current SLAC end station experiments. This would allow, for example, a Moller scattering measurement of the weak mixing angle at higher Q^2 than the E-158 experiment at SLAC.

There are a number of possible locations where the end station of JLC/NLC might be located downstream of the interaction point. When the beams are not in collision, a high brightness beam could be transmitted through the NLC/JLC detector to the end station. If fixed target positron experiments are interesting, a second end station could be constructed on the positron dump line.

While the use of an undulator renders the collider beam unsuitable for beam collision operations, the resultant energy spread is relatively small, 0.3 %, even at 250 GeV. Thus the "spent" beam from the undulator could be used for fixed target experiments. The same end station could be used for gamma and electron beam experiments.

References for Chapter 2

[1] "JLC Design Study." KEK Report 97-1, April, 1997.

[2] "Zeroth-Order Design Report for the Next Linear Collider," SLAC Report 474, LBNL-PUB-5424, UCRL-ID-124161, May, 1996.

[3] P. Wilson, "High Energy Electron Linacs: Applications to Storage Rings RF Systems and Linear Colliders," SLAC-PUB-2884, (1982).

[4] R.B. Palmer, "Prospects For High-Energy E+ E- Linear Colliders," Ann. Rev. Nucl. Part. Sci. **40**, 529 (1990).

[5] R.M. Jones and P.B. Wilson, "Minimizing RF system costs in a linear collider by an optimized choice of beam and structure parameters," *1997 IEEE Part. Acc. Conf.*, Vancouver, Canada, (1997).

[6] J.P. Delahaye et al., "Scaling laws for e^+/e^- linear colliders," *Nucl. Instr. Meth.,* **A421**, 369 (1999).

[7] LCOPT is a code written by K. Yokoya and modified by T. Raubenheimer.

[8] K. Kubo, "Tolerances of Random RF Jitters in X-Band Main Linacs," LCC-Note-0016 (1999)); available at: http://www- project.slac.stanford.edu/lc/ilc/TechNotes/LCCNotes/lcc_notes_index.htm.

[9] Y. Nosochkov, T.O. Raubenheimer, "Comparison of Lattice Options for the NLC Main Linac," LCC-Note-0024 (1999); available at: http://www- project.slac.stanford.edu/lc/ilc/TechNotes/ LCC-Notes/lcc_notes_index.htm.

[10] K. Yokoya, in Chapter 8.3 of Ref. [1].

[11] K. Bane, in Chapter 7.4.1 of Ref. [2].

[12] K. Yokoya, K.L.F. Bane, "The Longitudinal High Frequency Impedance of a Periodic Accelerating Structure," *1999 IEEE Part. Acc. Conf.*, New York, New York, (1999).

[13] J. Wang et al., "Accelerating Structure R&D for Linear Colliders," *Proc. of the 1999 Part. Acc. Conf.,* New York, New York (1999).

[14] C. Adolphsen et al., "Wakefield & Beam Centering Measurements of a Damped & Detuned X-band Accelerating Structure," *Proc. of the 1999 Part. Acc. Conf.,* New York, New York (1999).

[15] P. Tenenbaum and T. Shintake, "Measurement of small electron-beam spots," Ann. Rev. Nucl. Part. Sci. **49**, 125 (1999).

[16] R. Assmann et al., "Emittance and Trajectory Control in the Main Linacs of the NLC," *Int. Linear Acc. Conf.,* Geneva, Switzerland, (1996); R. Assmann, T.O. Raubenheimer, "Operation and expected performance of the NLC main linacs," *1996 DPF/DPB Summer Study on New Directions for High-Energy Physics*, Snowmass, CO, (1996).

[17] SAD (Strategic Accelerator Design) is a computer program complex for accelerator design which has been developet at KEK since 1996. See `http://www-acc-theory.kek.jp/SAD/sad.html` for resources.

[18] P. Tenenbaum, "Beam Based Alignment of the NLC Main Linac, Part One: Single-Bunch Comparative Study of Three Algorithms," LCC-Note-0013 (1999); available at: http://www-project.slac.stanford.edu /lc/ilc/TechNotes/LCCNotes/lcc_notes_index.htm.

[19] G. Stupakov, "Tilt and Bow Tolerances in NLC Linac," presented at ISG-3 Meeting at SLAC (1998); available at: http://www- project.slac.stanford.edu/lc/ilc/ISG_Meetings/isg_index.html.

[20] G. Stupakov and T.O. Raubenheimer, "Random Walk Model for Cell-to-Cell Misalignments in Accelerating Structures," *1999 IEEE Part. Acc. Conf.*, New York, New York, (1999).

[21] C. Nantista, T.O. Raubenheimer, "The Effect of Intrapulse RF Variation on Bunch Train Energy Spread," LCC-Note-0030 (1999); available at: http://www-project.slac.stanford.edu/lc/ilc/TechNotes/ LCCNotes/lcc_notes_index.htm.

[22] K. Oide, "Sunchrotron Radiation Limit on the Focusing of Electron Beams," *Phys. Rev. Lett.* 61, 1713 (1988).

[23] Conceptual Design of a 500 GeV e+ e- Linear Collider with Integrated X-ray Laser Facility, DESY 1997-048, May 1997.

[24] LCLS Design Study Report, SLAC-R-521, (1998).

Authors and Major Contributors of Chapter 2

- P. Emma

- J. Frisch

- K. Kubo

- N. Phinney

- T. Raubenheimer

- P. Tenenbaum

- K. Yokoya

Injection Systems

Contents

3.1 Introduction

3.1.1 Performance Requirements and Solutions

The Injector Systems for the JLC and NLC are designed to produce stable, low emittance, 8–10 GeV electron and positron beams for injection into the main linacs. Electron polarization of greater than 80% is required. Electron and positron beams are generated in separate accelerator complexes each of which contain the source, damping ring systems, linacs, bunch length compressors, and collimation regions.
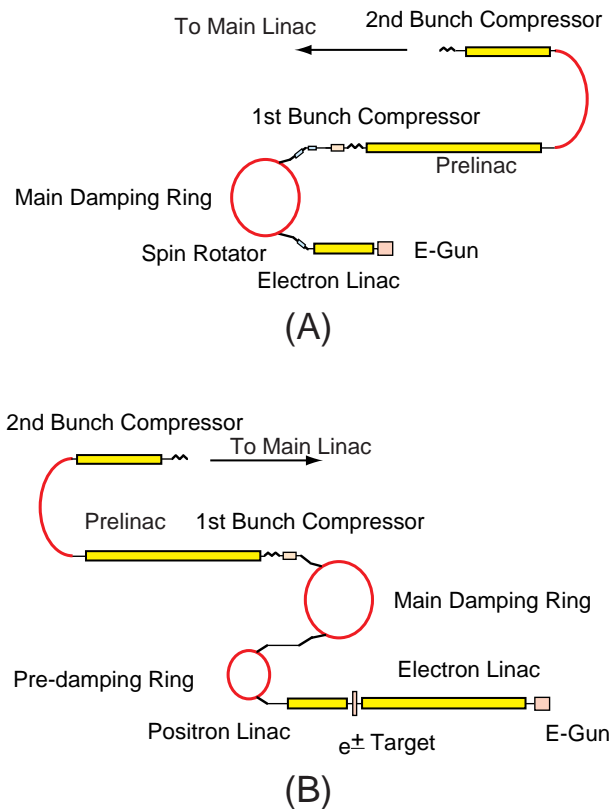
Figure 3.1: *Schematic layout of the injections systems that need to be built for JLC/NLC. (A) Electron injection system. (B) Positron injection system.*

Fig. 3.1(A) and (B) illustrate the salient systems common to all linear collider injectors. The beam parameters required in the JLC and NLC are very nearly identical and the overall design of the JLC and NLC Injector Systems are quite similar. However, there are several noteworthy differences. The NLC design has recently been re-optimized with cost considerations in mind. The injection energy is

now 8 GeV compared with 10 GeV for the JLC and earlier NLC designs. The NLC now has L-band, S-band, and C-band technologies for the injector linacs while the JLC uses S-band exclusively for the injector linacs (JLC and NLC specify L-band RF systems for first stage bunch compression). Both designs are expected to meet the performance requirements for the injected beams [1].

3.1.2   Historical Background

Collaborative effort between KEK and SLAC in the areas of Injector Systems design began in earnest with the development of the KEK Accelerator Test Facility (ATF) program in the late 1980's, nearly ten years prior to the formal ISG process. Since the early 1990s, initially motivated both by the requirements of the SLC and of future colliders, researchers at SLAC and Nagoya University–under the aegis of the SLAC-KEK Collaboration– have cooperated to develop improved photocathodes for the production of polarized electron beams. This effort has included numerous exchanges of laboratory visits, joint development of new ideas [2] , testing of new photocathode materials [3] , and such practical measures as cross calibration of polarimeters. This effort has proven very useful and continues today on an informal basis.

3.1.3   Summary of ISG Activities on Injector Systems

The effort of the Injectors Working Group of the ISG was focused on two complementary areas: (1) a comparison of the JLC and NLC injector designs; and (2) a discussion of progress in the commissioning and operation of the KEK ATF. An examination of the designs of the two injector systems has been made in order to look for advantages in one system over the other and to develop a mutual understanding of these differences in the designs. Over the course of the ISG meetings many aspects of the designs have pulled closer together. Recently the SLAC design team has made changes in the region downstream of the damping ring for the purposes of cost and performance optimization. These changes were discussed in detail at ISG4 and ISG5.

Progress in the commissioning and operations of the KEK ATF systems has been a natural part of the Injector Working Group discussion. This is not only because of the importance of the ATF effort for the design process but also because at both KEK and SLAC, there is a strong overlap of the personnel involved in the ATF effort and in the injector design. The emphasis of the ISG ATF discussions has been to concentrate on those aspects of the ATF experience that most strongly affect the design of the NLC/JLC injector systems. Because of manpower limitations, the KEK group has spent the bulk of their effort on ATF studies. Consequently, the design of the JLC injector systems has not changed significantly from the JLC Design Study [4], while the NLC has made significant changes to the Injector Systems design described in the ZDR [5].

A comparison of the JLC and NLC designs, as discussed in the ISG, is presented in section 3.2 of this report. Experiences with the commissioning and operations of the KEK ATF are presented in section 3.3 of this report.

ISG Progress Report, April, 2000

3.2 JLC / NLC Injector Comparison

3.2.1 Introduction

Nine subjects were discussed in detail in regards to the comparison of the JLC and NLC Injector Systems designs. These discussions were concentrated in those areas where differences in design choices were thought to exist. Minimal time was spent on areas of design which were in general agreement. Eight of the nine subjects fall into the three topics of particle generation (sections 3.2.2, 3.2.3, and 3.2.4), pre-damping ring and damping ring issues (section 3.2.5), and RF systems and issues (sections 3.2.6, 3.2.7, 3.2.8, and 3.2.9). Tabulations of JLC and NLC Injector System parameters comprise the ninth discussion subject. Section 3.2.10 presents a table of charge transmission through the injector chain and tables of JLC and NLC Injector System parameters, broken out by major systems.

3.2.2 Bunch Train Length and Bunch Separation

The JLC and NLC Injector Systems are designed to produce low emittance electron and positron beams at either 150 Hz for the JLC or 120 Hz for the NLC. Each beam consists of a train of 95 bunches spaced by 2.8 ns with a nominal bunch population of 1.15×10^{10} particles. Prior to 1998, both designs specified bunch trains of 90 bunches spaced by 1.4 ns with a population of 0.9×10^{10} particles per bunch. This change in the beam parameters was made to increase the design luminosity of the machines. At the first ISG meeting, the ramifications of this parameter change were discussed and found to be technically feasible, so the 2.8 ns bunch spacing was adopted. An option to further increase the machine luminosity in the future was also considered. For this option, the number of bunches would be doubled with a 1.4 ns bunch spacing and 0.6×10^{10} particles per bunch.

In general, few problems were identified due to the increase in bunch spacing from 1.4 ns to 2.8 ns. Doubling the bunch spacing increases the length of the trains by a factor of two while reducing the average beam current. Some design changes were required but these were incorporated into the ongoing detailed design and improvement activities without much perturbation. The reduction in bandwidth needed for operation and diagnostics eased the design margins in virtually all systems considered. For example, increased bunch spacing reduces the bandwidth required of the source stabilization feedback systems. Bunching systems at 357 MHz have looser tolerances than 714 MHz systems. Injector linac systems favor the reduced average beam current and while beam loading is reduced, it still must be compensated. The damping rings need to be increased in circumference to accommodate the longer trains. At 2.8 ns, it is possible to use 357 MHz for the damping ring RF systems which is favorable for considerations of beam loading, RF power, and exclusion of satellite bunches. However, both the JLC and NLC [6] have decided to retain the 714 MHz damping ring and pre-damping ring RF systems to preserve the 1.4 ns spacing upgrade option. The longer pulse flat top required of the injection and

extraction kickers are not deemed to be a problem. No particular problems are foreseen in regards to the timing system.

The desire to retain the 1.4 ns spacing as an upgrade pushes certain technologies harder than would be necessary if the systems were optimized for 2.8 ns. Retention of the 1.4 ns option may also compromise peak performance at 2.8 ns spacing, most notably in the areas of initial electron bunching and capture, and in beam instrumentation.

3.2.3   Polarized Electron Source

As the beam requirements of the Polarized Electron Sources of the JLC and NLC are very similar, the designs of the sources are also similar. Both use a DC powered electron gun with a III-V semiconductor photocathode to generate a longitudinally polarized electron beam. Guns of this type are in use at a number of labs, notably at SLAC. The design of the NPES-III gun at Nagoya University incorporates a number of improvements over older designs and may prove to be viable for JLC/NLC use. There is also R&D ongoing at KEK and at Nagoya University, which will lead to improved materials and processing techniques for gun manufacture.

The NEA surface III-V semiconductor photocathodes have exhibited a saturation effect (the "Charge Limit" [7, 8, 9]) which affects their ability to produce large currents. Recent results, notably from Nagoya University [10], indicate that cathodes may be prepared which do not show this limitation. The level of electron polarization for these photocathodes is approximately 70%, and research is underway at Nagoya and at SLAC to develop higher polarization cathodes and to demonstrate the high currents needed. The Charge Limit may be a more important problem in the 1.4 ns bunch spacing configuration, where the charge per pulse train is 1.5 times larger than for the nominal 2.8 ns spacing.

The design of the associated laser system is also under consideration at the two labs. As the pulse structure and source tolerances of the JLC and the NLC are identical, the laser requirements are the same. The laser will use Titanium-Sapphire to generate the light at the requisite wavelength of 750 - 850 nm. The pulse structure can be generated either by chopping a long laser pulse with fast Pockels cells, or directly with mode locking techniques. While there are conceptual designs for the lasers both at SLAC and Nagoya University, the ultimate laser design will depend on progress in laser technology.

3.2.4   Positron Generation

In the design of both the JLC and the NLC [11] positrons are produced by bringing a high energy electron beam onto a tungsten target and creating an electromagnetic shower. The positrons produced in the shower are collected by a flux concentrator and accelerated in structures encased in a solenoidal magnetic field, before injection into a linac. The primary issue for positron generation is to produce the required number of positrons in the proper 6-dimensional phase-space aperture without causing damage to the target. The critical concern for target damage is the instantaneous energy deposition

per unit volume, not average power. The average power deposited is compensated by water cooling, and the level of cooling required is not excessive. However, the energy deposited in the target is large and increases as the electromagnetic shower develops in the material. The damage threshold is not easily calculated and therefore the energy deposition, stresses in the material and shock to the target must all be simulated by computer codes for any positron source design.

One can increase the positron population by raising the energy or intensity of the incoming electrons, but this also increases the energy in the shower and the risk of damage. One can increase the beam size onto the target to reduce the energy deposited per unit volume, but this results in a larger emittance for the produced positrons and thus for a reduced collection efficiency. The parameters of the incoming electron beam must be chosen to maximize the collected positron population (the yield) while holding the energy deposition below the damage threshold. In the design of the JLC and the NLC different paths have been taken to optimize the balance between the positron yield and the instantaneous energy deposition in the target. The results of the optimizations are shown in Table 3.1 below.

Table 3.1: *JLC and NLC Positron Target Parameters. JLC parameters are from the JLC Design Study [4]; redesign calculations have not yet been done.*

	JLC	NLC	
Electron beam energy	10	6.2	GeV
Electron beam emittance	300	100	mm-mrad
Electron beam bunch length	20	17.5	ps (FWHM)
Electrons per bunch	0.7	1.4	$\times 10^{10}$
Population uniformity	1	< 0.5	%
Number of bunches per train	85	95	
Electron beam radius	1.2	1.6	mm (rms)
Average beam power	147	158	kW
Target thickness	6	4	Rad. Length
Target power deposition	53	22	kW

JLC uses an electron beam energy of 10 GeV with 0.7×10^{10} electrons per bunch while NLC has a 6.2 GeV beam of 1.4×10^{10} electrons per bunch. Considerations of positron yield and energy deposition lead to different choices for the optimal target thickness [12] JLC has a 6 radiation length (RL) target while NLC has only 4 RL. The thinner NLC target results in a lower energy deposition but also a reduced positron yield compared with JLC.

Table 3.2 summarizes the JLC and NLC positron capture and initial acceleration systems. The chief difference in the designs is the choice of S-band capture and acceleration for the JLC and L-band capture and acceleration for the NLC. The lower frequency choice for the NLC provides a larger acceptance for positron capture, improving capture efficiency and allowing the electron beam size onto the target to be increased. The higher frequency choice of the JLC selects a smaller phase space for the positrons, easing requirements on downstream systems.

Table 3.2: *JLC and NLC Positron Capture and Initial Acceleration*

	JLC	NLC	
RF frequency	2856	1428	MHz
Bunch length	20	30	ps (FW)
Final energy	90	250	MeV
Capture emittance ($\gamma\epsilon_{x,y}$)	0.027	0.06	m-rad (edge)
Energy spread	5	10	MeV (rms)

3.2.5   Pre-Damping Ring and Damping Ring Designs

The designs of the JLC and NLC pre-damping rings and damping rings have been changed from the JLC Design Report and ZDR to accommodate the adoption of the longer bunch trains ($\sim$ 100 bunches spaced by 2.8 ns) [13]. Comparisons of performance parameters for the JLC and NLC pre-damping and damping rings are presented in Table 3.3. Although quite similar in design, there are several differences. In the case of the JLC, the assumption of a smaller (than in the NLC case) incoming positron emittance has led to a design of the pre-damping ring with longer damping times and which does not require wigglers. The ring circumferences are set primarily by the bunch train lengths, number of trains being stored at the same time, and the allocation in length given over to the rise and fall time required for the injection and extraction kicker systems [14]. Ring circumferences are very similar in both sets of designs. Both the JLC and NLC base the designs of the two sets of rings on a TME (Theoretical Minimum Emittance [15]) cell. TME cell parameters are called out in Table 3.4. The JLC is specified to operate at 150 Hz in contrast to 120 Hz for the NLC. For equal numbers of stored bunch trains, there is less time at the JLC for damping. Hence, the damping times for the JLC main damping rings are necessarily shorter than for the NLC main rings. Also, the JLC has adopted a smaller design coupling (0.1% JLC, 1% NLC), resulting in a smaller vertical equilibrium emittance in comparison to that of the NLC. This is expected to lead to tighter tolerance specifications. The full tolerance studies have not yet been done for either design. Finally, both the JLC and NLC designs call for 714 MHz RF systems in all the rings; this is in accommodation to the 1.4 ns bunch spacing option.

Additional pre-damping and Damping Ring System Parameters are listed in Table 3.12 of Section 3.2.10.

3.2.6   Choice of the Low Frequency Accelerator Structures

Prior to ISG5 (February, 2000), both the JLC and NLC designs use low RF frequency linacs operating at S-band (2.856 GHz) and/or L-band (1.428 GHz) to accelerate the beams up to 8 or 10 GeV. The only difference between the two designs is the positron booster linac where the JLC uses S-band while the NLC uses an L-band linac. These linacs are required to deliver clean beams and to be able to operate with the 1.4 ns or 2.8 ns bunch spacing configurations. While less critical for L-band due to the larger aperture, the primary issues in the S-band linacs are the emittance degradation and multi-

Table 3.3: *Pre-damping and damping ring performance comparison*

	Pre-Damping Rings		
	JLC	NLC	
Injected emittance ($\gamma\epsilon_{x,y}$)	0.003	0.042	m-rad (rms)
Extracted emittance ($\gamma\epsilon_{x/y}$)	84 / 54	150 / 100	mm-mrad (rms)
Bunch trains stored	2	2	
Repetition rate	150	120	Hz
Required damping cycles	2.0	3.1	
Damping time	6.6	5.4	ms
Equil. emittance ($\gamma\epsilon_{0y}$)	30	10	mm-mrad
Wiggler length	0	17	m
Circumference	186	218	m
	Damping Rings		
	JLC	NLC	
Injected emittance ($\gamma\epsilon_{x,y}$)	100	< 150	mm-mrad (rms)
Extracted emittance ($\gamma\epsilon_{x/y}$)	2.6 / 0.004	< 3/ < 0.03	mm-mrad (rms)
Bunch trains stored	3	3	
Repetition rate	150	120	Hz
Required damping cycles	4.8	4.8	
Damping time	3.9	5.2	ms
Equil. emittance ($\gamma\epsilon_{0y}$)	3	20	nm-rad (rms)
Wiggler length	100	44	m
Circumference	308	297	m

Table 3.4: *Pre-damping and damping ring TME cell parameters*

Pre-Damping Rings			
	JLC	NLC	
Number of cells	24	12	
Bend length	0.96	2.0	m
Bend field	1.8	1.72	T
Quadrupole Length	0.2 (QF), 0.1 (QD)	0.3	m
QF Strength ($\int gdl$)	5.3	7.2	kG
QD Strength ($\int gdl$)	-2.6	-3.9	kG
Damping Rings			
	JLC	NLC	
Number of cells	40	30	
Bend length	0.9	1.2	m
Bend field	1.15	1.1	T
Quadrupole Length	0.2 (QF), 0.1 (QD)	0.25	m
QF Strength ($\int gdl$)	9.9	6.9	kG
QD Strength ($\int gdl$)	-3.3	-4.0	kG

bunch beam breakup (BBU) associated with the long- and short-range wakefields in the structure. The design goals of the accelerating structure are to maximize the RF efficiency while minimizing the dipole wakefield [16].

The methods used to reduce the dipole wakefield are to detune the first pass-band dipole modes and to damp them. Detuning of the dipole modes can be realized by gradually changing the dimensions of the cells in a structure while keeping the fundamental frequency unchanged. The damping can be achieved by either coupling the modes into manifolds running parallel to the structure or by damping locally using radial loads. While the detuning can effectively minimize the wakefield within a short distance from the bunch, it may produce a recoherence in the wakefield at longer distances due to the discreteness of the modes. The damping, on the other hand, will be effective at long distances depending on the Q factors of the modes. The structure with only detuning is referred as the detuned structure (DS), whereas the structure with both detuning and damping is referred to as the damped-detuned structure (DDS). The choice of DS vs DDS relies on the wakefield level achievable in the structures. In the X-band linacs it is clear that a DDS is required since the modes have larger kick factors. In the S-band linacs, the kick factors are a factor of about 64 times lower than X-band. On the other hand, due to the lower dipole frequencies, the detuning range of the modes is limited, which can affect the wakefield profile. Either the DS or DDS may be selected for the S-band structures.

The advantages of the DDS structure are that both the short and long distance wakefields are controlled (by detuning and damping respectively) and in addition, the signal from that higher-order-mode (HOM) coupler can be used for beam position monitoring. A properly designed DDS structure is reliable and can provide beam and structure alignment diagnostics by itself. However, there are potential problems with the DDS structure, as encountered in the X-band design, which may require significant effort to overcome. First of all, the uncoupled cells at the two ends of the structure due to the HOM coupler geometry may result in "uncoupled" modes. These high Q modes can have high kick factors which destroy the decoherence of cancellations among the smoothly detuned and damped modes and generate resonant components in the wakefields. Secondly, because of the additional HOM couplers at the two ends, the assembly becomes more complicated, which may increase the cost of the structure.

In the DS structure, the wakefields are controlled only by the decoherence among the modes by detuning. The spectrum of the dipole modes needs to be carefully optimized to control the wakefield profile throughout the length of the bunch pulse. Because of the tight requirement on the decoherence among the modes, the tolerance on frequency errors may be tight in the DS structure. The DS does not have the intrinsic BPMs as the DDS and built-in structure BPMs would need to be designed. The advantages of the DS structure, however, are the simplicity of the cell geometry and the end assemblies. The cells are simply two dimensional except for the fundamental mode coupler cells. The turnaround time for structure design and optimization can be shorter and the RF parameters can be determined more accurately.

Our present feeling at the NLC is to use the DS structure for the S-band if it can provide acceptable wakefield and tolerances. A systematic approach has been carried out since the JLC and NLC design reports. Both the short- and long-range dipole wakefields have been optimized by selecting a proper

structure type and dipole mode distribution. An acceptable design for an S-band DS structure that can accommodate both 1.4 ns and 2.8 ns operation configurations has been found. The present design has a length of four meters with a total of 102 cells and a phase advance for the fundamental mode of 135 degrees per cell. The tolerance on the random frequency error is dominated by the dipole frequency errors, which corresponds to cell profile errors that are thought to be achievable using conventional machining.

Beginning in the fall of 1999, the NLC group has begun investigations into the utilization of C-band (5.712 GHz) technology for the injector system. In particular, it has been proposed to replace the S-band RF systems with C-band RF systems in the NLC, 6-GeV prelinacs and 6-GeV electron drive linac (use in the production of positrons). This work is in its initial stages and will not be discussed further in this report other than to note that the tables in section 3.2.10 have been updated to reflect this move to C-band.

3.2.7 Bunch Compressor RF Systems

Both the JLC design and the NLC design utilize two stages of magnetic compression to reduce the 5 mm σ_z bunch length from the damping rings to a σ_z as short as 80 μm in the main linac. The two-stage design reduces the sensitivity to energy variations in the prelinacs which would cause phase variations at injection into the main linac. The designs of the JLC Design Study and the NLC ZDR bunch compression systems are very similar. Recent cost and performance optimization studies have led to several significant modifications in the design of the NLC bunch compression systems [17].

Both the JLC and the NLC designs use 140 MV of L-band RF for the first stage of compression (BC1). For the second stage (BC2), the new NLC design uses a lower beam energy, which reduces the radius of the 180° turn-around, and an X-band RF section. The JLC BC2 has a 10 GeV beam, a 100 m radius turn-around and 3.9 Gev of S-band RF. For the NLC, the beam energy is 8 GeV with a 53 m radius turn-around and 0.6 GeV of X-band RF. The tolerances in the NLC BC2 X-band RF section are significantly tighter than in the case of the JLC BC2 S-band RF section but is still less than what is required of the X-band main linacs in either the JLC or NLC. A considerable reduction in the overall cost is estimated for the NLC bunch length compressor design with regard to the estimated costs for the NLC/JLC ZDR design. Table 3.5 lists the parameters of the JLC and NLC bunch compressor systems.

3.2.8 Beam Loading Issues for the Gun and Buncher Systems

The required beam specifications for the polarized and unpolarized electron sources for both the JLC and NLC are such that considerable beam loading is expected in the bunching sections. Neither the JLC Design Study [4] nor the NLC ZDR [5] address the issues of beam loading in the gun structures themselves. However, beam loading compensation in the bunching cavities and initial accelerating structures are discussed briefly in both design reports. Table 3.6 lists parameters for the JLC and NLC electron sources.

Table 3.5: *Parameters of the JLC and NLC Bunch Compressors*

	JLC	NLC	
BC1: Initial energy	1.98	1.98	GeV
Initial bunch length (rms)	5	5	mm
RF wavelength	21	21	cm
Unloaded gradient	16	14	MV/m
Active RF length	9	10	m
Compressor energy	140	140	MV
Final bunch length	0.4	0.5	mm
Prelinac: Energy gain	8.0	6.0	GeV
180° Turn-around radius	100	53	m
BC2: Initial energy	10	8	GeV
Initial bunch length (rms)	0.4	0.5	mm
RF wavelength	10.5	2.6	cm
Unloaded gradient	25	60	MV/m
Active RF length	150	11	m
Compressor energy	3705	600	MV
Final bunch length	80	90–150	μm

In the case of the JLC, beam loading compensation in the SHB cavities is accomplished by using two 714 MHz RF drivers for each cavity. Prior to beam time, a 20 kW source is used to excite the cavity. At beam time, a fast rise time 30 kW RF source is used to compensate for the beam loading as the beam traverses the cavity. In the case of the NLC, beam loading compensation is accomplished by rapidly shifting the phase of the source RF when the beam is injected. For the NLC, SHB 1 requires 17 kW of RF power while SHB 2 requires 70 kW of RF. Beam loading compensation in the traveling wave (TW) bunchers has yet to be considered in both designs; ΔT compensation is used for compensation in the accelerating structures in both designs.

The designs of the bunching systems in both the JLC Design Study [4] and the NLC ZDR [5] assumed 1.4 ns bunch spacing with 90 bunches per train. The present parameter sets have similar bunch populations and number of bunches but with a 2.8 ns bunch spacing. This is approximately half the beam current (total charge in a train divided by train length). Also, the JLC design now uses 357 MHz bunching cavities rather than the 714 MHz systems documented in the JLC Design Study [4]. Thus, the beam loading compensation schemes need to be revisited for both designs.

3.2.9   Beam Loading Compensation for Injector Linacs

In the design of both JLC and the NLC, the first 10(or 8) GeV of energy for the electron and positron beams is obtained by using linacs operating at S- and/or L-band frequencies. (Please see the discussion of C-band contained in section 3.2.6. Beam loading compensation for the NLC injector system C-band linacs has yet to be detailed and will not be reported herein.) All of these linacs are fairly heavily

Table 3.6: *JLC and NLC Electron Source Parameters*

	JLC (pol.)	NLC (pol.)	JLC (unpol.)	NLC (unpol.)	
Particle per bunch	1.8	1.8	0.8	2	$\times 10^{10}$
Bunches per train	95	95	95	95	
Bunch separation	2.8	2.8	2.8	2.8	ns
Bunch frequency	357	357	357	357	MHz
Gun voltage	150	120	200	120	kV
Gun pulse width	0.7	0.7	0.7	0.7	ns
Number of SHB	3	2	3	2	
SHB frequency	357	714	357	714	MHz
SHB gap voltage	$40 \sim 70$	1.4,4.8	$40 \sim 70$	1.4,4.8	kV
SHB power	$3 \times 20,30$	17,70	$3 \times 20,30$	17,70	kW
TW buncher frequency	1428	2856	1428	2856	MHz
Accelerator frequency	2856	2856	2856	2856	MHz
Beam loading comp.	ΔT	ΔT	ΔT	ΔT	

loaded by beams with average currents up to 1 amp, or in the positron capture linac of up to 4.5 amps, and bunch train lengths of 266 ns. The effect of beam loading effect must be compensated to obtain uniform energy for each bunch in the train. With the current design parameters for the JLC and NLC, the pulse length of the bunch train is much shorter than the reasonable filling times of the structures which are in turn shorter than the ringing times, $2Q/\omega$, for the structures. Without compensation, the energy of the beam will drop approximately linearly with time during the pulse as a result of beam loading. There are two natural choices for the necessary beam loading compensation, ΔT and ΔF [40, 18].

In the ΔT compensation scheme, the beam is injected into the structure before the structure is full. The acceleration voltage rises along the bunch pulse as the RF keeps filling the structure. The tail of the pulse gets more acceleration which compensates the deceleration due to the beam loading. Fig. 3.2(a) illustrates the ΔT scheme in which the voltage $V_k(t)$ produced by a step function RF pulse is plotted as a function of time. Also plotted is the beam induced voltage $V_b(t)$ for the case where the beam is turned on before the linac structure is full. The resultant sum of $V_k(t)$ and $V_b(t)$, the loaded voltage, is required to be uniform. The ΔF compensation scheme uses one or more accelerating structures running at a frequency 1 to 2 MHz above or below the nominal frequency. The bunches in the compensation sections see a field which appears to vary with the difference frequency ΔF, thus the bunches are spread along a total RF phase span of $\Delta F \times t_b$. Phased roughly in quadrature from the accelerating phase, the beginning of the pulse is decelerated by the off frequency section(s), while the end of the pulse is accelerated. Fig. 3.2(b) illustrates the principle of ΔF compensation, where the voltage gain $V_{comp}(t)$ of a beam with an F_0 bunch structure in a ΔF compensation section operating at a frequency $F_0 \pm \Delta F$ is plotted in the ΔF-t phase space.

The advantage of ΔT compensation is that since it occurs in every accelerator section, the energy spectrum can be kept narrow throughout the linac, thus minimizing emittance growth from dispersion
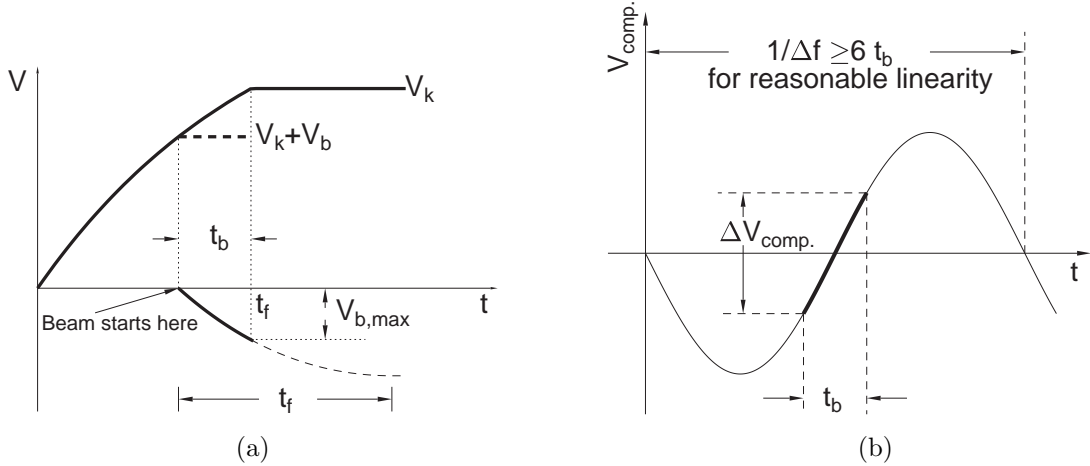
Figure 3.2: *(a) Δ T beam loading compensation for the rectangular RF input pulse; (b) Energy gain, $V_k(t)$, in the Δ F compensation section.*

and chromatic effects. It requires amplitude and phase modulation of the RF input to compensate for different beam loading conditions, which can be achieved by combining the low power level RF of two klystrons. The ΔF compensation allows flexibility in picking the filling time of the structures for maximum structure efficiency and different beam loading currents can be compensated easily by changing the RF power. The principal disadvantage of ΔF compensation is that the beam energy spread becomes large between compensating structures, and the poor energy spectrum causes associated emittance growth. It also requires additional off frequency RF systems, which complicates the RF distribution and control.

In the current JLC and NLC design, the beam currents are much lower than those proposed in the earlier design reports, which makes it more favorable to use the ΔT compensation scheme. Therefore, present plans are to use ΔT compensation for most of the S- and L-band linacs, except for the positron capture linac where a ΔF scheme is required due to the extremely high beam current. A more realistic numerical model for the beam loading compensation has been established, which includes the dispersive effects of the accelerating structure to simulate the actual response to the RF. Detailed numerical studies on using the ΔT scheme for the S- and L-band linacs have been carried out. The results have shown that the ΔT scheme is effective for beam loading compensation, and the linacs can provide good RF efficiency with this scheme. The ΔT scheme has been tested experimentally at the ATF in KEK and in a slightly varied ΔT configuration at the SLC in SLAC. Both have shown that the ΔT scheme is effective for beam loading compensation of long bunch trains.

The ΔT compensation for the bunch/energy compressors has been studied numerically and shown to be achievable by introducing phase modulation in addition to amplitude modulation of the klystron RF. The plan is to test the ΔT scheme for the compressors experimentally.

ISG Progress Report, April, 2000

3.2.10 Comparison of JLC and NLC Charge Transmission and System Parameters

Both the JLC and the NLC Injector System designs include assumptions on the amount of beam loss which will occur as the beam passes through each section of the machine. These losses determine the charge required from the injector to provide the specified beam into the Main Linacs. For the polarized electron beam, the JLC and NLC designs are similar. A 30% loss is assumed in the bunching of the electron beam for injection into the S-band linacs. An additional 10% is lost upon insertion into the electron Main Damping Ring.

For the positron source, the transmission from the positron main damping ring to the Main Linacs is the same as for the electrons. The design of the JLC and NLC differ, however, in the design of the positron source and thus on the positron yield and on the assumed losses at injection into the positron pre-damping ring. For the JLC it is estimated that three positrons are captured per electron on the target, and that 52% of these are injected in the pre-damping ring. For the NLC, with a lower electron beam energy, a thinner positron target and a larger emittance for the captured positron beam, it is estimated that two positrons are captured per electron on the target, and that only 40% of these are injected in the pre-damping ring. This low estimate of pre-damping ring injection efficiency is in part due to experience with the positron source at the SLC. These considerations require a much higher electron beam current in the NLC positron system design than in the JLC design. Table 3.7 shows the beam current transmission through the JLC and NLC Injector Systems.

A comparison of the JLC and NLC Injector Systems is presented in the following series of tables. System parameters for the Polarized Electron Sources, Thermionic Sources, and Bunching Systems are listed in Table 3.8. Positron Source System parameters are given in Table 3.9. Table 3.10 enumerates the system parameters for the Polarized e^- Booster Linacs, the Positron Drive Linacs and the Positron Booster Linac. The Injector Pre-Linac System parameters are given in Table 3.11. Finally, system parameters for the JLC and NLC Pre-Damping Rings and Damping Rings are listed in Table 3.12.

Table 3.7: *Beam Transmission through the JLC and NLC Injector Systems*

System	Losses		JLC	NLC	NLC
	JLC	**NLC**		scaled	design max.
Polarized Electron Side					
e^- Gun					
↓			1.8×10^{10}	1.8×10^{10}	2.9×10^{10}
Buncher	30%	30%			
↓			1.2×10^{10}	1.2×10^{10}	2.0×10^{10}
1.98 GeV Linac					
↓			1.2×10^{10}	1.2×10^{10}	2.0×10^{10}
Main DR	10%	10%			
↓			1.1×10^{10}	1.1×10^{10}	1.6×10^{10}
BC1					
↓			1.1×10^{10}	1.1×10^{10}	1.6×10^{10}
pre-Linac					
↓			1.1×10^{10}	1.1×10^{10}	1.6×10^{10}
BC2 Arc	1%	1%			
↓			1.1×10^{10}	1.1×10^{10}	1.6×10^{10}
BC2	1%	1%			
↓			1.1×10^{10}	1.1×10^{10}	1.6×10^{10}

System	Losses		JLC	NLC	NLC
	JLC	**NLC**		scaled	design max.
Positron Side					
e^- Gun					
↓			1.0×10^{10}	2.0×10^{10}	2.9×10^{10}
Buncher	30%	30%			
↓			0.7×10^{10}	1.4×10^{10}	2.0×10^{10}
10/6.2 GeV Linac					
↓			0.7×10^{10}	1.4×10^{10}	2.0×10^{10}
e^+ Target			$\times 3$	$\times 2$	$\times 2$
↓			2.1×10^{10}	2.8×10^{10}	4.0×10^{10}
1.98 GeV Linac	20%				
↓			1.7×10^{10}	2.8×10^{10}	4.0×10^{10}
Pre-DR	35%	55%			
↓			1.1×10^{10}	1.3×10^{10}	1.9×10^{10}
Main DR	0%	10%			
↓			1.1×10^{10}	1.1×10^{10}	1.6×10^{10}
BC1					
↓			1.1×10^{10}	1.1×10^{10}	1.6×10^{10}
pre-Linac					
↓			1.1×10^{10}	1.1×10^{10}	1.6×10^{10}
BC2 Arc	1%	1%			
↓			1.1×10^{10}	1.1×10^{10}	1.6×10^{10}
BC2	1%	1%			
↓			1.1×10^{10}	1.1×10^{10}	1.6×10^{10}

Table 3.8: *Comparison of JLC and NLC Electron Sources System Parameters*

Polarized Electron Source		JLC	NLC	
Energy	E	150	120	keV
Energy Spread	$\Delta E/E$	< 1	< 1	%
Single-Bunch	σ_E/E	0.2	< 1	%
Emittance (edge)	$\gamma\epsilon_{x,y}$	30	5	$\times 10^{-6}$ m-rad
Bunch Length	σ_z/c	700	700	ps (FWHM)
Particles/Bunch	n_b	1.8	1.8	$\times 10^{10}$
Pop. Uniformity	$\Delta n_b/n_b$	1	< 0.5	%
Number of Bunches	N_b	95	95	
Bunch Spacing	T_b	2.8	2.8	ns
Repetition Rate	f	150	120	Hz
Polarization	P_e	85	80	%
Thermionic Electron Source		**JLC**	**NLC**	
Energy	E	keV	200	120
Energy Spread	$\Delta E/E$	< 0.5	< 1	%
Single-Bunch	σ_E/E	0.2	< 1	%
Emittance (edge)	$\gamma\epsilon_{x,y}$	30	5	$\times 10^{-6}$ m-rad
Bunch Length	σ_z/c	700	700	ps (FWHM)
Particles/Bunch	n_b	0.8	2.0	$\times 10^{10}$
Pop. Uniformity	$\Delta n_b/n_b$	1	< 0.5	%
Number of Bunches	N_b	95	95	
Bunch Spacing	T_b	2.8	2.8	ns
Repetition Rate	f	150	120	Hz
Bunching System		**JLC**	**NLC**	
Energy	E	80	80	MeV
Energy Spread	$\Delta E/E$	< 1	< 1	%
Single-Bunch	σ_E/E	< 1	< 1	%
Emittance (edge)	$\gamma\epsilon_{x,y}$	100	45	$\times 10^{-6}$ m-rad
Bunch Length	σ_z/c	20	17.5	ps (FWHM)
Particles/Bunch, pol.(therm.)	n_b	1.2(0.7)	1.2(1.4)	$\times 10^{10}$
Pop. Uniformity	$\Delta n_b/n_b$	1	< 0.5	%
Number of Bunches	N_b	95	95	
SHB frequency	f_{SHB}	357	714	MHz
Bunch Spacing	T_b	2.8	2.8	ns
Repetition Rate	f	150	120	Hz
Beam Power(at exit)	P_B	2.2	1.8	kW

Table 3.9: *Comparison of JLC and NLC Positron Source System Parameters*

Target		JLC	NLC	
Energy	E	10	6.2	GeV
Emittance (edge)	$\gamma\epsilon_{x,y}$	100	100	$\times 10^{-6}$ m-rad
Bunch Length	σ_z/c	20	17.5	ps (FWHM)
Particles/Bunch	n_b	0.7	1.4	$\times 10^{10}$
Pop. Uniformity	$\Delta n_b/n_b$	1	< 0.5	%
Number of Bunches	N_b	95	95	
Beam radius	σ_r	1.2	1.6	mm (rms)
Beam Power/Area		1.5	1.0	$\times 10^{12}$NGeV/mm^2
Absorbed Power/Vol.		6.9	3.6	$\times 10^{10}$NGeV/(mm$^2\times$ RL)
Bunch Spacing	T_b	2.8	2.8	ns
Repetition Rate	f	150	120	Hz
Average Beam Power	P_B	160	158	kW
Target Thickness	$W_{75}Re_{25}$	6	4	RL
Absorbed Target Power	P_T	53	22	kW
Capture		**JLC**	**NLC**	
RF Frequency	f_{rf}	2856	1428	MHz
Bunch Length	σ_z/c	20	30	ps (FW)
Capture Emittance(edge)	$\gamma\epsilon_{x,y}$	0.027	0.06	m-rad
Final Energy	E	90	250	MeV
Energy Aperture	ΔE	± 10	± 10	MeV (FW)
pre-DR Acceptance		0.17	0.09	m-rad
e^+ Capture into Linac	e^+/e^-	3.0	2.0	
e^+ Capture into pre-DR	e^+/e^-	2.0	$0.8 = 0.4 \times 2.0$	

Table 3.10: *Comparison of JLC and NLC Booster and Drive Linac System Parameters*

Polarized e^- Booster Linac		JLC	NLC	
Frequency	f_{rf}	2856	2856	MHz
Energy	E	1.98	1.98	GeV
Energy Spread	$\Delta E/E$	± 1	± 1	%
Single-Bunch	σ_E/E	tbd	< 0.5	%
Emittance (edge)	$\gamma\epsilon_{x,y}$	< 100	100	$\times 10^{-6}$ m-rad
Bunch Length	σ_z/c	20	17.5	ps (FWHM)
Particles/Bunch	n_b	1.2	1.2	$\times 10^{10}$
Pop. Uniformity	$\Delta n_b/n_b$	1	< 0.5	%
Number of Bunches	N_b	95	95	
Bunch Spacing	T_b	2.8	2.8	ns
Repetition Rate	f	150	120	Hz
Positron Drive Linac		**JLC**	**NLC**	
Frequency	f_{rf}	2856	5712	MHz
Energy	E	10	6.2	GeV
Energy Spread	$\Delta E/E$	± 1	± 1	%
Single-Bunch	σ_E/E	tbd	< 0.5	%
Emittance (edge)	$\gamma\epsilon_{x,y}$	< 100	100	$\times 10^{-6}$ m-rad
Bunch Length	σ_z/c	20	17.5	ps (FWHM)
Particles/Bunch	n_b	0.7	1.4	$\times 10^{10}$
Pop. Uniformity	$\Delta n_b/n_b$	1	< 0.5	%
Number of Bunches	N_b	95	95	
Bunch Spacing	T_b	2.8	2.8	ns
Repetition Rate	f	150	120	Hz
Positron Booster Linac		**JLC**	**NLC**	
Frequency	f_{rf}	2856	1428	MHz
Energy	E	1.98	1.98	GeV
Energy Spread	$\Delta E/E$	± 1	± 1	%
Single-Bunch	σ_E/E	tbd	< 1.2	%
Emittance (edge)	$\gamma\epsilon_{x,y}$	0.003 (rms)	0.06 (edge)	$\times 10^{-6}$ m-rad
Bunch Length	σ_z	2.5	3.7	mm (rms)
Particles/Bunch	n_b	1.4	2.8	$\times 10^{10}$
Pop. Uniformity	$\Delta n_b/n_b$	1	< 1	%
Number of Bunches	N_b	95	95	
Bunch Spacing	T_b	2.8	2.8	ns
Repetition Rate	f	150	120	Hz
pre-DR Acceptance		0.17	0.09	m-rad
pre-DR Energy Acceptance	$\Delta E/E$	± 2	± 1.5	%

Table 3.11: *Comparison of JLC and NLC Pre-Linac System Parameters*

Injector Pre-Linac		JLC	NLC	
Frequency	f_{rf}	2856	5712	MHz
Energy	E	8.0	6.0	GeV
Energy Spread	$\Delta E/E$	± 0.1	± 0.1	%
Single-Bunch	σ_E/E	tbd	< 0.025	%
Emittance (rms)	$\gamma\epsilon_x$	3	3	$\times 10^{-6}$ m-rad
Emittance (rms)	$\gamma\epsilon_y$	3	3	$\times 10^{-8}$ m-rad
Electron Polarization	P_e	85	80	%
Positron Polarization	P_p	0	0	%
Bunch Length	σ_z	tbd	500	μm (rms)
Particles/Bunch	n_b	1.2	1.2	$\times 10^{10}$
Pop. Uniformity	$\Delta n_b/n_b$	%	1	< 0.5
Number of Bunches	N_b	95	95	
Bunch Spacing	T_b	2.8	2.8	ns
Repetition Rate	f	150	120	Hz

Table 3.12: *Comparison of JLC and NLC Pre-Damping Ring and Damping Ring System Parameters*

JLC and NLC Pre-Damping Rings		JLC	NLC	
Number of Stored Bunch Trains	N_t	2	2	
Number of Bunches per Train	N_b	95	95	
Bunch Spacing	T_b	2.8	2.8	ns
Kicker rise/fall gap	T_k	60	100	ns
Repetition Rate	f	150	120	Hz
Injected Emittance (rms)	$\gamma\epsilon_{x,y}$	3000	< 42000	$\times 10^{-6}$ m-rad
Extracted Emittance (rms)	$\gamma\epsilon_x$	82	150	$\times 10^{-6}$ m-rad
Extracted Emittance (rms)	$\gamma\epsilon_y$	53	< 100	$\times 10^{-6}$ m-rad
Extracted Bunch Length	σ_z	4.1	7.5	mm (rms)
Extracted Energy Spread	σ_δ	0.12	0.09	% (rms)
Ring Energy	E	1.98	1.98	GeV
Ring Circumference	C_o	186	218	m
Horizontal Damping Time	τ_x	6.6	5.0	ms
Vertical Damping Time	τ_y	6.6	4.9	ms
RF Frequency	f_{rf}	714	714	MHz
Harmonic Number	h	444	520	
Gap Voltage	V_{rf}	2	1.5	MV
Energy Loss per Turn	U_o	370	583	keV
Momentum Compaction	α_p	1.68	3.4	$\times 10^{-3}$
JLC and NLC Damping Rings		**JLC**	**NLC**	
Number of Stored Bunch Trains	N_t	3	3	
Number of Bunches per Train	N_b	95	95	
Bunch Spacing	T_b	2.8	2.8	ns
Kicker rise/fall gap	T_k	65	65	ns
Repetition Rate	f	150	120	Hz
Injected Emittance (rms)	$\gamma\epsilon_{x,y}$	100	< 150	$\times 10^{-6}$ m-rad
Extracted Emittance (rms)	$\gamma\epsilon_x$	2.6	< 3	$\times 10^{-6}$ m-rad
Extracted Emittance (rms)	$\gamma\epsilon_y$	0.003	< 0.03	$\times 10^{-6}$ m-rad
Extracted Bunch Length	σ_z	5.1	4.0	mm (rms)
Extracted Energy Spread	σ_δ	0.08	0.09	% (rms)
Ring Energy	E	1.98	1.98	GeV
Ring Circumference	C_o	308	297	m
Horizontal Damping Time	τ_x	3.9	5.2	ms
Vertical Damping Time	τ_y	3.9	5.2	ms
RF Frequency	f_{rf}	714	714	MHz
Harmonic Number	h	735	520	
Gap Voltage	V_{rf}	1.2	1.5	MV
Energy Loss per Turn	U_o	1040	761	keV
Momentum Compaction	α_p	0.53	6.6	$\times 10^{-3}$

3.3   Issues as Learned from ATF

3.3.1   Introduction

The Accelerator Test Facility (ATF) at KEK was built as a prototype accelerator complex for the injector portion of a linear collider. The project was designed to serve as a test bench for developing numerous beam control techniques for a linear collider as well as a training ground for the next generation of physicists and engineers. Fig. 3.3 shows a schematic diagram of ATF. It consists of an electron gun which is capable of producing multi-bunch trains of electrons, an S-band 1.54 GeV injector linac with a maximum accelerating gradient of 33 MV/m, a beam transport line (BT), a 1.54 GeV damping ring (DR) and an extraction line (EXT) for beam diagnostics.
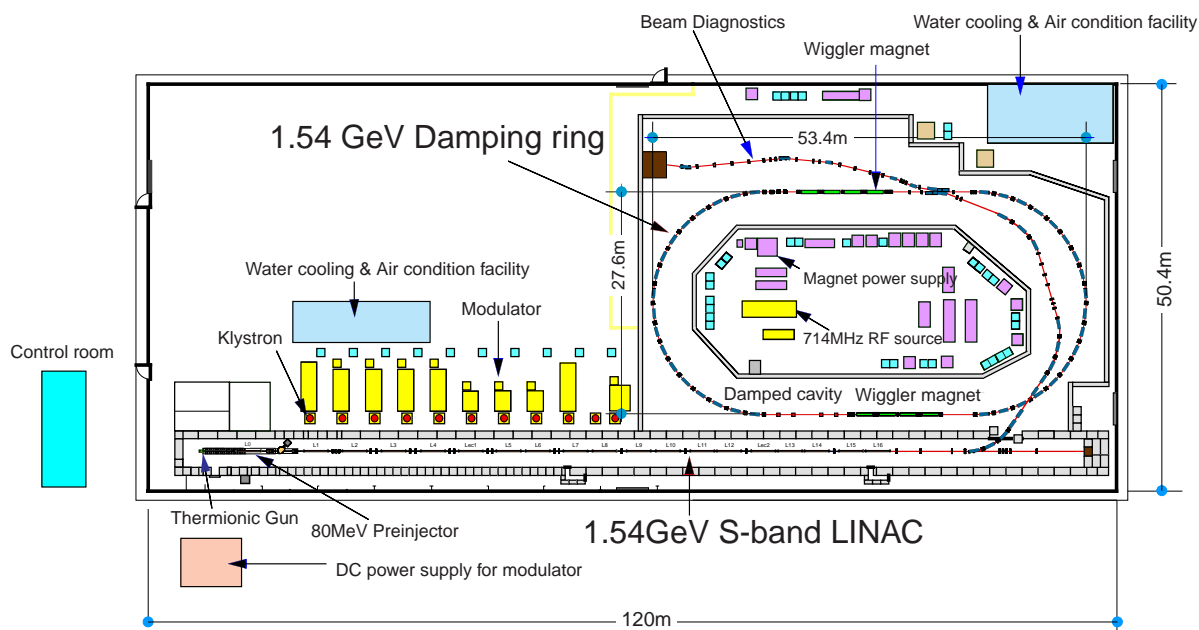
Figure 3.3: *Schematic layout of ATF at KEK.*

The main technical goal of ATF is to demonstrate production and control of a multi-bunch train electron beam with the ultra-low emittance that will be required at JLC. The specific target emittance is 1 nm horizontal and 10 pm vertical at 1.54 GeV.

The design for the ATF was mainly conducted by a collaboration in Japan, led by the KEK group. It was reviewed through several LC workshops and meetings, which included discussions with collab-

ISG Progress Report, April, 2000

orators from SLAC. The actual construction of ATF began in 1993. The pre-injector was completed in August 1993, and the development of multi-bunch beam-diagnostics began. In November 1995, the high-gradient linac was completed for experiments on the acceleration of a multi-bunch beam and on compensation of multi-bunch beam loading. In January 1997, after installation of the main hardware components, beam commissioning of the damping ring began. In November 1997, an extraction line that allows high-precision beam diagnostics was completed.

Typical conditions in recent study operations of the damping ring are listed in the Table 3.13.

Items	Achieved Values	Design
ATF Linac Status		
Maximum Beam Energy	1.42 GeV	1.54 GeV
Maximum Gradient with Beam	28.7 MeV/m	30 MeV/m
Single-Bunch Population	1.7×10^{10}	2×10^{10}
20 Multi-bunch Population	7.6×10^{10}	40×10^{10}
Damping Ring Status		
Maximum Beam Energy	1.28 GeV	1.54 GeV
Single-Bunch Population	1.2×10^{10}	2×10^{10}
COD(peak to peak)	$x \sim 2$ mm, $y \sim 1$ mm	1 mm
Bunch Length	~ 7 mm	5 mm
Horizontal Emittance	$(1.3 \pm 0.2) \times 10^{-9}$	1.4×10^{-9}
Vertical Emittance	$(3.6 \pm 1.0) \times 10^{-11}$	1.0×10^{-11}

Table 3.13: *Achieved and design parameters at ATF.*

Throughout this period the beam development work has been done by an international collaboration consisting of nine overseas laboratories and nine Japanese universities [19, 20, 21, 22, 23]. Participation by US physicists and engineers, led by the SLAC group, has had two functions: (i) to contribute to the international ATF collaboration, and (ii) to participate in ISG activities in pursuit of optimized injector design schemes for JLC/NLC.

Several issues particular to the injection systems of a linear collider have been noted since the early stage of design development of ATF:

1. Since the goal for the emittance coupling at the damping ring is on the order of 1 %, precise alignment (particularly vertical) of all magnetic components and beam position monitors is essential.

2. For improved efficiency and accuracy in tuning the damping ring, fast,non-multiplexed read-out electronics for beam position measurements are required.

3. Since sophisticated beam tuning methods are to be employed, the control system must provide the scientists with easy-to-implement tools for integrating numerous analysis techniques of applying modeling calculations to the beam data.

4. Machine stability over various time scales is important. Given the small emittance and low-energy (∼1.5 GeV) of the beam, relatively small mechanical, magnetic and electrical instabilities in the accelerator system significantly impact both machine performance and the interpretation of beam data.

5. Since a large amount of particle charge needs to be handled in multi-bunch train operation, the beam loss across the accelerator system must be minimized for radiation safety considerations.

At ATF we encountered a number of issues, some expected, some unexpected, related to the items above. The purpose of this section is to present the issues that have been learned at ATF as lessons for the design of NLC/JLC injector systems.[1]

In subsequent sections, we present a summary of the achieved performance of the ATF system and several lessons that are worth noting as of spring of the year 2000.

3.3.2   Summary of ATF Performance

Single-Bunch Operation

The majority of beam studies at the damping ring have been conducted in a single-bunch mode in which one bunch is injected into the ring for each machine pulse. This allows studies in an operating mode that is much less complex than the multi-bunch beam operation. Table 3.13 summarizes some of the achieved accelerator performance parameters of the ATF.

The beam energy has been reduced from 1.54 GeV to 1.28 GeV to improve operability of the linac klystron system. The pulse repetition rate is limited to 0.78 Hz to keep the radiation level sufficiently low inside and outside the accelerator housing. This is an issue which will be discussed in more details later. The charge per bunch is limited by injection efficiency due to the small energy acceptance of the beam transport line. Observed fluctuations of the stored charge are thought to be due to energy and energy spread fluctuations from the linac. No significant beam loss was observed at extraction after extraction line tuning.

Typical amplitudes of the closed-orbit distortion (COD) in the damping ring were about ±2 mm horizontal and ±1 mm vertical. These results are larger than those predicted by simulations, even those simulations which include misalignments and corrections using steering magnets. Possible explanations for this discrepancy include errors in the BPM system, errors in the alignment measurements or errors in the optics model. So far, we have not been able to firmly identify the source of the discrepancy.

Energy spread was measured in the extraction line using a screen monitor at low bunch population and found to agree well with calculations. Dependence on the bunch population was also measured and used to cross check the measurement of the vertical emittance[33]. Bunch length was measured in the damping ring by observing the synchrotron light with a streak camera. Apparent bunch length

---

[1] The issues more closely connected to the specific hardware configurations of ATF are discussed in a separate report, "The study report JFY 1996-1999 on the ATF" [23].

dependence on the bunch population indicates an existence of an inductive impedance of about 50 nH. This is much higher than our model calculation of 14 nH [42]. However, the systematic errors in the streak camera measurements are still large. So far, no other significant experimental studies have been done on beam instabilities.

The horizontal beam emittance, measured by using wire scanners in the extraction line, agrees well with the theoretical calculation[32]. The vertical emittance has been measured both in the damping ring using a synchrotron radiation (SR) interferometer and in the extraction line using wire scanners. We have also estimated the vertical emittance from the dependence of the energy spread on the bunch charge. The apparent vertical emittance has been estimated to be approximately 0.05 nm, or 3 % of the horizontal emittance[33]. Our target value for the emittance coupling is 1 %. Simulation studies show that the target emittance should be achievable after COD corrections and local bump tuning[41] for the currently known level of component alignment. However, this has not yet been achieved.

The discrepancy between the measured and the predicted (target) vertical emittance could be due to inherent inaccuracies in present measurement techniques. For example, we have observed orbit oscillations in the ring at a frequency of 100 Hz with an amplitude of 10 microns. The SR-interferometer requires a gate width of ~ 30 msec to accumulate enough light for an accurate beam size measurement. This gate width is sufficiently large with respect to the period of the orbit oscillation that the measured beam size appears to be dominated by the oscillation amplitude.

Emittance measurement in the extraction line could be affected by x-y coupling. In principle, we can solve for the x-y coupling and calculate the 'intrinsic' emittance from beam sizes measured with five wire scanners each of which has three wires at different angles. However, simulation studies show that the accuracy of the beam size measurements is much poorer than required for this kind of analysis [36, 38]. In addition, residual dispersion in the wire scanner region and jitter in the extraction kicker system made measurement in the extraction line difficult.

Multi-Bunch Operation

A $\pm \Delta F$ beam loading compensation experiment in the ATF linac was successfully conducted at 1.16 GeV with 23 bunches/pulse in 1996[40]. To date, damping ring beam studies have been limited to single-bunch operation by high radiation levels due to beam loss. We need to reduce the beam losses and increase the radiation shielding to the extent that we can perform single-bunch beam operation at a repetition rate greater than 6.25 Hz. At that point, multi-bunch operation will be possible at a repetition rate of 0.78 Hz.

3.3.3   Accelerator Physics Issues: Highlights

Physical and Dynamic Aperture of the Damping Ring

The standard design physical aperture of the ATF damping ring is 12 mm in the arcs. Narrower physical aperture exists at a mask in the south straight section (6 mm), the photon masks in the wiggler sections (5 mm), and the vacuum chamber for the extraction kicker (5 mm). All the quoted numbers are for the half aperture. [2]

The physical aperture was checked by steering the beam at injection. We also measured physical aperture by detecting beam loss over the first few turns for different injection orbits. The result was consistent with expectations. From first-turn beam loss induced by various global and local orbit changes, a physical acceptance of $(2 \sim 10) \times 10^{-6}$ mrad was deduced, in good agreement with the known aperture restrictions[29]

The measured acceptance corresponds to a 1 mm half aperture at a location with 10 m beta function. The design physical aperture is much larger than this.

Theoretical calculation of the damping ring beam dynamics yields an estimated dynamic aperture of ± 6 mm. Simultaneous measurements of beam current decay and vacuum pressure permit a straightforward evaluation of the ATF transverse acceptance in the actual beam operation. The measured acceptance was found to be $1 \sim 2$ orders of magnitude smaller than the design physical and dynamic acceptances (a factor 5 smaller in aperture). It depends strongly on the strength of the horizontal sextupoles, the RF voltage, and to some extent, on the working point in the tune diagram. However, it is fairly independent of vertical sextupoles and skew-quadrupole settings. The lifetime reduction observed with an orthogonal set of closed-orbit distortions shows an aperture limit in both betatron phases at a 1 mm amplitude, roughly consistent with the beam lifetime. The aperture restriction in the horizontal plane appears to be tighter than that in the vertical. The measured acceptance reduction near the 1/3 and 1/2 integer resonances points to the presence of a large nonlinear field.

We conclude that an extremely small dynamic aperture is the most probable explanation for the short beam lifetime. In the near future, we intend to reconstruct the nonlinear Hamiltonian governing the beam motion in the ATF damping ring from multi-turn orbit data[30].

Intra-Beam Scattering

Given the extremely low emittance of the ATF damping ring beam, it is difficult to directly and accurately measure the vertical beam size in the damping ring. In addition, the Touschek effect is expected to be the dominant beam loss mechanism, making the beam lifetime much shorter than in many ordinary storage rings. These are challenges that we must also face at JLC/NLC.

---

[2]The vacuum chambers going through the injection and extraction septa magnets have half aperture of 3.5 mm. Attentions should be paid to them in the light of beam loss during beam injection and extraction. However, they are not considered to cause major aperture restrictions during the beam store time, because the DR vacuum chambers for the stored beam in the neighborhood of septa have half aperture of 7 mm.

On the other hand, the Touschek effect causes the beam lifetime to be approximately proportional to the bunch volume at equilibrium. We can take advantage of this fact to infer the beam size in the ring. The bunch volume, or equivalently the vertical emittance when horizontal and longitudinal beam sizes are known, can be evaluated from the measurement of the Touschek lifetime, leading to the possibility of a new beam diagnostic technique [34]. Thus a beam lifetime model, which includes the effects of the potential well distortion, the intra-beam scattering, the photo-desorption and Touschek effect was proposed [35].

The measured dependence of the lifetime and the energy spread on the beam intensity indicates an emittance ratio of ~ 2 %, assuming that the intra-beam scattering effect is the source of the beam-size variation. Here we used the dynamic aperture that has been actually measured at the DR rather than the calculated value. The evaluation obtained there turned out to be consistent with the vertical emittance measured by the wire scanner beam profile monitors $(3.6 \pm 1.0) \times 10^{-11}$. It was found that this method of emittance evaluation is effective in the lower emittance region, and the measurement demonstrated a high resolution.

3.3.4 Issues with Instrumentation and Beam Tuning Procedures

A noteworthy requirement for beam instrumentation at NLC/JLC is the need to make measurements on a pulse-by-pulse basis. This is somewhat different from a conventional storage ring, although both types of rings share a number of common beam tuning techniques. This section summarizes the development of beam instrumentation and tuning techniques at ATF which are considered particularly relevant to JLC/NLC.

Instrumentation

To analyze and tune the linear collider beam, single pulse instrumentation and synchronous measurements are as necessary as high resolution and high precision. Single pulse BPMs are installed in every beam line of the ATF. A pulse-by-pulse data acquisition system has been developed and is used as an optics diagnosis tool. ATF has adopted a BPM electronics system consisting of a baseline clipping circuit and an inexpensive, 16-channel charge sensitive ADC. The baseline clipping circuit was found to have a poor S/N ratio in its output as well as non-linear response. To improve the S/N ratio, a preliminary modification was made to the input stage circuit. After further modification to fix a problem found in the beam test, the resolution was improved from 40 μm to 20 μm at nominal beam intensity. The circuit still has a non-linear response coming from the diode clipping circuit, and there has been a continuous effort to correct this. An operational amplifier with high speed response and output voltage limit function is used for a new baseline clip circuit instead of the diode. This circuit was installed in the linac, BT and EXT BPMs using the pre- amplifiers already in place. The linearity of this combination holds over 30dB input range, and the resolution, estimated at EXT wire scanner line BPM, is better than 20 μm. The next step of this development is to produce a unified module containing this circuit combination with higher resolution at a lower cost.

In the DR, higher resolution orbit measurements are required for procedures such as beam-based alignment and dispersion measurement. Software to provide high resolution by processing multiple BPM readings over a 600 ms store has been developed. By using multiple CAMAC access commands in one QIO, this software can realize 20 to 30 position readings per store and average the results to improve resolution. Unfortunately, implementation of this software correlates with otherwise unexplained control system lockups, so its use has been minimal.

For multi-bunch beam operation, some specialized multi-bunch BPM hardware is needed. The present BPM system's clipping circuit is sensitive to rising edge of an RF burst signal, and as a result, the BPM will read back the position of the first few bunches in a train. For the most part, this is sufficient for multi-bunch beam position measurement requirements. However, true multi-bunch BPMs, devices that can produce individual position readbacks for each bunch in a multi-bunch train, are required in four locations: downstream of the energy analyzer at the 80 MeV section, downstream of the BT bend magnet, in the damping ring, and in the extraction line. The former two are required for tuning transient beam loading compensation and charge transmission, the latter two are needed to monitor orbit and energy deviations. At present, an oscilloscope is used to measure multi-bunch beam position, while the fast BPM electronics are under development.

A beam size monitor for the ring using SR interference was developed [26]. The principle of object profile measurement by means of the spatial coherency of the light is known as the Van Cittert-Zernike theorem. The application of this theorem into beam profile measurement has been done using a double slit and its interferogram of SR light. The modulation of the SR interferogram is directly related to the beam size, making it possible to measure down to 5 μm beam size (beyond the limit of diffraction dominated SR optics). An on-line system for measuring the vertical beam size measurement was constructed and utilized for beam tuning. However, because of the high sensitivity of the light interference, vibration in either the optics components or the beam seems to limit the measured beam size to around $11 \sim 12\mu$m, while target beam size is $6 \sim 7\mu$m. Since the SR optics room is located on top of the damping ring concrete shielding supported by large steel pillars and frames, the optics table is affected by low frequency floor vibrations during CCD camera exposure. In addition, a correlation between the light intensity and the measured beam size was found. The measured beam size decreased by $10 \sim 20$ % as the light intensity decreased. This systematic error must be understood and taken into account.

Beam Tuning Software

The SAD modeling program[31] is used to calculate settings for steering magnets in orbit and dispersion corrections. The dispersion in the DR is measured from the difference of orbits taken at different RF frequencies. The dispersion correction works well, typically yielding about ± 5 mm vertical dispersion which is close to the correction goal. The COD correction in the damping ring was partially successful although the results fell short of those expected from simulations.

To correct x-y coupling, the trim coils of the sextupole magnets are connected to produce skew quadrupole fields. It has been seen that these knobs can be used to tune apparent coupling, observed

as (i) "cross talk" of x betatron oscillation into y betatron oscillation and vice versa, and (ii) betatron coupling measured from tune separation near the coupling resonance. However, so far, no significant improvement of the measured beam emittance ratio has been observed.

Beam-based measurement of the linear optics has been performed. Errors in the quadrupole fields as large as 2% were deduced from the beam orbit and the data was used to correct the optics model. In addition, some initial tests of beam based alignment were made by changing the strength of individual quadrupole magnets and measuring the beam orbit. The results are consistent with measurements using optical alignment techniques but the accuracy is not significantly better; simulations indicate that better BPM resolution is needed [44].

3.3.5   Long-Term Stability of the Damping Ring

In a linear collider, stability of relative phase between the accelerated beams and RF systems is more critical than other accelerators. Although RF phase stabilization systems have been developed, thermal expansion and contraction of beam line components and the accelerator housing can create unacceptable phase errors. Building an accelerator tunnel that can maintain the required dimensional stability may be very difficult and it may be more practical to include a path length compensation scheme.

During the operation of the ATF damping ring, we observed that the ring RF frequency had to be changed by up to ± 20 kHz over an extended period. The frequency changes were required to keep the beams centered in the beam position monitors and sextupole magnets in the arc sections. This behavior was found to be consistent with measured variations in the ring circumference. Changes in the ring circumference were independently measured using standard beam line alignment techniques.

Fig. 3.4 shows the difference between the measured and design circumference of the damping ring where the change is in the range of ± 3 mm.

After some studies we concluded that the most likely source of this problem was thermal expansion of damping ring's concrete floor [24]. The observed circumference changes are consistent with the measured temperatures and the linear heat expansion coefficient of concrete of $\sim 10^{-5}/^{\circ}$C.

Data from concrete floor temperature measurements are shown in Fig. 3.5. After turning on the magnet power supplies, the temperature of the floor increased at the rate of $2.4 \times 10^{-4 \circ}$ C/min. At the same time we measured the horizontal position of the beam in the arc sections. Having previously measured the dispersion function at BPMs using the RF ramp technique, as shown in Fig. 3.6, the energy drift was calculated with equation 3.1:

$$\Delta E/E = \Sigma \eta_i \Delta x_i / \Sigma \eta_i^2 \tag{3.1}$$

A 0.01% energy drift corresponds to 30μm circumference expansion when we assume a momentum compaction factor α_C of 0.0022 (design and measured value) according to following equation:
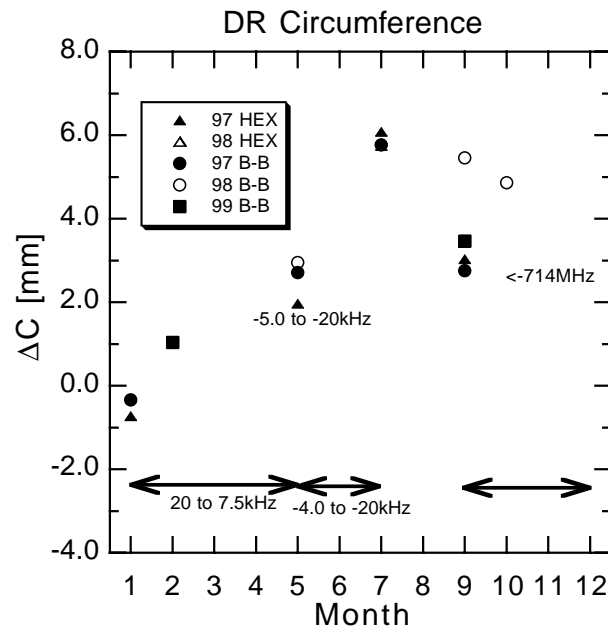
Figure 3.4: Change of DR circumference, horizontal axis indicates month during which the circumference was measured. The horizontal axis numbers indicate the month in each year. Vertical axis denotes the difference between measured and design values. "B-B" indicates data based on bend-to-bend distance measurements. "HEX" indicates data based on ATF hexagon measurements.
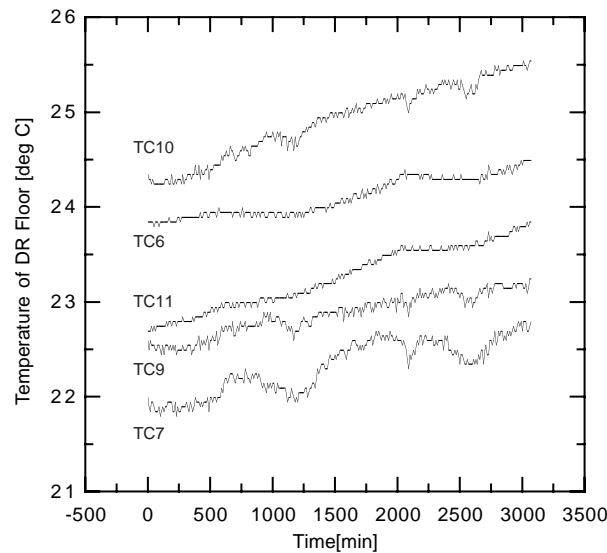
Figure 3.5: Temperature Drift of the Ring Floor, average slope is $2.4 \times 10^{-4\circ}$ C/min.
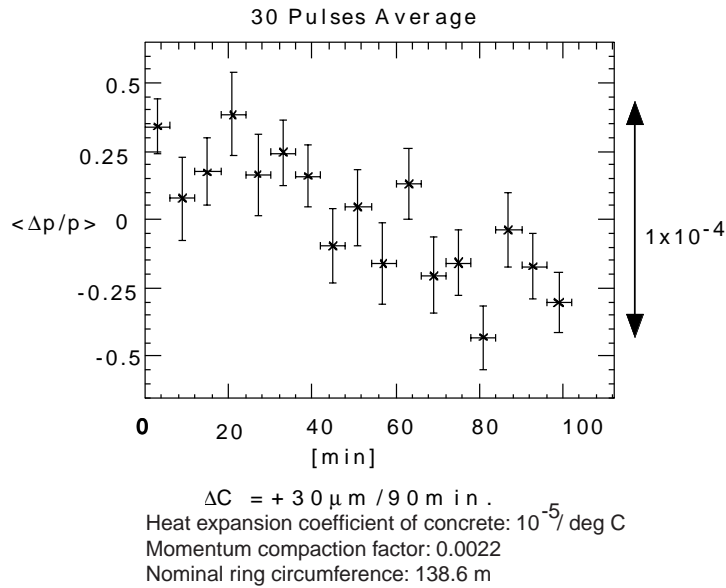
Figure 3.6: *Energy Drift, horizontal axis is time. Vertical axis is beam energy drift.*

$$\delta E/E = -\frac{\delta C/C}{\alpha_C}, \tag{3.2}$$

where δE is energy drift and C the circumference.

Fig. 3.7 shows the stored current and the beam energy in the ring for a period of 400 minutes. When the injection and stored beam orbits were precisely tuned, almost 100% beam capture efficiency was achieved. This stability only lasted a few hours.

The observed variation of the ring circumference creates a tune drift of∼ 0.01. As this is large enough to cause beam instabilities, stabilization measures need to be taken. For this purpose, direct ventilation of the heated air from power supplies has been implemented in 1999. In addition, automatic control of RF frequency, and installation of two chicanes to control the orbit length are being planned[37]. The two straight sections (2m-long, each) of the damping ring can accommodate these. However, there is a limit to the range of circumference adjustment that can be accomplished by these chicanes. Consequently, our first priority is to reduce the circumference variation to the range of ±1 mm with the first two actions mentioned above.

3.3.6   Short-Term Stability of the Damping Ring

The most critical stability issue at ATF is the variation in DR stored beam intensity on a pulse-to-pulse basis. Injection beam intensity is directly related to linac energy jitter and drift. The BT orbit is affected by variation in the energy gain in the middle of the linac, which directly affects the injection
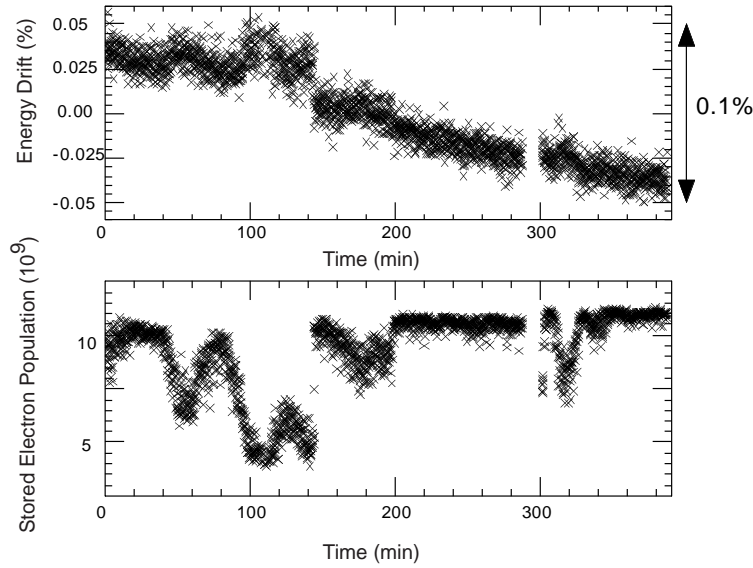
Figure 3.7: *The status of Energy Drift and Stored Current for 400 min., Typical stored charge is* 1×10^{10} *electrons/bunch.*

angle in the septum magnet region. In addition to the energy jitter, bunching jitter also directly affects the energy spread jitter, leading to injection intensity jitter. In order to stabilize the extracted beam current, stabilization of the linac energy and bunch length is the first priority. To look for sources of jitter, the correlation plot system was installed. The system was implemented into the BPM reader which takes BPM data synchronously with beam repetition. Several sets of ADCs were added to the BPM reader facility and various signals such as AC voltage, klystron voltage, gun voltage, and bunch length signal were put into ADC channels[39]. Correlation analysis showed that gun HV fluctuations coming from the AC line was one of sources of bunching jitter. AC line fluctuation also affected the klystron voltage and beam energy. The gun HV station was modified to eliminate corona discharge, and to reduce the time jitter in the grid pulser trigger to less than 4 ps rms. As for input AC line fluctuation, an AC line stabilizer was introduced for both the gun HV (0.5% stability) and the gun thyratron system (1% stability). The klystron thyratron system was similarly stabilized to the order of 1 %.

Since the klystron modulator system is driven by a large, central DC power supply, voltage stabilization of this system is difficult. Instead, we introduced a feed-forward deQing system which reduced klystron voltage fluctuation by half. The AC line fluctuation of $2 \sim 3\%$ comes mainly from cyclic operation of the KEK proton synchrotron. With these upgrades, beam intensity fluctuation in the BT line was reduced from $4 \sim 5\%$ to $1 \sim 2\%$. Nevertheless, the DR stored current still has a $2 \sim 3\%$ fluctuation. Efforts to reduce the DR intensity jitter to less than 1 % are still underway.

The DR stored orbit stability was analyzed using a pair of fast turn-by-turn electronic digitizers which were connected to a pair of arc BPMs, approximately 90 degrees apart in x and y betatron phase. The electronics consist of a pre-amplifier and a self-triggered 14bit sample-hold ADC with a 3 Mega

samples/sec 64k deep word memory. The system was newly developed for use at ATF. It can be used to monitor injection orbit excitation and damping, stored orbit excitation and damping, and stored orbit stability. The turn-by-turn monitor can also be used for precision tune measurements when combined with the beam exciter kicker. The 64k turn position data showed a 20 μm (peak-to-peak) 100 Hz oscillation in vertical direction everywhere during the storage period. The vertical tune also was oscillating with 0.01 amplitude at 100 Hz. After several surveys and further analysis, we found the main bending power supply had a ripple of $\sim 6 \times 10^{-3}$ at 100 Hz which was directly identified as the source. The ripple of the bend power supply came from a difference between the design and actual load inductance, the former being estimated at a higher frequency rather than several 10 Hz. In order to resolve this problem, we added an inductance in series with the bend magnet load and got $\sim 5 \times 10^{-4}$ ripple. The 100 Hz orbit oscillation disappeared, and instead we observed a 7 μm 300 Hz oscillation and a 20 μm 50 Hz oscillation. The analysis of these instabilities is ongoing.

The extracted beam stability has also been the subject of study. The ATF double kicker system (section 3.3.8) is intended to compensate for kicker related instabilities but, even operating at design, residual beam trajectory jitter remains. In addition, different waveforms in the two kickers reduce the effectiveness of the cancellation. Trigger timing jitter and drift are of special concern since they cause an error in the horizontal wire scanner beam size measurement. The trigger jitter relative to beam is ~ 10 ns (peak-to-peak) and the drift over a several minute interval is around ± 20 ns. These values are relatively big compared with pulse flat-top width and flat-top ripple. The jitter and drift originate in the low voltage thyratron trigger pulser and in the drift of various auxiliary thyratron power supplies. Reduction of the thyratron trigger timing jitter and drift is a critical effort. We will work to resolve this issue by introducing a stable DC power supply into the heater, reservoir, grid power supply systems (for drift problems), and a steep rising grid trigger pulser for jitter reduction.

3.3.7   Beam Loss Issues

The beam repetition rate of the ATF, presently 0.78 Hz, is dictated by the allowed limitation on radiation dose rates (0.2 μSv/h for gamma-ray and neutrons combined) outside of the radiation control area. Beam losses have proven to be much worse than the design expectations. External radiation monitors are positioned in order to take the beam loss pattern into consideration. The areas of most concern are the beam collimation area, the linac beam dump area, the DR injection area and the dump for the extracted beam. There are four interlocked peripheral radiation monitors (0.2 μSv/h interlock level) and two interlocked proximity wall side monitors(20 μSv/h interlock level). Each of the monitors operates at close to 60 $\sim$ 80% of their interlock level at 0.78 Hz beam rate. The DR has never run with the design 25 Hz repetition rate.

In Tables 3.14 and 3.15 we compare the beam loss estimation in the radiation shielding design to the actual beam loss for damping ring mode operation.

The big difference between the design and achieved losses occur at the BT collimator1 and DR injection areas, illustrating the difficulty of estimating both the beam energy tail fraction at the end of the linac and the effectiveness of the collimators.

Area	Beam Energy	Loss
Buncher section	240 keV	20%loss (PARMELA simulation)
L0 accelerator section	150 MeV	0.5% loss (safe-side assumption)
Linac from 150 MeV to 1.54 GeV	no beam loss	(aperture >> beam size)
BT collimator1 (downstream of BH10T)	1.54 GeV	0.3% ($> 3_-$)
BT collimator2 (upstream of movable Dump)	1.54 GeV	0.3% (safe-side assumption)
DR injection	1.54 GeV	no beam loss (beam is well collimated)
DR storage	1.54 GeV	4×10^8 electrons/sec (Touschek life)
EXT 2nd EXT-kicker	1.54 GeV	0.3% (safe-side assumption)

Table 3.14: Beam losses assumed during the ATF design stage

Area	Beam Energy	Loss
Buncher and L0 accelerator section	80 MeV	$\sim 30\%$ loss
Linac	from 80 MeV to 1.3 GeV	no beam loss (undetectable)
BT collimator1 (downstream of BH10T)	1.3 GeV	$\sim 25\%$ loss
BT collimator2 and DR injection	1.3 GeV	$\sim 20\%$ loss
DR storage	1.3 GeV	no beam loss (lifetime ~ 180 sec)
EXT 2nd EXT-kicker	1.3 GeV	no beam loss (undetectable)

Table 3.15: Actual beam losses measured by an integrating current transformer(ICT) at ATF in winter 1999 with a single-bunch starting at 1.8×10^{10} from gun (0.78 Hz operation).

We would like to understand the beam tail in the linac and the energy tail after collimation. To characterize the beam losses, a beam loss monitor and a set of well calibrated beam current monitors are needed. A long ion chamber beam loss monitor was installed by D. McCormick of SLAC and has been utilized in beam tuning.

Linac Energy Spread

The large single-bunch energy spread and tail comes from the long bunch length created in the buncher section and propagated through the linac. This is one of the most important issues at ATF. In order to solve this problem, the injector buncher section was redesigned using the simulation code PARMELA[45]. An RF bunch length monitor was also installed[46], and has been utilized for buncher tuning and real-time bunch length monitoring.

Insufficient bunching creates a significant longitudinal tail which is converted to an energy spread tail at the end of the linac. PARMELA simulations showed the long tail at the injector 80 MeV output point. To increase the bunching with only small changes in the existing hardware, we rearranged the sub-harmonic cavity and the Helmholtz focusing coil positions and set the Helmholtz coil current according to PARMELA results. The upgraded bunch length was around $10 \sim 12$ ps FWHM which was similar to the simulation result. The simulation predicted 80% of the charge would be focused

into a 20 ps range. We therefore predicted 80% of the charge would be transmitted into the BT line. However, the current transmission was still ∼60% even though the spot size after first bend of the BT was significantly reduced. We are still investigating possible sources of the poor transmission of the BT collimator section.

Multi-bunch energy spread, defined as the energy centroid bunch-by-bunch difference, is caused by transient beam loading of accelerating structures. The spread is estimated to be ±4.2% at 2×10^{10} electrons/bunch and 20 bunches/multi-bunch train. Since the energy acceptance of BT and DR is no more than 1%, an energy compensation system using ΔF accelerating structures is proposed and commissioned. In order to synchronize with DR injection, an offset frequency of 2856 ±4.327 MHz was chosen for the ΔF structures (4.327 MHz is twice the DR revolution frequency). This slight difference in accelerating field frequency causes a phase shift in the acceleration of each bunch so that it compensates by decelerating the head bunches and accelerating the tail bunches. The ± frequency for multi-bunch compensation corrects for the slope of the accelerating field within a single bunch. The experiment demonstrating this scheme used 6×10^9 electrons/bunch and 20 bunches/train. The multi-bunch energy spread was 5% from head to tail. It was corrected within 0.6 % using 25 MW klystron output into 3 m ΔF structures without any problem[40].

3.3.8   Injection and Extraction Kickers

The linear collider will require kickers with very fast rise and fall times and with no ripples following the pulse. The kickers in use at ATF have had problems reaching the target parameters. The 12.5Ω impedance injection kicker, made through a collaborative effort with SLAC, has very good rise and fall times of 25 ns rise (10% to 90%) with a 50 ns long flat top (±3% peak-to-peak). However, there is a long trailing edge or pulse tail which brings the total pulse width to 170 ns, about 50 ns longer than the design 120 ns width (30 ns full rise + 60ns flat-top + 30 ns full fall, in case of 20 bunch × 5 train operation). The post field ripples are 3.8% of full field. Even with the ripple we could inject and store three trains in the ring. In order to achieve full five train operation, the post field ripples should be smaller than 3.8%.

On the other hand, the 50Ω impedance extraction kicker, (made at KEK), has long rise and fall times and large post field ripple. It has a 40 ns rise time (10% to 90%), 60 ns fall time (90% to 10%) and 55 ns of flat field region (31 kV) with < 0.6% ripple. However, the post field ripple is as large as 6%, making the total pulse length around 230 ns, roughly twice the design. Three train operation is not possible with this kicker waveform. In order to improve the waveform and post-pulse ripple, we will improve the kicker magnet connector impedance match, the PFL (pulse forming line) charging circuit isolation and the thyratron turn-on rise time.

The extraction pulse-to-pulse stability tolerances require the use of an achromatic kicker magnet pair. The double kicker system consists of one pulsed power supply, two identical kicker magnets placed optically π phase advance apart in order to compensate for the pulse-to-pulse kick angle variation for each bunch in a multi-bunch train. We expect a factor of ten improvement in the stability of the extracted beam. Analysis of beam stability data by fitting the orbit of each extracted beam pulse

shows that the system reduced the orbit jitter to less than the BPM resolution of 24 μm in some conditions. When the kick angle is relatively large, the reduction is less. The source of this big kick angle variation seems to come from thyratron timing jitter. If the two kickers do not have identical waveforms, the system becomes more sensitive to timing jitter. The two transmission cables from the pulser to the kickers have different lengths because of beam travel time delay between the kicker magnets. The kicker magnet with the longer of the two cables has a somewhat slower, more distorted waveform than the other. Our first priority for improving the double kicker system is to fix thyratron trigger time jitter and drift. The adjustment of the two kicker flat-top waveform using additional wave-shape modification components inside the kicker magnet will be considered as a next step.

3.3.9   Comments on Wiggler Studies at ATF

A wiggler magnet system is required in order to achieve low emittance in a short damping time. The wiggler magnets in the ATF have only been used during specifically dedicated study times.

There are eight wiggler magnets in the ATF DR, each one with a length of 2 m made up of five magnet period cycles. The wigglers are installed in two sets of four magnets each. Each pole has a length of 0.1 m except those at the ends, both of which are 0.05 m long. The maximum magnetic field at the normal pole is 1.6 T, giving a bending angle of 39 mrad at the nominal beam energy of 1.54 GeV and taking into account the effective pole length of 0.144 m.

Studies were done in 1997[25] and again in 1999 at energies of 0.96 GeV and 1.28 GeV, respectively. The beam size, measured by SR monitor and fit results gave the transverse damping time. Emittance measurements were not done, however, so the wiggler effect on the emittance was not studied. Table 3.16 summarizes the measurement results and the SAD calculation.

Beam Energy [GeV]	Wiggler Magnet [A]	τ_x (meas) [msec]	τ_y (meas) [msec]	τ_z (meas) [msec]	τ_x (calc) [msec]	τ_y (calc) [msec]	τ_z (calc) [msec]
0.96	0	36 ± 12	100 ± 10	54 ± 2	46.8	68.5	44.6
	400	29 ± 2.4	58 ± 10		30.0	39.7	56.3
1.28	0	10 ± 2	33 ± 1.4		17.7	28.3	
		36 ± 11	46 ± 14				
	350	14 ± 1.9	23 ± 0.8		14.8	21.8	
	550	7.5 ± 1.8	17 ± 1.1		12.4	17.5	
	600	7.4 ± 1.2	18 ± 0.9		12.0	16.8	
		9.9 ± 1.7	16 ± 0.5				
		7.7 ± 0.4	16 ± 0.9				

Table 3.16: *Summary of measured damping times of the ATF damping ring with and without wiggler magnets excited.*

The table shows good agreement of the measurement and the calculation, so we can conclude that the wiggler magnets worked well in reducing the damping time.

ISG Progress Report, April, 2000

However, several operational problems with the wiggler magnets have been observed. The primary problem is that the B field is not properly canceled within each magnet pair. A more detailed analysis of the wiggler field leakage is needed and care must be taken to include these effects in future damping ring designs.

3.3.10 Conclusions from ATF Experiences

The Accelerator Test Facility damping ring and linac have proven vital for developing the designs of the NLC/JLC injector systems. Important issues in beam dynamics, beam stabilization, monitoring of extremely small beams and supporting technologies have emerged during our commissioning efforts and have, in many cases, been understood and solved. The design vertical emittance and multi-bunch intensity have, however, not reached the expected performance levels and we have mounted ongoing efforts to achieve the goal performance. Beyond the attainment of these two critical parameters, we hope to develop stabilization and optimization systems that will become model systems for JLC/NLC.

References for Chapter 3

[1] V. Bharadwaj et al., "The NLC Injector System", Proc. 1999 Particle Accelerator Conference, p. 3447, New York 1999.

[2] J. E. Clendenin et al., "Prospects for generating polarized electron beams for a linear collider using an RF gun," Nucl. Instrum. and Meth. A 340 (1994) 133.

[3] J. Kurihara et al., "A high polarization and high quantum efficiency photocathode using GaAs-AlGaAs Superlattice," Jpn. J. Appl. Phys. 34 (1995) 355.

[4] JLC Design Study, KEK Report 97-1, April, 1997.

[5] NLC Zeroth-order Design Report, SLAC Report 474, May, 1996.

[6] J. N. Corlett et al., "The Next Linear Collider Damping Ring RF System", Proc. 1999 Particle Accelerator Conference, p. 800, New York 1999.

[7] M. Woods et al., J. Appl. Phys. 73, 8531 (1993).

[8] H. Tang et al., Proc. of the Workshop on Photocathodes for Polarized Electron Sources for Accelerators, Stanford, CA, p.344. (1993); H. Tang et al., Proc. of the 4th European Particle Accelerator Conference, London, England, p. 46 (1994).

[9] A. Herrera-Gomez et al., J. App. Phys. 79, 7318 (1996).

[10] K. Togawa et al.,DPNU-98-11, Mar 1998. 22pp. Published in Nucl.Instrum.Meth.A414:431-445,1998.

[11] T. Kotseroglou et al., "Recent Developments in the Design of the NLC Positron Source", Proc. 1999 Particle Accelerator Conference, p. 3450, New York 1999.

[12] H. Braun et al.,"A Possible Design for the NLC e+ Source", Proc. of the 3rd European Particle Accelerator Conference, Berlin, Germany, p. 530 (1992).

[13] J. N. Corlett et al., "The Next Linear Collider Damping Ring Complex", Proc. 1999 Particle Accelerator Conference, p. 3429, New York 1999.

[14] C. Pappas and R. Cassel, "Damping Ring Kickers for the Next Linear Collider", Proc. 1999 Particle Accelerator Conference, p. 1500, New York 1999.

[15] L. C. Teng, "Minimum Emittance Lattice for Synchrotron Radiation Storage Rings," LS-17 Argonne (1985).

[16] Z. Li et al., "Parameter Optimization for the Low Frequency Linacs and Compressors in the NLC", Proc. 1999 Particle Accelerator Conference, p. 3486, New York 1999.

[17] P. Emma,"Cost and Performance Optimization of the NLC Bunch Compressor Systems", LCC-0021 (1999).

[18] Z. Li et al., "Beam Loading Compensation for the Low Frequency Linacs in the NLC", Proc. 1999 Particle Accelerator Conference, p. 3483, New York 1999.

[19] Edited by F.Hinode et al., KEK Internal 95-4, June 1995.

[20] J.Urakawa, KEK/ATF Damping Ring, PAC97, pp.444-448, Vancouver, May 1997.

[21] H.Hayano, presented at 11th symposium on accelerator science and technology.

[22] J.Urakawa et al., presented at 17th International Conference on High-Energy Accelerators (HEACC98), Dubna, Russia, 7-12 Sep. 1998. KEK Preprint 98-154.

[23] Edited by H. Hayano et al., to be submitted to KEK Internal Report.

[24] J. Urakawa et al., presented at 12th symposium on accelerator science and technology, pp.48-50 (1999).

[25] T. Naito et al 1997 Particle Accelerator Conference, Vancouver,BC,Canada

[26] T.Mitsuhashi and T.Naito;"Measurement of beam size at the ATF damping ring with the SR interferometer", Proc. of 6th European Particle Accel= erator Conference, Stockholm 1998

[27] F.Zimmermann et al., presented at HEACC98.

[28] F.Zimmermann et al., "Measurement and Simulations of the Transverse Acceptance in the ATF Damping Ring", ATF-98-10 (1998).

[29] M. Minty, M. Woodley, ATF 98-11(1998).

[30] F. Schmit et al., ATF-99-14(1999)

[31] SAD (Strategic Accelerator Design) is a computer program complex for accelerator design which has been developet at KEK since 1996. See `http://www-acc-theory.kek.jp/SAD/sad.html` for resources.

[32] T. Okugi et al., "Evaluation of extremely small horizontal emittance" Phys. Rev. ST Accel. Beams 2, 022801.

[33] T. Okugi et al., "Vertical Emittance in the KEK Accelerator Test Facility", 1999 Particle Accelerator Conference, New York, p256-258, 1999

[34] C. Montag et al., ATF-97-18 (1997).

[35] T. Okugi et al., "Lifetime of Extremely Small Emittance Beam and Effective Method to Evaluate Vertical Emittance", to be submitted to Physical Review Letters.

[36] K. Kubo, ATF-99-02 (1999).

[37] P. Emma and T. Raubenheimer, "Circumference Correction Chicanes for Damping Rings", Proc. 1999 Particle Accelerator Conference, p. 3438, New York 1999.

[38] P. Emma, M. Woodley, ATF-99-04 (1999).

[39] V. Vogel, unpublished.

[40] S. Kashiwagi et al., "Preliminary Test of $\pm\Delta f$ Energy Compensation System", Proc. of the 18th International Linear Accelerator Conference, Geneva, p848, 1996

[41] K. Kubo, H.Hayano and J. Urakawa, "Simulation study on Low Emittance Beam Tuning in KEK-ATF Damping Ring", 12th Accelerator Science Study Meeting, Wako city, 1999. K .Kubo et al., "Optics Diagnostics and Tuning for Low Emittance beam in KEK-ATF Damping ring" 1999 Particle Accelerator Conference, New York, p3432-3434, 1999

[42] N.Terunuma, et.al., "Impedance Measurement of ATF DR", Procedings of 1998 European Particle Accelerator Conference (EPAC98), Stockholm, p469-471, 1998.

[43] K .Kubo, H.Hayano and J. Urakawa, "Simulation study on Low Emittance Beam Tuning in KEK-ATF Damping Ring", 12 th Accelerator Science Study Meeting, Wako city, 1999. K .Kubo, et.al., "Optics Diagnostics and Tuning for Low Emittance beam in KEK-ATF Damping ring" 1999 Particle Accelerator Conference, New York, p3432-3434, 1999

[44] K .Kubo, "Preliminary Simulation of a Beam-Based Alignment Technique", ATF internal, ATF-98-36.

[45] A.D. Yeremian, "Proposed Scenario for Tuning the L0 Accelerator Phase at ATF", ATF internal, ATF-98-30.

[46] T. Kotseroglou et al, "Injector Bunch Length Monitors", ATF internal, ATF-99-10.

Authors and Major Contributors of Chapter 3

- J. E. Clendenin
- P. Emma
- H. Hayano
- T. Kotseroglou
- K. Kubo
- M. Kuriki
- S. Kuroda
- T. Okugi
- Z. Li
- K. K. Millage
- T. Nakanishi
- M. C. Ross
- D. C. Schultz
- J. C. Sheppard
- N. Terunuma
- N. Toge
- J. Urakawa
- F. Zimmermann

CHAPTER 4

Klystron Modulator

Contents

4.1   Introduction

Modulators are a critical component of the JLC/NLC. Modulators convert AC line power into the train of high-voltage high-current pulses needed to drive the klystrons, which in turn generate the high power radio frequency (RF) waves that accelerate the linac beams. Modulators are needed in the main linacs that operate at X-Band (11.424 GHz) as well as in several prelinacs in the Injection areas operating at the lower frequency L, S and C band frequencies. The specifications for modulator voltage, current and pulse duration vary with the application, but ideally all the required designs can be configured from a common set of building blocks. Table 4.1 shows the range of requirements for the NLC as currently configured. All systems operate at 120 Hz.

Modulator	# Klys. /Mod.	Klys. % Eff.	Mod. % Eff	Volt. kV Pk	Curr. A Pk	Width μSec	Avg Pwr Out-kW	Est Pwr In-kW	Klystrons/ Modulators
Main (X)	8@75MW	60	75	490	2041	3.0	360	480	1656/207
Injection (L)	2@75MW	60	70	388	644	6.0	180	257	30/15
Injection (S)	2@65MW	45	70	350	825	5.0	173	248	17/9
Injection (C)	2@75MW	60	70	388	644	4.0	120	171	93/47
Compressors (X)	4@75MW	60	75	490	1020	1.5	90	120	8/2

Table 4.1: *Modulator Requirements for 0.5 TeV Main Linacs (3.0 μs Modulator Pulse), 6 GeV S, C & L Band Injection Linacs & X-Band Compressors. The pulse repetition rate is 120 Hz for all.*

4.1.1   Historical Background

Since the modulator provides the primary power used by the RF sources, its efficiency, reliability and cost are major factors in a successful machine design. The NLC/JLC requires more than an order of magnitude more klystrons than the existing SLAC Linear Collider (SLC). The modulator design used in the SLC is called a line-type. It operates by charging a lumped-constant transmission line (Pulse Forming Network, or PFN) to high voltage, then dumping the PFN stored charge through a high-voltage high-current thyratron switch into a step-up transformer, which in turn drives the klystron. The output is a rectangular pulse of duration determined by the electrical length of the PFN. The line-type design has three main deficiencies for use in the JLC/NLC: (1) The thyratron switch tube requires frequent adjustment and has a relatively short lifetime; (2) overall efficiency is only 50-60% due to losses in the various components including the lumped line, switch tube and pulse transformer; and (3) unit cost is high making these modulators a dominant cost driver in the NLC/JLC RF power system. Designing a modulator to minimize all three deficiencies is critical to a successful JLC/NLC.

The development of pulsed modulators for the NLC/JLC is closely linked to the development of both the klystron and the RF system of the accelerator. Initially the system designs for the accelerator asked for klystrons with a pulse width of approximately 800 nanoseconds. At the same time the initial klystrons were expected to operate at an output of 100 MW. This approach called for modulators of

greater than 400 kilovolts peak pulse. It was obvious that conventional modulators would be very inefficient at these narrow pulse widths and high voltages due to slow rise and fall times. In addition, the energy required to charge the natural system stray capacitance and the inherent capacitance of the klystron would be an appreciable part of the total pulse energy. R. Cassel of SLAC designed and built a Darlington modulator[1] to try to overcome the slow rise and fall times of the conventional designs. This design proved to be limited by the internal inductance of the high voltage capacitors. Basic high voltage modulator R&D continued at SLAC to support klystron development including work at 550kV[2]. Around this time H. Mizuno et al at KEK worked on development of modulators with Blumlein PFN for improved operating efficiency at relatively short pulse length of 400 ns[3]. The KEK team also developed an all solid-state modolator[11] which used a pulse-forming line, a pulse transformer and a magnetic switch. The modulator successfully produced an output pulse with a peak voltage of 600 kV, a flat-top of 420 ns and a rise time of 152 ns with a dummy load (impedance 450 Ω).

The pulse width of the klystrons then began to widen to 1.1, 1.2 and eventually 1.5 microseconds and the power of each klystron dropped to 50 MW. Klystron R&D continued to eventually produce a 75 MW klystron which was tested at 1.5 microseconds and beyond. However, these prototypes used electromagnetic focusing, and the power required for the magnet was almost equal to the average RF output power of the klystron. Efficiency concerns led to a Periodic Permanent Magnet (PPM) focussed klystron development program. In order to keep the beam current below a level that could be handled with PPM focusing the klystron voltage had to increase, eventually approaching 500kV as discussed in Chapter 5 of this Report (also see [4, 5]). Most recently, a 3.0 microsecond PPM 75 MW klystron has been successfully demonstrated, leading to yet another change in requirements for the main linac modulators as reflected in Table 4.1 above.

4.1.2   Summary of ISG Activities on Modulator R&D

R&D teams at SLAC, LLNL and KEK have pursued programs to improve reliability, energy efficiency and costs of modulators. Two main directions are being pursued. The first, called the Conventional Model, was to improve the line-type modulator with better components and packaging techniques. This model aimed to lower costs primarily by compact packaging, driving two loads with one switched PFN, and obtaining more reliable HV components (thyratrons, pulse capacitors and output transformers). Additionally reliable solid state switches that could replace thyratrons were investigated. Efficiency would remain relatively low (∼60%) because of component and PFN losses and the relatively slow pulse rise and fall times through the high ratio step-up transformer (low waveform efficiency).

Another modulator variant has come to be called the hybrid type. An example is a configuration where the HV supply charges a capacitor rather than a PFN, followed by an on-off IGBT stacked switch driving a step-up transformer to the final load or loads. The pulse is formed by only partially discharging the capacitor each time the IGBTs cycle on and off. This type has fewer components and develops double the voltage of a PFN type for the same switch voltage.

A second major R&D direction, the Solid State Induction design, was started at SLAC in 1998. It is

based on an induction linac principle in which the high voltage is developed by magnetically stacked cells driven at low voltage ($\sim$2 kV) by separate electronic switches on printed boards. A stack of N cells develops a voltage of $\sim$ 2 kV$\times N$ in each turn of the secondary. This model exploits the IGBT Insulated Gate Bipolar Transistor power switch recently developed for the electric train and motor drive industries. These devices switch short pulses with excellent rise times at much higher currents than their nominal maximum current rating. A stack of very high permeability low loss amorphous magnetic cores (1-turn toroids) leads to a design with potentially $\sim$80% efficiency, 10,000 hour MTBF (Mean Time Between Failure) overall reliability, and 2-3 times lower cost per klystron. Successful demonstration of a simple 6-cell prototype at SLAC in 1998 spurred a major development program in 1999 with LLNL and its mechanical engineering contractor, Bechtel-Nevada. In view of the success of this early development, resources are currently heavily concentrated on a full prototype demonstration of the Induction design.

4.2 SLAC Conventional Modulator Development

The baseline modulator for the NLC was defined as one that could be built today with known technology. A conventional line Type modulator approach was chosen as the initial baseline. A study was undertaken to quantify the energy losses and predict or measure the maximum achievable efficiency. A simple analysis of system reliability was done to show that this basic design could meet the minimum requirements for the NLC, assuming a 3% redundancy in RF stations.

4.2.1 Circuit

The basic modulator circuit (Fig. 4.1) is a conventional PFN, incorporating two parallel lines with mutual coupling, discharged by a hydrogen thyratron through a 1:14 pulse transformer into a klystron load. This design yields a transformer leakage inductance reflected to the primary of approximately 0.5 μhy, places the charging power supply voltage between 75 and 80kV, and uses a three-gap thyratron for superior cathode lifetime.

The PFN is made up of two parallel, ten-section lines. Each line incorporates a single mutually coupled coil. A single thyratron discharges the two lines into a single pulse transformer. The mutually coupled line produces a flatter pulse without requiring high voltage tuning of each line. Low inductance in the primary discharge circuit is critical to fast output rise time. An inverse diode across the thyratron prevents reverse conduction which is very detrimental to lifetime. The pulse transformer has a bifilar secondary to power the klystron heater directly with either AC or DC.

The thyratron, PFN's, pulse transformer and related circuitry are all housed in one oil tank with two klystrons mounted on top, named a 2-Pack (Fig. 4.2). The RF of these two klystrons are combined as the first step in the NLC RF design which eventually combines eight klystrons to produce 600MW of
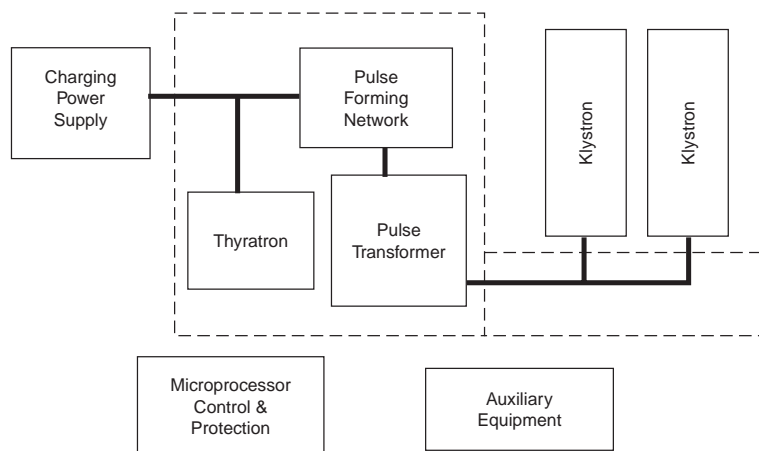
Figure 4.1: *Basic Line Type Modulator*

peak power. All connections into the oil tank are low voltage except for the charging power supply. The components in the oil tank are mounted on a sliding platform allowing easy access to all components once the oil is removed and the end plate lifted away[6], (Fig. 4.3).
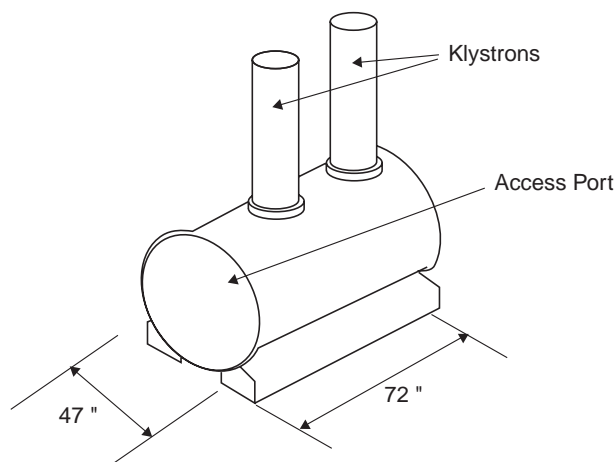
Figure 4.2: *2-Pack Concept*

4.2.2   Component R&D

The 2-Pack is more cost effective because it saves on power components, controls, etc. and achieves a smaller package. This configuration dictated the requirements for R&D into components and impedances. A Test Bed consisting of a large rectangular oil tank was set up at SLAC to configure and test various components and assemblies, using both resistive and klystron loads. A 5045 klystron was operated in the TL (temperature limited) region to obtain the correct perveance. This also limited voltage to between 400 and 450kV. The specific areas investigated were pulse capacitors,
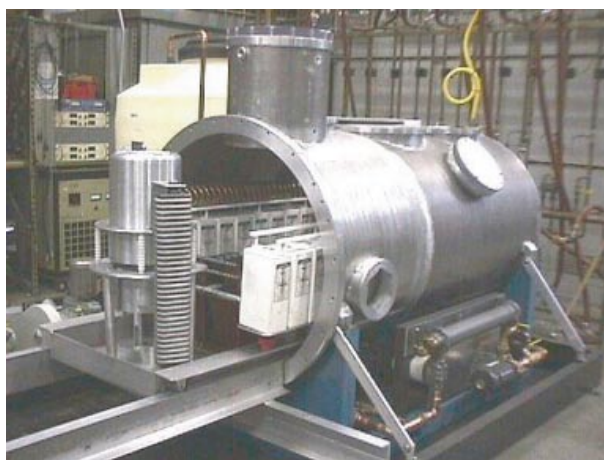
Figure 4.3: *2-Pack Prototype Under Construction*

the pulse transformer, and thyratron loss as a function of number of gaps. Akemoto of KEK analyzed both the pulse transformer which was eventually purchased[7], and the PFN pulse shape with mutual inductance[8].

Capacitors

The internal inductance of capacitors has always appeared to be a limiting factor in the rise time of the PFN. This problem is accentuated at very high discharge currents. One promising candidate appeared to be a glass enclosed dielectric called Sicond[9], which showed an internal inductance of 30nHy or less when tested under high discharge current. Samples of a 10nF, 40kV capacitor made in St. Petersburg were obtained from BINP and Dubna. The capacitor measured approximately 4 inches in diameter with a thickness of about 0.5 inch. Two of these capacitors were placed in series and configurations with both three and four parallel PFN's were built and tested. Initial results were good with the PFN waveforms showing fast rise times into a resistive load. However, when the energy transfer was calculated, the PFN's exhibited 8 to 10% loss. This loss was in the capacitor itself. This was later confirmed, by the scientists in St. Petersburg, to be a characteristic of the dielectric material at room temperature and the loss decreased with increased temperature above 100°C. These capacitors were eventually deemed impractical for the NLC or JLC.

The question of capacitor loss versus rise time and overall efficiency prompted further investigation of the energy transfer during a high current discharge for various types of capacitors. Tests were performed on mica, film and Sicond glass capacitors at 600 volts and 3kV. The standard foil wound capacitors were consistently in the 1% loss range and have a history of long life in high pulse discharge operation[10]. Taking into account the rise time limitations of the pulse transformer L and C and the magnetization of its core, the foil wrapped capacitors seemed to be the best compromise for the modulator.

Pulse Transformers

Two pulse transformer configurations were tested. The transformer design in use at the SLC at SLAC, called single basket due to its basket-like shape, showed the best overall result. However, this transformer is designed with higher stress margins and needs redesign to operate to 500kV. A second transformer from a different vendor with a double basket configuration was also tested. This transformer had a slower rise time and higher loss than the conventional design. On investigation the core material in this transformer was discovered to be 3-3.5 mil instead of 2 mil steel, which could explain the lower performance. It was concluded that the conventional technology can meet minimum requirements and that the double basket design may offer improved performance.

Anther pulse transformer design proposed by industry was a split primary, a design with a separate primary around each of a number of core segments that are pulsed at a lower voltage. (This is similar to the Induction design to be described later). A toroid design was suggested by Kazarezov of BINP and implemented at KEK by Akemoto and Takeda along with a magnetic switch[11]. KEK results for the pulse transformer show promise in reducing the leakage inductance and warrant further investigation.

Thyratrons

Initial tests were performed using a four-gap EEV thyratron (CX2593), later replaced with a CX1836A, a two-gap thyratron which exhibited reduced losses. The forward voltage drop during heavy discharge is approximately 100 volts per gap.

4.2.3   System Issues: Power Supply, Efficiency, Reliability, Production Costs

Power Supply

The Charging Power Supply is a significant cost driver in the line-type modulator system. The baseline model assumed one power supply per modulator (two klystrons). This affords maximum adjustability and independence and makes maintenance straightforward, but it is also expensive. SLAC is using the DOE SBIR program to fund small business in the development of a lower cost charging power supply, with a target of 25 cents per watt. Presently two contracts have been awarded for Phase I proposal work in this development.

Alternatively, a larger power supply may be less expensive per socket depending upon the configuration. Since four 2-Packs are combined for RF power, two or four modulators might share one power supply. New power supply designs using HV IGBT stacks of up to 160 devices have been built commercially. A large DC power supply with separate Buck Regulators (switching type) for each group of modulators looks very economical. SBIRs are in process to investigate this area of R&D.

ISG Progress Report, April, 2000

Efficiency

The overall efficiency of the modulator without the charging supply is the product of the efficiency of the output waveform (usable RF pulse to total pulse), and the efficiency of the discharge from the total PFN energy to the total output pulse energy. The output waveform is the weakest link in the chain because of the narrow RF pulse width. The rise and fall times from the pulse transformer dominate and limit the efficiency. Waveform efficiencies range from 80 to 83% and discharge efficiencies from 88 to 92%. For efficiency calculations the high voltage charging supply was chosen to be a solid state, switching type supply with tight regulation to charge the line directly to its desired voltage. This type of system is more efficient than a conventional resonant charging system with deQueing, which throws away power. Manufacturers of this type of power supply have estimated efficiencies of between 92 and 96%. The remaining inefficiencies are due to losses in capacitors, thyratron, transformer, and line mismatches. In summary, these investigations show that an efficiency gain over existing SLAC line-type modulators of $\sim$10% should be achievable, for an estimated 63% overall.

Reliability

The required reliability of the modulator is based upon the number of klystrons which can be out of service while the accelerator continues to deliver full collision energy. Factored into this is the Mean Time To Repair (MTTR) a failed unit, the number of extra units on line that can instantly be switched on to compensate for a failed unit, and the number of units in storage. A modulator and a pair of klystrons are replaced as an assembly. The estimated failure rates of the main components were used to calculate an overall Mean Time Between Failure (MTBF). These were the PFN, the pulse transformer, the thyratron, the charging supply and the rest of the components lumped together. The PFN, pulse transformer, and lumped miscellaneous components were assigned a 100,000- hour lifetime based upon SLAC experience. The thyratron was assigned a 15,000 hour lifetime, although a 50,000 hour lifetime is planned. The charging supply was estimated at 60,000 hours. From these numbers the MTBF for the modulator calculates to 8800 hours. The MTBF of the modulator/klystron system is based upon the modulator and its two klystrons. The klystrons were conservatively given a 20,000- hour lifetime. Taken together with the modulator, the modulator/Klystron system has a MTBF of 4700 hours.

A further discussion of reliability and system availability is given later in the chapter.

Production Cost Estimate

A detailed bottom-up cost estimate was made based on the 2-Pack preliminary design. This estimate was based upon small quantities (1 to 10 modulators). Some of the component prices were from actual vendor quotes while others were from engineering estimates. A large part of the cost is in the High Voltage Charging Power Supply (initial estimates are at $1 per watt). This is an area to target for cost savings. The estimate, broken down by sub-assembly, was for construction after a prototype and drawings were complete. The small quantity estimate for the modulator came to $200K each. The

estimate for additional engineering both at SLAC and at the vendor was estimated at 10% each for $240K total. Quantity production estimates were then based upon learning curves (85% on labor and 92% on material) for 2 linacs with 46 sectors of 72 klystrons with 36 modulators in each for a 1 TEV NLC.

4.3   KEK Modulator R&D

4.3.1   Blumlein PFN Modulator

Modulators with Blumlein-type PFN (Fig. 4.4) were initially the main focus of modulator R&D efforts at KEK[3, 12] for X-band linacs. The Blumlein method allows a lower turn ratio at the pulse transformer, yielding a reasonably fast rise time, and hence, an improved efficiency.
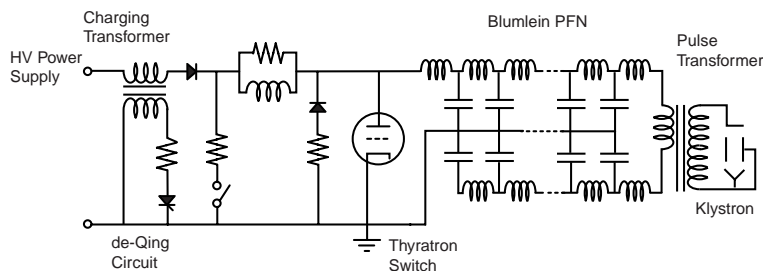
Figure 4.4: *Schematic circuit diagram of a Blumlein type modulator.*

The first prototype of the PFN modulator built at KEK had components placed in the air. It produced a peak output voltage of 470 kV with a flat-top width of 400 ns on a klystron load. The rise and fall times were 350 ns and 400 ns (both 10% - 90%), respectively, achieving the target value. The pulse flatness was good within 1 %. The observed output pulse shape was in an excellent agreement with a computer simulation. By increasing the numbef of PFN sections from the original 16 to 20, this modulator was later upgraded to produce 1.5 μs output pulses for testing the X-band klystrons to the ISG specifications.

The second prototype was built to be contained within an oil tank, 1.8 m in diameter and 1.6 m in height, for studies of engineering implementation of Blumlein-type modulators. With a ceramic resistor load, it produced 280 kV output pulses with a flat-top width of 400 ns. The rise and fall times were 210 ns and 280 ns, respectively.

The existing Blumlein-type modulators are a valuable asset for testing X-band klystron prototypes at KEK. However, since the requirement on the length of the output pulse was made substantially longer with the new ISG parameters, the focus of the modulator R&D has shifted towards employment of

solid-state devices as reliable switches in combination with more conventional PFN circuits.

4.3.2 Solid-State Switch Development

To improve the reliability, KEK has developed a solid-state switch to replace the thyratron tubes[13]. The Static Induction SI-thyristor is suitable for the switch device because of its high-power handling and fast turn-on capability. KEK has investigated the NGK RT103N 4kV reverse conducting SI-thyristor (including freewheeling diode with press-pack ceramic housing)[14]. To evaluate the performance of this device, the fast turn-on characteristics of five stacked SI-thyristors connected in series were studied using a very low-inductance circuit. By using a coaxial structure, the residual inductance was successfully reduced to less than 136 nH. When an anode voltage of 15 kV was applied, a maximum peak current of 10 kA, dI/dt of 110 kA/μs, and switching time of 128ns were obtained. The switching time is the time required for the anode voltage to decrease to 10% of its maximum value. It was confirmed that the turn-on characteristics of the SI-thyristors are comparable to thyratrons.

Next, a 45kV solid-state switch was designed and built using the same devices . The switch uses a stack of 15 circuit card assemblies in series. Each circuit card assembly consists of an SI-thyristor, a resistor capacitor network and a gate-driving circuit. The trigger and DC power for each card were isolated from high voltage through ferrite core transformers. A photograph of the stack assembly is given in Fig. 4.5. The stacked devices are housed in a single cylindrical tank with a diameter of 300mm and a height of 550mm. The tank is filled with oil to insulate and cool the internal devices.

The solid-state switch performance was investigated with a line-type 5045 klystron modulator at the KEK Accelerator Test Facility, ATF. The switch was successfully operated at 45kV and 6000A with a 6μs pulse-width at 25 Hz. Fig. 4.6 gives typical switch voltage and current waveforms at a PFN voltage of 45kV. The switch losses were measured by calorimetry and found to be 41 J/pulse at 45kV. This value corresponds to 5% of the total PFN stored energy, with about 90% of this loss dissipated in the devices themselves. Therefore, these switches still need to be improved to further reduce losses. However, it has been confirmed that the 45 kV Si thrystor-switch has a switching capability comparable to a thyratron.

4.3.3 Waveform Efficiency Studies

KEK has also developed a waveform compensation circuit to improve efficiency (usable RF to total pulse). This circuit is connected in series to either the primary or the secondary ground side of the pulse transformer. The waveform compensation circuit consists of a series combination of diodes, which have a switch and DC power supply respectively. By controlling both the timing and width of the trigger for each switch, this circuit generates an arbitrary waveform. Fig. 4.7 shows the effects of the compensating circuit in simulation. In this case the compensation circuit is connected to the primary side of a pulse transformer with a turns ratio of 1:14. The simulation shows significant improvement in the klystron waveform with an over-shoot, narrow flat-top and droop. It is also possible to compensate a ripple on the flat-top at the same time. The efficiency improves with higher

(a)   (b)
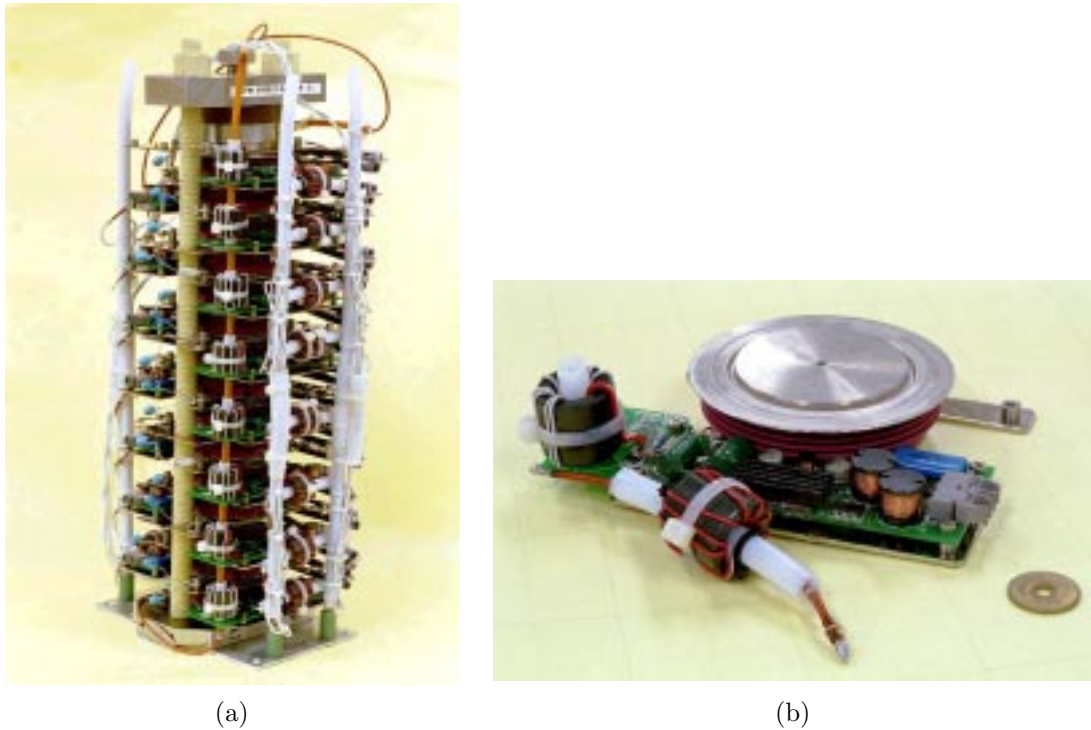
Figure 4.5: *45kV solid state switch (a) and gate-driving circuit (b).*
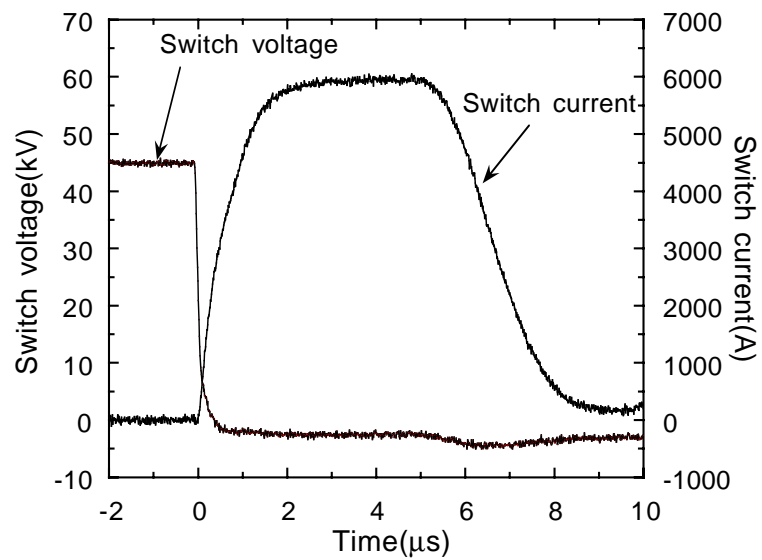
Figure 4.6: *Typical switching characteristics of 45kV solid state switch*

compensation voltage. For example, if the compensation voltage is more than 30% of the output voltage, the efficiency can reach more than 90%.
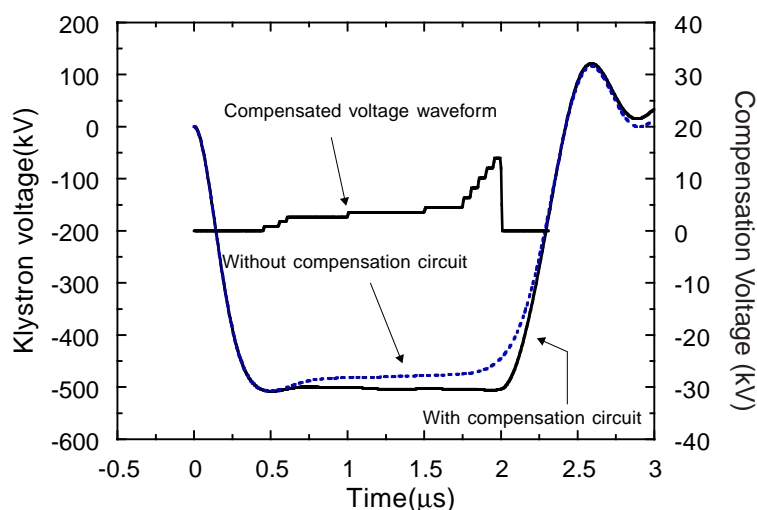
Figure 4.7: *Effects of the compensation circuit*

The waveform compensation can also be used to reduce the capacitor size in a direct switching hybrid modulator. In this type modulator, the required capacitance of the storage capacitors is in inverse proportion to the droop. If twice the allowed droop can be compensated, then the storage capacitor sizes can be reduced by half.

A preliminary low-power test was performed to study the waveform compensation circuit. The test circuit consists of a PFN with impedance of 15Ω, a 15Ω resistor as a dummy load, an IGBT switch and a waveform compensation circuit. The compensation circuit was connected in series between the ground of the IGBT switch and the dummy resistor. It was made up of 12 diode sections where each section consisted of a diode, FET switch and 10 μF capacitor. Each gate circuit for the FET was connected with a trigger generator through optical cables. A programmable trigger generator was used to modify the input and fine tune the output waveform.

Fig. 4.8 shows an example of the output current waveform compensated at a PFN voltage of 7kV and a compensation voltage of 1kV. The original output current waveform was rounded with no flat-top but the compensated waveform became rectangular with a wide flat-top, showing a significant improvement from the compensation circuit.

Fig. 4.9 shows a block diagram of a line-type modulator with a solid-state switch and a waveform compensation circuit.
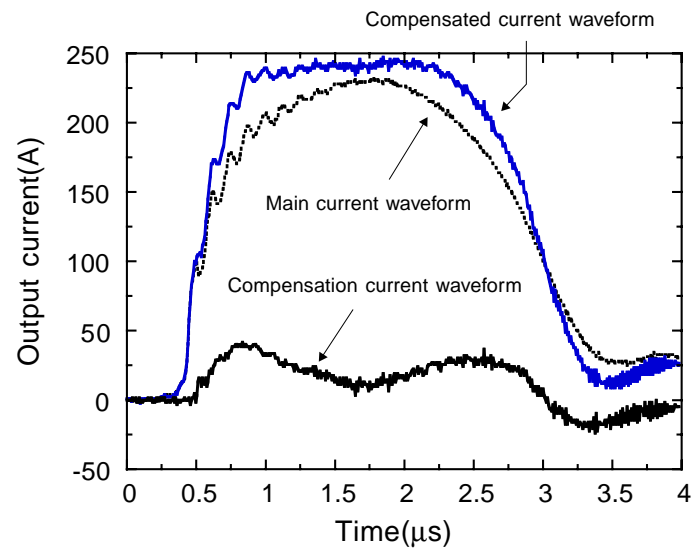
Figure 4.8: *Output current waveforms*
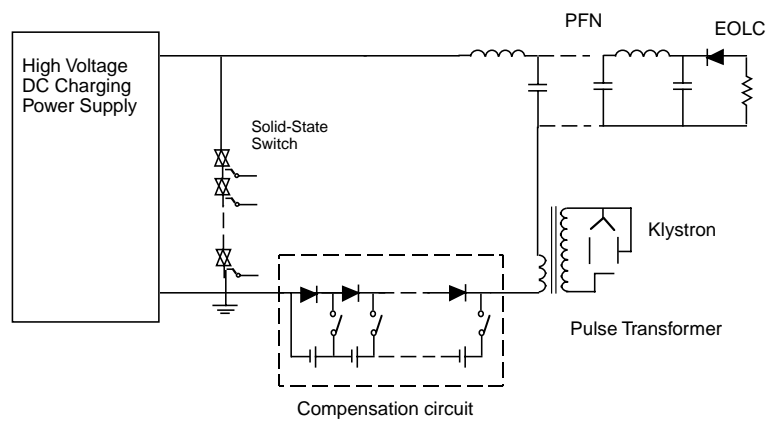
Figure 4.9: *Basic circuit with waveform compensation circuit*

4.4 Hybrid Modulator (IGBT and Pulse transformer) R&D

The hybrid modulator is a cross between a direct switch and a line-type modulator. The concept started with the desire for a solid state replacement for the thyratron and led to the possibility of using IGBTs as the switch. Since an IGBT is an ON/ Off device, it became apparent that for the same IGBT switch voltage as the thyratron, the needed output voltage could be obtained with half the turns-ratio in the pulse transformer and half the current in the IGBT. A Phase I SBIR (Small Business Innovation Research grant) is in progress to develop this technology. Present R&D is toward developing a higher voltage power supply and switch with a lower turns-ratio pulse transformer.

4.4.1 Circuit

The hybrid design (Fig. 4.10) assumes a DC Power Supply at 80kV maintaining the charge on an energy storage capacitor. A solid state switch, made up of a series-parallel arrangement of high voltage, high power IGBTs, turns on into the primary of a pulse transformer with a ratio of 1:7. At the end of the desired pulse width the IGBTs are turned off, interrupting the current flow to the pulse transformer and terminating the pulse. The IGBTs have shown a faster turn-off than turn-on characteristic. The physical configuration of the hybrid modulator follows that of the baseline modulator. The energy storage capacitor, the switch and the pulse transformer would be housed in a single oil tank, which will also mount the klystrons. The 80kV level for the power supply was chosen to be compatible with the baseline design. The droop across the pulse is a function of the droop in the pulse transformer and the droop in the energy storage capacitor. This droop can be minimized and/or compensated externally at a slight loss in efficiency. However, since the pulse width is adjustable, the pulse width can be optimized for the RF pulse to obtain maximum efficiency based upon waveshape.
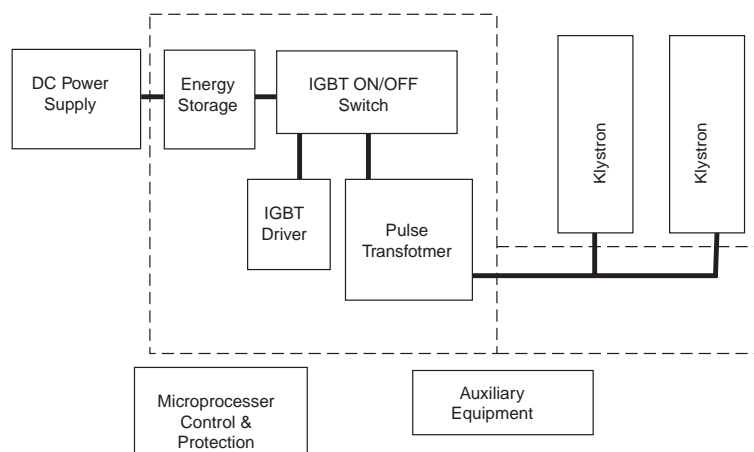
Figure 4.10: *Hybrid Circuit*

Transformer Options

The hybrid pulse transformer would be similar to that for the baseline modulator but with a smaller turns-ratio. Assuming the same secondary leakage inductance as the baseline design, the 1:7 pulse transformer would increase the primary leakage inductance by a factor of four. The inductance of the primary switch is still critical and must be minimized. The switch must be 80kV and 3500 amperes over the transformer excitation current. A commercial vendor has built IGBT switches at higher voltage and lower peak current that are being used in industry and laboratories today. That company is presently under contract for a Phase I SBIR for a switch and pulse transformer for a hybrid modulator that meets the requirements. Other transformer options that may be fruitful for hybrids are the split primary and the toroid designs mentioned earlier. Although a toroidal transformer is more complicated to wind, it may have reduced fields and better voltage standoff. Both approaches need further investigation.

4.4.2 System Issues: Power Supply, Efficiency, Reliability, Production Costs

Power Supply

The power supply issues here are similar to those for the baseline modulator. The supply provides the same average power but only replenishes a small voltage drop on a larger capacitor, rather than recharging from near zero to 80 kV. Therefore it should be somewhat less stressed, more efficient and create lesser problems with the AC power lines.

Efficiency

The overall system configuration chosen remains a single modulator for two klystrons rather than one modulator per klystron for the same reasons as the baseline modulator. The hybrid design is envisioned to become a direct replacement for the baseline design with no change in linac layout. The difference would be a solid state design which was hopefully more reliable and more efficient. The PFN capacitors would be replaced by DC energy storage capacitors at the same 80kV level. However, the capacitance would be at least ten times greater. This means that the capacitors would discharge less than 10% of their energy instead of the full discharge of the PFN. This is easier service for the capacitor and therefore the capacitor should have increased life. The IGBT switch would have an ON voltage drop of about 400 volts as compared to the thyratron ON voltage drop of 300 volts for a three-gap tube, but at half the current. Therefore the IGBT would have less power dissipation and would avoid the additional energy losses of the thyratron heater and reservoir, which averages more than 500 watts. The transformer losses will be approximately the same except the waveshape should show an improved fall time, thereby increasing waveshape efficiency above 80%. Overall there should be an increase in efficiency compared with the baseline modulator.

ISG Progress Report, April, 2000

Reliability

There should be an increase in reliability for the hybrid modulator over the baseline design. The IGBT switch should be significantly more reliable than the thyratron switch with no known wear-out mechanism. However, there is no real history of operating IGBTs in this fast, high current pulse mode. This is true for all of the solid state designs. This will soon be tested at SLAC with a prototype version of the induction modulator into a pulse transformer which operates a 5045 klystron. The main components considered to estimate the modulator Mean Time Between Failure (MTBF) were the IGBT switch, the pulse transformer, the energy storage capacitor, the charging supply and the rest of the components lumped together. The IGBT switch was assigned an MTBF of 100,000 hours. The pulse transformer, storage capacitor and the lumped miscellaneous components were assigned a 100,000-hour lifetime based upon SLC experience. The charging supply was estimated at 60,000 hours. From these numbers, the MTBF for the modulator is 17600 hours. The MTBF of the modulator/ Klystron system is based upon the modulator and its two klystrons. The klystrons were conservatively given a 20,000-hour lifetime. Together the hybrid modulator/ Klystron system would have a MTBF of 6400 hours.

Production Cost

The production cost of a hybrid modulator is being estimated. The number of klystrons operated per modulator will have a large effect on dollars per socket. Preliminary estimates are that this approach will be cheaper than a conventional modulator.

4.5 Solid-State Induction Modulators

4.5.1 Early Conceptual Work

In 1998 the NLC modulator working group at SLAC was searching for a breakthrough in modulator design that would significantly reduce costs while improving performance and reliability. Progress was lagging until R. Cassel suggested combining new IGBT switch technology with very low loss magnetics in an Induction design. In this design, Fig. 4.11, separate low voltage driven cells are stacked to provide magnetic coupling to a secondary that produces a voltage equivalent to N times the cell voltage in a single turn.

Calculations showed that waveform efficiency should be improved due to faster switching times, lower inductance, lower core losses and higher DC power supply efficiencies. Reliability should be improved by the solid state switch technology. The remaining question was whether costs could also be lower. Both the IGBT power devices and the amorphous magnetic materials are very expensive. The answer
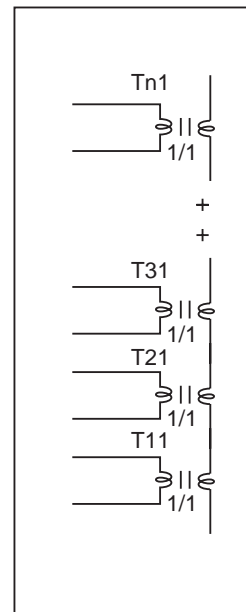
Figure 4.11: *Induction Modulator Concept*

that emerged was that costs could be significantly lowered if a modulator could be designed to drive several klystrons at once, more than the two units in the baseline design. The logical maximum number that could be driven was the number to be combined at the RF level, which was eight. Therefore the design that emerged is called an 8-Pack.

Cassel's first prototype was demonstrated in late 1998 (Fig. 4.12). This consisted of six toroidal cores each with an IGBT driver and a rather complicated four-turn secondary. This tiny unit used 1.7 kV IGBTs operating at 1 kV to develop the expected 24 kV across the secondary. From this success a full development program was set up for 1999. There were many technical issues to resolve before this system could be assumed to work, although it was clear by this time that the main issues were not feasibility but engineering design, long term reliability and cost.

4.5.2   The SLAC-LLNL-Bechtel Collaboration

At this time NLC management began developing a collaboration with LLNL on a number of technical fronts. The Induction modulator was a natural fit because LLNL had a vast experience in designing and operating Induction linacs as well as some very specialized short pulse high repetition rate modulators using all solid state FET switching. In addition, the LLNL group had contracts with Bechtel to provide mechanical engineering, detailed design and sophisticated machining capabilities. In early 1999, a collaboration was formed to design and build the first full prototype that could drive eight klystrons in parallel, a feat that requires the modulator to deliver a Gigawatt of peak power for 3 microseconds at 120 times a second. The reliability goal is to operate the NLC with 85% availability for nine months per year for twenty years.

ISG Progress Report, April, 2000
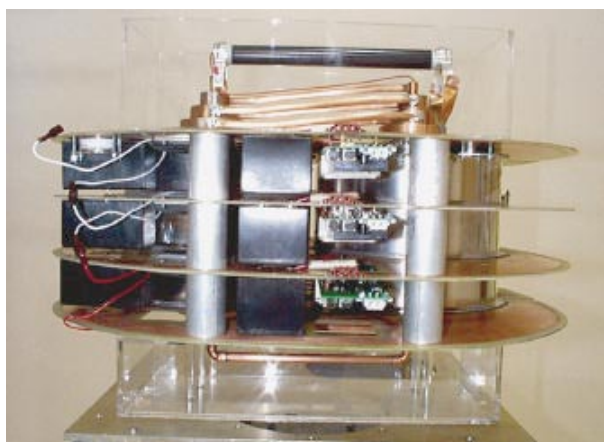
Figure 4.12: *First Induction Prototype 1988*

4.5.3 Circuit Design

The basic circuit is shown in Fig. 4.13[15]. The features will be mentioned only briefly. The IGBT drives the core from a charged capacitor that is sized according to the total charge to be drawn with a specified voltage droop. The output specification of the modulator is a nominal 2% flat top. Fig. 4.14(a) shows the current, voltage and magnetizing current waveforms. Fig. 4.14(b) shows a simulation of the modulator output pulse with and without compensation of the leading edge overshoot. The large overshoot could cause breakdown in the klystron, as well as wasting the early part of the pulse. The simulation shows how this effect can be eliminated by a delay in triggering an appropriate fraction of the IGBT drivers. Since overshoots and ripple are difficult to model and will not be known until the unit is built, compensation by timing control is a powerful tool to tune the modulator to the actual load. The IGBT typically operates at 2.2 kV and switches up to 3000 A peak. Suitable devices are now available from two vendors. The magnetic core size is chosen to support the volt-seconds necessary to deliver the load current without saturating the core. In the current design the cores are 1.5 in. high by 7.25 in. ID by 14.75 in OD.

4.5.4 System Design

The cell design can be extremely flexible so that it can match many different requirements. The primary current is matched to the loads through the induction transformer cells and then through the secondary turns. For example, in the 8-Pack under design, the optimum configuration that matches the available primary current that can be delivered by the IGBT to the load is to use two IGBT drivers delivering 3000 A peak each, operating at 2.2 kV, and a 1:3 step-up secondary to give 2000A output. This is sufficient to drive 8 klystrons at 500 A each. The 500 kV output voltage requires 76 cells. Adding a few spare cells makes it possible to continue operation without interruption if cells fail, and moreover, feedback to the main power regulator can maintain a constant output voltage when cells fail by increasing the voltage slightly on the stack. Most likely it will not be necessary to also
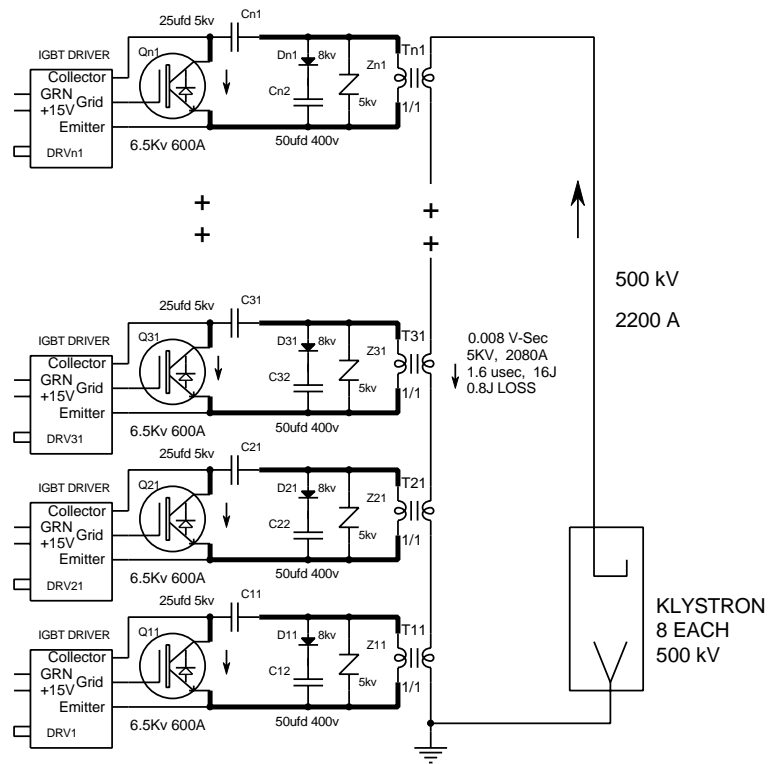
Figure 4.13: *Induction Circuit Diagram*
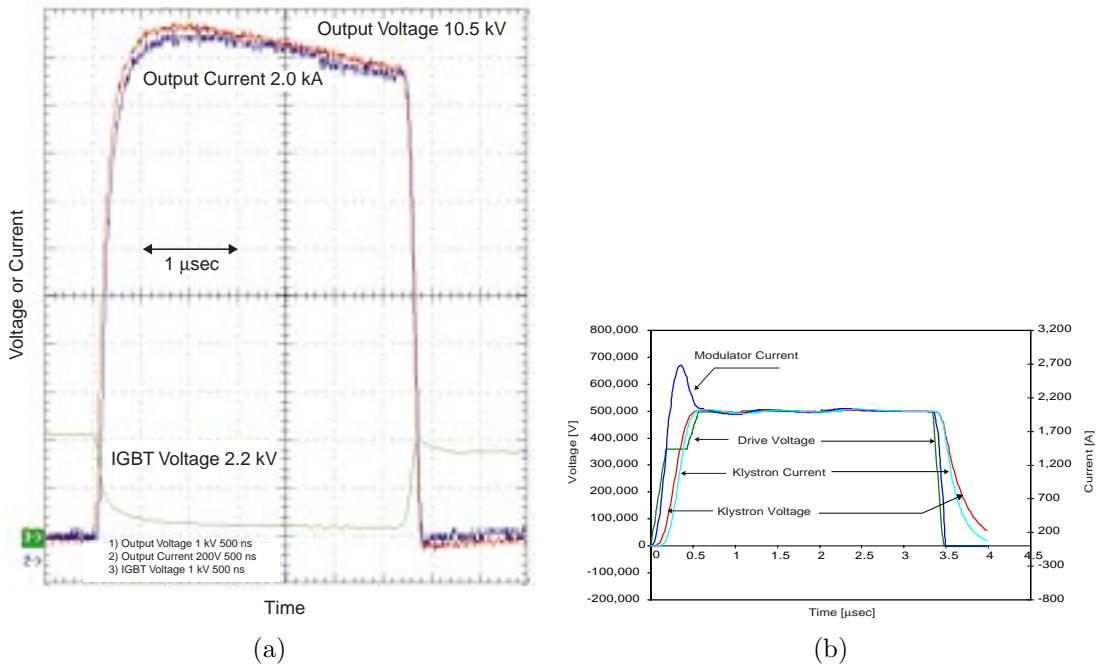
Figure 4.14: *Induction Cell Waveforms (a) and simulated 500 kV Compensated Output (b)*

have spare cells in the stack if voltage feedback is used.

The IGBT driver board and magnetic cell are shown in Figs. 4.15 and 4.16. The collaboration has worked very closely to develop the electro-mechanical design. The driver is designed as a plug-in module that can be easily accessed and replaced in the field. It houses a single IGBT, storage capacitors, a Gate Driver board and a Core Reset board. The magnetic core water-cooled housing cools the core and conducts heat away from the IGBT. Significant effort has gone into the design of the machined cell, the board plug-in contacts, the board supports, the water cooling band and the core potting and sealing of the central column for oil to cool and insulate the high voltage transformer secondary section.

Figure 4.15: *Driver Board*
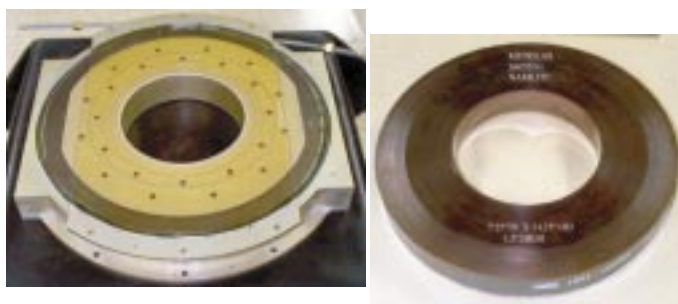
- 6.5" ID double ended drive core
- 0.006 Volt-Sec core
- 4 kV 1.7µs 0.5 Joules Loss

Figure 4.16: *Potted Magnetic Core*

The full stack concept including the klystron loads is shown in Fig. 4.17. An oil reservoir at the bottom contains the HV distribution to the loads. A small oil reservoir at the top of the Induction stack keeps the HV columns filled. The klystron loads will be installed in pre-assembled, matched and tested pairs. The main Induction stack will weigh about 6,000 lbs. Each klystron pair with its lead shielding will weigh about 6,000 lbs. In the final configuration the weights will be borne by a concrete floor with the HV section recessed into a pit.
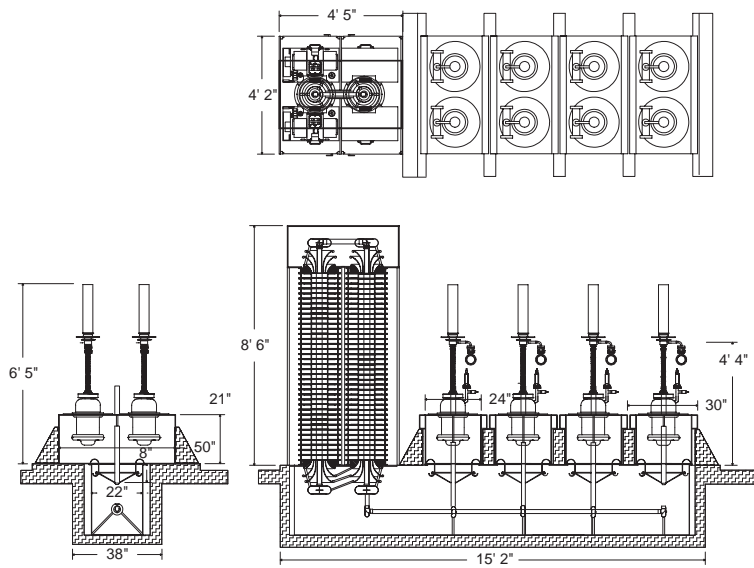
Figure 4.17: *8-Pack Modulator Conceptual Design*

4.5.5   System Issues: Power Supply, Efficiency, Reliability, Production Costs

Power Supply

Each 8-Pack will be powered by a low voltage Buck regulator that draws from a primary 34.5 kV feeder system (Fig. 4.18). Each 8 Pack will have a separate disconnect capability so it can be taken off line without interrupting nearby 8-Packs in a Sector of nine 8-Packs. This type of regulator is typically more than 95% efficient.
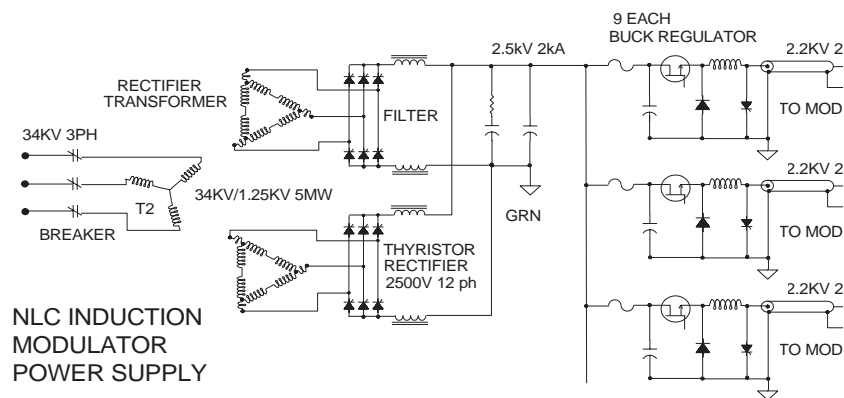
Figure 4.18: *8-Pack Power Supply*

Efficiency

Detailed efficiency calculations for a stack have been measured and extrapolated to the full design. Switch, reset and core losses are all very low. A detailed summary of losses per pulse is shown in 4.2. The efficiency estimated from these measurements is 81.2%, compared with ∼60% for the line-type and a yet to be determined number for the hybrid type. This improvement represents a 20% reduction in the site power bill, an enormous saving.

NLC 8 Klystron Induction Modulator Losses (3μs)

Efficiency		joules	120Hz watts	74 watts/cell	
Total power 500kV × 2120 A × 1.5 μs		3,180	381,600		
Efficiency	81.2%	570.3	88,434		
Pulse wave form (200 ns)	88.5%	365.7	43,884		
Core loss pulse	98.6%	44.4	5,328	72	0.60
Core loss reset	99.7%	8.9	1,066	14	0.12
Solid State (IGBT + diodes)	98.0%	62.9	7,548	102	0.85
Stray impedance	98.2%	58.4	7,008	95	
Capacitor & Snubbers	99.0%	30.0	3,600	49	
Power Supply 2.5 kV 500 kW	96.0%		20,000	0	
		joules	watts	watts/cell	
Total power used		3,750.3	470,034	332	

Table 4.2: *8-Pack Efficiency Calculation*

Reliability

Details of reliability for the Induction design are difficult to quantify because the switch technology is new. Two main issues have been identified so far:

Once the IGBTs were in use, vendors began issuing warnings that the operating voltages should be de-rated to avoid catastrophic failure due to penetration of cosmic rays. Recent research into the phenomenon has pretty well identified the problem as a single event failure when a cosmic produced neutron traverses the high field area of the semiconductor and creates a discharge path. The failure rate apparently increases very steeply with voltage and it has been determined by testing that one can safely operate at about 2/3 voltage without reduced reliability. More modeling and actual testing should be done on the devices that are proposed for use before designs are finalized. Also, plans are underway to run a section of the prototype on a real klystron load to gain confidence in the operational

reliability in an actual accelerator environment.

The second issue is whether the klystron loads in an 8-Pack configuration can be protected from the energy stored in such an array if one of the loads arcs, as happens frequently in practice. The design relies for protection on a combination of sufficient isolation between loads plus the very fast turn-off capability of IGBTs. Some significant arc tests are discussed in a later section, and a plan has been devised to test the protection mechanisms in a safe manner before risking operation with real loads.

Production Costs

Detailed bottom-up estimates have been made for various configurations of modulators following a similar path as reported for the baseline design. The recent design change to a 3 microsecond output pulse effectively doubled the load on every klystron and modulator. To accommodate this extra load the cell operating voltage was lowered to gain the needed volt-seconds from the cores already on hand, capacitance had to be added to the driver boards, and the number of cells had to be increased somewhat. These simple changes were all that was required to adapt the prototype from a 1.5 to a 3.0 microsecond design, once again demonstrating the flexibility of the modular design. This change would mean a major reconfiguration for a line-type modulator and likely a whole new design. The Induction design using the 1:3 step-up was already predicted to reduce the costs by a factor between 2 and 3.

4.6   Present Status of Induction Modulators

4.6.1   Stress Cone HV Test

In 1999 a model of the critical 500 kV transformer section of the proposed solid state modulator was fabricated at LLNL and Bechtel and delivered to SLAC for test. The stress cone at the end of the tubular transformer secondary (Fig. 4.19) was designed to test the full 500 kV stress at an applied voltage of 250 kV. It was mounted atop an existing modulator (Fig. 4.20), filled with oil and pulsed successfully at above 300 kV. This basically confirms the feasibility of the 3-turn secondary design proposed in Fig. 4.21.

4.6.2   10-Stack Prototype Development

In 1999, top priority was been given to advancing the full prototype, now known as the 8-Pack, with the following specifications:

The prototype cell, IGBT driver board, gate driver board, core reset board and all critical interfaces were designed and tested. A set of five complete cells and driver boards was fabricated at LLNL and Bechtel and delivered to SLAC. There it was assembled into a 5-Stack and tested to the design
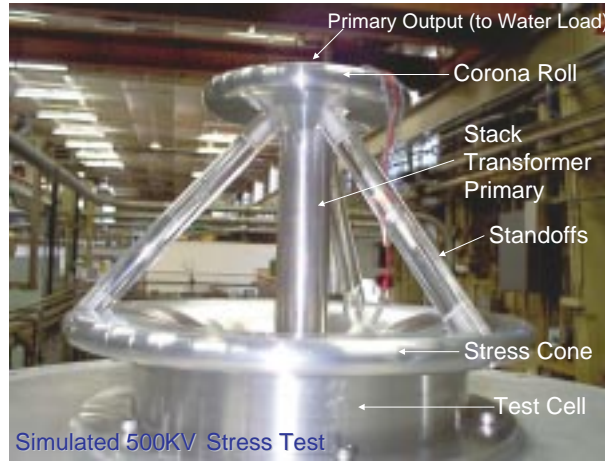
Figure 4.19: *Stress Cone Prototype*

Figure 4.20: *Stress test assembly*
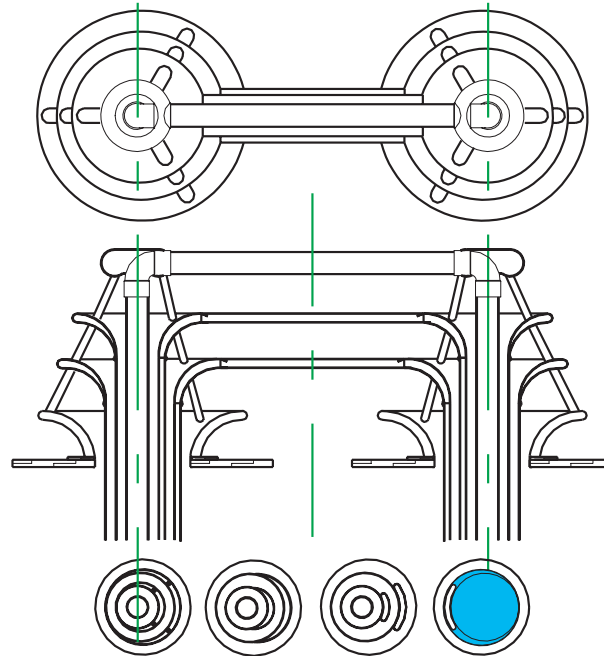
#1   1.44" ID X 1.50" OD
#2   2.83" ID X 3.33" OD 0.19" OFFSET
#3   4.67" ID X 5.17" OD 0.19" OFFSET
CORE 6.5" ID

Figure 4.21: *3-Turn Transformer Concept*

Item	Requirement
Output:	500 kV, 2120 A, 3.0 μs, 1:3 step-up
Rise & Fall	200 nsec loaded
Droop/flatness	1% nominal
Repetition rate	120 Hz
Load	Eight 75 MW klystrons in parallel
Power Supply	550 kW continuous for full load at 120 Hz
Efficiency	82%
Reliability	>10,000 hrs MTBF

Table 4.3: *Main linac modulator requirements*

peak power output into a dummy load at low repetition frequency, rate-limited by the available power supply. A number of problems were identified and solutions have been implemented. This 5-Stack, operating at 2.2 kV per cell, produces 11 kV into a single turn secondary driving the dummy load.

Late in 1999, a new model of the NLC RF system was developed seeking to take advantage of a klystron that could deliver a 3 μs pulse, or twice the original design power. A new concept for the RF delay line distribution system was devised to deliver the power to a double length section of the machine, so the proposed specification for the modulator changed to 3 μs output at 120 Hz and 550 kW average power. Fortunately this change to the modulator proved relatively trivial: Because of superior low loss performance and cooling design, full performance at double the output power as the drive pulse was dialed from 1.5 to 3 μs could be achieved by simply doubling the capacitance ahead of the IGBT. The prototype impressively passed this wide pulse test.

The 5-Stack was recently extended to a 10-Stack (Fig. 4.22). This unit is in the process of being extended with ten additional driver boards and a 150 kW power supply to support full power, full repetition rate tests. The power capabilities per cell will be equivalent to the full 8-Pack operating at 3.0 microseconds and 120 Hz.
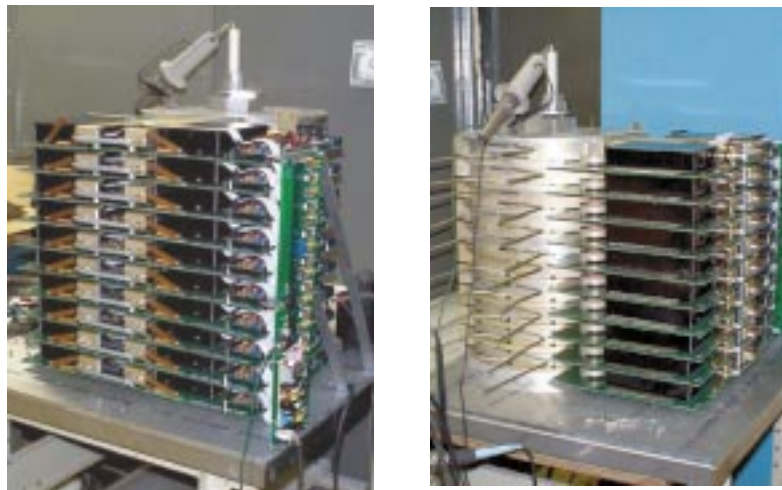
Figure 4.22: *10-Stack 22 kV @ 6000A Peak Prototype (1/2 Driver Boards Shown)*

4.6.3   Klystron Arc Tests

A serious concern of the 8-Pack design is the ability to adequately protect the klystron loads in case of an internal arc. line-type conventional modulators have an internal impedance approximately equal to the impedance of the klystron and therefore have a limited energy discharge and limit the peak discharge current to twice the operating current. Paralleling two klystrons on one modulator lowers the modulator internal impedance such that the peak current can increase by a factor of four during a klystron arc. Other modulators with a low impedance drive have to be turned off quickly to limit the energy discharge. The idea of running eight klystrons on a single modulator prompted the need to understand potential klystron arc damage.

This task was undertaken at SLAC with 5045 and XL4 klystrons singly, and with one of each tube in the dual klystron XL4 setup at NLCTA. The klystrons in the parallel tube operation are isolated from each other by lead inductance and leakage inductance between the two baskets of the pulse transformer.

Figs. 4.23 and 4.24 show current and voltage relationships for representative arcs for an XL4 klystron in a one tube configuration in the Test Lab and in the two-tube operation at NLCTA. It is apparent that the rate of rise of the arc current and the fall of the cathode voltage are on the order of hundreds of nanoseconds. This is in line with the time it would take a plasma to traverse an approximate 2cm gap in a vacuum of at least 10^{-8} torr. Note that the energy measured in the arcs exceeds by about a factor of five the levels that were thought to be catastrophic. The two-tube configuration does not appear to dump significantly more energy into the arc than a single tube discharge. Table 4.4 shows a summary of all data collected.
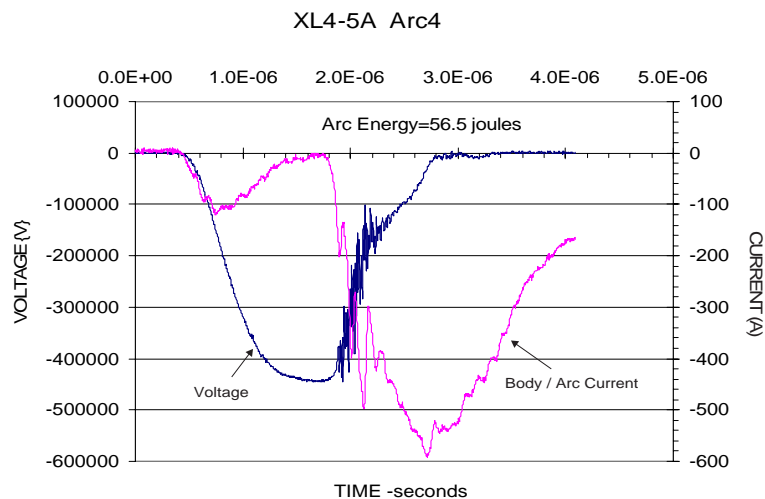
Figure 4.23: *Single Klystron Arc fault*

Further experiments and analysis are indicated. Historical data from the SLC also needs to be analyzed. The measured results are clearly influenced by the external circuit, and the 8-Pack circuit is considerably different from the test setup. Nevertheless, if some isolation between loads is included
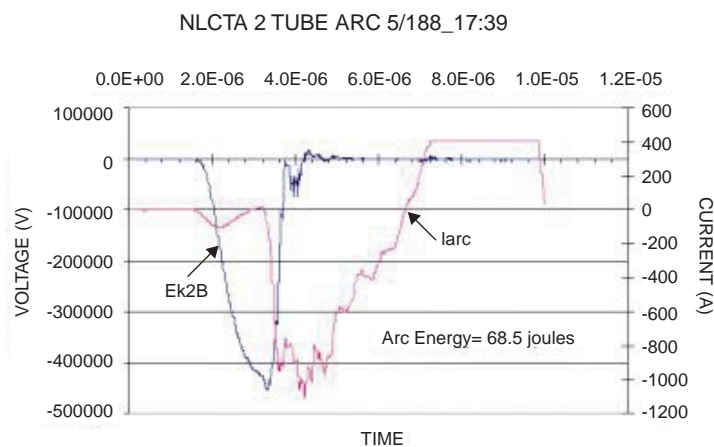
Figure 4.24: *Double Tube Arc Fault*

in the design, it appears quite feasible to provide adequate load protection in the 8-Pak configuration.

4.6.4   Reliability & Machine Availability

The RF power sources are a major system of the NLC and require a high uptime in order to reach the overall goal of 85% machine availability[16]. Since the NLC is made up several major systems in addition to klystron-modulator assemblies the availability goal for each system must be higher than 85%. Currently the goal for each major system is at least 95%. The original analysis of the modulator-klystron system was based on the conventional or PFN-type modulator. The following discussion compares the conventional and solid state induction systems.

The conventional system model (2-Pack) has five components which are the major contributors to reliability: two 75-MW klystrons, a thyratron, a pulse-forming network (PFN), and an end of line clipper (EOLC). A groups of four of these 2-Packs makes up the basic building block of the RF system, the 8-Pack. Each sector contains nine 8-Packs for a total of 1656 modulators for the 500 GeV machine. A reliability block diagram (RBD) for the conventional 2-Pack was developed and the MTBF was computed to be 1500 hours.

The solid state induction klystron-modulator consists of eight 75-MW klystrons, one modulator using solid state IGBT switches and one power supply. The reliability model assumed a 15 times better reliability for the solid state modulator, based on solid state technology and an inherently redundant design. There was some concern that the combination of one modulator with 8 klystrons would cause the availability to be unacceptable. Clearly a single failure takes eight rather than two klystrons off line. It is believed that the increased reliability of the solid state modulator will make up for this. The reliability calculation with the stated assumptions resulted in a MTBF of 2400 hours for the solid

Klystron	Voltage Fall (ns)	Peak Voltage (kV)	Current Rise (ns)	Peak Current (A)	Energy (joules)	Notes:
XL4-5A(4)	1000	445.7	1000	600	56.5	
XL4-5A(0)	1300	445.7	200	200	21.8	End of pulse
XL4-5A(1)	1300	449.8	800	600	66.5	
XL4-5A(2)	1700	451.9	300	400	51.2	Late in pulse
XL4-5A(3)	1000	445.7	800	600	48.2	
XL4-5A(5)	1500	443.7	500	400	47.2	Late in pulse
XL4-5A(6)	1400	454.0	300	80	9.65	End of pulse
XL4-5A(7)	1600	454.0	600	300	59.5	
5045(7)	3000	300.9	400	550	46.4	
5045(3)	1200	346.0	300	500	39.0	
5045(10)	1200	368.0	200	525	35.9	
NLCTA 2 tubes	1100	430.0	300	900	61.0	
NLCTA 2 tubes	1000	443.0	400	900	68.5	

Table 4.4: *Klystron Arc Data Summary*

state system.

For overall performance, the critical parameter is availability which is defined as MTBF divided by the sum of the MTBF and MDT (mean down time). Reliability is built into a device or system, and can only be improved by changing the design. Availability is impacted by both reliability and by how long it takes to fix a problem. It is easily seen that if we do not repair the klystron-modulator assemblies as they fail the system will not survive 9 months of continuous operation. MDT is the expected time for a response from the logistic support system to restore operation. MDT also figures directly into the number of ready spares required to maintain operation. The MDT term was computed to be 21.7 hours for the solid state modulator system.

There is one more factor needed as input to an availability model for the Induction 8-Pack. The design of the main linacs currently includes a 3% overhead. These extra units are automatically switched online if a modulator goes offline temporarily or permanently. This means that only 402 of the 414 systems need to be working for the main linacs to be operational. The simulation was run for the 46 sectors in the current design of the NLC main linacs using the component lifetimes and MDT as stated.

One the outputs of the simulation is a condition monitor of the main linac (Fig. 4.25) which shows the instantaneous availability of the linac during operation.

The result of several simulation runs led to a projected availability for klystron-modulator assemblies in the main linacs of 99.6%, a number which comfortably meets the overall goals. It should be noted that the design is still immature and availability may go down as more is known. However the solid state design is inherently robust as well as internally redundant so the assumed reliability should be
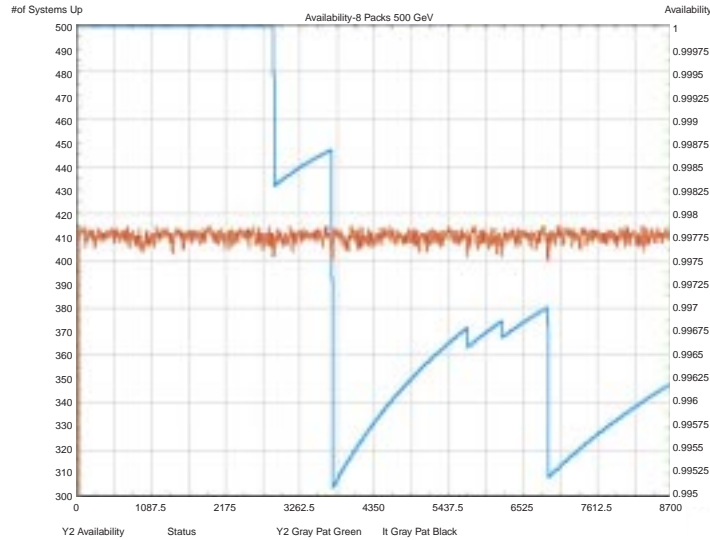
Figure 4.25: *Machine Availability vs. Time*

a conservative estimate. The sensitivity of availability to the percentage of online overhead units was analyzed using the same model (Fig. 4.26).

4.6.5   Modulator Workshops with Industry

Industry has also contributed significantly to development efforts through a series of Modulator Workshops. Since the NLC is in an R&D phase, the workshops have been designed to introduce colleagues in other laboratories and universities as well as industrial designers and manufacturers to the NLC requirements and to seek their cooperation. These sessions have been helpful in focusing the R&D work into fruitful directions, including discussions of a very wide range of options. One output of these meetings is that small businesses are able to approach the DoE SBIR (Small Business Innovation Research) program with funding initiatives. The program continues to fund R&D in solid state and thyratron switches, capacitors, pulse transformers, charging supplies and full prototype modulators.

Another major goal of the workshops is to involve industry at an early phase in preparations to build prototypes of critical components or integrated systems. Industry can also help validate engineering cost estimates that will eventually go into the NLC Conceptual Design Report.

The Second and Third Modulator Workshops were held at SLAC in July 1998 and May 1999 respectively[17, 18]. The Fourth Workshop is planned for June 26-29, 2000 in Norfolk, Virginia in conjunction with the Twenty-Fourth International Power Modulator Symposium.
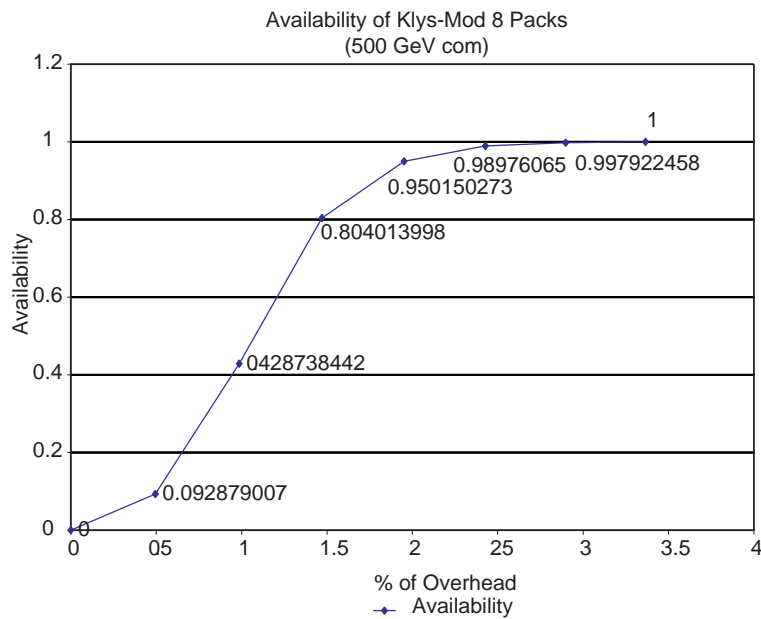
Figure 4.26: *Machine availability vs. % Online Overhead Units*

4.7   Future Program

4.7.1   Conventional and Hybrid Modulators

SLAC

In 1999 a 2-Pack conventional modulator tank was built and delivered to SLAC for the baseline prototype. The project was limited by available manpower and funding for parts, and this effort is currently proceeding on an as-available resource basis. A larger test stand for 3 microsecond 500 kV operation is the top priority for the group. There are presently no plans to set up the 2-Pack as a test stand or to develop the extensive instrumentation required.

There is continued strong interest in tracking hybrid design developments that are being aggressively pursued by industry, largely through SBIR programs. In 2000 and 2001 it is likely that more than one prototype modulator as well as very useful components will emerge from this program.

The SLAC group will also extend the arc testing work started in 1999 that has already produced very useful results.

KEK

At the present time, the performance of a 45kV SI-thyristor semiconductor switch has been evaluated by KEK. To investigate long-term reliability of this switch, it will be installed and operated in a

modulator to collect lifetime data. Other high power semiconductors such as IGBTs will also be investigated to determine the most suitable switch. The same studies will be carried out for the IGBT and IEGT (Injection Enhanced Gate Transistor) devices. Other aspects of the semiconductor switch R&D effort include mechanical packing studies to lower cost and gate driving circuit development for faster rise time. This will be a joint effort with industry.

The pulse transformer is a key component which affects power efficiency. To improve on the conventional pulse transformer, it is possible to produce a fast rise time design by reducing the number of secondary turns. However, this produces a larger pulse droop and requires a large core size. These problems can be ameliorated by using a core material with excellent magnetic properties. In order to improve the pulse droop and core losses, an evaluation of Hitachi FT-1 Finmet and other nanocrystalline alloys will be carried out in collaboration with SLAC.

To reduce the cost and size of storage and PFN capacitors, joint R&D with SLAC will continue. KEK will also support IGBT (on-off switch) R&D jointly with SLAC, and will continue developing compensation techniques for improving the modulator waveform efficiency.

4.7.2   Solid State Induction Type

The solid state induction modulator future program includes the following major goals:

1. FY 2000: Adapt the 10-Stack to a 5045 klystron in the SLAC linac as a full power test bed for the cell design. This requires early completion of a 150 kW power supply.

2. FY 2000: Complete the full ∼75 cell prototype under construction at LLNL-Bechtel and prepare it to begin full testing on (a) water loads and (b) 5045 klystron loads at SLAC. The proposed setup is shown in Fig. 4.27. The water load will occupy the first socket for initial testing.

3. FY 2001: complete a Buck regulator power supply capable of supplying at least 275 kW and preferably upgradeable to 550 kW continuous power for full power testing at 3 microsecond operation.

4. FY 2001: Complete water load testing and advance to 5045 testing. The 5045 will enable a good test of high power operation as well as the arc protection system.

5. FY 2001: Design and build a second full modulator after a DFM (design for manufacture) design cycle. The goal is to streamline the design for more efficient and lower cost manufacturing. An example is to make all currently machined cell parts into cast or extruded parts that can be prepared for assembly with minimal machining.

6. FY 2002: Install the finished unit and power supply at NLCTA to become part of the high power component test program for the main linac RF systems. The finished installation is depicted in Fig. 4.28.

Comments:
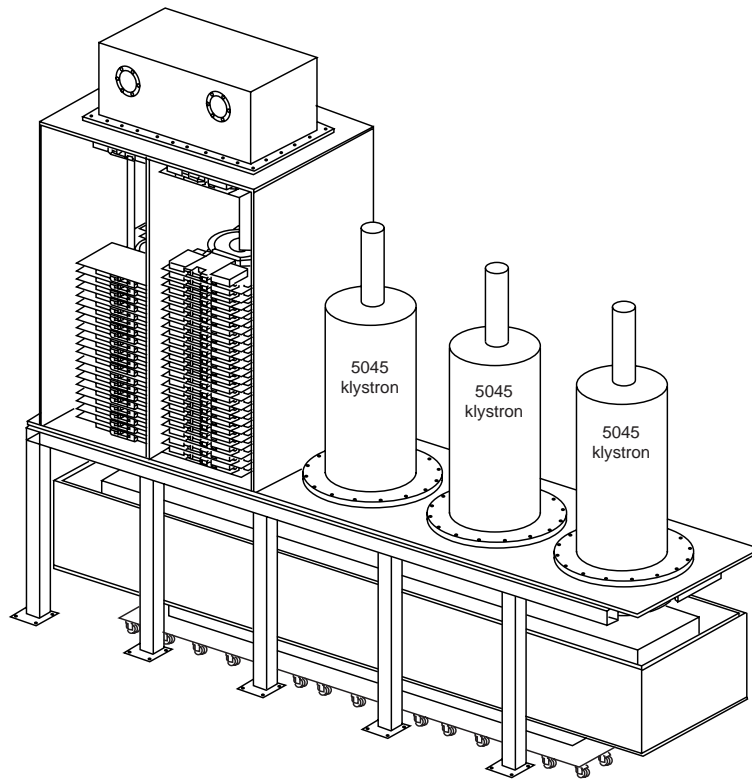
Figure 4.27: *First Full Prototype Test Unit with Dummy Loads*
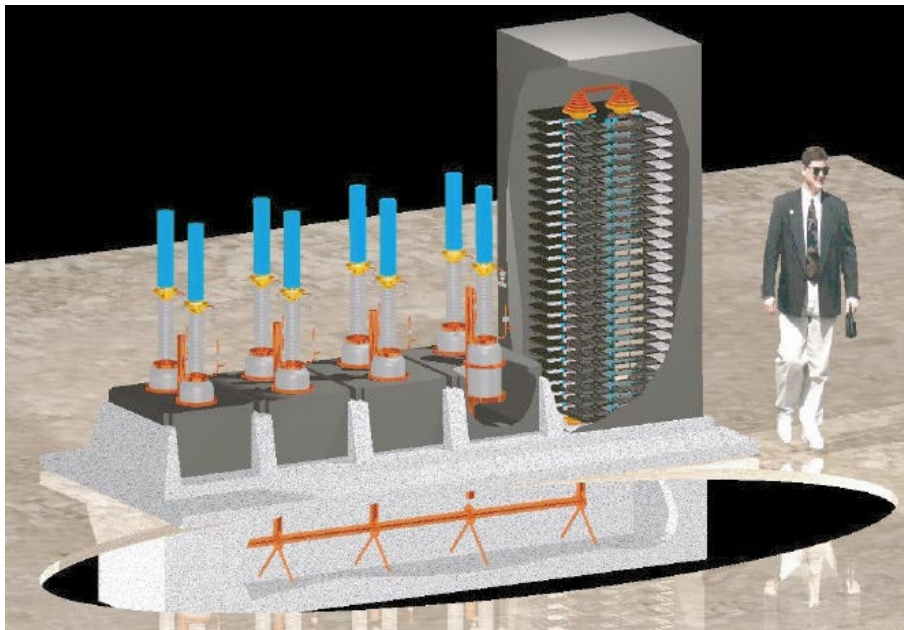
Figure 4.28: *Finished Installation Concept*

1. The 10-Stack prototype delivers a primary drive current of 6000 A peak at 22 kV. This is the same power as an existing SLAC line modulator (in about 1/10th the volume) so the plan is for a prolonged test on a 5045 klystron in the SLAC linac. The output coupling will be a single turn (coaxial cable) connected from the center hole of the toroidal stack to the 5045 tank containing a 1:14 step-up transformer. The test will provide valuable data on the robustness of the design, efficiency, cooling and serviceability over months of operation.

2. The remaining program will provide a facility to receive the first 75MW klystrons and begin testing first, the high power individual RF components and second, the full power RF delivery and acceleration systems. The first induction prototype will continue as a test bed for modulator development.

3. Industrial providers will be heavily involved in the DFM phase. Key goals are: Machined cells replaced with lower cost castings; core assembly, potting and testing automated with new tooling; board assembly and testing streamlined; burn-in tests performed on all components; and vendors developed both for critical components such as IGBTs, magnetics and capacitors, as well as fabrication of assemblies.

4.7.3   Architecture for Injection Linacs

No firm decisions have been made on the modulators for the injection system linacs except to determine feasibility by some simple extrapolations of the induction design. There are several candidates including hybrid types being developed by industry. The injection linacs have far fewer stations (Table 4.6.2) and are not physically clustered like the main linacs, so a 2-Pack model has been assumed. A concept of such a unit is shown in Fig. 4.29.

The output of a single cell is limited to a certain number of volt-seconds irrespective of current. In the current model, operating at a 20% lower cell voltage can provide the 4 μs pulse required for C-Band operation. Alternately, adding 20% more cells will lower the cell voltage further to enable the unit to develop the 5 μs pulse needed for S-Band operation. Since in these applications waveform efficiency is less critical, the hybrid design works well and the output transformer can be chosen for best power transfer efficiency. The induction cell is a flexible building block that can be tailored to different output voltage and current requirements. An optimum solution would be to use a standard cell and driver design to solve all of the various modulator requirements. This would provide enormous economic advantages in future operations and maintenance.

4.8   Conclusions

The ISG Collaboration has been effective in promoting the development of new technologies applied to klystron modulators. The working groups have stimulated discussion of a wide range of problems and potential solutions as represented by the details of this report. It seems quite clear that solid state technologies will dominate future designs in spite of the known issues of susceptibility to radiation
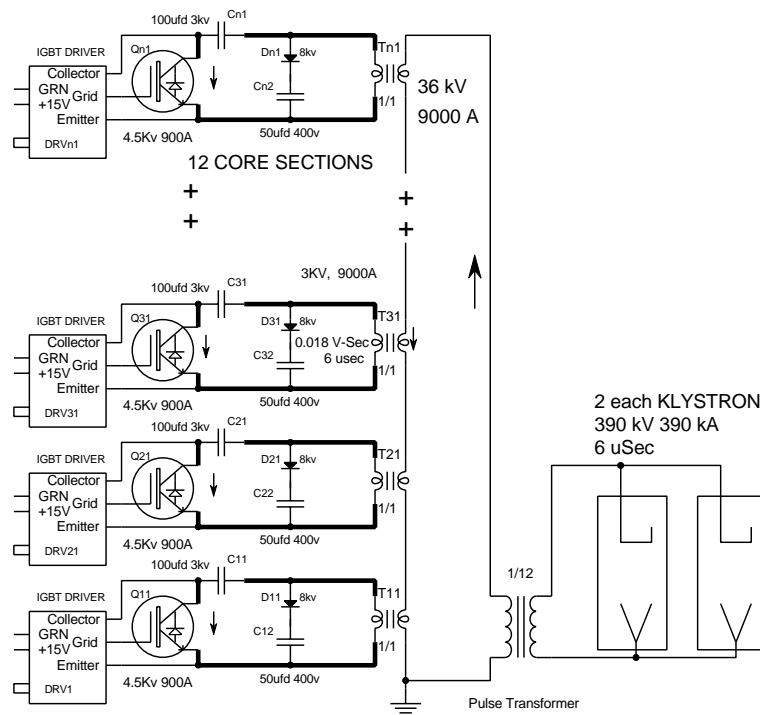
Figure 4.29: *Injection Modulator 2-Pack Concept, Induction Design*

and a lack of history in high current pulsed operations or in driving multiple loads. It is mandatory for the JLC/NLC to make a major reduction in the high cost of the modulators and to eliminate the difficulties of maintaining and tuning conventional line-type systems. The flexibility of a solid state switch and partial discharge capacitor design has already been demonstrated by the ease with which the recent main linac design change from 1.5 to 3.0 microseconds could be accommodated without any change in the driver board layout.

Costs continue to be the key issue for all NLC/JLC systems. The most critical components for induction and hybrid designs are now available from multiple sources and prices are dropping. SBIR efforts are continuing to seek optimization of various design options. The ideal klystron-modulator package for the JLC/NLC depends on many factors that are influenced by topology as well as details of the RF loads and how they are combined. It does seem clear that costs can be minimized if the modulator drive capabilities are well matched to the loads, and the induction building block offers powerful matching options. However, a single packaged modulator-klystron with a wall plug on one end and RF out the klystron would be ideal in many ways if it could be built small enough and cheaply enough.

Tremendous progress has been made in the past two years. The ISG Collaboration plan outlined above will continue to explore these options with the collaboration of industry. This process should bring the modulator design to a state of readiness to procure one or more industrial prototypes by the end of FY2002.

ISG Progress Report, April, 2000

References for Chapter 4

[1] R. Cassel et al, "600kV Modulator Design for the Next Linear Collider Test Accelerator" 20th International Power Modulator Symposium. Myrtle Beach, SC, 1992(?)

[2] R.F. Koontz et al., "Pulse Modulator Developments in Support of Klystron Testing at SLAC" 1993 Particle Accelerator Conference (PAC93), Washington DC

[3] "JLC Design Study." KEK Report 97-1, April, 1997.

[4] D. Sprehn, G. Caryotakis, E. Jongewaard, R. Phillips, "Periodic Permanent Magnet Development for Linear Collider X-band Klystrons", Invited talk at RF 98 Conference, Pajaro Dunes, CA

[5] Y. H. Chin, M. Akemoto, S. Fukuda, S. Matsumoto, S. Michizono, H. Mizuno, K. Takata, N. Toge, S. Tokumoto, H. Tsutsui, S. Yamaguchi, and J. Wang, and S. Kazakov, "Development of the X-band RF power sourcefor JLC", in Proc. of the 1999 Particle Accelerator Conference (PAC99), New York, USA, March 29-April 2, 1999, p.3414.

[6] R. Koontz, M. Akemoto, S. Gold, A. Krasnykh, Z. Wilson, "NLC Klystron Pulse Modulator R&D at SLAC"

[7] M. Akemoto, S. Gold, A. Krasnykh, R. Koontz, "Development of the Pulse Transformer for NLC Klystron Pulse Modulator" 1997 Particle Accelerator Conference (PAC97), Vancouver, B.C., Canada

[8] M. Akemoto, S. Gold, A. Krasnykh, R. Koontz, "Design of a PFN for the NLC Klystron Pulse Modulator" First Asian Particle Accelerator Conference,1998, KEK, Tsukuba, Japan

[9] R. Koontz, G. Blokhina, S. Gold, A. Krasnykh, "High Dielectric Constant Materials for Pulsed Energy Storage Capacitors"

[10] S. Gold, JP Eichner, R. Koontz, A. Krasnykh, "Developments in the NLC Modulator R&D Program at SLAC", 23rd International Power Modulator Symposium, Rancho Cordova, CA, 1998

[11] M. Akemoto and S. Takeda, "High-Power Klystron Modulator Using a Pulse-Forming Line and Magnetic Switch" KEK-preprint-93-41, June 1993, Presented at PAC93, Washington DC.

[12] H. Mizuno, T. Majima, S. Sakamoto and Y. Kobayashi, "A Blumlein type Modulator for a 100 MW-class X-band Klystron," Proc of the European Particle Accelerator Conference, 1994.

[13] M. Akemoto et al., "Development of a High-Power Klystron Modulator with SI-thyristor Switch," The 13th Symposium of Static Induction Devices, SSID-00-5, 2000.

[14] N. Shimizu et al., "4kV Reverse Conducting Static Induction Thyristor," The 10th Symposium of Static Induction Devices, SSID-97-6, 1997.

[15] R.L. Cassel, G.C. Pappas, M.N. Nguyen, J.E. DeLamare, "A Solid State Induction Modulator for the NLC", in Proc. of the 1999 Particle Accelerator Conference (PAC99), New York, USA, March 29-April 2, 1999,http://ftp.pac99.bnl.gov/Procs/MAIN/PAPERS/TUP9.PDF

[16] Z.   Wilson,   "NLC   Reliability   Analysis   Notes: Klystron-Modulator
     System,"   SLAC   Linear   Collider   Note   LCC-0029,   November   1999,
     http://wwwproject.slac.stanford.edu/lc/ilc/TechNotes/LCCNotes/PDF/lcc-0029.pdf

[17] Second   NLC   Modulator   Workshop   Proceedings,   June   29-July   2   1998,
     http://www.slac.stanford.edu/grp/kly/mkw/

[18] Third   NLC   Modulator   Workshop   Proceedings,   June   23-35   1999,   http://www-
     project.slac.stanford.edu/lc/local/Reviews/modulators/workshop/mod-wrkshop.htm

Authors and Major Contributors of Chapter 4

- Mitsuo Akemoto

- Shozo Anami

- Dick Cassel

- Ed Cook

- Jeff DeLamare

- Tony Donaldson

- Saul Gold

- S. Hawkins

- R. Keith Jobe

- Ron Koontz

- Anatoly Krasnykh

- Ray Larsen

- Bernie Merritt

- Hajime Mizuno

- Minh Nguyen

- Chris Pappas

- Jim Sullivan

- Koji Takata

- Seishi Takeda

- Shuichi Tokumoto

- Karl Van Bibber

- Zane Wilson

X-band RF Power Sources

Contents

5.1   Introduction

To deliver a beam energy of 1 TeV in the center-of-mass, both the JLC and NLC projects require a total of roughly 600 kJ of RF power on each beam pulse in a pulse length of 385 ns. This power is then delivered to the 9000 accelerator structures. Both designs use klystrons to convert the high voltage pulse from the modulators into X-band RF power. In this section, we will discuss the development of the X-band klystrons and the RF windows.

The X-Band klystrons are among the most complex components in the RF system envisioned for the JLC/NLC. The design of such tubes is as much an art as a science. During the past decade, both SLAC and KEK have devoted a considerable portion of their linear collider R&D effort to developing X-Band klystrons with output power in the range of 50 to 120 MW. For the present bunch train format, the length of the RF pulse at the accelerating structures needs to be 385 ns whereas klystrons and modulators can produce micro-second long pulses. To achieve good efficiency and reduce the number of klystrons and modulators, pulse compression techniques are used to sum and partition the long klystron pulses to produce the 385 ns long pulses needed to power the accelerating structures; these techniques are discussed in Chapter 6.

Currently, the klystron design goal is to produce 75 MW in 1.5 microsecond pulses. The pulses from eight such klystrons will then be summed and subdivided by the Delay Line Distribution System (DLDS) into four pulses of 385 ns and directed to four sets of three accelerating structures. In this case, roughly 6600 klystrons would be needed to accelerate the beams to produce 1-TeV center-of-mass energy. The power, pulse length and number of klystrons required were specified in the summer of 1998 in a joint NLC/JLC parameter set, based on the status of klystron and DLDS development at that time. However, recent experimental results indicate that it may be possible to design klystrons which produce 75 MW in 3.0 microsecond pulses. If these results are confirmed, then only half as many klystrons will be required.

In this chapter, we present the progress the R&D program has made through the end of 1999. The development of the X-band power source has been one of the major goals for the JLC and NLC R&D program. The actual R&D on these sources began 15 years ago and has been much more difficult than initially anticipated. The recent success of the high power Periodic Permanent Magnet (PPM) klystrons has been very gratifying. This success is in a large part due to the development of the simulation and modeling tools. In the following, we will discuss the klystron development program, including the experimental results and simulations, as well as the RF window development.

5.1.1   Historical Background

During most of 1990's, the design efforts for the KEK program were centered at BINP in Russia. This collaboration yielded a series of solenoid-focused, 80 MW klystrons (the XB72K series) that improved over the years but did not converge on a fully functional design. In the early 1990's, SLAC also built a

series of solenoid-focused tubes as part of its 100 MW "XC" program, again with limited success. The output power goal at SLAC was then lowered to 50 MW, and after three prototypes were produced, a robust design was achieved in this "XL" series. Since then, ten of these "XL-4" tubes have been built and are being used for testing and beam acceleration in the NLCTA.

In recent years, KEK has revamped its klystron design program. The first priority was to improve its klystron modeling capability. The initial focus was to use the computer simulation code MAGIC to model the XL-4 and tubes in the XB72K series to see if their performance could be predicted accurately enough to trust it for future designs. During this period, the ISG meetings provided a forum to compare these results, which were very encouraging, with those from SLAC where the programs EGUN and CONDOR are used. Also, the SLAC experience with the XL series development was communicated to KEK. With their renewed program, KEK improved on the XB72K design and built a solenoid-focused tube with Toshiba which produced 50 MW, 1.5 microsecond pulses.

As both KEK and SLAC developed solenoid-focused tubes, it was known that ultimately a less energy consuming scheme of focusing the klystron beams would be needed to keep the JLC/NLC operating costs manageable. In 1996, SLAC produced the first 50 MW klystron that used a series of permanent magnets to focus the beam. Although this periodic permanent magnet (PPM) tube eliminated the need for power-consuming solenoid magnets, the resulting focusing was weaker which required design changes that made it more susceptible to instabilities (but also more efficient). The 75 MW PPM klystron that SLAC produced next was indeed much more of a challenge, and although the initial design goals were met, it is not considered a robust tube. Nonetheless, it did achieve a 3 microsecond pulse length, which is now the goal for the next generation of klystrons. SLAC is currently developing a klystron incorporating "Design-for-Manufacture" (DFM) methodology.

At KEK, all design work has likewise shifted to PPM tubes, beginning in 1998 with the testing of a tube developed by BINP. Although high output power has been achieved, oscillations in this tube are still a problem even after several improvements were made. More recently, KEK has begun a collaboration with Toshiba to build a 50 MW tube followed by a 75 MW version: the 50 MW design is complete and construction is underway. The programs at KEK and SLAC have benefited from the exchange of information at the ISG meetings, in particular, on design and testing of the permanent magnet stacks. As part of this research exchange, a prototype detachable stack being developed by Toshiba will be tested on one of the DFM tubes at SLAC.

Another klystron component that has been a hot topic in the ISG discussions is the ceramic window in the output waveguide that isolates the klystron vacuum from that of the RF transport system. Although this window may seem like a minor part, it is prone to cracking as a result of the high RF fields that pass through it. Several designs have been developed at KEK and SLAC with the goal of minimizing the transverse electric fields at the windows. A number of prototypes have been built and tested with various degrees of success. The best result to date is with the enlarged TE01-type window from SLAC which has been tested up to 130 MW in a resonant ring. It is likely that one or two robust designs will emerge from this effort in the next year or two.

5.1.2   Summary of ISG Activities on R&D on Klystrons and Windows

The ISG meetings provided an ideal forum for discussion and review on development efforts at KEK and SLAC and for exchanges of interesting ideas and development plans. It inspired the participants from both sides to work together to solve many common problems such as parasitic oscillations and to develop a more accurate and realistic modeling of the klystron. Successful collaboration works include:

1. Establishment of realistic and comprehensive klystron simulation methods from the gun to the collector using the MAGIC code.

2. Creation of a new subgroup on X-band klystron development to mutually review the SLAC and KEK development efforts on high-power X-band klystrons using permanent magnets for beam focusing.

3. High power testing of the mixed-mode window at KEK and SLAC

In the following sections, we will discuss the progress in klystron development and then the RF modeling studies. This will be followed by a discussion of the RF window development program.

5.2   Klystron Development

KEK and SLAC have actively been working towards the design of a high power reliable X-band klystron for many years. The JLC or the NLC will require thousands of klystrons generating many tens of mega-watts of X-band power in micro-second pulses. The initial efforts of the laboratories focused on the development of solenoid focused klystrons however the solenoids on these klystrons consume 20 to 30 kW apiece which would double the AC power needed by the collider. For this reason, alternate focusing approaches were considered including both superconducting systems and permanent magnet based systems. Periodic Permanent Magnet (PPM) focusing is utilized in Traveling-Wave Tube (TWT) devices for commercial and military applications. Instead of a solenoidal magnet with its associated overhead of power supply, cooling, and controls, permanent magnets are used to reduce operational cost and weight. In PPM focusing, the axial field changes polarity with every magnet. If the magnetic period is small enough when compared to the beam plasma wavelength, λ_p/L, then sufficient beam stiffness can maintain the beam profile in the presence of large space charge forces due to RF bunching.

Because these magnets require a high energy-product and have tight geometrical constraints, it is usually not possible to thread as much flux through the cathode as it is with solenoidal focusing. As a result, particular attention must be paid to the gun design and beam transport issues. The drawback with PPM focusing is that the increased complexity of the tube may cause higher construction costs

as well as higher failure rates. The magnetic focusing strength is fixed and so there may be no easily accessible "knob" for the operator to turn in case adjustment is required. If the beam voltage is too low, λ_p/L becomes small and the beam will impact the drift tube. This is known as the "stop-band" voltage. Since the high voltage beam pulse has a finite rise and fall time, a portion of the beam pulse is always below the stop-band and interception occurs. There are also areas of beam instability in PPM focused tubes and the possibility of coupling to modes that grow from an undulating beam.

In the following sections, we will first describe the solenoid-focused and PPM klystrons and then discuss the RF modeling simulations that are being used to design the new tubes.
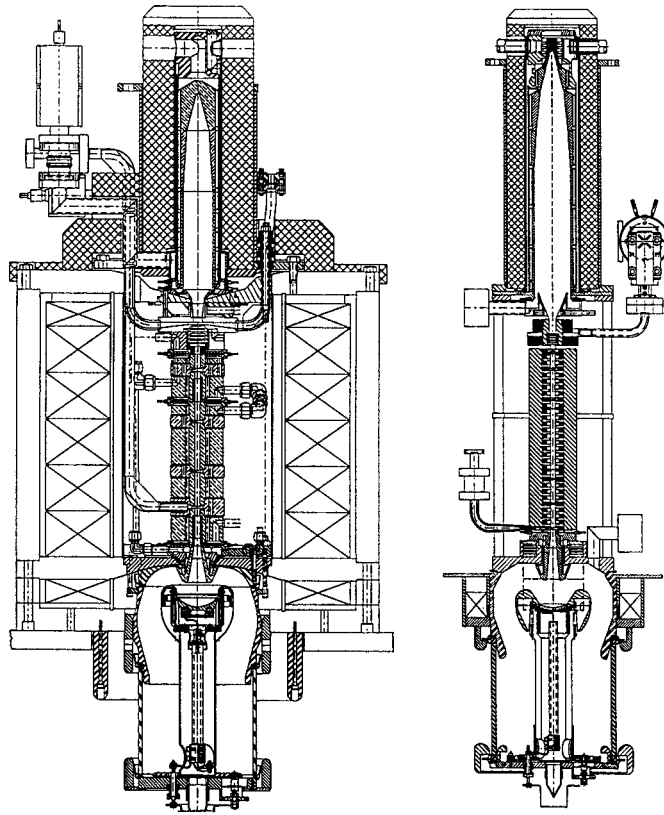
Figure 5.1: *Comparison of the Solenoid-focused and PPM klystron.*

5.2.1 Solenoid-focused Klystrons

At KEK, 10 klystrons with a solenoidal focusing system (so-called XB72K series) have been produced, with a maximum power of 50 MW achieved in the last two klystrons at 1.5 μs pulse length and 25 Hz repetition rate. All of these tubes had the same gun (the beam area convergence of 110:1) and buncher (one input, two gain and one bunching cavities) except the last tube where one more bunching cavity was added. The TWT multi-cell structure has been used since the XB72K No.6. To improve the

efficiency (the solenoid magnet needs about 30kW DC power), the XB72K series was terminated (at least temporarily) in 1999 and the development of the PPM focussed klystron is now under way in a two year project with Toshiba and Sumitomo[1].

Table 5.1: *KEK & SLAC solenoid-focused klystron parameters*

	KEK			SLAC
	XB72K #8	XB72K #9	XB72K #10	XL-4
Operating frequency (GHz)	11.424	11.424	11.424	11.424
RF pulse length (μs)	0.5	1.5	1.5	1.5
Peak output power (MW)	55	50	50	75
Beam voltage (kV)	520	440	466	400
Perveance ($\times 10^{-6}$)	$\sim$1.35	$\sim$1.35	$\sim$1.05	1.2
Repetition rate (pps)	5	25	25	120
RF efficiency (%)	22	31	35	43
# of tubes built	1	1	1	9
Year	1997	1998	1999	1995-7

At SLAC, the klystron group designed the XL-series of solenoid-focused X-band klystrons for the NLC Test Accelerator project (NLCTA) which was completed in 1996. Presently, the workhorse of that program is the XL-4 klystron which nominally produces 50 MW in pulse lengths up to 1.5μs at a repetition rate of 120 Hz and an efficiency of 43%. Nine of the XL-4 series klystrons have been constructed to date and they are used to power the NLCTA as well as to produce power for X-band component testing. To study the feasibility of different NLC klystron configurations, the XL-4 has been operated at 75 MW with a 1.5μs pulse length and at 50 MW with a pulse length greater than 2.4μs demonstrating production of the RF pulses required by the JLC and NLC. Of course, it should be noted that although the XL-4 klystrons can deliver the desired RF pulses, the efficiency of the klystrons, especially when including the solenoid power, is too low to work as a power source for the JLC or NLC.

5.2.2   Periodic Permanent Magnet Klystrons

Periodic Permanent Magnet (PPM) klystrons are being developed at both KEK and SLAC to eliminate the expense and power requirements of the focusing solenoids. At SLAC, the prototype 50 MW XL-PPM klystron was built and tested in 1996 and then the 75 MW XP-1 was constructed in 1997. Presently, a 75 MW Design for Manufacture (DFM) klystron, the XP-3, is being developed. At KEK, two separate programs are being pursued: one with Toshiba and another with BINP in Russia [1]. Throughout this R&D effort, SLAC and KEK have compared designs by exchanging drawings and simulation results. Both efforts have also benefitted by sharing the results of their operational experience.

SLAC 50 MW PPM Diode and Klystron (XL-PPM)

The first SLAC PPM klystron was built in 1996. It was based on experience with the highly successful SLAC XL-4 klystrons, with a number of modifications. First, considerations of cathode life lead to an electron gun design with an area convergence ratio of 144:1. Since this value is higher than previous SLAC klystrons, a beam test diode was fabricated to prove gun and drift region optics for the PPM design. The diode design was very conservative to eliminate any impediments to the study of the PPM beam formation and transmission. It was decided to control the magnetic field in the gun with a standard bucking coil and the field in the region from the gun to the beam minimum with three compact coils closely wound around the drift tube. The gun and magnetic circuit were constructed so that operation with and without flux at the cathode was possible.

Both the diode and klystron drift sections were fabricated from brazed stacks of alternate iron pole pieces and Monel spacers. These stacks were welded together at the end pole pieces to form the complete drift tube. The klystron cavities were fabricated from brazed spacer sub-assemblies that were in turn brazed into a stack assembly. The magnets were high quality individually die-pressed Samarium-Cobalt $SmCo$.

Next, the RF circuit was designed to allow for a lower perveance and for the different construction technique and materials required for the magnet structure. The circuit was adapted to the lower perveance beam by increasing the cavity spacings, altering tunings, and adding a cell in the traveling-wave output structure for a total of five cells. The number of cavities was kept constant and the bandwidth reduced to maintain the required gain. The decrease in gain between the two designs was due to the lossy materials used in the PPM cavities leading to a lower Q_0 than for copper cavities. An advantage of the lossy drift tube material may be a dampening of possible trapped oscillations and of any coupling between the gun, cavities and collector. The klystron magnetic field is very similar to the test diode until the last three cavities where the field gradually tapers up to confine the beam better as the space charge forces increase with RF current as shown in Fig. 5.2. The field in the output structure is unidirectional, unlike the rest of the klystron where it is periodic.

Table 5.2: *Design parameters for the SLAC PPM klystrons*

Tube	XL-PPM	75XP-1	75XP-3 (DFM)
Operating frequency (GHz)	11.424	11.424	11.424
Bandwidth (MHz)	35	100	100
Beam voltage (kV)	464	490	490
Perveance ($\times 10^{-6}$)	0.60	0.75	0.75
Peak output power (MW)	50	75	75
RF pulse length (μs)	1.5	1.5	3
Repetition rate (Hz)	120	120	120
RF efficiency (%)	55	55	55

The diode was tested successfully, demonstrating very stable operation up to 2.8 μs pulse length at 120 Hz and 490 kV, where the average beam power was 42 kW and the beam transmission was 99.9%.

Table 5.3: *Actual values for the SLAC PPM klystrons*

Tube	XL-PPM	75XP-1	75XP-3 (DFM)
Operating frequency (GHz)	11.424	11.424	11.424
Bandwidth (MHz)	40	?	?
Beam voltage (kV)	464	518	548
Perveance ($\times 10^{-6}$)	0.60	0.75	0.75
Peak output power (MW)	50	80	72
RF pulse length (μs)	2.37	1.5	3.13
Repetition rate (Hz)	60	1	1
RF efficiency (%)	55	56	43
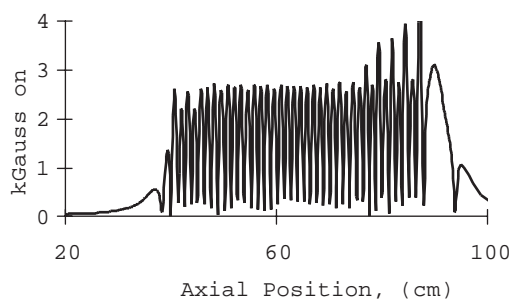
Figure 5.2: *Axial field (Gauss) vs. axial distance (cm) for the SLAC 50 MW PPM klystron.*

This excellent result gave confidence that a magnet structure could be designed with no allowance for shunting or adjustment. The beam perveance was found to be 12% higher than the design value of 0.6 mK; the reason for this discrepancy has not been completely determined.

Initial testing of the 50 MW klystron revealed that the gun behaved identically to the test diode performance. An unusual gain curve containing several jumps was believed to be due to multipactoring in more than one location along the drift tube and/or cavities. To eliminate these discontinuities, the tube was opened and was coated with a titanium-nitride (TiN) layer roughly 100 Angstroms thick to suppress the onset of multipactoring. After re-testing, only one gain step remained.

Sampling of all coupling ports and of the collector ceramic insulator revealed no oscillations higher than 50 dB below the fundamental. Small signal bandwidth was measured at 40 MHz, in close agreement with the predicted value of 35 MHz. Measurements over a 70 dB range of RF drive power showed the small signal gain to be 65 dB at the design current, falling by 10 dB at the 50 MW power level. After reconfiguring the magnetic circuit for the shielded flow condition, the tube was re-tested. An output power of 50 MW was achieved with essentially the same gain and efficiency and a beam interception of roughly 2%.

Despite the remaining step in the gain profile which is believed to be due to multipactoring in the
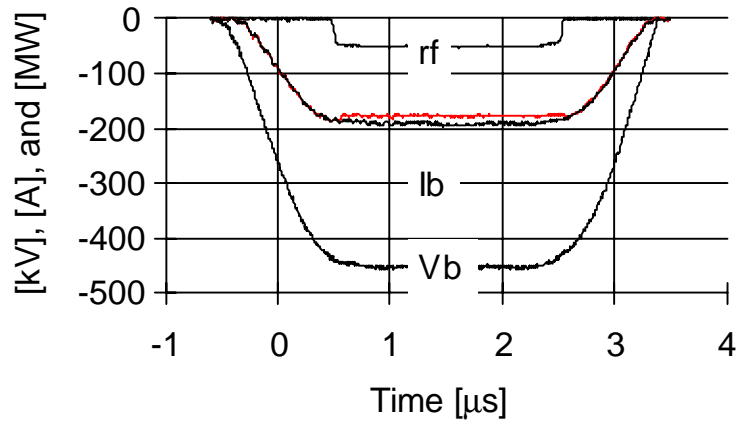
Figure 5.3: *50 MW RF output, beam current (with and without RF present), and beam voltage vs. time for the SLAC 50 MW PPM klystron.*

input cavity, the klystron reached the full operational specification of 50 MW at 2 μs as illustrated in Fig. 5.3. The efficiency at 50 MW was well over 55%, and over 60% at 60 MW, based on calorimetric diagnostics. The intercepted beam power at 50 MW was about 1% of the total beam power, but the beam current lost about 7% while passing through the tube, suggesting that the average energy of the intercepted electrons was approximately 66 keV.

Recently the 50 MW klystron was re-tested to explore longer pulse operation, where 50 MW at 2.37 μs and 60 Hz with 55% efficiency were achieved.

SLAC 75 MW Klystron (75XP-1)

Next, a 75 MW PPM klystron was designed and constructed in 1997. In comparison to the 50 MW design, a number of major changes were made in the design, including an enlarged stainless steel drift tube for higher beam current and the elimination of the gun focus coils. Opening the beam tunnel by 13% to 0.425 inches, reduced the efficiency of the beam-cavity interaction and thereby forced the inclusion of an extra gain cavity. This also allows more modes to propagate within the drift tube, including the second harmonic TM mode. The construction of the 75 MW PPM magnetic circuit differed in that the drift tube is a semi-continuous stainless steel structure interrupted by the cavities, with the iron pole pieces and non-magnetic spacers placed outside the vacuum envelope. This design change addressed three separate issues: avoiding the multipactoring seen in the 50 MW klystron, taking a step toward the eventual low-cost design of a production klystron using a clamp-on magnetic circuit, and adding loss in the drift tube to increase the start-oscillation currents of the various parasitic modes which may arise.

The large drift tube resulted in a lower beam area convergence and lower current density in the beam, which in turn reduced the necessary magnet strength. On the other hand, moving the pole

pieces outside of the vacuum envelope increased the required magnet strength and the overall affect was a slightly higher energy-product required for the 75 MW design. Previously, $SmCo$ magnets, which are highly resistant to radiation and temperature, had been used. The 75 MW design used NdFeB magnets which have higher energy-products, are easier to machine and less brittle, but have a lower Curie temperature and are more sensitive to radiation damage. However, at 500 keV photon levels, the radiation effects do not seem to be a limitation given the projected lifetime of the magnets. Furthermore, $NdFeB$ magnets are less expensive the $SmCo$ in bulk quantities.

Simulations of the klystron using CONDOR, a 2.5-D particle-in-cell code, show approximately 80 MW at the design beam power while maintaining low gradients in the output structure.

When delivered, most of the completed magnets failed to meet specification. Specifically the magnets at the beam convergence area near the gun, the gain cavity magnets, the penultimate cavity magnet, and the output magnets were all below specifications. Due to time constraints, it was decided to proceed with testing anyway. Short pulse (1 μs FWHM) testing revealed a 20 GHz oscillation at the end of the beam pulse that could be suppressed by tuning the gun coil and increasing the RF drive. By carefully adjusting the gun coil current and RF drive, it was possible to raise the peak voltage to 463 kV and attain 71 MW peak in a 200 ns pulse. The gain was found to be between 55 and 60 dB with an efficiency of 60% at 70 MW saturated output power. The magnets were transferred from the klystron to a test pole piece stack where they were shunted to achieve a more desirable field profile.
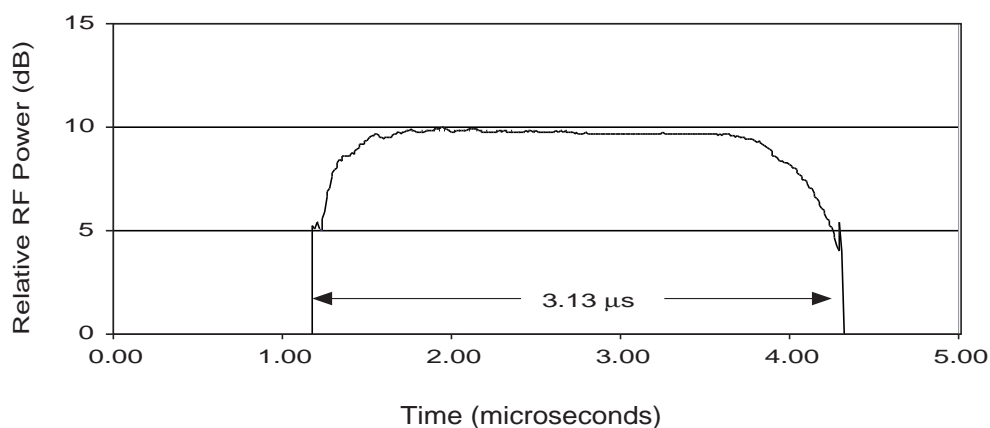
Figure 5.4: *84 MW Peak and 72 MW average RF power output over 3.13 μs pulse length at 1 Hz repetition rate for the SLAC 75XP-1 klystron.*

Subsequent testing of the klystron revealed a very strong 1.5 GHz gun oscillation, which was confirmed with SUPERFISH analysis of the gun geometry. A lossy collar of $BeO\text{-}SiC$ ceramic was designed and fabricated along with a set of screens to isolate the potential cavities formed in the gun structure. These components were installed after carefully venting the tube and opening the gun HV seal. The seal was replaced and the tube reprocessed with a heater tape bake. Re-testing confirmed the elimination of the gun oscillation but rediscovered the 20 GHz oscillation seen earlier. A replacement transition from the output cavity to collector was designed using HFSS to damp the RF energy in the 20 GHz

range. This device was installed in the klystron and the klystron was again re-tested. Now, the 20 GHz oscillation was found to be effectively suppressed, allowing operation of the tube at over 90 MW in a 300 ns pulse length and 72 MW at 3.13 μs as seen in Fig. 5.4. This latest operation was limited to 1 Hz repetition rate due to heating of the un-cooled magnet stack.

SLAC XP-3 Diodes and Klystron (DFM)

A lower-cost design of a 75 MW klystron, known as the Design For Manufacture klystron (DFM) or the XP-3, has been under investigation for the past three years and seeks to minimize parts count, decrease complexity, and reduce construction labor, while increasing the reliability of the klystron. The main areas of scrutiny are a smaller gun and collector, better output waveguide hardware such as mode converters and windows, and a simplified drift tube and magnet structure.

One key to the lower cost will be the development of a clamp-on magnet structure, which can be reused repeatedly as klystrons reach the end of their useful lifetime; a similar structure will be developed for the Toshiba PPM-2 klystron. A prototype clamp-on structure has been fabricated using surplus $SmCo$ magnets from the 50 MW PPM diode. This structure served as a test vehicle for the proposed fabrication method, where precision tooling is utilized to align the magnets and pole pieces and allow them to be epoxy potted into a support structure. The structure has been tested in an automated magnetic measurement system designed and built to support our PPM development. The axial field performance was as predicted and the transverse field was found to be adequate.

Further testing of the clamp-on magnetic circuit concept will be accomplished with two beam-test diodes being fabricated presently. The diodes incorporate the same electron gun and collector that will be used for the klystron with the addition of a shortened version of the full klystron magnetic circuit. The first diode uses an integral magnetic circuit design where the pole pieces are brazed onto the stainless steel drift tube that forms the vacuum envelope of the device. This fabrication technique is identical to that used for the XP-1 klystron described earlier. The second diode will be identical to the first with the exception of the magnetic circuit that will be a clamp-on structure. The body of this diode consists of a simple stainless steel tube over which the clamp-on magnetic circuit is attached. This will allow a direct comparison of the focusing and beam transmission performance of the two different types of magnet structures.

The RF design is very similar to the design of XP-1 with modifications to allow for a smaller drift tube diameter throughout the gain section of the tube. Large signal simulations are currently underway using the MAGIC 2.5-D pic code described in Section 5.2.3. This work is expected to be finished by mid-2000 at which point the magnet circuit, cavity positions and tunings, and output circuit dimensions can be finalized. Since this klystron is in the transition regime between R&D devices and production prototypes, it will incorporate features of both.

The klystron will use the smaller gun and collector utilized in the two diodes as well as a clamp-on magnetic circuit. The output is through a single large TE01 window, the details of which are reported on in Section 5.3.2. A dual directional coupler will be installed between the output cavity and output window of the klystron for diagnostic purposes. An adjustable gun coil/anode coil assembly will be

used to allow tuning of the entrance magnetic field into the PPM stack. Once the klystron behavior is well characterized, this assembly can be replaced with fewer, smaller coils for the production version of the tube. The number of vacuum pumps will be reduced from five, as found on the XP-1 klystron, to three with one pumping the anode region, one on the output region and one on the output window. It is anticipated that the production version of the tube will have only one vac-ion style pump for monitoring purposes with addition pumping provided by NEG pumps as needed.

It is anticipated that testing the two beam diodes will begin at the end of summer 2000 and the klystron testing will begin in the early summer of 2001.

BINP PPM

KEK began the PPM klystron development effort in collaboration with BINP in Protvino, Russia. The first of these PPM klystrons was designed and built by BINP and tested at KEK in May 1998. The testing results are listed in Table 4 and are in good agreement with the MAGIC simulations as shown in Fig. 5.5; the MAGIC simulations are discussed in Section 5.2.3. The beam transmission is nearly 100% above a beam voltage of 500kV. However, above 500 kV there are clear signs of RF oscillations at frequencies of 14.5, 16.3, 19.5, 21.2 GHz, and higher. The DC current monitor in the collector shows about 30% beam loss when the drive RF is on. The MAGIC simulation results of the output cavity indicated a large number of particles (about 40%) intercepted just after the final cell of the output cavity. The interception is caused by the lack of focusing for particles that drop to the stop-band voltage after losing energy to the traveling wave.

	BINP PPM-1		BINP PPM-2		
Operating frequency (GHz)	11.424		11.424		
Perveance ($\times 10^{-6}$)	~ 0.93		< 0.93		
Beam voltage (kV)	500	550	501	516	550
Peak output power (MW)	55	77.4	20	28	75
RF pulse length (μs)	0.43	0.1	1.5	1.0	0.2
Efficiency (%)	33	38	20	21	35

Table 5.4: *Testing results of the BINP PPM-1 and -2 klystrons at KEK.*

In order to stop the oscillations and increase the efficiency, the BINP PPM klystron was rebuilt with several improvements: (1) a new buncher that produces an RF current of 1.62 times the DC current; (2) use of stainless steel in the output cavity and all tubes between the cavities to damp parasitic oscillations; (3) a change in the magnetic field at the output cavity to a unidirectional one by using a coil to control the focusing field and to stop the particle interception. This rebuilt PPM (BINP PPM-2) klystron was tested in fall 1999. Fig. 5.6 shows the test setup. Despite all the improvements and precautions, oscillation problems still limited the performance, primarily at 14.5 and 15.5 GHz. The output power at various beam voltages is shown in Table 5.4. Here, the perveance was reduced by decreasing the heater current to suppress the oscillations during the RF pulse length. The sources of the RF oscillation are currently under investigation.

ISG Progress Report, April, 2000
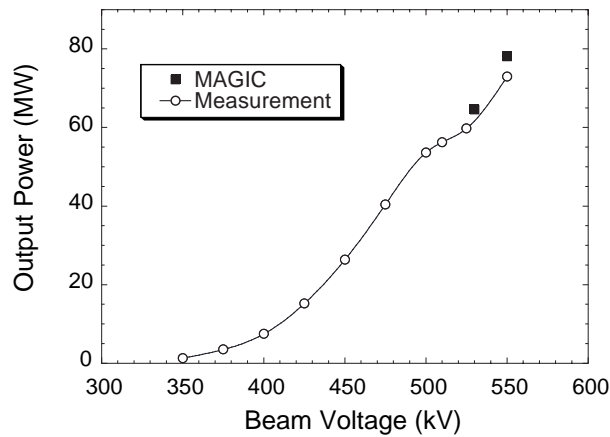
Figure 5.5: *Simulation and measurement results for the BINP PPM-2 klystron.*

Figure 5.6: *Experimental set-up for testing the BINP PPM-2 klystron.*

Toshiba PPM

In parallel with the BINP effort, KEK has also begun a two-year project with Toshiba to produce two PPM klystrons in two stages. The design parameters of those klystrons are shown in Table 5.5.

The main emphasis of the Toshiba PPM-1 klystron is to test a new gun design and to study the design and manufacturing of the PPM circuit. For the first time in the X-band klystron development at KEK, stainless steel and Monel are being used for tube and cavity materials to damp possible RF oscillation modes. The design has been completed and most of the components are presently being manufactured. According to MAGIC simulations, the expected peak power exceeds the original design goal and reaches 70-75 MW with an efficiency greater than 55%. Fig. 5.7 shows the MAGIC simulation of the beam in the output cavity region. The output power in this example is 74MW. The beam size is tunable between 2.3 mm and 3.3 mm by changing a combination of the bucking coil and matching coil currents. A critical issue for klystron performance is the actual dimensions of the gun at operating temperature (so-called hot dimension). The PPM-1 hot dimension was estimated by the

	Toshiba PPM-1	Toshiba PPM-2
Peak power (MW)	> 50	75
Beam voltage (kV)	480 - 500	480 - 500
Micro-perveance	0.8	0.8
Efficiency (%)	> 50	60
Pulse length (μs)	1.5	1.5
Repetition rate (pps)	50	150
Bandwidth (MHz)	80 at -1 dB	80 at -1dB
Cathode current density (A/cm^2)	< 10	< 10
Cooling	Air	Water

Table 5.5: *Main parameters of the Toshiba PPM-1 and PPM-2 klystrons.*

thermal code ANSYS and an actual measurement will be conducted using a anode-like test fixture and a laser beam. The prototype of the 4.5 period (13.5cm long) PPM circuit is shown in Fig. 5.8. The measurement results are in good agreement with the PANDIRA calculation. This prototype demonstrated the required quality control on the magnet pieces of <0.5%. Testing of the Toshiba PPM-1 is scheduled to start in June 2000.

The Toshiba PPM-2 klystron will incorporate experience and knowledge gained from the design and testing of Toshiba PPM-1. The main goals of the Toshiba PPM-2 are to manufacture a PPM klystron that meets the specifications of the JLC project and to refine the design and manufacturing process for future mass production. To meet these goals, the PPM-2 will have water cooling to allow a higher repetition rate and will use a clamp-on PPM stack for cheaper and easier production. A new high power multi-mode window, described in Section 5.3.1 will also be developed to support higher peak power and the full repetition rate. High power testing is scheduled to start in Spring 2001.
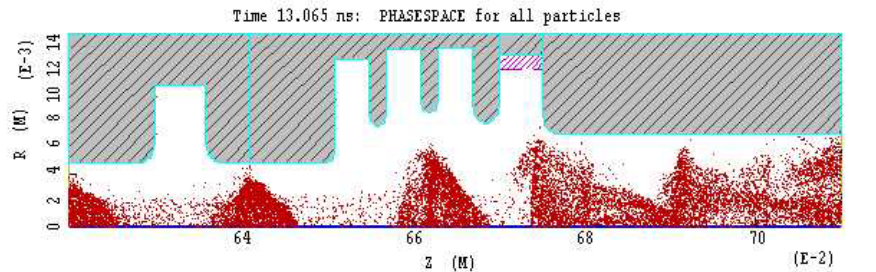
Figure 5.7: *MAGIC simulation of Toshiba PPM-1 gun.*

Figure 5.8: *Prototype of Toshiba PPM magnetic circuit.*

5.2.3 Modeling Simulations

A number of different simulation codes have been used to design klystrons, however most of them have had a quite limited range of utility. A new klystron simulation code MAGIC [3] has been used for the design of the KEK XB72K No.10[4], Toshiba PPM and SLAC DFM klystrons, as well as the SLAC XP-1 and XP-3. MAGIC is a 2.5-D or 3-D, fully electromagnetic and relativistic particle-in-cell code for self-consistent simulation of a plasma. It solves Maxwell's equations directly at particle presence using the finite difference method in the time domain like ABCI or MAFIA. It requires only the geometrical structure of the cavity and assumes no model (neither port approximation nor equivalent circuit) for the beam-cavity interaction. In addition, a static magnetic field can be applied to a structure.

The advantages of MAGIC are its accuracy and versatility. Even an electron gun can be simulated with results in good agreement with measurements. Simulation results can be imported/exported from one section of the klystron to another, allowing a consistent simulation of the entire klystron without loss of physics. The only disadvantage is that it is time consuming, but with the rapid development of computing facilities, this is not so important. In the following sections, we will first compare the code against others and then describe various situations in which it has been used at KEK and SLAC.

Functional Comparison of Available Codes

Table 5.6 shows the functional comparison of computer codes available for klystron simulations. MAGIC is the only code that can simulate all parts of a klystron from the gun to the collector. ARSENAL[6] is closest to MAGIC in functional performance, but cannot handle a TW multi-cell structure. CONDOR[7] can simulate a TW structure, but requires beam input from a gun that needs to be simulated by another code such as EGUN[8]. In the migration of beam and fields from one code to another, two programs must be well matched to avoid any incomplete transfer of information and resulting unphysical phenomena.

	Dimension	Gun	Buncher	Single-cell output cavity	Multi-cell output cavity
MAGIC	2.5, 3	yes	yes	yes	yes
EGUN	2.5	yes	no	no	no
CONDOR	2.5	no	yes	yes	yes
FCI[9]	2.5	no	yes	yes	no
ARSENAL	2.5	yes	yes	yes	no
JPNDISK	1	no	yes	yes	no
DISKLY	1	no	yes	yes	no

Table 5.6: *Functional comparison of available klystron modeling codes.*

Simulation of Traveling-Wave (TW) Output Structures

Simulation of a TW output structure is as straightforward as any other cavity. In order to simulate effects of a non-axially-symmetric output coupler by the 2.5-D version of MAGIC, it is modeled as a ring-shaped conductor that has the same complex S_{11}-matrix element (i.e., the reflection coefficient for amplitude and phase). This is illustrated in Fig. 5.9.
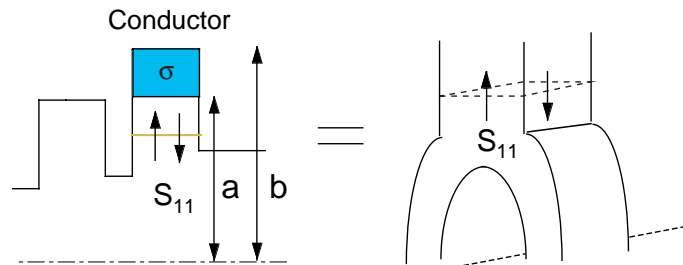
Figure 5.9: *Illustration for 2.5-D modeling of 3-D*

There are three free parameters to fit the frequency dependent S_{11}-matrix element: the conductance, and the inner and the outer radii of the conductor. For details of the output coupler modeling, refer

to [10]. As shown later, simulation results for many klystrons seem to verify the validity of this approximation. Fig. 5.10 shows the simulation results for the output structure of XB72K No.10.
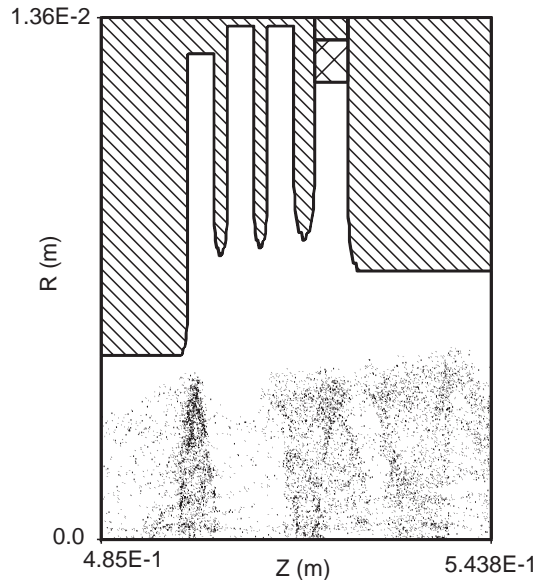
Figure 5.10: *Simulation of the region near the output structure of the KEK XB72K #10.*

Simulations of the KEK XP72K and SLAC XL-4 Klystrons

The simulation techniques are described in detail in [4] and briefly summarized here. The klystron is divided into three sections:

1. Electron gun

2. Buncher section (an input, gain and bunching cavities + drift space)

3. TW output structure

The gun simulation is done by specifying an emission area (cathode) and an applied voltage along a line between the focus electrode (Wehnelt) and the anode. The number of emitted particles can be specified per unit cell volume and unit time-step. The applied magnetic fields (both B_z and B_r) must be specified over the entire structure, not just on beam axis. They can be calculated using codes such as POISSON (for the solenoid field) and PANDIRA[5](for the permanent magnets). These programs require the exact configuration of coils, yokes, or permanent magnets and their properties as input. The input cavity needs a different treatment from other cavities, because the RF power is given externally, rather than being induced by a beam. Since a beam stays almost DC while passing the input cavity, the beam-induced voltage is negligible. Therefore, we just need to specify the applied RF voltage along an electric field line between the cavity gap. The field distribution of the fundamental

mode should be computed beforehand using MAGIC and used as input. Other cavities need to be tuned to correct their fundamental frequencies by adjusting the cavity aperture. The beam-induced voltage in the cavities is monitored to measure the necessary RF cycles for saturation. In most of the cases, about 200-300 RF cycles are enough. To speed up the saturation, a DC beam current from the gun is increased smoothly and slowly from zero to the full value in the first 10-20 RF cycles.

Fig.s 5.11 and 5.12 show the simulation results from MAGIC and the experimental data for the saturated output power vs. beam voltage for the XB72K No.8 klystron and XL-4 klystron. Excellent agreement can be seen. The closed triangles in Fig. 5.11 are DISKLY simulations which indicate the limited accuracy of the 1-D disk model code.
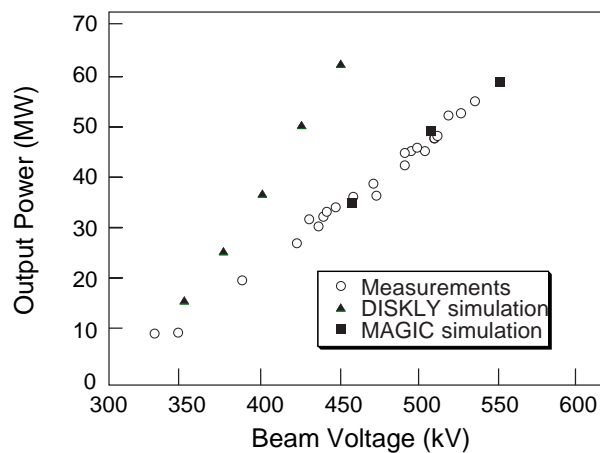
Figure 5.11: *Simulation results of MAGIC and DISKLY and the measurement data for the KEK XB72K #8 klystron.*
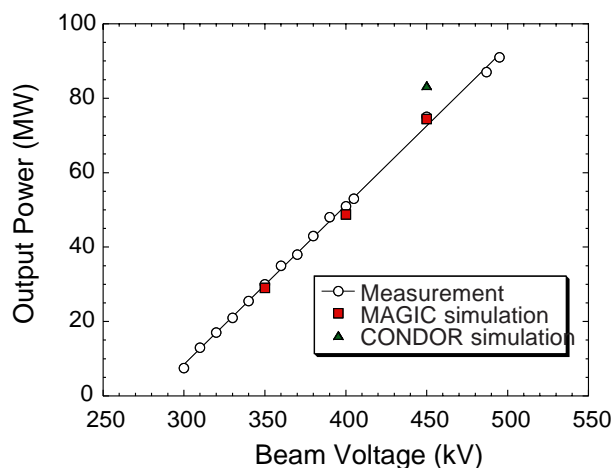
Figure 5.12: *Measured performance of the SLAC XL-4 klystron and results from simulations with MAGIC and CONDOR.*

ISG Progress Report, April, 2000

Simulations of the SLAC XP-1 and XP-3 Klystrons

The SLAC XP-1 was also simulated using the MAGIC code. The simulation divided the klystron into three parts, the four bunching cavities, two penultimate cavities, and the last penultimate cavity with a five-cell traveling-wave output section. "Import/Export" boundaries are used to transfer the particle and field data from one section to the next. A "laminar beam" input option permits a beam to be launched upstream of the input cavity with an initial angular momentum allowing matching of the beam to the entrance of the PPM magnet stack. This beam model is a shortcut method of introducing a beam into the problem without including the actual gun geometry. Each cavity is tuned to its design frequency and Q value using the "shim" and "conductance" options, respectively. The PPM field profile is obtained from POISSON. The output structure is modeled by first tuning the cells in pairs to give the correct coupling and cell frequencies according to SUPERFISH. The coupling is tuned by adjusting the iris height and the cavity heights are adjusted for the correct frequencies. After the couplings and frequencies have been adjusted, the final cell is tuned to the frequency and Q-value of an actual test cell.

The simulation produced a peak output power of 84 MW. This was obtained for a klystron operating at 490 kV and 275 A with a drive power of 300 W. The plots in Fig. 5.13 show the electron beam, starting at the emission boundary, progressively modulated by each cavity. Note the spreading of the bunches as the RF power is extracted in the output structure. Fig. 5.14 shows the time evolution of the Poynting vector power flow into the final cell of the output structure. The actual klystron had a slightly lower current of 259 A and delivered an output power of approximately 75 MW. The simulated efficiency of 62.7% compares well with the ∼60% efficiency measured during testing of the SLAC XP-1. An earlier simulation using the code "CONDOR" predicted an efficiency of 63% for this klystron.
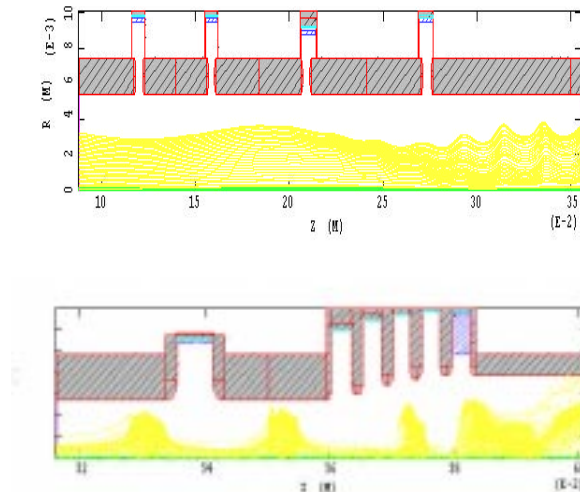
Figure 5.13: *The 490kV, 275A beam in the SLAC XP-1 (a) in the four bunching cavities with 300w driven power,(b) in the first two penultimate cavities, and (c) in the output cavity.*
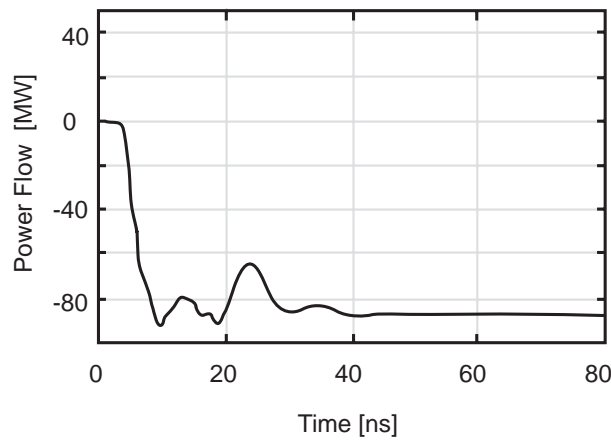
Figure 5.14: *The Poynting power flow into the last cell of the output cavity in the XP-1.*

Simulations are continuing for the SLAC XP-3 klystron. This PPM klystron will be the second 75 MW PPM klystron designed at SLAC. Unlike its predecessor the XP-1, this tube is designed for full average power operation and enhanced manufacturability. The XP-3 incorporates new designs for the gun, collector, RF circuit, output waveguide components and magnetic focusing.

5.3   RF Window Development

The ceramic windows are one of the vital parts of a high power pulsed klystron system. They are located at the exit of the output coupler and serve as a gate keeper to maintain a high vacuum inside the klystron while allowing the transmission of power from the klystron to the outside with minimum losses. A window consists of a circular ceramic plate and a copper cavity to house the ceramic. The development of X-band windows with high power handling capacity has been an important effort since the first stage of X-band R&D at KEK and SLAC. At KEK, a so-called Otake window was developed and used for the entire series of XB72K klystrons. It utilizes a traveling-wave TE11 $1/2\Lambda_g$ mode at the ceramic. The large ceramic diameter (51mm) helps to reduce the electric field at both the center and at the peripheral area where the ceramic is brazed to the copper housing. High power testing in a resonant ring showed an RF breakdown at 80MW with a pulse length of 800 ns.

At SLAC, a traveling-wave TE01 mode window with a 47mm diameter ceramic was developed and was used with the XL-4 klystrons. The advantage of the TE01 mode is that the electric field diminishes at the brazing area and thus the high power handling capability should be better than for the TE11 windows. However, RF breakdown at the ceramic center has been observed at a power level much lower than the theoretical prediction, presumably due to insufficiently careful treatment of the ceramic. The disadvantage of the TE01 mode window is that it needs expensive TE10-TE01 mode converters

Parameter	53 mm	64 mm
Max. tangential E-field on the surface of ceramic	7.5 kV/mm	5.0 kV/mm
Max. normal E-field on the surface of ceramic	6.0 kV/mm	5.5 kV/mm
Max. E-field on the surface of ceramic	7.5 kV/mm	5.5 kV/mm
E-field at place of metal-ceramic brazing	1.0 kV/mm	1.0 kV/mm
Passband (SWR < 1.2)	> 300 MHz	> 300 MHz

Table 5.7: *Simulated parameters of TW Mixed-Mode Windows for 100 MW power.*

at both sides of the window. The development of a more robust and economical window with lower electric field everywhere in the ceramic was emphasized at the first ISG meeting. A program was started at both KEK and SLAC to develop a window capable of handling 100MW of power with a 1.5 μsec pulse length.

5.3.1 Mixed-Mode Window

New types of RF windows have been proposed by Kazakov and designed in collaboration between BINP and KEK, [11]. The main feature of these is that the windows are operated in multi-mode. The combination of modes on the surface of the ceramic significantly reduces the electric and magnetic fields in the junction between the ceramic and the metal. In addition, a traveling wave configuration is used to reduce the field further. The windows have a simple shape for manufacturing and small overall dimensions.

So far two types of high power windows at 11.424 GHz frequency have been fabricated. These windows have ceramic disks with a diameter of 53mm and 64mm. The results of simulations are shown in Table 5.7.

The basic characteristic of the mixed-mode window is that the electric field strength at the periphery of the ceramic disk is very weak, and this has been verified by a bead-pull method using a low power model. The window shows very small reflection (VSWR=1.04 for operating frequency) and wide bandwidth (260 MHz for VSWR less than 1.1) (see Fig. 5.16).

A high power model of the window was fabricated and tested in a resonant ring. The surface of the ceramic disk was coated with TiN (10 nm). Fig. 5.17 shows conditioning history of the resonant ring test. A maximum circulating power of 81 MW with 300ns duration or 66 MW with 700 ns duration was achieved. The pulse repetition rate was 10 Hz. Light emission was observed for a power level of over 10 MW. The test was terminated due to lack of machine time and not because of RF discharge. Later, both windows with the diameter of 53mm and 64mm were shipped to SLAC for even higher power testing using combined power from two klystrons. The first window (53mm diameter) achieved a circulation power of 80MW with 1.5μs duration at 30Hz repetition. Although it was not destroyed and more testing will improve the performance, it was replaced by the second window with 64mm diameter due to lack of machine time. High power testing of the second window is still ongoing, and
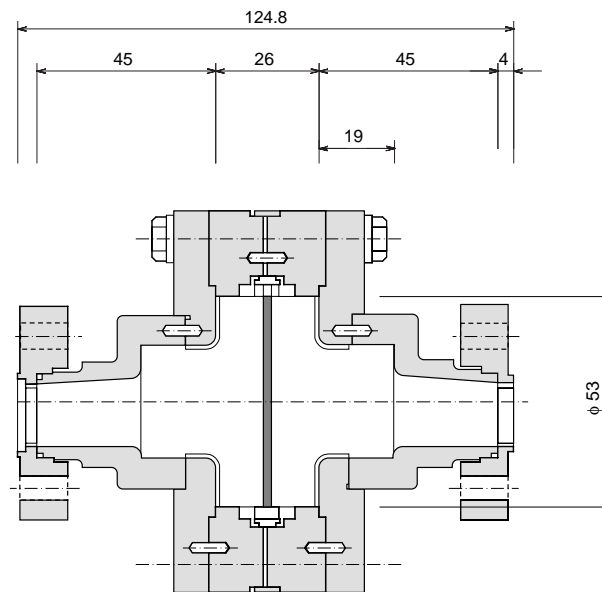
Figure 5.15: *High power model of 53mm mixed-mode window.*

the testing of the first window will be restarted with a new ceramic later.
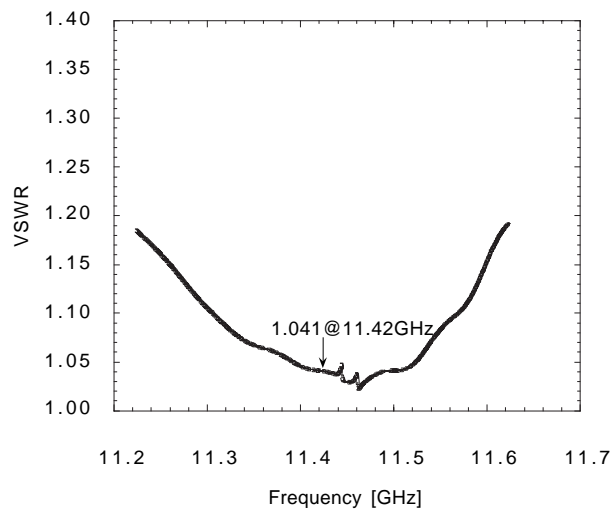
Figure 5.16: *Reflection characteristic of the high-power model mixed-mode window.*

5.3.2   The Enlarged TE01 Window

Ceramic windows are traditionally used to isolate the klystron vacuum from that of the RF transport system to which it connects. The challenge of using these windows at high power is to prevent cracking

ISG Progress Report, April, 2000
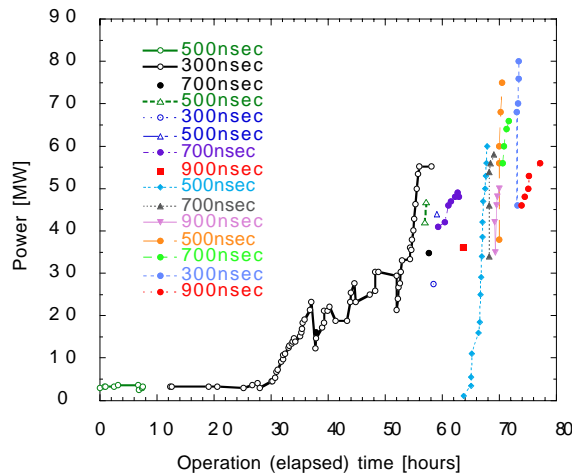
Figure 5.17: *Conditioning history of the high power model mixed-mode window in a resonant ring test.*

of the ceramic due to RF breakdown within the ceramic and along the surfaces. Failure can also occur from puncturing by electrons and overheating. The most recent class of windows are designed so that there is no axial or radial component of electric field at the window surface. The circular TE01 mode is useful for this purpose because the transverse azimuthal electric field is zero at the ceramic to metal braze where breakdown typically starts in conventional TE11 windows.

The first window of this type was 47 mm in diameter and was used initially on the XL4 klystrons. From various tests of these windows, it was observed that the probability for damage rises significantly when they are operated above about 40 MW. In fact, four XL4 windows have had to be replaced over the course of several years. From this experience, the diameter of the windows used on the newer XL4's and for the 75 MW PPM klystron was enlarged to 65 mm where the peak electric field at 75 MW is about the same as that in the 47 mm design at 40 MW. Specifically, the maximum RF electric field at the ceramic surface is 3.4 MV/meter at 75 MW.

As with the 47 mm design, the enlarged version operates in the TE01 mode using a field reduction scheme whereby the impedance at the ceramic surface is 'forced' to a lower value using a pair of inductive elements symmetrically located on each side of the window. This results in a pure traveling wave within the ceramic. The 65 mm diameter design is highly over-moded at the operating frequency of 11.424 where 17 modes could propagate if excited. For this reason, it is important that the wrap-around mode transducer that produces the TE01 mode have exceptionally high mode purity.

The rectangular to circular wrap-around mode transducer has an output diameter of 38 mm, which can support 6 propagating modes that the operating frequency. It was necessary to design a compact transition from 38 mm to 65 mm diameter that did not cause conversion to any of the 16 unwanted modes. Perfect circular symmetry prevents all but conversion to TE02. A double stepped circular transition from 38 to 65 mm was designed using the MLEGO mode matching program to suppress this unwanted conversion to TE02. This pair of tuned, transitions have a reflection coefficient of 0.34 each.

This reflection is conveniently used to supplement that of the inductive irises described previously to produce a total reflection of 0.56 that is required to create the field reduction and pure TW condition within the ceramic. The complete geometry is shown in Fig. 5.18
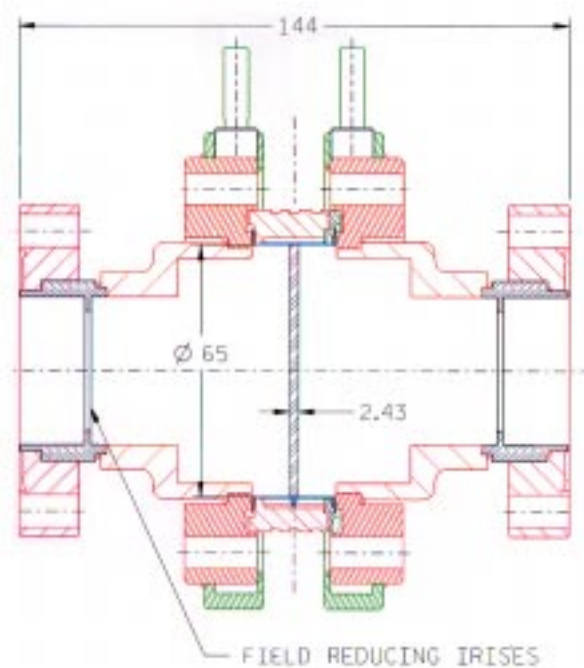
Figure 5.18: *The SLAC reduced field over-moded traveling wave TE01 window.*

Three windows of this design have been tested on the Traveling Wave Resonator at SLAC, two of them to 135 MW and the other to 85 MW. None were destroyed during processing. The peak power was limited in each case by problems with the klystron and waveguide system used to drive the Traveling Wave Resonator and not the windows themselves. Two of these windows are presently in use as a single output windows on klystrons XL-4 #7 and 8. These have operated to 50 MW, 1.5 microseconds with no failures to date.

5.4   Conclusions

For more than a decade, both SLAC and KEK have devoted a large portion of their linear collider R&D funds toward developing X-band klystrons for the NLC/JLC. This has been an arduous learning process requiring much patience and foresight due to the year-long development cycle needed to produce each new version of a tube. The initial program was aimed at demonstrating that the JLC/NLC power requirements could be met with standard solenoid-focused klystrons. The initial success in this regard was with the SLAC XL-4 tube which has produced 1.5 microsecond, 75 MW

ISG Progress Report, April, 2000

pulses with about a 50% efficiency. More recently, the emphasis has switched to developing periodic permanent magnet focused tubes in order to eliminate the energy consuming solenoid magnets. There also has been a renewed interest in klystron modeling in an effort to make the development of these tubes faster and more efficient. The best result to date is from the SLAC XP-1 which has met pulse performance requirements and has in fact been run at twice the nominal pulse length. Although successful, this tube is not considered sufficiently robust and a new version is being developed that is also more suited to mass production. The KEK program is also on the threshold of success in both its PPM development with BINP and its newer PPM program with Toshiba.

In the near future, both labs will continue on essentially parallel paths to develop robust, production quality PPM tubes. Once the designs begin to converge, reliability and system integration issues will begin to be addressed. In particular, the life time of components such as the output windows will be better evaluated. Throughout this period the ISG meetings will continue to serve as a forum to learn from each other's experiences and to discuss future directions.

References for Chapter 5

[1] Y. H. Chin, M. Akemoto, S. Fukuda, S. Matsumoto, S. Michizono, H. Mizuno, K. Takata, N. Toge, S. Tokumoto, H. Tsutsui, S. Yamaguchi, and J. Wang, and S. Kazakov, "Development of the X-band RF power source for JLC", in Proc. of the 1999 Particle Accelerator Conference (PAC99), New York, USA, March 29-April 2, 1999, p.3414.

[2] D. Sprehn, G. Caryotakis, E. Jongewaard, and R. Phillips, "Periodic permanent magnet development for linear collider X-band klystrons", presented at the Pajaro Dunes RF98 conference, 1998.

[3] MAGIC User's Manual, Mission Research Corporation, MRC/WDC-R-409, 1997.

[4] Y. H. Chin, "Modeling and design of klystron", in Proc. of the 1998 Linear Accelerator Conference (Linac98), Chicago, USA, August 23-28, 1998, p.367.

[5] J.H. Billen and L.M.Young, "Poisson Superfish", LA-UR-96-183, 1997.

[6] A. N. Sandalov, et. al., in Prof. of RF96, KEK Proc. 97-1, pp.185-194, 1997.

[7] B. Aimonetti, et. al., "CONDOR User's Guide", Livermore Computing Systems Document, 1988.

[8] W. B. Herrmannsfeldt, SLAC-PUB-6498 (1994).

[9] T. Shintake, Nucl. Instr. Methods A363, p.83, 1995.

[10] H. Tsutsui, S. Michizono, S. Matsumoto, Y. H. Chin and S. Fukuda, "X-band klystron output cavity simulation", in Proc. of the 1999 Particle Accelerator Conference (PAC99), New York, USA, March 29-April 2, 1999, p.851

[11] S. Yu. Kazakov, "A New Traveling-Wave Mixed-Mode Window with a Low Electric Field in Ceramic-Metal Brazing Area", KEK Preprint 98-120, Aug. 1998, A.

Authors and Major Contributors of Chapter 5

- Chris Adolphsen

- Vladimir Balakin

- Yong Ho Chin

- George Caryotakis

- Randy Fowkes

- Shigeki Fukuda

- Eric Jongewaard

- Serguei Kazakov

- Alex Larionov

- Rod Loewen

- Shuji Matsumoto

- Shinichiro Michizono

- Hajime Mizuno

- Keiji Ohya

- Robert M. Phillips

- Daryl Sprehn

- Vladimir Teryaev

- Shuichi Tokumoto

- Hiroshi Tsutsui

- Arnold Vlieks

- Seiya Yamaguchi

CHAPTER **6**

RF Pulse Compression and Distribution Systems

6.1 Introduction

During the past few years, high power RF pulse compression systems have developed considerably. These systems provide a method for enhancing the peak power capability of high power RF sources. Future linear colliders, such as the proposed NLC and JLC, require peak RF powers that cannot be generated directly by the current state-of-the-art microwave tubes. Such tubes generally can, however, provide pulses of several times the required duration. Pulse compression matches the source capabilities to the input requirements by exchanging pulse width for peak power.

The SLED Pulse compression system [1] was implemented to enhance the performance of the two-mile linac at the Stanford Linear Accelerator Center (SLAC). One drawback of SLED is that it produces an exponentially decaying pulse. To produce a flat pulse and to improve the efficiency, the Binary Pulse Compression (BPC) system [2] was invented. The BPC system has the advantage of 100% intrinsic efficiency and a flat output pulse. However, The implementation of the BPC [4] requires a large assembly of over-moded waveguides, making it expensive and extremely large in size.

The SLED II pulse compression system is a variation of SLED that gives a flat output pulse [5, 6] by substituting shorted delay lines for resonant cavities. The SLED II intrinsic efficiency is better than that of SLED, but not as good as that of BPC. However, for gains greater than two, SLED II is considerably more compact than BPC. Several attempts have been made to improve its efficiency by turning it into an active system [7]. However, the intrinsic efficiency of the active SLED II system is still lower than that of the BPC.

The DLDS [8] is a similar system to BPC which utilizes the time of flight of the beam in the accelerator to reduce the length of the over-moded waveguide assembly. However it still uses more over-moded waveguide than that required by SLED II. To make the DLDS even more attractive, the concept of multi-moding was introduced [9]. The resulting system (see Fig.6.3) further reduces the length of the waveguide system by multiplexing several low-loss RF modes in the same waveguide; hence the name Multi-moded DLDS (MDLDS). The system has an intrinsic efficiency of 100%, and the total over-moded waveguide length is less than that required by the compact SLED II system. In this chapter, we describe the progress towards a Multi-moded DLDS, which is currently being proposed as the preferred system for a future X-band linear collider.

The MDLDS is being developed in a collaboration between KEK and SLAC at both the system and component levels. The component developments have to achieve two major goals: high efficiency and reliable high power handling capabilities. From the system point of view, the choice of waveguide modes, number of modes and the characterization of these modes determine the architecture of the system. The first mode of choice is the TE_{01} mode in circular waveguide. Component development and system architecture for the DLDS system using only that mode is a proven technology, due to the long history of component development at SLAC for both RF hybrids and mode converters; see for example [6, 10] and the references cited therein. Designs for launchers that use different modes and devices that manipulate several modes have been proposed theoretically [11, 12] or prototyped

and will be reported on here along with some proof of principle experiments.

Each of the main linacs in the NLC have 2,484 structures. If three structures are powered with each RF feed, 828 feeds are required. Eight 75 MW (plus overhead) klystrons per RF system will provide enough power to serve these triplets with 200 MW per structure. Combined in pairs, these klystrons can provide four input signals to a "times four" MDLDS with four feeds. A total of 207 such systems, interleaved in 23 sectors of nine systems each, is required for the entire linac (twice as many for the whole collider). This amounts to 1,656 klystrons per linac.

One path to significant further savings is to push the klystron pulse duration towards 3 μs in order to provide an equivalent pulse compression of seven or eight rather than four. In this case, the eight klystrons in each cluster would provide eight independent input signals to a "times eight" MDLDS. With seven feeds per system, 13 sectors could power 2,457 structures from 936 long-pulse klystrons in each linac. Such a "long-pulse" system would mean transporting the power over greater distances, probably requiring larger diameter delay lines to keep losses down. It would also increase the total length of delay line needed. This provides motivation for exploring the possibility of increased multi-moding, beyond two or three modes per waveguide.

6.1.1 Status before the ISG

SLAC had recently demonstrated high-power SLED II RF pulse compression, using highly over-moded waveguide, when the DLDS was first presented by KEK. At that time, SLED had enabled the first linear collider, the SLC, to achieve its energy goal, and SLED II was seen as its logical successor for a long-bunch-train, next generation machine. BPC had been passed over, after an initial high-power prototype, as too expensive and space consuming. The NLC Zeroth-Order Design Report, consequently, offered SLED II as the proposed system, although it was not considered suitable for a 1 TeV upgrade. The DLDS, however, was recognized immediately for its promise of restoring high efficiency in a passive system without the full bulk of the traditional BPC. For the JLC, KEK proposed a DLDS system with three feeds, matched to the klystron performance goals at the time.

When the idea of multi-moding was developed at SLAC, and its feasibility acknowledged, both laboratories turned their sights towards the MDLDS as the most efficient and economical means of delivering the required peak power to X-band linac structures from state-of-the-art klystron tubes. Thus, in the area of RF pulse compression/power distribution, as elsewhere, the period leading up to the formal ISG relationship saw significant convergence between the Japanese and American linear collider designs.

6.1.2 Goals and Progress of the ISG

This dynamic interaction between KEK and SLAC has since been facilitated by the International Study Group meetings, leading to much progress. Prominent examples of successful collaboration include: - multi-moded components based on SLAC RF designs built and cold tested by KEK (see

section 7.5). - a joint mode transmission experiment (see section 7.6).

We are now confident that some variation of an MDLDS should be realizable. There is still work to be done towards achieving this end, but the path has become clearer. Goals for the coming year include:

- building and characterizing RF components

- performing high-power tests on components

- determining experimentally if chokes at flange joints can be eliminated

- developing final system elements

- optimizing system layout

- adapting system to klystron development (long pulse)

- exploring ways of increasing multi-moding

6.2   Principle of DLDS (Delay Line Distribution System)

In the simplest DLDS (Delay Line Distribution System), illustrated in Fig. 6.1 and 6.2, the RF power from two klystrons with independent phasing is combined through a 3-dB coupler. One output port of the 3-dB hybrid is connected, through low-loss waveguide, to a linac feed about one half of the compressed pulse width times the speed of light upstream of the klystrons; the other port is connected to a local feed. The first half of the input RF pulse, of duration equal to the sum of the structure fill time and the bunch train time, is sent to the upstream feed through the delay. The second half of the RF pulse is fed into the linac close to the klystrons, without delay. The delay line introduces a delay time of $T_{\text{delay}} = L/v_g$, and the beam flight time between the two structures is $T_{\text{beam}} = L/c$. These time delays must satisfy the following relation, neglecting delays in the rest of the RF transport system such as the 3-dB hybrid, etc.

$$T_{\text{delay}} + T_{\text{beam}} = \frac{L}{v_g} + \frac{L}{c} = \tau_a \tag{6.1}$$

Here τ_a is the pulse length of the linac operation, which is just the sum of the structure filling time and the duration of the bunch train. It is easily recognized that the timing of the bunch train and the RF pulse must be adjusted to accelerate the beam just as for ordinary linac pulses. Thus, a factor 2 DLDS can be constructed which works equivalently to other factor 2 RF compression systems. The timing relation of this delay line scheme is illustrated in the "train diagram" shown in Fig. 6.2 for the case where the RF pulse from the klystrons is divided into two consecutive RF bins. The most important advantage of this new DLDS pulse compression system is the high energy efficiency which, as mentioned in the previous section, has an intrinsic value (neglecting losses) of 100% [8, 13, 14].
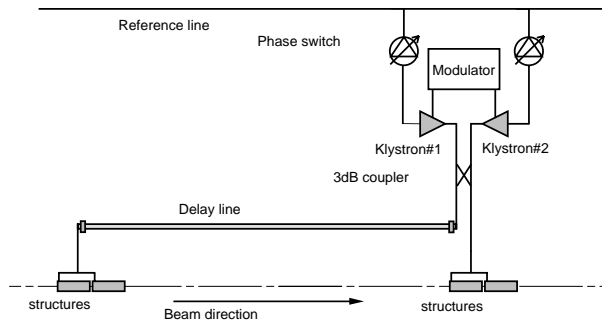
Figure 6.1: *A schematic diagram of the simplest factor-2 delay line distribution system*

In general, this scheme can be extended to increase the combined pulse height by a factor of 2^n as follows. Each of the klystrons in the factor-2 scheme described above, can be replaced by a pair of klystrons combined through a 3-dB hybrid coupler. This new system also works as a factor-2 system, and the remaining 2 output ports of the couplers can be connected to one more 3-dB hybrid coupler which gives an additional factor of 2 DLDS as in Fig. 6.1. This process can be repeated n-1 times to construct the factor-2^n DLDS system.

It should be noted that in this scheme the time domain compression equivalent factor, i.e. klystron pulse length divided by τ_a, can be chosen from 1 to 2^n. A given system is generally specified as a factor $2^n/m$ Delay Line Distribution System ($2^n/m$ DLDS), where 2^n represents the number of independent RF sources, and m represents the time domain compression equivalent factor. In such a system, the remaining $(2^n - m)$ ports are left unconnected to any structure.

6.3 Multi-Moded DLDS

Fig.6.3 shows a schematic of a proposed multi-moded system. Basically, four pairs of klystrons, operating at 11.424 GHz, feed a multi-mode launcher. The launcher then injects one of four modes into a large (12.7cm-diameter) circular waveguide delay line. The choice of mode is controlled by the relative phases between the four RF power sources. The four modes are chosen to minimize the losses in the delay line. These modes are TE_{01}, vertically polarized TE_{12}, horizontally polarized TE_{12}, and TE_{21}. The TE_{21} mode is quite lossy, and hence is extracted from the delay line immediately and converted to the TE_{01} mode in the waveguide that feeds the closest set of accelerating structures. The power carried by any of the other three modes is extracted at the appropriate point and then converted into TE_{01} mode to feed a set of accelerating structures.

The output pulse of the power sources is divided into four time bins, each with duration τ_a. The total RF power supply pulse width is $4\tau_a$. During the first time bin, the phases are adjusted to inject one of the polarizations of the TE_{12} mode. This signal does not get affected by any of the mode
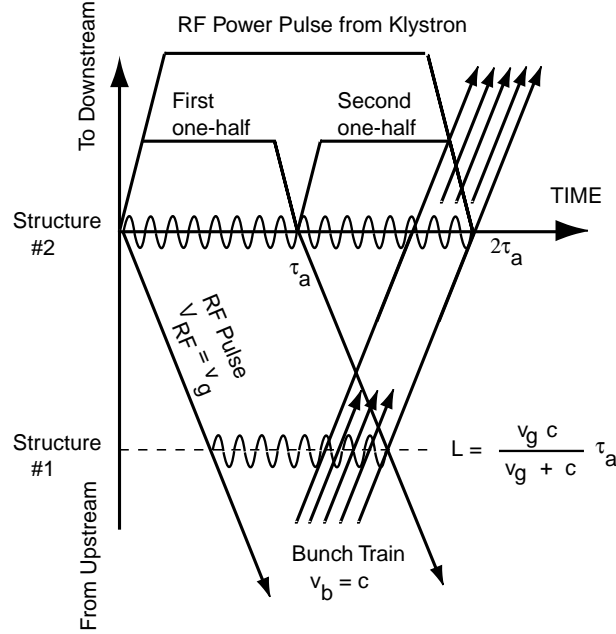
Figure 6.2: *A train diagram of factor 2 DLDS*

extractors. However, after the last mode extractor it gets converted into the TE_{01} mode, thus, feeding the most distant accelerating structure. Then, in the second time bin, the second polarization of the TE_{12} mode is injected. This signal is converted into the TE_{01} mode just after the first extractor. The second extractor extracts this signal. In the third time bin the TE_{01} mode is injected. The first extractor extracts that mode. Finally, in the fourth time bin, the TE_{21} mode is injected and extracted immediately to feed the closest set of accelerating structures. In this manner, each of the four accelerating structure sets will see the combined power from the four power sources during the appropriate time-bins. This is equivalent to a pulse compression system with a compression ratio of four. Since, in this scheme, the electron (or positron) beam and delay line RF power move in opposite directions, the total delay line length required between the feed points to the different accelerating structure sets is $\sim c\tau_a/2$. Here c is the speed of light in free space, with which we approximate the RF group velocity as well as the beam velocity.

In addition to taking advantage of the finite time that electrons and positrons spend traveling between the accelerating structure sets, the multi-moded scheme further reduces the total length of waveguide required by eliminating the shorter delay lines in each system. The power extracted from the RF delay line with the appropriate mode transducer is converted immediately into the TE_{01} mode and fed to three different accelerating structures. The manipulation and feeding is done with circular waveguides that have a diameter of 7.4cm. Each accelerating structure is fed with a different tap-off, a mode transducer from TE_{01} to TE_{10} in rectangular waveguide. Obviously, the first tap-off is a 4.77 dB coupler, the second is a 3 dB splitter, and the third is a low-loss mode converter. Each power source (a pair of klystrons) will produce 150 MW for 1.5 μs. The total amount of power in any time
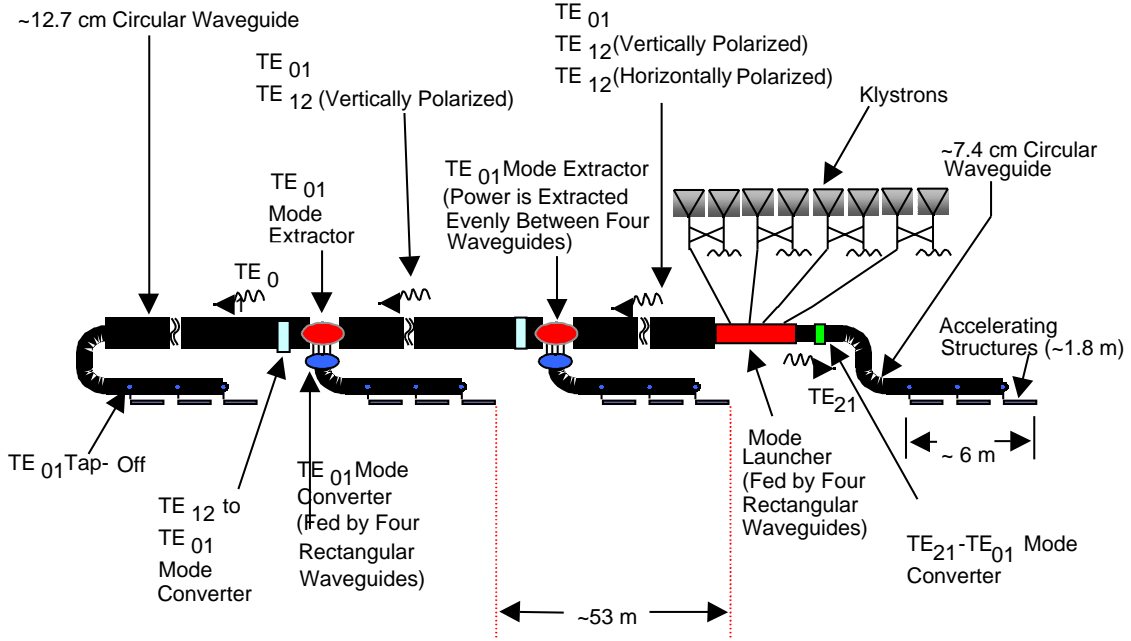
Figure 6.3: *Multi-Moded Delay Line Distribution System*

bin is 600 MW for a duration of 375 ns. One of the design goals is to keep the surface electric field in this RF system below 40 MV/m. The total efficiency of the system should be above 85%.

Because the RF power is being injected at different times into different modes that have different group velocities, one must pay special attention to timing. For each group of accelerating structures to get an RF pulse for a duration at the appropriate time, the following set of equations need to be satisfied:

$$\tau_a = \left(\frac{L_1}{v_{01}} + \frac{L}{c} \right) + (\delta_2 - \delta_1), \tag{6.2}$$

$$\tau_a = \left(\frac{L_2}{v_{01}} + \frac{L}{c} \right) + (\delta_3 - \delta_2) + L_1 \left(\frac{1}{v_{12}} - \frac{1}{v_{01}} \right), \tag{6.3}$$

$$\tau_a = \left(\frac{L_3}{v_{01}} + \frac{L}{c} \right) + (\delta_4 - \delta_3) + L_2 \left(\frac{1}{v_{12}} - \frac{1}{v_{01}} \right); \tag{6.4}$$

where L is the distance between accelerating structure sets, L_1 is the distance between the launcher and first extractor, L_2 is the distance between first and second extractor, L_3 is the length of the delay line after the second extractor, v_{01} and v_{12} are the group velocities of the TE_{01} and TE_{12} modes respectively, and δ_1 through δ_4 are the delays due to the transmission of power from the main RF delay line system to the accelerating structure sets, i.e., the delay through and after the extractors.

There are several choices for the lengths L, L_1 through L_3, and δ_1 through δ_4 that satisfy the above set of equations. An attractive choice is to set L_1 through L_3 equal to L, $\delta_2 = \delta_3 = \delta_4$ and

$$\delta_2 - \delta_1 = L \left(\frac{1}{v_{12}} = \frac{1}{v_{01}} \right) \tag{6.5}$$

This would lead to a fairly symmetric system.

Several ideas for the launcher have been proposed. All of them preserve a fundamental property which is that the launcher has only four inputs and that it has to launch four and only four modes. If this is preserved and the launcher is matched for all four different input conditions, because of unitarity and reciprocity the scattering matrix representing the launcher has to take the following form:

$$S = \begin{pmatrix} 0 & 0 & 0 & 0 & 1/2 & 1/2 & 1/2 & 1/2 \\ 0 & 0 & 0 & 0 & -1/2 & -1/2 & 1/2 & 1/2 \\ 0 & 0 & 0 & 0 & -1/2 & 1/2 & -1/2 & -1/2 \\ 0 & 0 & 0 & 0 & -1/2 & 1/2 & -1/2 & 1/2 \\ 1/2 & -1/2 & -1/2 & -1/2 & 0 & 0 & 0 & 0 \\ 1/2 & -1/2 & 1/2 & 1/2 & 0 & 0 & 0 & 0 \\ 1/2 & 1/2 & 1/2 & -1/2 & 0 & 0 & 0 & 0 \\ 1/2 & 1/2 & -1/2 & 1/2 & 0 & 0 & 0 & 0 \end{pmatrix} \tag{6.6}$$

This form forces the isolation between inputs; i.e., if one of the four power supplies drops out or fails, the rest of the power supplies will not receive any reflected power.

In each launcher design, four rectangular waveguides are coupled to a circular waveguide at four different places $\pi/2$ apart in azimuth. The four waveguides supply equal amounts of power with different phases, and the modes excited are TE_{11}, TE_{21} and TE_{01}. The TE_{11} modes are converted later to TE_{12} modes using a Marié mode converter. A circular waveguide large enough to support the TE_{01} mode will support a set of TM modes and the TE_{31} mode. To avoid exciting these modes, one suggested launcher perturbs the cross section of the circular guide to a quatrefoil, or cross-like shape, thus allowing only four modes to propagate. Another launcher uses longitudinal resonant slot coupling to avoid the excitation of unwanted modes. In both cases, these launchers follow the scheme shown in Fig. 6.4, which consists of two parts: a TE_{21} extractor and a TE_{11}-TE_{01} launcher. The TE_{21} extractor extracts the local TE_{21} mode prior to the launching of the remote modes into the distribution waveguide. With the TE_{21} extracted beforehand, the multi-mode launcher now only needs to launch the two polarizations of the TE_{11} mode and the TE_{01} mode. The TE_{21} extractor has to be transparent to the modes with the TE_{11} and TE_{01} phase configurations, which can then bypass the TE_{21} extractor and be launched by the TE_{11}-TE_{01} mode launcher into the circular waveguide upstream. The TE_{21} local mode extractor and the TE_{11}-TE_{01} launcher in this launcher system are separate components that can be designed and tested separately.

The design of the TE_{01} extractor is quite complicated and will be a subject of further publications. However, a design based on the wrap-around mode converter[6] is possible. In this design a rectangular waveguide is wrapped around the circular guide. The power is extracted using an azimuthal resonant coupling between the two guides. The design is shown in Fig. 6.5.

First, we taper down so that both polarizations of the TE_{12} mode are converted into TE_{11} mode
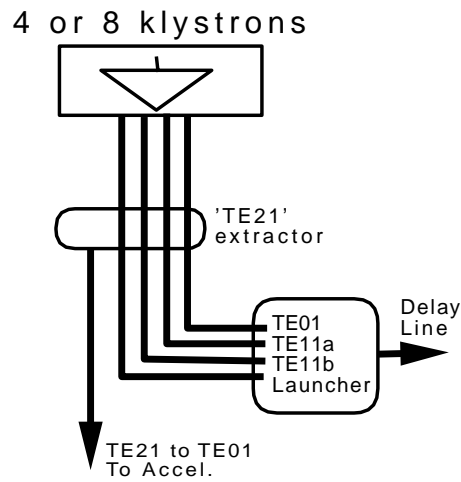
Figure 6.4: *Multi-mode Launcher System.*

using a Marié mode converter. The power is extracted into four different rectangular waveguides using the wrap-around mode converter. The exit end of the wrap-around mode converter is tapered down so that it cuts off the TE_{01} mode, while allowing the TE_{11} modes to go through. In this way a 100 % extraction of the TE_{01} is possible. After the wrap-around mode converter, a serpentine mode converter converts only one of the polarizations of the TE_{11} mode into the TE_{01} mode. The remaining TE_{12} polarization is converted back to TE_{12} through a Marié mode converter. The next extractor extracts the TE_{01} and converts the only remaining polarization of the TE_{11} mode into the TE_{01} mode in a similar manner. Different approaches based on longitudinal resonant coupling are also possible.

After the signal is extracted into four different rectangular waveguides it is injected again into a circular waveguide. The four rectangular waveguides inject signals that are equal in amplitude and phase. If the circular guide is small enough in diameter to cut-off the TE_{41} mode, the only mode that can get excited under this azimuthal symmetry condition is the TE_{01} mode. Matching is accomplished by adjusting the rectangular waveguide size and by the correct positioning of the back wall, which acts as a short circuit at one side of the circular guide.

To taper up the circular waveguide diameter to a value large enough to get into the low loss regime of the TE_{01} mode, we use a compact step-up structure. The diameter of the waveguide is increased in two steps. Although, the final diameter can support the TE02 mode the structure does not excite that mode. In addition it has an excellent match at the operating frequency of the system. This type of taper is possible due to the limited frequency bandwidth requirement of the system.
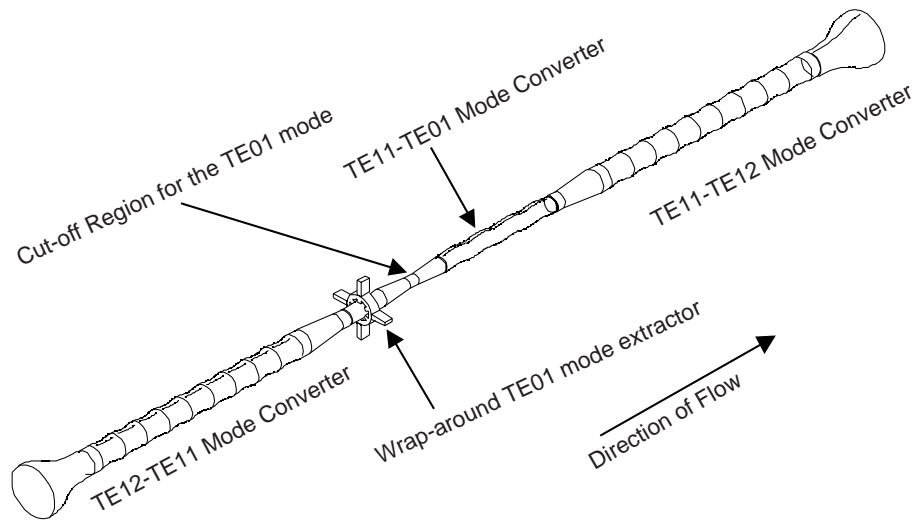
Figure 6.5: *Mode Extractor*

6.4 2×2 **DLDS**

The largest drawback of the original (single mode) DLDS is that it requires long waveguides: a maximum of 17 waveguides run together inside the linac tunnel. A conceptual improvement was proposed by SLAC to further reduce the length of waveguide system by multiplexing several low-loss RF modes in a same waveguide. Thus, the sub-pulses in the distribution waveguide are carried by different waveguide modes so that they can be extracted at designated locations according to their mode patterns. Taking advantage of both the single mode and the multi-mode DLDS, a 2×2 DLDS was proposed at KEK to deliver RF power to four RF clusters. Its scheme is illustrated in Fig. 6.6. It consists of almost identical dual mode DLDS systems with long and short waveguide. Only two modes (TE_{01} and TE_{12} or TE_{11}) are used in each waveguide to minimize the complication caused by handling of multi-modes in one waveguide, while still providing some of the benefit of multi-mode operation by considerably reducing the total length of waveguide. The advantages of 2×2 DLDS can be summarized as:

1. Cost saving: It reduces the total length of waveguide to 2/3 of single mode DLDS

2. High efficiency: The power loss is about 30 % smaller than the 3+1 DLDS (described later).

3. High expandability: It can be easily expanded to feed up to 5-7 RF clusters.

The last advantage is truly beneficial for cutting the construction cost of LC if a long RF pulse (2-3 μs) is available from klystrons in the future.

ISG Progress Report, April, 2000
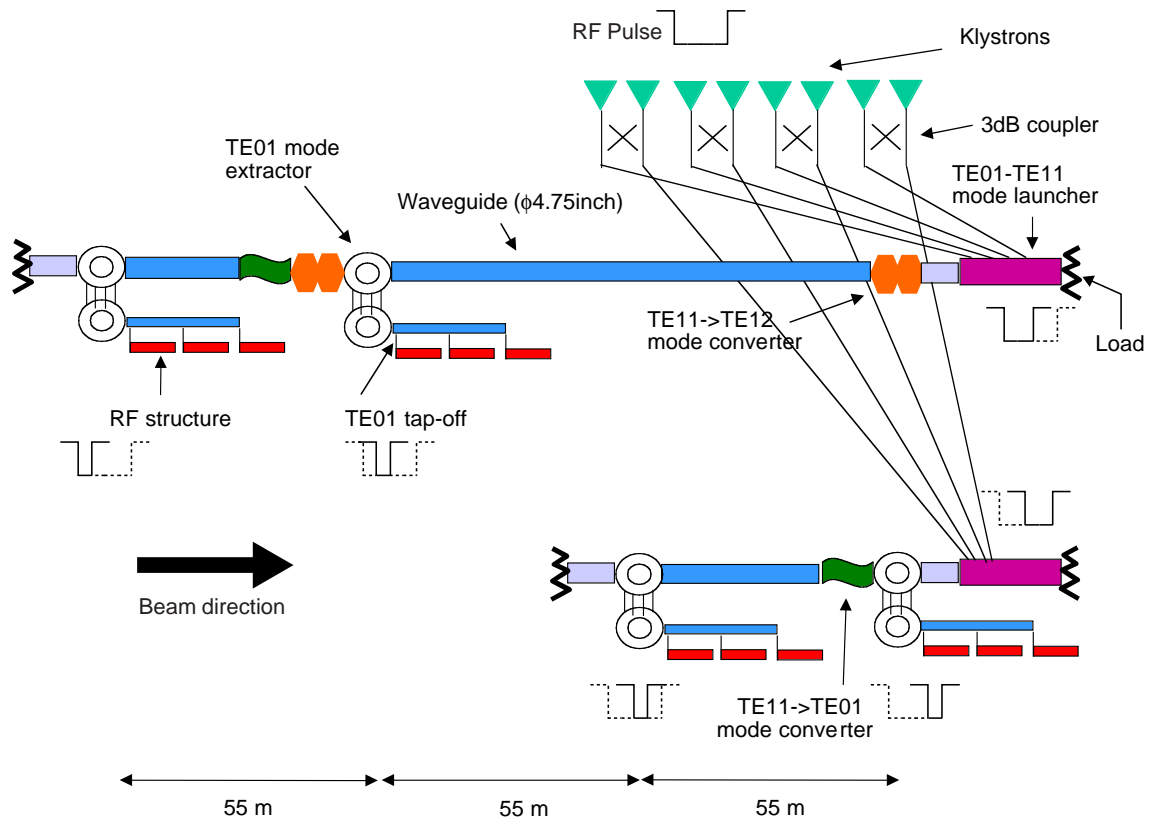
Figure 6.6: *Schematic view of 2×2 DLDS.*

To demonstrate the fundamental principle of the 2×2 DLDS, a cold model of the dual mode DLDS basic unit (almost identical to the system with the shorter waveguide in Fig. 6.6 was manufactured and tested at KEK. The testing results proved that it was plausible to deliver power at different places using different modes with good efficiency (better than 95%).

6.5   Low Power Testing of Components

All components of the 2 mode DLDS basic unit (mode launcher, mode converter and mode extractor) were fabricated and tested[19]. In this test, mode purity of each component at the output port was measured. Fig. 6.7 shows the configuration for each component test.

For all configurations, RF power was launched with the slot-coupled mode launcher. TE_{11} and TE_{01} modes were generated by exciting two or four waveguides at the input of the mode launcher. The RF power from the output port of each component was absorbed with a dummy load. Mode purity was
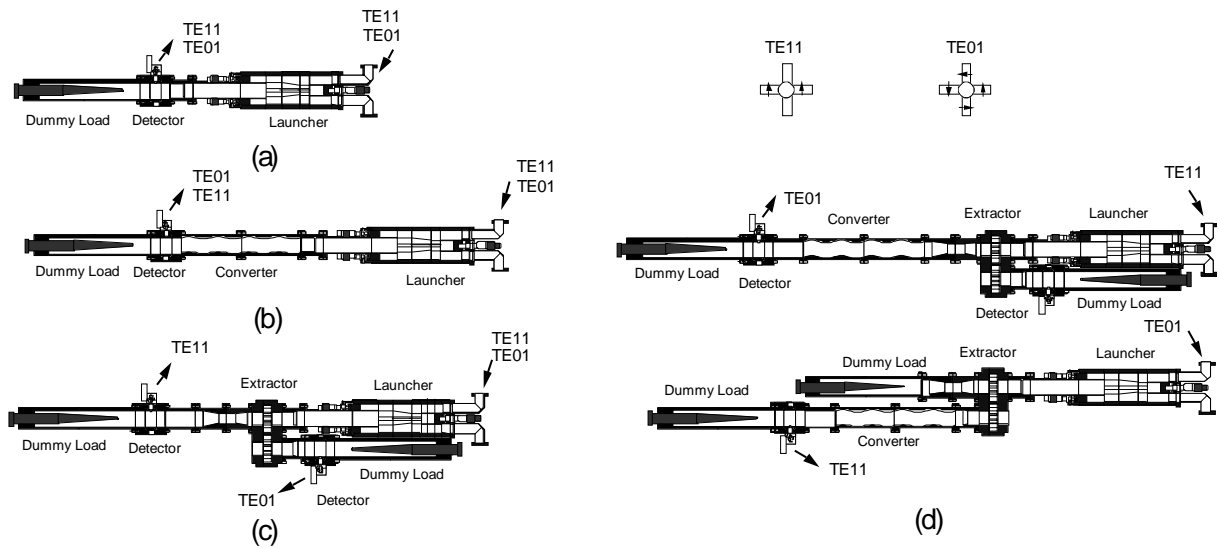
Figure 6.7: *Low power test configuration for DLDS basic unit, (a) mode launcher, (b) mode converter, (c) mode extractor and (d) whole system.*

estimated from the angular distribution of electric field measured with a mode detector composed of cylindrical waveguide, which is rotatable by $180°$, and an antenna. Both a loop antenna and a probe antenna were used for TE_{01} mode and TE_{11} mode, respectively. Fig. 6.8 shows the measured angular distributions for each component (a, b, c) and for the whole system (d).

The mode purity of the mode launcher is fairly good but is not perfect because of an imbalance in the amplitude and phase of the input RF power into the two or four waveguides. The purity of the mode converter is not as good as the mode launcher. The reason for this may be that the small mode impurity from the mode launcher is "enhanced" by the mode converter. On the other hand, the mode purity for the mode extractor is fairly good. The reason of this may be that the mode impurity from the mode launcher is "reformed" by the mode extractor. It can be said that mode extractor worked as a mode filter. The angular distributions of electric field for the whole system were measured with the mode converter in two locations and two orientations: the original one and one rotated by $180°$. The result shows that the TE_{21} mode is mixed during passing through the mode converter. The amount of mixing is a few percent, a value comparable with the HFFS [15] calculation.

The measurement of mode purity was completed successfully. A measurement of transmission will be done in the near future.

6.6   Mode Stability Experiment
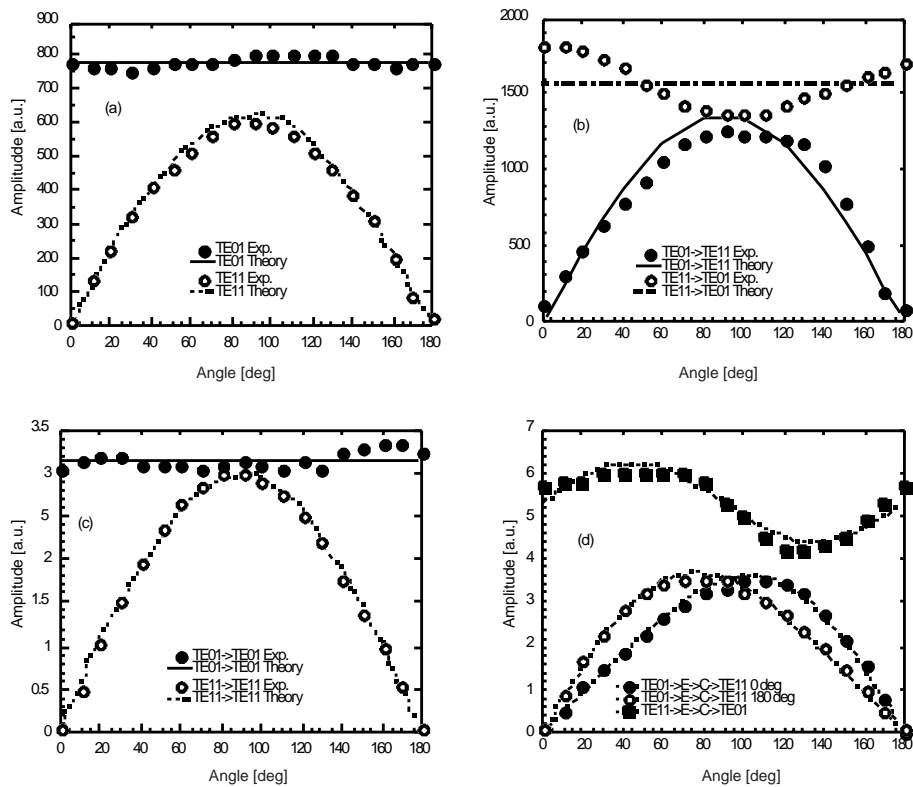
Figure 6.8: *Angular distributions of modes for each components, (a) mode launcher, (b) mode converter, (c) mode extractor and (d) whole system.*

With the use of multiple modes in a single waveguide, the quantity of interest is the attenuation per unit time delay for different modes. The most efficient modes in a delay line of reasonable cross-section are the low-loss TE_{01} and the two polarizations of TE_{12}. We have considerable experience with the former and have recently studied the technical aspects of using the TE_{12} mode. Joint experiments were performed at KEK on a delay line assembled in the ATF linac tunnel. The typical setup is illustrated in Fig. 6.9.

The generation of the TE_{12} mode was accomplished using four different types of mode transducers. These transducers were characterized using a mode analyzer; and their transfer characteristics were measured against each other. The transport line in our experiment was composed of eleven sections of a circular waveguide with a diameter of 12.065 cm. Each section was five meters long, for a total length of 55 meters. The sections were connected using a choked flange. This connection was designed to operate well for both the TE_{01} mode and the TE_{12} mode.

The mode analyzer was installed at the end of the line to measure mode conversion due to this highly over-moded waveguide (102 modes can propagate in this guide.). The resulting spectrum is shown in Fig. 6.11. Fig. 6.10 shows the spectrum of the mode transducer without the transport line. Comparing Fig. 6.11 with Fig. 6.10, one can make the following observations:

1. The angle of rotation of the TE_{12} mode before and after the transport line is almost the same. Furthermore, the level of the circularly polarized component in both cases is very small. Hence one can conclude that there is no significant mode cross polarization mixing. This can be explained by assuming that the circular waveguide that comprises the transport line has a wall displacement with a very small second azimuthal harmonic.

2. In general, mode contamination in all modes has an elevated level is greater after the transport line. However, this is most noticeable in the case of, the TE_{41} mode. The level of this mode has increased from -39 dB to -23.5 dB. This mode has the highest level of all parasitic modes after the transport line. It happens that the TE_{41} mode is virtually degenerate with the TE_{12} mode; the beat wavelength between those two modes is 72.89 m. Combined with the fact that the coupling coefficient between the TE_{12} mode and the TE_{41} is greater than that of the cross polarization coupling coefficient, this indicates that the 3rd and 5th azimuthal harmonics in the waveguide wall displacement play an important role in the transport of signals over the TE_{12} mode.

3. The level of the TE_{13} mode has dropped. It is smaller than the value measured without the transport line and smaller than the mode matching prediction for the mode analyzer. This could be explained by a very small amount of TE_{13} being generated in the transport line. Levels as low as -35 dB interfering out of phase with the contamination generated by the mode analyzer could lead to this effect.

Although mode rotation was not a problem, for completeness, we tested a polarization rotator designed to correct for rotation in the line. We installed the polarization rotator at the beginning of the transport line, rotated the mode transducer 90° to produce horizontal polarization, and then used the polarization rotator to bring it back to the vertical direction. The modal spectrum of this system was quite similar to that shown in Fig. 6.11.

The overall level of the signal received is -0.37 dB, which indicates that approximately 8.5% of the input power has been lost. This cannot be accounted for by the losses in the two mode transducers and the arc-tapers (4.5%), the transmission line losses (theoretically 2.8%), plus mode conversion to TE_{41} mode (0.5%; see Fig. 6.11). One can only conjecture that there are additional losses due to conversion to some TM modes, which were not measured by our mode analyzer.
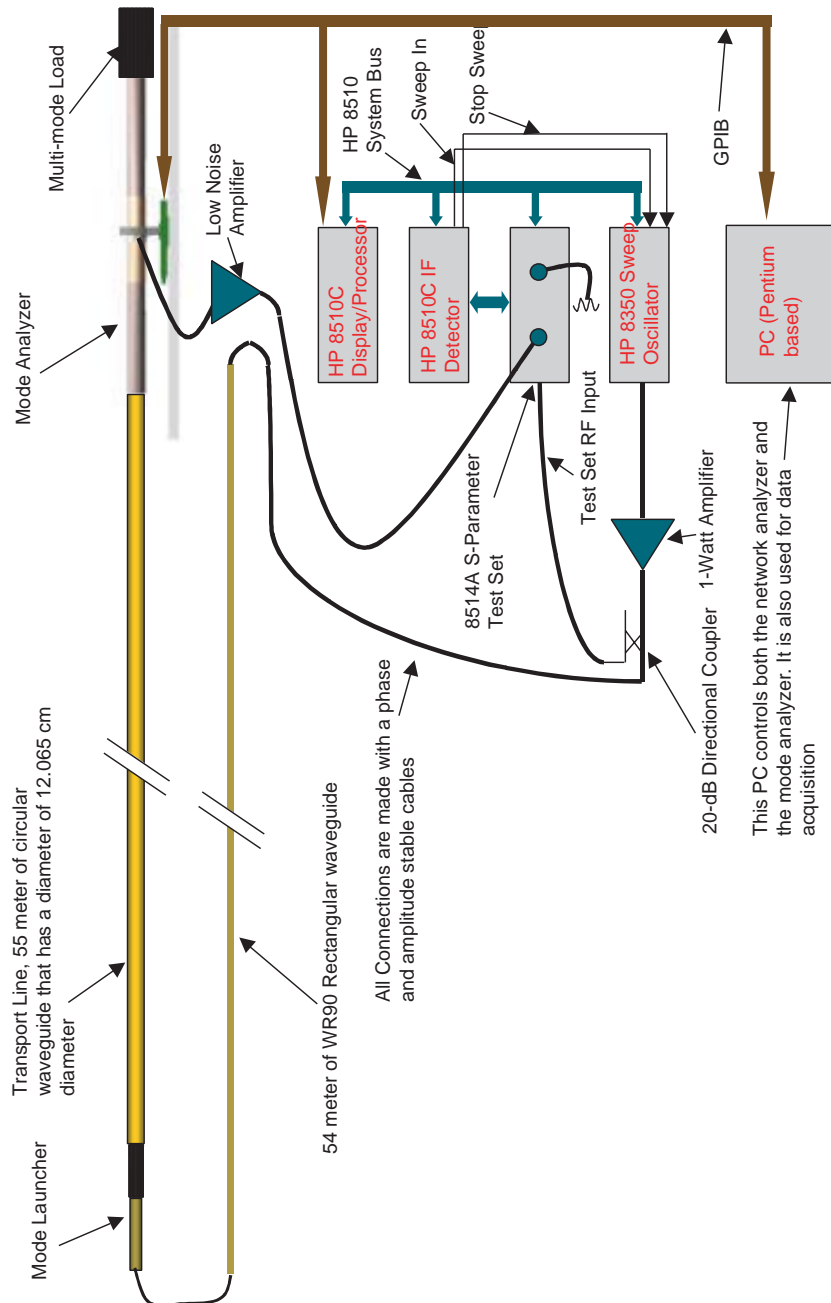
Figure 6.9: *Experimental setup for TE_{12} mode transmission experiment.*
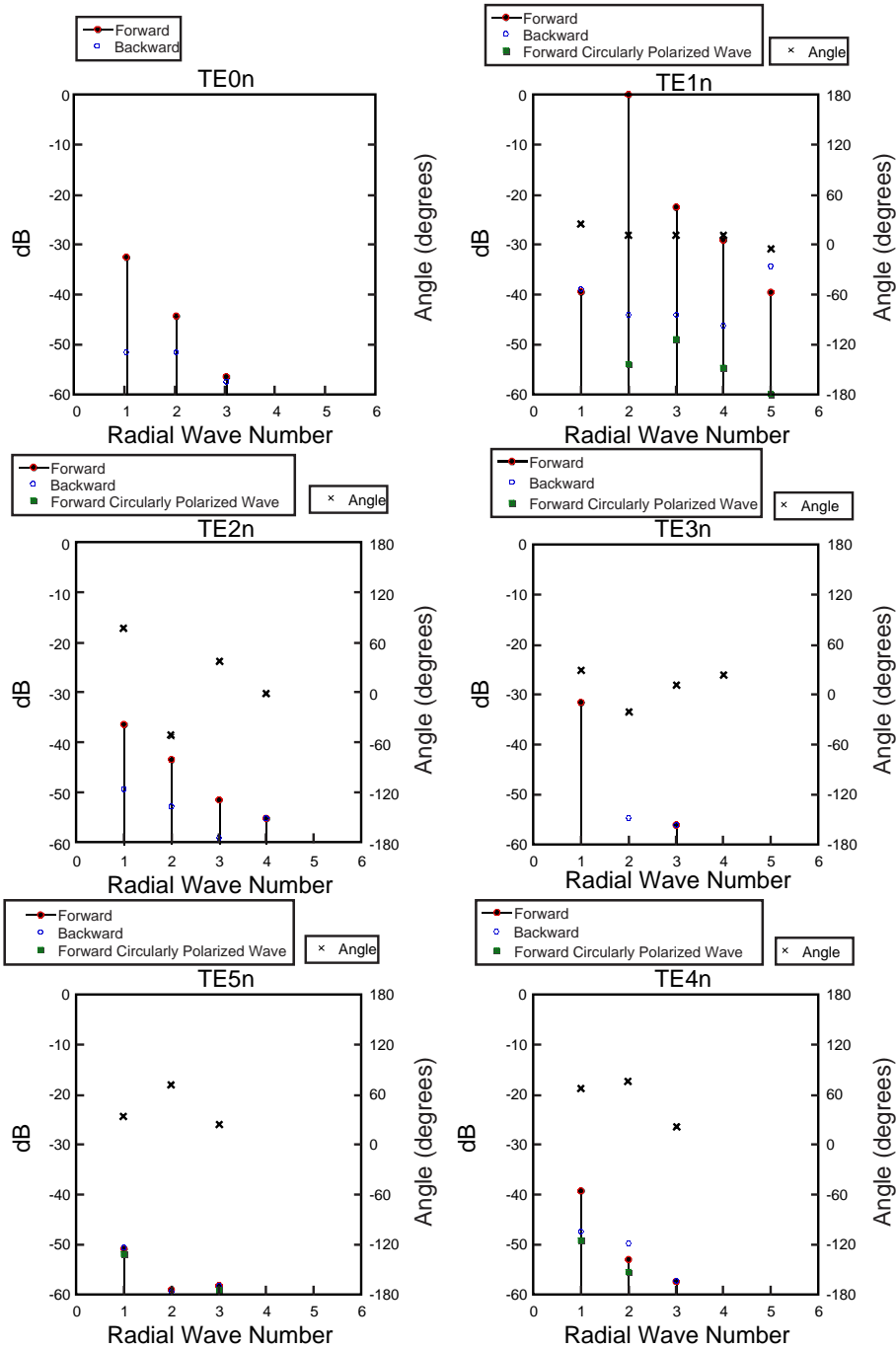
Figure 6.10: *Measured Mode spectrum of the TE_{12} mode transducer. The decomposition is done in terms of a linearly polarized component and a circularly polarized one. The angles in these graphs are the inclination angle of the linearly polarized field component with respect to the vertical direction.*
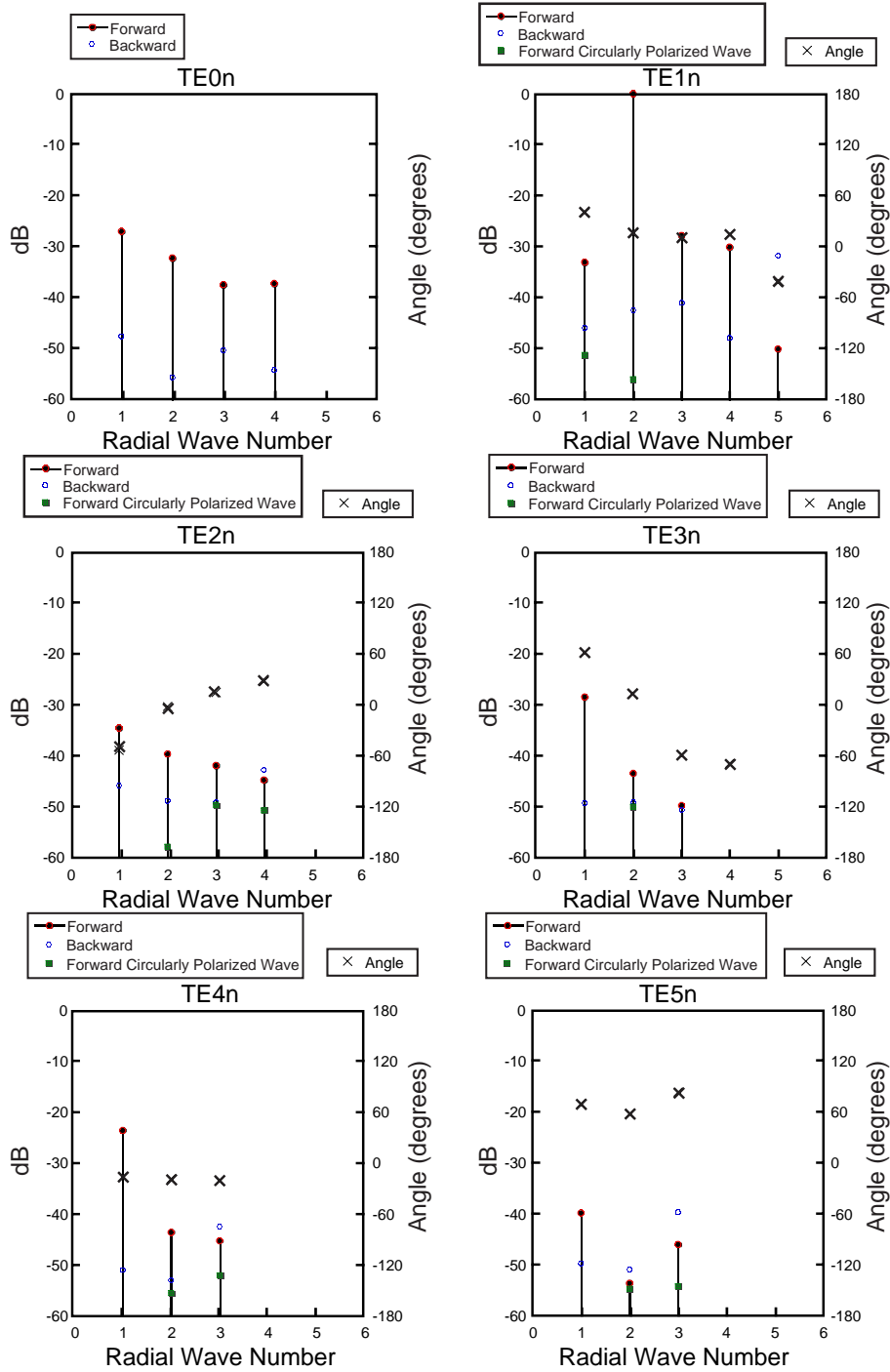
Figure 6.11: *The mode spectrum of after the transport line when the injected signal is the TE_{12} mode.*

6.7   High Power Experiments for NLC:

Several high power RF experiments [6, 18] were performed at SLAC (ASTA) to evaluate the performance of key RF components useful for NLC.

The minimum goal of these experiments was to evaluate proposed high power components at power levels of at least 300 MW. In addition, the KEK M2 accelerating structure was tested to measure dark current production at higher peak fields. To reach the high power levels necessary for the tests, a pair of 50 MW klystrons was operated in parallel, with the combined power serving as the input power for a SLED-II pulse power compressor. This device served to raise the peak power from the klystrons to values approaching 0.5 GW, while reducing the pulse width to 150 ns. (from 1.2 μs). Several design iterations were necessary in order to develop components suitable for the required high peak power.

The key components to be evaluated were high power "dry" loads [16], "flower petal" mode converters (converting rectangular TE_{10} mode to circular TE_{01}) and "magic T" 3 dB hybrids. In addition, the ability to transport high power RF efficiently in over-moded circular waveguide was studied. Early tests showed that the new compact loads could handle the required power levels when operated in groups of four. It was also shown that both the "magic T" and the mode converters suffered serious degradation in performance when operated above 220 MW. New versions of both these components were developed to reduce the peak field levels. In addition, a new type of mode converter, the "wrap-around" mode converter[6], was installed in the system. Fig. 6.12 shows the new setup.

These new components gave a marked improvement in system performance. As the peak power levels approached 270 MW, however, it became clear that the limiting component was one of the SLED-II "flower petal" mode converters. To measure the radiation and to further pinpoint the location of this radiation, measurements were made through a 0.64 cm aperture of a lead-shielded survey meter in 1 cm intervals along the centerline of the mode converter. The results indicate that the radiation is emanating at or behind the coupling irises (or "flower petals").

To estimate the energy of these X-rays, aluminum and copper absorbers of various thicknesses were used to measure the X-ray attenuation coefficient at a power level of 200 MW. Since the slope of the attenuation is quite linear (on a semi-log plot) with absorber thickness, we may assume that the walls of the mode converter selectively removed the low energy portion of the X-ray spectrum leaving only X-rays with the highest energies. Under these assumptions, we find the peak X-ray energy to be near 150 KeV as shown in Table 6.1. For electrons accelerated from rest across the petal gap, this corresponds to a peak gradient of 510 kV/cm.

At the conclusion of this experiment, both delay line mode converters were replaced with wrap-around mode converters and testing resumed. In the next round of experiments we were able to drive the SLED-II system to a power level of 320 MW with no evidence that a power limit had been reached. The X-ray intensity at the "magic T" was similar to previous measurements, and the wrap-around mode converters showed no evidence of excessive radiation (i.e. no greater than WR90 waveguide).
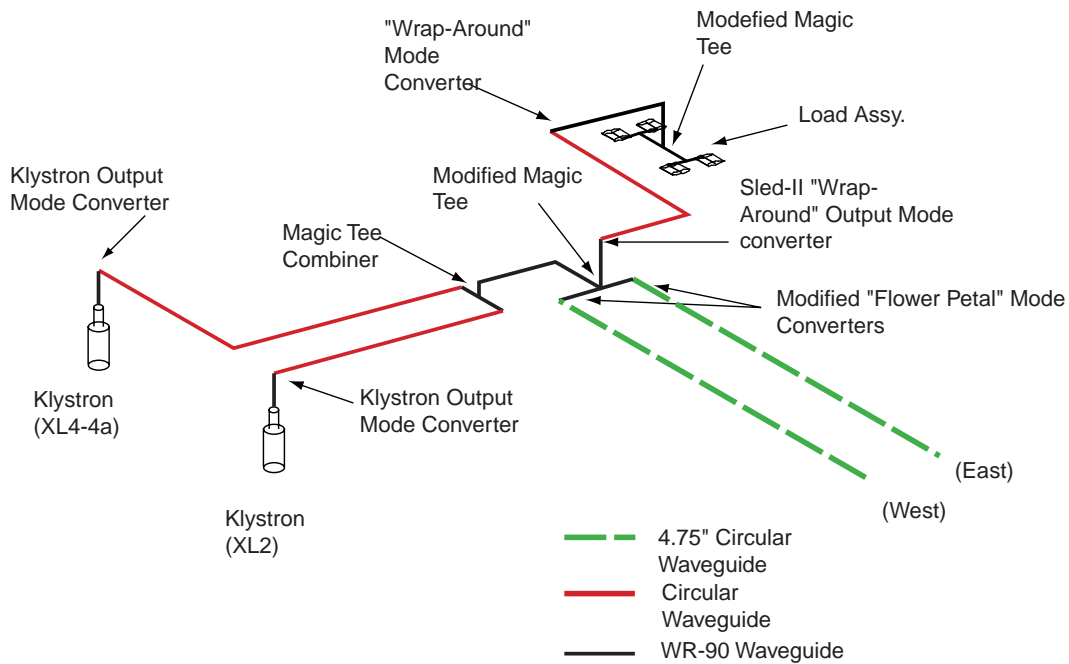
Figure 6.12: *Initial experimental setup*

Absorber	Measured attenuation ($\mathrm{cm^2/g}$)	Tabulated attenuation
Aluminum	0.134	0.134 @ 150kV
Copper	0.191	0.208 @ 150kV
		0.148 @ 200kV

Table 6.1: *Comparison of measured attenuation coefficient with tabulated values near 150 kV.*

Since it was believed that the high radiation levels in the "magic T" was an indication of excessively high fields, two new 3 dB hybrid designs were developed to replace the "magic T"[10]. Simulations indicated that the peak fields in these designs would be significantly lower than those in the "magic T". It was decided to test these devices to a peak RF power of 400 MW. One of these, the "Tantawi" hybrid (two-rung), replaced the SLED-II "magic T" and the other, the "Nantista" hybrid (magic H), was used to split the RF power into a pair of load assemblies. The total load assembly, in fact, was made more robust by doubling its power handling capacity. In addition to the original four "low power" dry loads arranged in parallel, a pair of new "medium power" dry loads was added. In comparison to the original dry loads, these new loads were designed to individually handle at least double the average power with no increase in peak fields.

The goal of 400 MW was reached within 24 hours of operation and was limited in speed only by the general out-gassing and conditioning of the entire vacuum system. Because of the ease in reaching our goal another week was spent in raising the peak power to 485 MW. At this point, both Klystrons were operating at their maximum power and the experiment was successfully concluded. X-ray mea-

surements were taken of the components emitting the most X-rays. The highest readings came from WR-90 waveguide components.

As can be seen, the highest reading came from the SLED-II 55dB output directional coupler. The second highest reading came from a nearby 90° H-plane bend. Of interest is the performance of the new hybrids and the wrap-around mode converters. Both hybrids performed well although the x-ray emission of the "Nantista" hybrid seemed to increase with time. This hybrid was cold-tested again after the high power tests were complete and showed no change in its RF characteristics.

In conclusion, a set of RF components has been designed and tested to peak power levels expected in a future electron-positron linear accelerator.

6.8   Conclusion

As this chapter demonstrates, development of an optimal RF power distribution system for a next-generation linear collider is the object of an on-going, active program of R&D being carried out both autonomously and collaboratively at SLAC and KEK. As plans have evolved, a number of novel, passive waveguide components have been designed. Several have been built, and a few have been tested up to hundreds of MW pulsed power. A list of components designed to date is given in Table 6.2.

We have also experimentally demonstrated the efficient transmission of power in different modes in a large circular waveguide. Multi-moding reduces the amount of highly over-moded delay line waveguide required. Currently both research groups have in mind base designs in which a maximum of two modes are used in a delay line. This allows for simpler mode manipulation and components less likely break down under the very high-power operating conditions. Eight klystrons per RF station will power one MDLDS, which will deliver the combined power, in turn, to four separate accelerator feeds, each serving three structures. The effective pulse compression factor, or ratio of accelerator pulse to klystron pulse, is then four.

Recent modulator designs and klystron goals hold out the promise of longer klystron pulses, on the order of $3\mu s$. This would allow the same set of klystrons to serve up to eight feeds, potentially halving the total number of klystrons required, although doubling the amount of delay line and lowering the efficiency. Further study is needed to determine the actual cost-saving potential of this approach.

In any case, we are convinced that a robust and efficient configuration of MDLDS is achievable and provides the best means of interfacing the klystron designs with the linac designs. For the immediate future, it is essential that we fabricate recently designed components, mostly based on over-moded rectangular waveguide, and test them to high-power and long pulse width. Continued close contact between the two laboratories regarding the RF distribution system and, as appropriate, cooperation and joint effort will help assure that this work proceeds quickly and effectively.

Parts	Designed by:	Built?	Cold Tested?	High-Power?
Multi-Mode Launchers:				
Quatrefoil Launcher [11]	SLAC	N	N	N
Slot Launcher [12]	SLAC	Y(KEK)	Y(KEK)	N
Cross Potent Launcher	SLAC	N	N	N
Kazakov Launcher	BINP / KEK	N	N	N
Mode Converters:				
TE11-TE12 (sausage/taper)	Calabazas Creek	Y	Y	N
TE11-TE12 (sausage)	Calabazas Creek / Univ. of Maryland	Y(KEK)	Y	N
TE01-TE11 (serpentine)	Inst. of Appl. Phys. (Gorky, Russia) / SLAC	Y(KEK)	Y(KEK)	N
TE01-TE11 (zig-zag serpentine)	BINP / KEK	Y(KEK)	Y	N
TE10, TE20 prelauncher 1,2,3	BINP / KEK	N	N	N
TE20, TE30 prelauncher	BINP / KEK	N	N	N
TE20- TE01 (transparent for TE12)	BINP / KEK	N	N	N
TE01-TE12 (serpentine)	Univ. of Maryland / Calabazas Creek	Y	Y	N
TE10-TE12 (compact)	SLAC	Y	Y	N
TE10-TE01 (wrap-around) [6]	SLAC	Y	Y	Y [18]
TE10-TE01 (choke)	BINP/KEK	Y(KEK)	Y	N
Rect. TE10-TE20 (step)	SLAC	N	N	N
Rect. TE20-TE30	SLAC	N	N	N
Rect. TE10-TE20 (jog)	SLAC	N	N	N
Tapers:				
Circ. Step Taper (1.5"-2.93")	SLAC	Y	Y	Y
Circ. Taper (2.0"-4.75")	Calabazas Creek	Y	Y	N
Circ.-Rect. Taper [17]	SLAC	N	N	N
Rect. Height Taper	SLAC	N	N	N
Extractors:				
TE01 Extractor (wrap-around) [19]	SLAC	Y(KEK)	Y(KEK)	N
TE30 Extractor	SLAC	N	N	N
TE10 Extractor	SLAC	N	N	N
Bends:				
TE01-Rectangular Bend	SLAC	Y	Y	Y
TE01-Rect. Bend (modif.)	BINP / KEK	Y	Y	N
Overmoded H-Bend	SLAC	N	N	N
Overheight E-Bend	SLAC	N	N	N
Power Combiner/Splitters:				
Two-Rung Hybrid [10]	SLAC	Y	Y	Y
Magic-H Hybrid [10]	SLAC	Y	Y	Y
Cross Potent Superhybrid	SLAC	Y	N	N
4.8 / 3 dB Tap-offs	SLAC	N	N	N
Resonance H-Hybrid	BINP/KEK	N	N	N
Non-Resonance Bend H-Hybrid	BINP/KEK	N	N	N
Boomerang Superhybrid	BINP/KEK	N	N	N
Other:				
TE12 Choke Flanges	SLAC	Y	Y	N
TE12 Polarization Rotator	SLAC	Y	Y	N

Table 6.2: *DLDS component prototypes built by SLAC, KEK and BINP.*

References for Chapter 6

[1] Z.D. Farkas et. al., "SLED: A Method of Doubling SLAC's Energy," Proc. of the 9th Int. Conf. on High Energy Accelerators, 1976, p. 576.

[2] Z.D. Farkas, "Binary Peak Power Multiplier and its Application to Linear Accelerator Design," IEEE Trans. MTT-34, 1986, pp. 1036-1043.

[3] T.L. Lavine et. al., "High-Power Radio-Frequency Binary Pulse Compression Experiment at SLAC," Proceedings of the IEEE Particle Accelerator Conference, San Francisco,1991, pp. 652-654.

[4] Z.D. Farkas et al., "Two Klystron Binary Pulse Compression at SLAC," presented at the 1993 Particle Accelerator Conference (PAC93), Washington, D.C., May 17-20, 1993; SLAC-PUB-6100.

[5] P.B. Wilson, Z.D. Farkas, and R.D. Ruth, "SLED II: A New Method of RF Pulse Compression," Linear Accel. Conf., Albuquerque, NM, Sept. 1990; SLAC-PUB-5330.

[6] Sami G. Tantawi et al., "The Generation of 400-MW RF Pulses at X Band Using Resonant Delay Lines," IEEE Trans. MTT, vol. 47, no. 12, December 1999, p. 2539-2546; also in SLAC-PUB-8074.

[7] S.G. Tantawi, et. al, "Active RF Pulse Compression Using Switched Resonant Delay Lines," Nucl. Inst. and Meth, A, Vol. 370 (1996), pp. 297-302; Also in SLAC-PUB 6748.

[8] H. Mizuno and Y. Otake; "A new RF power distribution system for X-band linac equivalent to an RF Pulse compression scheme of Factor 2n";Proceedings of the 17th International Linac Conference, Tsukuba, Japan, August 21-16 1994: P-463.

[9] S.G. Tantawi et al., "A Multi-Moded RF Delay Line Distribution System for the Next Linear Collider," proc. of the Advanced Accelerator Concepts, 1998, pp. 967-974.

[10] C.D. Nantista et al., "Planar Waveguide Hybrids for Very High Power RF," presented at the 1999 Particle Accelerator Conference, New York, NY, March 29-April 2, 1999; SLAC-PUB-8142.

[11] K. Eppley, Z. Li, R. Miller, C. Nantista, S. Tantawi, N. Kroll, "A Four Port Launcher For A Multimode DLDS Power Delivery System," EPAC98

[12] Zenghai Li, Sami Tantawi, Kwok Ko, "Mode Launcher Design for the Multi-moded DLDS," EPAC98

[13] *JLC Design Study*, Chapter-10 "X-band main linacs: RF power generation and delivery"; KEK report 97-1, April 1997, P335.

[14] H. Mizuno; "RF pulse compression for linear colliders," Proceedings of the 19th International Linac conference, Chicago, Illinois, U.S.A., August 23-28, 1998: P737.

[15] The HP High Frequency Structure Simulator, Version 5.4, copyright 1996-1999 Hewlett-Packard Co.

[16] Sami G. Tantawi et. al, "Compact X-band High Power Load Using Magnetic Stainless Steel," Proc. IEEE International Conference on Particle Accelerators, Dallas, Texas, May 1995, p. 2132-4.

[17] S.G. Tantawi et al., "RF Components Using Over-Moded Rectangular Waveguides for the Next Linear Collider Multi-Moded Delay Line RF Distribution System," presented at the 1999 Particle Accelerator Conference, New York, NY, March 29-April 2, 1999.

[18] A.E. Vlieks et al., "High Power RF Component Testing for the NLC," presented at the 19th International Linear Accelerator Conference (LINAC 98), Chicago, Illinois, August 23-28, 1998.

[19] T. Kobayashi et al., "Cold Model Tests of the Multi-Moded DLDS for an X Band Linac," (in Japanese) The 24th Linear Accelerator Meeting in Japan, July 1999; KEK-PREPRINT-99-41.

Authors and Major Contributors of Chapter 6

- Y. H. Chin

- K. Fant

- Z.D. Farkas

- H. Hayano

- S. Kazakov

- N. Kroll

- Z. Li

- H. Mizuno

- S. Tantawi

- N. Toge

- C. Nantista

- A. Vlieks

- V. Vogel

- S. Yamaguchi

- J.Q. Wang

- P. Wilson

Accelerating Structure

Contents

7.1 Introduction

7.1.1 Performance Requirements and Solutions

The function of an accelerating structure is to provide the beam particles with a series of resonant cavities where they are accelerated through the interaction with the RF field. Both the JLC and NLC R&D efforts have focused on main linacs whose accelerating structures are made of room temperature copper.

As frequently emphasized, the critical requirements for the next generation of linear colliders are high luminosity and high RF efficiency[1, 2]. In practical terms this means that the accelerating structures in the main linacs of the JLC/NLC have to provide up to $50 \sim 70$ MV/m[3] of acceleration, while controlling the short and long range transverse wakefields to preserve the very low emittance of the multi-bunch beams. Deflecting modes must be suppressed to a level where the wake function remains below 1 V/pC/mm/m. Otherwise, the coupling of the bunches in a multi-bunch train will resonantly amplify any betatron motion, resulting in beam breakup (BBU).

The suppression of transverse wakefields in accelerating structures built with normal temperature copper is usually accomplished by using the following techniques:

1. Mode detuning, where the frequencies of the lowest (and strongest) band of dipole modes are systematically varied along the series of cells. The variation is such as to produce a Gaussian distribution in the quantity: "the mode density" × "the mode coupling strength to the beam." With this detuning, the modes excited by off-axis particles add in a deconstructive manner, and lead to an approximately Gaussian fall-off in the net wakefield that is left after each bunch.

2. Damping, which is achieved by introducing some number of single-moded waveguides (manifolds) that are running parallel to the structure and that couple to the cells through slots. Whenever the cell-to-cell variation of the excited mode matches that of the manifold mode, a power flow takes place from the cell to the manifold. By terminating into matched loads, the mode Q values can be suitably reduced. Depending on the geometry choices of manifolds and slots, a varying degree of damping can be accomplished at the cost of a varying degree of complexity in fabrication and assembly. It is also possible to introduce pieces of absorbing material within individual cells to further reduce the mode Q values.

7.1.2 Historical Background

An active collaboration between KEK and SLAC on the development of X-band accelerating structures began more than 10 years ago, well before the signing of the ISG agreement. Various types of accelerating structures have been built as either joint or parallel efforts. Exploration of an accelerating

structure design with pure detuning started in $\sim$ 1990. Several prototype structures were built based on the detuning design[4, 10, 11]. In this period, SLAC chose a structure design with 1.8 m length and a 61 mm outer diameter, while the KEK design had 1.3 m length and an 80 mm outer diameter.

The wake function of a pure detuned structure (DS) exhibits a recurrent behavior as a function of the time after the passage of the initial bunch of particles (Fig. 7.1). This is because the mode distribution within a structure, which is made up of a finite number of cells, has to be discrete. One possible solution, which was pursued by KEK, is to use a set of four structures as a group where each structure consisted of $\sim$ 150 cells with slightly offset distributions of the dipole modes. This has the effect of making the mode distribution much denser, which keeps the recoherence of the wakefield at an acceptable level for the entire duration of the multi-bunch beam pulse. Another solution, which was pursued by SLAC, is to introduce a moderate damping of the wakefields by adding four manifolds which couple to the cell via thin slots. This scheme is called the damped detuned structure (DDS).

For the first DDS prototypes (DDS1 and DDS2), KEK provided SLAC with machined copper disks for assembly into SLAC structures. SLAC provided the ASSET test site which has been used by KEK, SLAC and recently also CERN to make beam measurements of the wakefield characteristics of structures. SLAC also provided the necessary assistance in data acquisition and analysis for the ASSET tests. Hence, while the collaborative relationship continued between the two laboratories, the efforts proceeded somewhat in parallel.
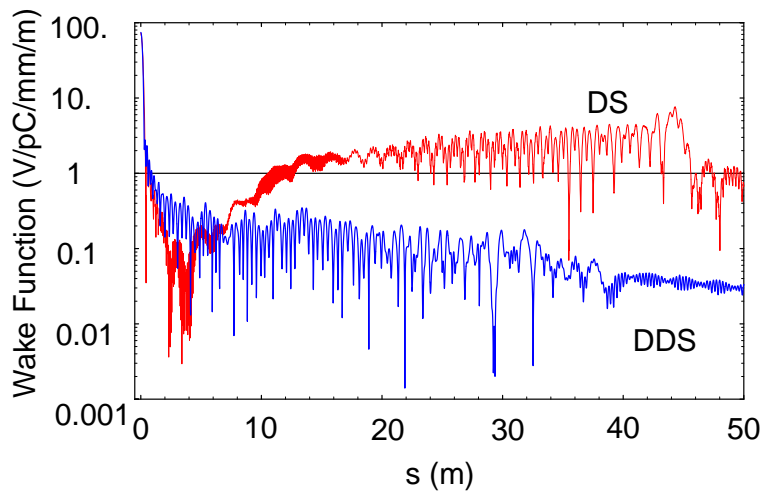
Figure 7.1: *Calculated wakefield profiles of detuned structure (DS) and damped-detuned structure (DDS).*

By around early 1998, it had become reasonably clear that either the DS or DDS design, with suitably aggressive efforts, could lead to a viable accelerating structure that would satisfy the design requirements of the X-band main linacs for JLC or NLC.

At the same time, it also became rather clear that combining the expertise of both KEK and SLAC into a unified development effort could greatly expedite the R&D progress of both groups. SLAC had a

Structures Name	75cm	DS1	DS2	DDS1	DDS2	DDS3	RDDS1	M2
Structures Type	Constant Impedance	Detuned	Detuned	Damped Detuned	Damped Detuned	Damped Detuned	Damped Detuned	Detuned
Length(m)	0.75	1.8	1.8	1.8	1.8	1.8	1.8	1.3
Number of Cells	86	206	206	206	206	206	206	150
Cell Shape	DLWG	DLWG	DLWG	DLWG	DLWG	DLWG	RDS	DLWG
Phase Advance Per Cell	$2\pi/3$	$2\pi/3$	$2\pi/3$	$2\pi/3$	$2\pi/3$	$2\pi/3$	$2\pi/3$	$2\pi/3$
HOM Manifold Shape/ Size(mm)	N/A	N/A	N/A	Rect./ 5x11.0 -5x9.8	Rect./ 5x11.0 -5x10.0	Rect./ 5x11.0 -5x10.0	Circular/ Diameter 9.6-7.3	N/A
Iris Diameter, 2a(mm)	8.56	11.43-7.86	11.43-7.86	11.43-7.86	11.43-7.86	11.43-7.86	11.21-7.77	10.46-7.34
Cell Diameter, 2b(mm)	21.58	22.87-21.39	22.87-21.39	22.87-21.39	22.87-21.39	22.87-21.39	24.04-22.16	22.48-21.34
$<a>/\lambda$	0.163	0.180	0.180	0.180	0.180	0.183	0.179	0.166
Disk Thickness, Web/Tip(mm)	1.46	1.0-2.0	1.0-2.0	1.0-2.0	1.0-2.0	1.0-2.0	0.8/1.2-1.4/2.2	1.2 / 2.4
Filling time, T_f (ns)	52	100	100	100	100	95	104	106
Shunt Imperdance r(MΩ/m)	88.0	67.5 - 88.0	67.5 - 88.0	65.7 - 84.2	65.7 - 84.2	65.7 - 84.2	77.1 - 101.8	72 - 80
Group Velocity (v_g/ c)	0.048	0.118 - 0.03	0.118 - 0.03	0.118 - 0.03	0.118 - 0.03	0.118 - 0.03	0.111 - 0.029	0.098 - 0.02
$<Q>$,Fundamental Mode	~7000	~7030	~7030	~6780	~6780	~6800	~7810	~6400
$<Q>$,Lowest Dipole Band	~6500	~6500	~6500	~1000	~1000	~1000	~1000	~6500
Lower Dipole Band Detuning, $\Delta f_{1,tot}$ /$<f_1>$	N/A	10.1% dn/df$_1$ (4σ)	10.1% dn/df$_1$ (4σ)	10.1% dn/df$_1$ (4σ)	10.1% dn/df$_1$ (4σ)	10.159% kdn/df (4.78σ)	11.25% kdn/df (4.75σ)	11.20% dn/df (5 σ)
Detuning Standard Deviation, σf_1/$<f_1>$	N/A	2.5%	2.5%	2.5%	2.5%	2.125%	2.368%	2.240%
Attenuation,τ	0.267	0.505	0.505	0.533	0.533	0.508	0.483	0.609
Ep/Ea	2.3	3.06-2.10	3.06-2.10	3.06-2.10	3.06-2.10	3.06-2.10	3.00-2.10	2.92-2.02
Machining Method	Single Diamond	Regular	Single Diamond	Single Diamond	Single Diamond	Single Diamond	Single Diamond	Single Diamond
Cell Joint Method	Nested Brazing	Stacks, Nested Brazing	Stacks, Nested Brazing	Stacks, Diffusion Bonding	Stacks, Diffusion Bonding	Section, Diffusion Bonding	Section, Diffusion Bonding	Section, Diffusion Bonding
Completion Time	6/1993	1/1994	11/1996	7/1996	4/1997	10/1998	Spring 2000	7/1996
Wakefield Measurement		ASSET 3/1994		ASSET 8/1996		ASSET 11/1998		ASSET 8/1996
Power Needed for $<E_a >$=50 MV/m	52.2	88.8	88.8	89.8	89.8	94.5	82	61
Operated E-field $<E_a>_{max}$(MV/m)	79	68	50	68	50	N/A	N/A	85

Table 7.1: *Characteristics of major prototypes of the X-band accelerating structure, which have been built by the year 2000.*

major group of experts on the electrical design of accelerating structures, and a strong engineering team with much experience with mechanical and RF measurements, and with brazing. KEK had developed a laboratory with ultra-precision lathe and milling machines, and had gained a substantial amount of experience with the process of diffusion bonding and with mechanical measurements. Table 7.1 tabulates representative prototype accelerating structures that have been built at SLAC and KEK.

Fig. 7.2 shows the genealogy of several of the prototypes that led up to the latest RDDS1 structure.
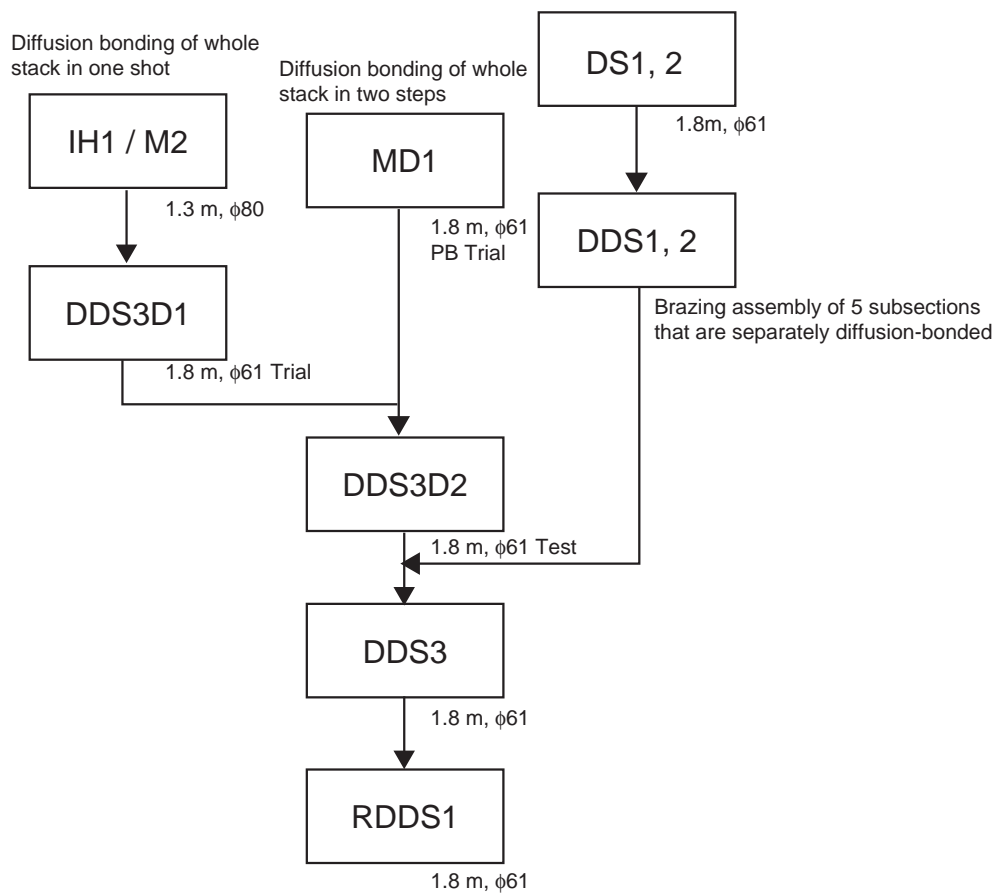
Figure 7.2: *Genealogy of prototype accelerating structures which have been built at KEK and SLAC. Numbers within parentheses below some prototypes indicate the section numbers where some related discussions appear.*

7.1.3   Summary of ISG Activities on R&D of Structures

The ISG agreement between SLAC and KEK had a major impact on the accelerating structure development. It gave both SLAC and KEK the opportunity to reexamine research strategies and the specifics of the collaborative work. Major research activities that took place at SLAC and KEK under

the ISG agreement are summarized below:

1. A joint task force was formed to build and test the 3rd DDS prototype (DDS3) based on a SLAC design completed in September 1997, prior to the signing of the ISG MOU. SLAC developed the electrical design for the copper disks which were then fabricated by LLNL, diffusion bonded by KEK, and brought back to SLAC for final assembly and wakefield measurements. The DDS3 was built and tested at ASSET with encouraging results.

2. After considerable discussion, agreements were made to unify the design parameters of the accelerating structures to be developed for both NLC and JLC. This is detailed in Chapter 2 of this report.

3. In 1998 KEK and SLAC agreed to jointly develop a new, damped detuned structure with optimized rounded cavities (RDDS). SLAC developed the electrical design of the first prototype (RDDS1). KEK fabricated the copper disks, assembled the structure and performed the diffusion bonding. The structure was then shipped to SLAC for final assembly work in preparation for wakefield measurements now planned for Spring of 2000.

The following sections describe some highlights from the activities on DDS3, RDDS1 and high power testing of accelerating structures that were conducted within the ISG collaboration.

7.2   Electrical Design of Accelerating Structure

7.2.1   Introduction

This section describes in detail the research steps that were followed in establishing the electrical design of an accelerating structure. The emphasis is on RDDS, the Rounded Damped Detuned Structure, which is the latest design adopted by the ISG collaboration. Design considerations for previous models are treated in [1, 2] and elsewhere.

As stated earlier, the primary technique we have chosen to control long range dipole wakefields is detuning. In a simplified view, our structure can be considered to be 206 cells or resonant circuits, each of which will ring at its characteristic dipole frequency if driven by a delta function bunch of electrons passing through it off center. If each cell has a different frequency, then they will get out of phase with each other, and later bunches will see an integrated transverse kick, which is much smaller than the sum of the amplitudes of all the cells.

We have chosen a transverse impedance density, which is a truncated Gaussian function of frequency as shown in Fig. 7.3. It is because that produces an initial falloff of the wakefields which is a Gaussian
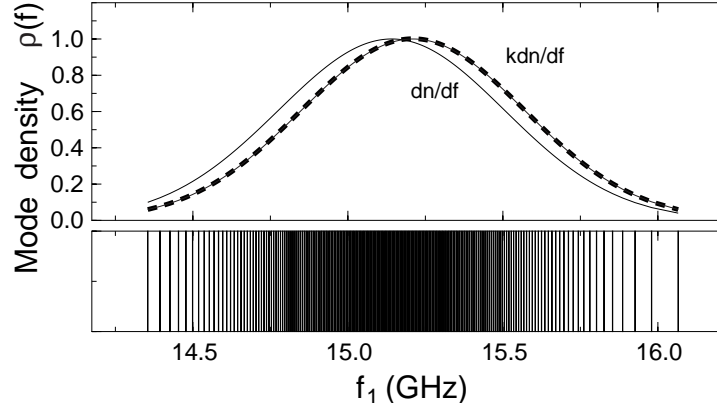
Figure 7.3: *RDDS structure dipole spectrum. $K\mathrm{d}n/\mathrm{d}f$ is the density of the transverse kick factor. $\mathrm{d}n/\mathrm{d}f$ is the modal density.*

function of time. The width of the Gaussian in time, σ_t, is equal to the reciprocal of the width of the Gaussian in the frequency domain, σ_w. However, the actual picture is more complicated, because the Gaussian dipole impedance function is not a smooth curve; rather, it is made up of 206 discrete resonances and thus the distribution fall off ends and a recoherence begins when $t = 1/\Delta f$, where Δf is the space between adjacent resonances.

There are two fixes for this problem. One is to decrease Δf by having more cells in each structure, or by having several structures included in the same Gaussian distribution. The other fix, which we have chosen, is to increase the width of the resonances through damping so that they overlap and, ideally form a smooth curve. The damping can be done locally by damping each cell. In this case the damping can be quite strong, causing the fields to decay rapidly and monotonically.

We have chosen to damp the resonances by coupling every cell (except for a few at each end) to 4 damping manifolds. These are single mode waveguides which run the length of the structure and are spaced every 90 degrees of azimuth around the cells. Coupling slots couple each cell to each of the four manifolds. The damping manifolds also provide position monitor information for the structure. Since the dipole frequencies vary monotonically from about 14.3 GHz at the input end to about 16.1 GHz at the output, a frequency filter on the output from the damping manifolds can give good longitudinal resolution. The transverse resolution can be a few micrometers. The manifold damped structure has been discussed in detail by R.Miller et al[5]. To get an accurate calculation of the wakefield it is necessary to include the cell to cell coupling for at least the lowest two dipole bands. This has been done with an equivalent circuit analysis, which will be discussed later.

The manifold damping has several advantages over local damping:

1. The damping manifolds provide position monitor information from the ports localized at the output end of the structure.

ISG Progress Report, April, 2000

2. It is easier to keep degradation of the Q_{acc} value small.

3. Only 4 lossy ceramic loads are required: one at the downstream end of each manifold, while the locally damped structure has four loads for each cell.

4. The manifolds improve the longitudinal vacuum conductance of the structure.

The manifold damping also has several disadvantages as compared with local damping:

1. The damping manifolds require a very good match. A VSWR as small as 1.05 produces a non negligible degradation of the wakefield suppression.

2. Only rather weak damping can be used. With heavier damping the wakefields get worse with the Q's varying dramatically from mode to mode.

3. Because of items 1 and 2, it is difficult to achieve monotonically decreasing wakefields.

4. Since the damping must be rather weak the dipole frequency error tolerances are tighter than for a locally damped structure.

In spite of the disadvantages, it appears possible to design a structure with manifold damping which suppresses the wakefields by more than a factor of 100. Thus it does not cause beam breakup for NLC/JLC parameters, and has the very desirable integrated beam position monitor.

7.2.2 Basic Structure Parameters

The design of a linear accelerating structure involves compromises to best satisfy a number of conflicting requirements. Chapters 2 of this Report presents extensive discussions on these issues. In a shorter summary, we would like to have a filling time of about 120 ns to take advantage of the high Q obtained with our improved rounded cell profile. However, to do so would require reducing the beam aperture and it would result in larger short range dipole wakefields.

Alternatively, we might make the structure longer and keep the same average iris size. However, there are concerns over the difficulty of maintaining the very tight cell alignment and bowing tolerances required to get acceptable dipole wakefields during the assembly of a longer structure. Thus the present design has a structure length of 1.8 m and a filling time of 100 ns which gives an attenuation through the structure of about 0.5 nepers.

7.2.3 Design Procedure

The design procedure can be broken down into 6 steps.

1. We pick a desired synchronous frequency density distribution. Up to now we have used truncated Gaussian distributions such that the Fourier transform of the Gaussian in the time domain falls

by a factor of about 100 in 1.4 nanoseconds (the shortest period between bunches which we anticipate for JLC/NLC). Using a 2-D code, Omega2, the parameters (a, b) for all the cells are calculated to realize this frequency distribution of the dipole-mode, while maintaining the canonical accelerating mode frequency constant across the entire structure. In addition, the parameters r_a and t are varied along the structure to detune the third- and sixth-band dipole mode frequencies. The disk thickness t is kept at least 0.8 mm to retain the strength of the disks.

2. Using a 3-D field solver (typically MAFIA[6]) we calculate 5 representative cells whose synchronous frequencies in a periodic structure are uniformly distributed over the desired frequency range.

3. We calculate the dispersion diagrams for each of these cells in a periodic structure including the manifold and the lowest two dipole bands.

4. We fit the dispersion curves for each cell using 8 or 9 equivalent circuit parameters for the 3 coupled periodic structures (2 dipole periodic structures: a TE and a TM mode plus the manifold) and the intercoupling constants[7]. The equivalent circuit is shown in Fig. 7.4. The matrices used in analyzing the circuit are inverted using sparse matrix procedures. Solving for the dipole impedance as a function of frequency over the bandwidth of interest (about 15 %) takes about 1/2 hour on a modern desktop computer.

5. We then assume that these circuit parameters are appropriate for these same cells in an adiabatically tapered structure. The parameters of all the intermediate cells are obtained by interpolation from the 5 calculated cells.

6. The couplings between the damping manifolds and the cells are adjusted to optimize the wakefields.

7.2.4   Cell Profile Optimization

Although standing wave linear accelerators have for many years used curvilinear cell profiles to optimize shunt impedance, most traveling wave linear accelerators have used disk loaded waveguides with flat disks and cylindrical cells. For more efficient use of RF power to create the accelerating field, the NLC/JLC design has now chosen what is called the Rounded Damped Detuned Structure (RDDS)[8]. Cross-sections of the original flat disk (DLWG) and improved rounded design (RDS) are shown in Fig. 7.5.

The average improvement in shunt impedance is about 15 %. For vanishingly small currents and equal attenuation through the structure this would save 15 % in power, or 7.5 % in both power and overall length. However, with the present design parameters the accelerator is operating at about 40 % efficiency, i.e. 40 % of the power (in steady state) goes into the beam. So ideally the saving would be 0.6×15 % or 9 %. In reality the improvement is somewhat less because we cannot lengthen the filling time to keep the attenuation constant and thus take full advantage of the 12.5 % improvement
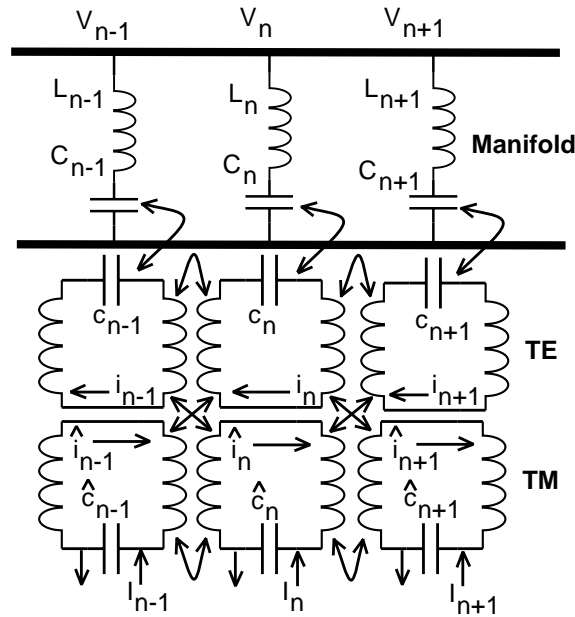
Figure 7.4: *Circuit model for DDS structures.*
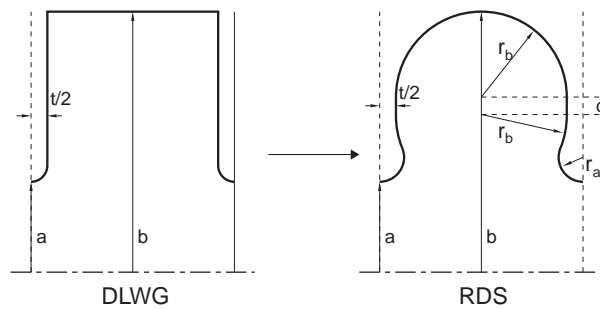
Figure 7.5: *Cell shapes for different disk loaded waveguides.*

in Q. To increase the filling time would require decreasing the iris radius a which increases the short range wakefield by an unacceptable amount. With the filling time unchanged at 100 ns, the saving in power for the rounded design is 5.5 %.

7.2.5 Determination of Final Dimension Table

While the calculation of resonant frequencies of accelerating cells appears to be a matter of solving Maxwell's equations, and thus a purely computational problem, in practice it is not a straightforward procedure. This is because of various errors that creep in due to numerous approximations used in the calculations, effects of skin depth and others. Cross-checking with the measurement of resonant

frequencies of machined disks is not a trivial matter either, because various types of machining and measurement errors need to be taken into account. The problem in the case of RDDS is particularly aggravated because of the inherently 3-dimensional cavity interior shapes. Thus special attention must be paid to establish the dimension table that accurately describes the set of copper disks to be fabricated.

Computation code used in the past for DS and DDS did not have capability to specify the cell dimensions with a precision better than the machining accuracy. Consequently, we used a microwave measurement of stacked cells to determine the final cutting dimensions of these disks. For RDDS1, we desired to calculate the regular cells with a precision better than the machining tolerance. For this purpose, a newly developed finite element parallel processing code, Omega3P, was tried for the calculations.
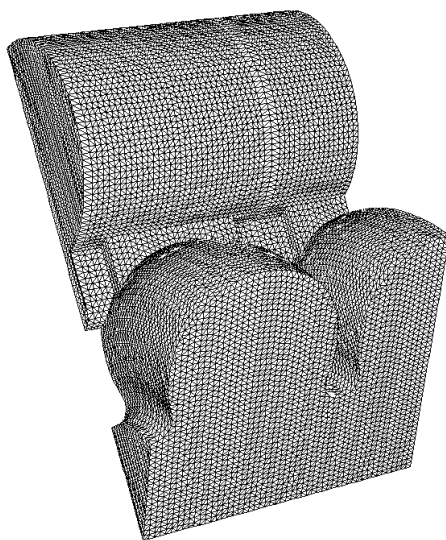
Figure 7.6: *Finite element mesh for modeling RDDS cell using Omega3P.*

Fig. 7.6 shows the finite element mesh for modeling one and a half RDDS cells with about one million degrees of freedom. The typical run time on such a grid using 48 processors on the NERSC T3E parallel supercomputer is less than half an hour. Five typical disks; No.1, No.52, No.102, No.153 and No.203 were designed using the linear element version of Omega3P. KEK fabricated more than six instances of each of these types of disks. All disks were carefully measured mechanically on a CMM (Coordinate Measuring Machine) and their microwave properties measured with a network analyzer. So-called weighting functions were calculated to quantitatively estimate the frequency perturbation due to the measured profile deviation. The weighting functions W represent the sensitivity of the resonant frequencies f to adding or removing copper material on various portions of the cavity surface:

$$f^2 = f^2_{\text{no perturb}}(1 + W \Delta s \Delta d), \tag{7.1}$$

where $f_{\text{no perturb}}$ is the resonant frequency without perturbation, Δs is the length along the contour of the cavity surface and Δd the perturbation, measured as the thickness of copper material added.

In the first order approximation, it leads to:

$$\frac{\delta f}{f_{\text{no perturb}}} = \frac{W}{2}\Delta s \Delta d \tag{7.2}$$

The dimension of the weighting function W is m^{-2}. Fig. 7.7 shows the weighting functions of both the $2\pi/3$ fundamental mode and the synchronous dipole mode for five typical disks.
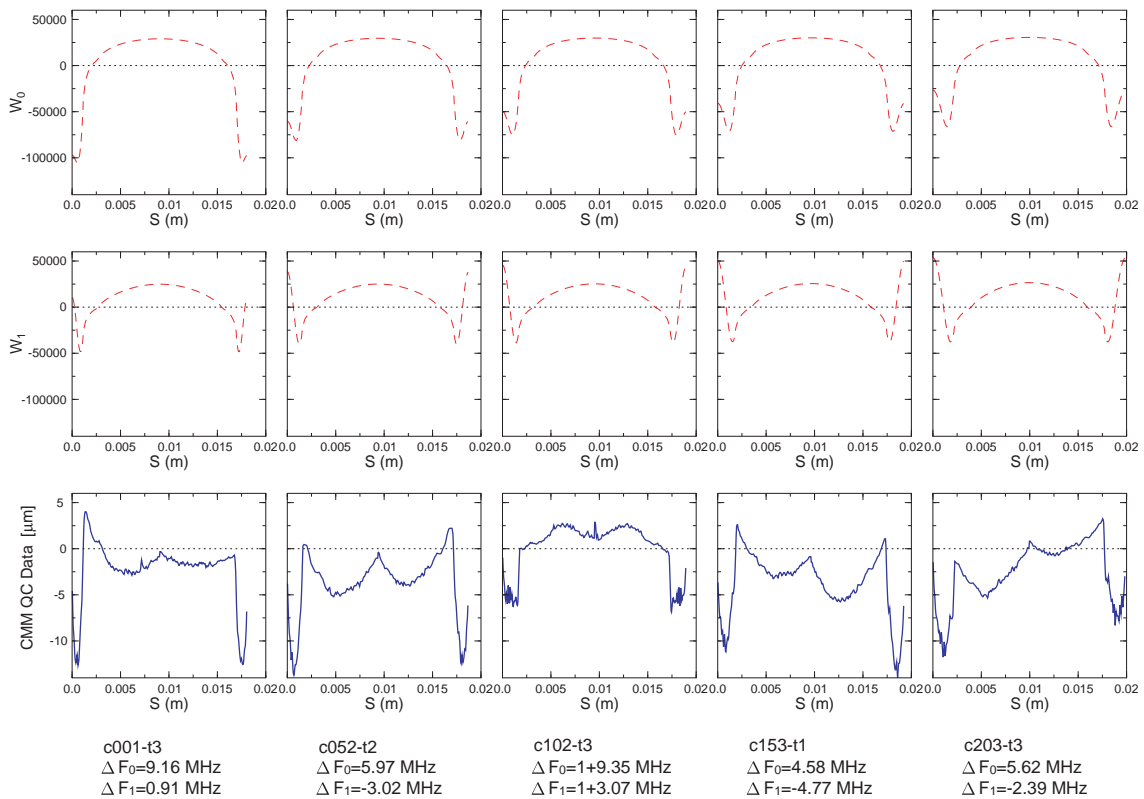
Figure 7.7: *Weighting functions of $2\pi/3$ fundamental mode and synchronous dipole mode, and CMM QC data for five typical RDDS1 test disks.*

It was found that the measured frequencies of the test disks were about 3.1-4.1 MHz lower than predicted by the linear element formulation. Afterwards the Omega3P code was extended to use quadratic instead of linear elements and the degrees of freedom were increased to 5.8 million. Very accurate extrapolation towards zero mesh size has thus become possible. The quadratic element results indicated a correction of about 3.1-3.7 MHz compared to the linear calculation, in excellent agreement with the measurements on the previously fabricated disks. At this stage, we became confident that Omega3P with the quadratic element formulation can create a final 3-D table of dimensions with an accuracy of better than 1 MHz. Fig. 7.8 show the $2a$ and $2b$ parameters against the disk number from the final dimension table.
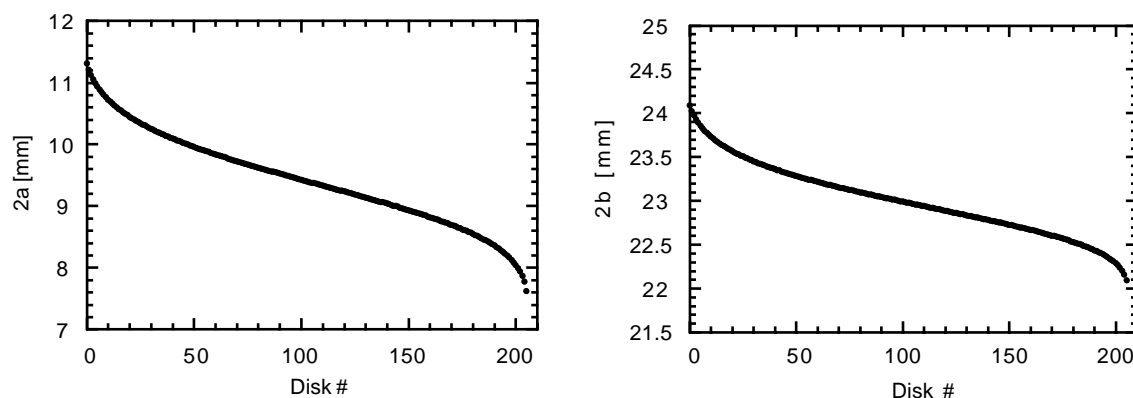
Figure 7.8: *Parameters 2a and 2b as functions of the disk number as plotted from the final disk dimension table.*

7.2.6   Design of Special Portions of Accelerating Structures

The input and output fundamental couplers and higher order mode (HOM) couplers are important elements of the accelerating structures. The critical goal for the design and fabrication of these complicated structures is to provide a good match for the RF signals traveling through them.

The input coupler must provide an excellent match between the rectangular waveguide and the accelerating structure at the correct frequency. To preserve a low emittance in multi-bunch beams, transverse deflections must be avoided by making the RF field and phase symmetric across the coupling cavity. Traditionally, the waveguide bends and flanges were costly and time consuming to tune. In order to achieve the required machining precision while reducing the manufacturing cost and improving mechanical stability, the design for RDDS1 has become more compact than for previous structures (DDS series)[9]. Fig. 7.9 shows a schematic view of the RDDS1 input end.

The RF design has two parts, an upper T-branched WR90 rectangular waveguide and a lower symmetric side-coupled accelerator cavity. A new time-domain code Tau3 was employed for the numerical simulation. Fig. 7.10 shows the 3-dimensional model of the coupler structure. The model consists of two cells coupled to rectangular waveguides and two regular accelerator cells. The transmission properties of the structure are determined by driving the TE10 mode at the input rectangular waveguide. The reflection coefficient at the input waveguide and the transmission coefficient at the output waveguide are computed once steady state is reached. A bench cold test of a coupler assembly was performed to make a final determination of some critical dimensions like the coupling iris and coupler cavity diameter.

The output coupler has a similar function to the input coupler for the fundamental mode. Fig. 7.11 shows a schematic view of the RDDS1 output end. For RDDS1 we have improved the output coupler design to provide dipole mode damping. From the ASSET test for DDS3, we found that the power spectrum of the horizontal transverse dipole wakefield did not have the several high Q peaks found in the vertical wakefield. An equivalent circuit model and MAFIA simulation showed that the output
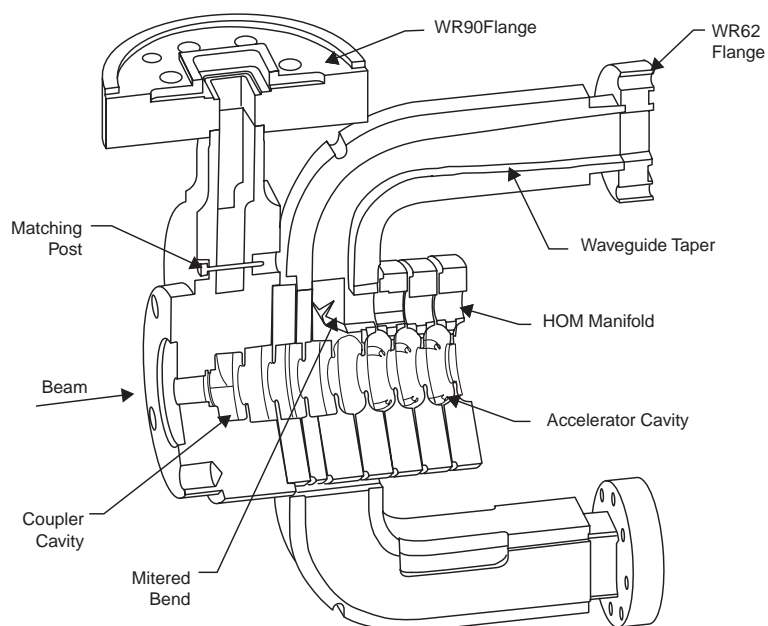
Figure 7.9: *Cross-sectional view of the input end for RDDS1 structure.*
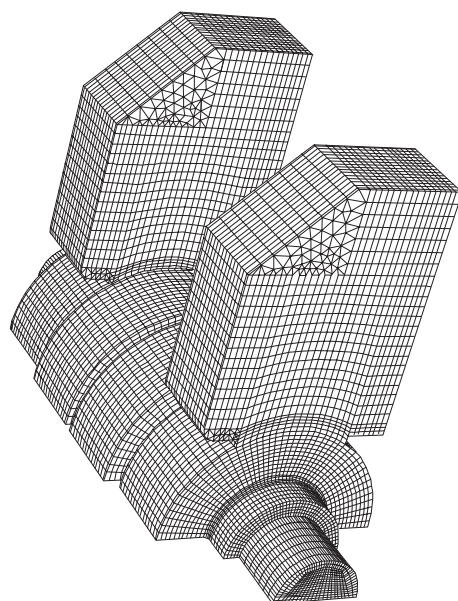
Figure 7.10: *Mesh for modeling a 4-cell geometry of the input coupler.*

coupler had a damping effect for dipole modes near the output end. The wakefields 10 - 20 m behind
the driving bunch were reduced by a factor of 2 or more. Therefore, the output coupler was redesigned
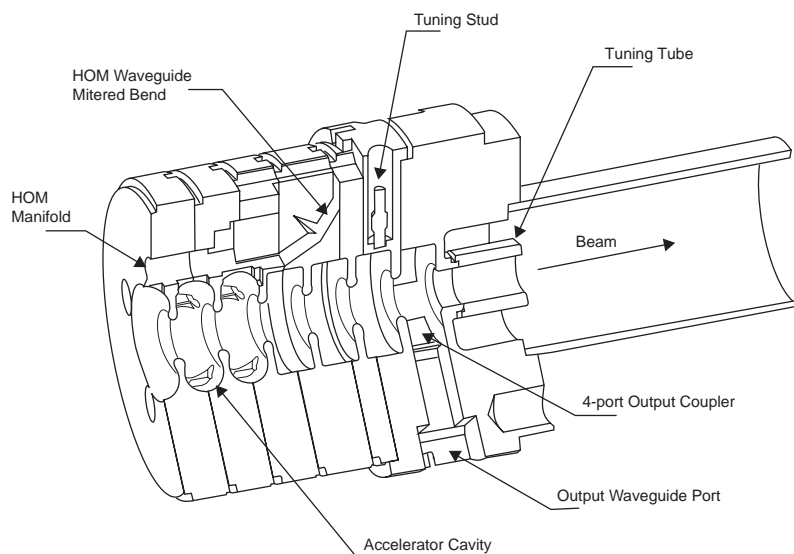with four coupling WR62 waveguides oriented at +45 and −45 degrees.

Figure 7.11: *Cross-sectional view of the output end for RDDS1 structure.*

The HOM coupler assembly must be matched to the manifold over a broad band of dipole mode frequencies. Figs. 7.9 and 7.11 show cross-sectional views for the input and output ends of the RDDS1 structure. Each tapered manifold is connected to a rectangular waveguide by means of a 90 degree mitered bend followed by a 90 degree H-bend, a taper to WR62 waveguide, and finally a matched load. The quality of the match of this assembly to the manifold has a very critical effect on the long range wakefields. The HOM coupler with mitered bend and tapered waveguide were modeled using the MAFIA code and bench tested in a cold test assembly. Since the manifolds are circular for the RDDS1 structure, a special matching junction between the manifold and rectangular waveguide was designed.

7.2.7   Mechanical Design

Besides achieving the required precision in fabrication and in assembly, as detailed in Sections 7.3 and 7.4, the mechanical design of the accelerating structure has to pay attention to the following issues:

- The accelerating structures are 1.8 meter long and weigh approximately 50 Kg. In the main linacs of JLC/NLC, they must be mechanically supported and aligned on the beam axis of the accelerator to 5 μm to avoid beam deflections from induced wakefields.

- In the fully annealed state in which the present 61 mm diameter copper structure leaves the brazing furnace, it is too soft to be supported as a rigid body with supports only at the ends. Multiple support points are needed along the length. They can be also used to elastically adjust the straightness.

ISG Progress Report, April, 2000

- To keep the cavity in tune the temperature of the structure must be stabilized and kept to agree with the design assumption within a fraction of a degree C.

- The vacuum along the beam line must be maintained below 10^{-8} Torr during operation to minimize RF breakdown and reduce ion interactions with the beam.

Support System

The RDDS1 prototype uses a support system similar to previous DDS structures so that it can be easily tested at the SLAC ASSET facility and at NLCTA. The structure is supported at 5 points along its length above an extruded aluminum box beam strongback. Fig. 7.12 schematically shows the RDDS1 support system.
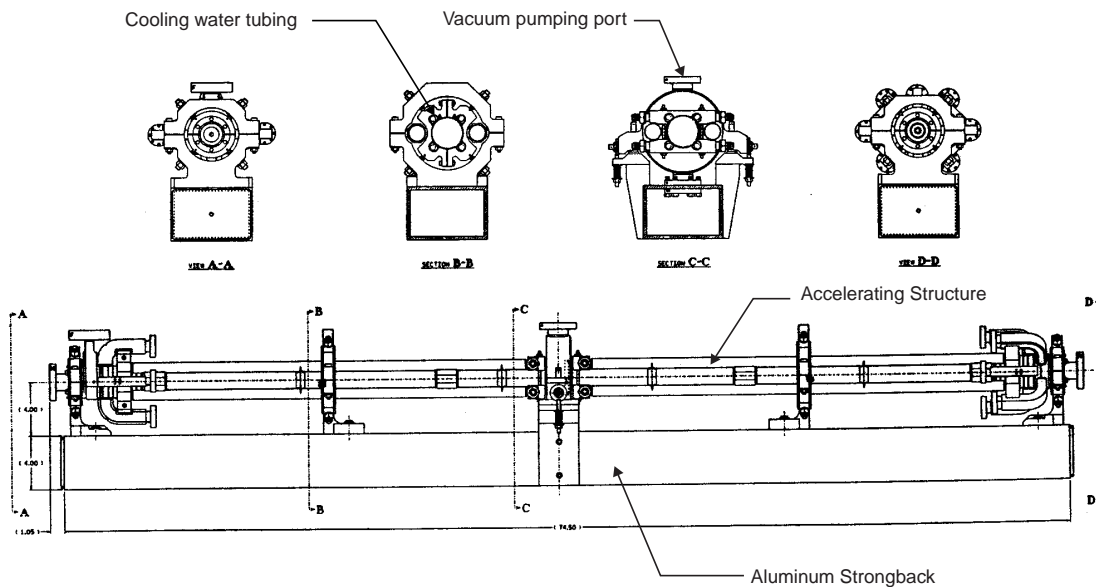
Figure 7.12: *Schematic view of the RDDS1 support system.*

To minimize relative thermal expansion between the structure and the strongback, RDDS1 is fixed at the midpoint of its length rather than at one end as in previous structure supports. This reduces the maximum motion by a factor of two. At each support point, the structure is positioned on steel balls which are free to roll as the structure expands. Previous supports used aluminum flexure plates to accommodate this expansion. Steel ball supports are more compact and avoid introducing any bending moments into the structure during alignment. Small elastic corrections to the structure straightness are made with sets of opposing fine pitch screws. Alignment at the 5 micron level is facilitated by a small elastic deformation of the supports during adjustment.

Development and design of the supporting system to be used in the actual NLC/JLC environment remains a critical task for the near future. Ease of handling, compatibility with various types of tubing

and wiring, mechanical stability and reduced cost during construction and maintenance are important considerations.

Cooling System

The water cooling system follows the layout of the original SLAC S-band accelerator. Water is supplied at the middle point of the structure and flows out to the ends before returning to the mid-point. This counter flow layout gives a nearly uniform temperature distribution along the structure length. Cooling tubes brazed to the sides of the structure are identical to previous DDS prototypes.

Tube cross-section and water flow parameters remain to be further optimized for the final JLC/NLC systems. Issues to consider include: the operating temperature of the main linacs, the presence or absence of components other than the accelerating structure which emit heat, the final decision on the outer diameter of the accelerating structure, and compatibility of the cooling pipes with the vacuum pumping port, alignment marks and others.

Vacuum System

RDDS1 is the first structure provided with vacuum manifolds along each side. The earlier DDS3 structure was pumped from below to its strongback, which also served as a vacuum manifold. In both cases, the pumping is through 2×5 mm^2 slots which connect the HOM manifolds to the vacuum manifolds in groups of 3 disks at 4 locations nearly evenly spaced along the structure. The pumping slots are the largest impedance in the vacuum pumping circuit because they must be sufficiently small to block the leakage of RF fields from the HOM manifolds.

The vacuum profile of RDDS1 is shown in Fig. 7.13. In the simulation the out-gassing rate of 10^{-13} Torr ℓ s^{-1} mm^{-2} for copper, 10^{-15} Torr ℓ s^{-1} mm^{-2} for stainless steel is assumed. The pumping speed used in the simulation is 14 ℓ s^{-1}. This performance is expected to be acceptable for the beam dynamics requirements on the vacuum level, and for out-gassing characteristics of the structure in the high gradient environment. However, some studies remain to be conducted before a final conclusion.

7.3   Fabrication of Copper Disks

7.3.1   Introduction

An accelerating structure body consists of a stack of thin, cylindrical, copper disks which are machined to form a series of resonant cavities when assembled together. Fig. 7.14 shows schematic cross-section views of DS, DDS and RDDS disks. Issues noted during the fabrication of copper disks for DDS3
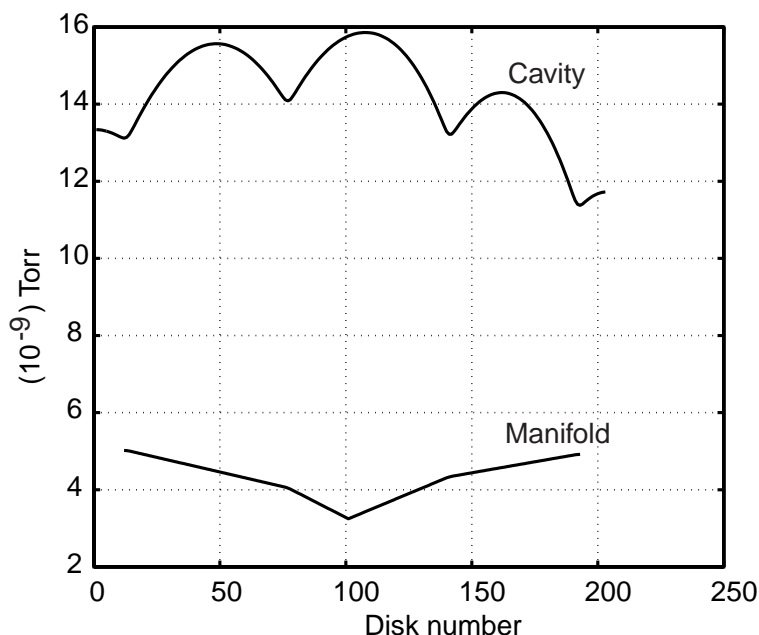
Figure 7.13: *Vacuum calculations for the RDDS1 structure.*

(the latest model of DDS prototypes) which was done at LLNL, have been reported in [12]. For the purposes of presenting the more recent technological advances, we focus here on the R&D steps that led to the successful fabrication of the first prototype set of RDDS disks. For RDDS1, the electrical design was done by SLAC, and the copper disks were fabricated by KEK, which had also fabricated disks for a series of previous prototype structures such as M2, DDS1 and DDS2. The results from studies on the earlier prototypes are discussed in [1] and [2].

A major challenge associated with RDDS1, compared to previous structure prototypes, was to apply the diamond turning technique to produce round cell shapes. The technical issues and solutions that have been developed to successfully fabricate the RDDS disks are described in great detail in [13] and [14]. Subsequent sections present some highlights learned from this study.

The resonant frequencies of the disks are mainly determined by the cavity parameters $2a$ and $2b$, in addition to the width w of the slots that connect the cavity and manifolds. The sensitivities are summarized in Table 7.2 for the case of RDDS1.

The fabrication tolerances for the disks are determined from the following two considerations:

1. The accelerating mode frequency of these disks should be set to the canonical 11.424 GHz, so that the total phase slip that the accelerated particles experience does not exceed 5 degrees.

2. The lowest order dipole mode frequencies across a structure must be smoothly distributed. They should not deviate from a smooth curve by more than 1 MHz if the detuning is to be sufficiently
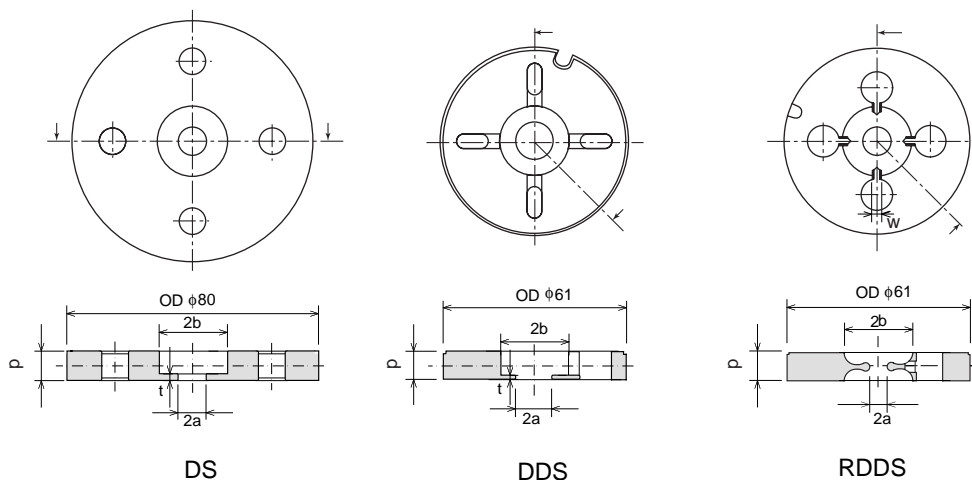
Figure 7.14: *Schematic cross-section views of DS, DDS and RDDS disks.*

Sensitivity	Accelerating Mode	Dipole Mode
$\delta f/\delta a$	$+0.6 \sim +0.3$	$+0.1 \sim -0.6$
$\delta f/\delta b$	-1.2	-1.2
$\delta f/\delta w$	-0.06	-0.06

Table 7.2: *Sensitivity of resonant RF frequencies of RDDS1 disk to cavity parameters 2a (iris diameter) and 2b (cavity diameter). The sensitivity actually varies across the structure and their ranges are also shown. The unit is in MHz/μm.*

effective.

According to the point 2 above, frequency errors of the order of less than 1 MHz rms are acceptable for the lowest HOM. This translates into machining tolerance of the order of $\pm 1\mu$m or better. High precision diamond turning, which is now widely used in many engineering fields, appears to be the suitable technique for satisfying such requirements. Previous investigations have shown that by using diamond turning[2, 12], disks for DS and DDS could be fabricated with a precision of the order of $0.5 \sim 1\mu$m, in a lab environment.

However, since the point 1 above states that the total phase slip must be also kept small, the errors in the fundamental mode resonant frequencies and the resulting accumulated phase slip need to be tightly controlled. This cannot be accomplished simply by maintaining machining accuracies of $\sim 1\mu$m. As a solution, a feed-forward correction scheme has been developed and successfully applied. This will be also discussed.

ISG Progress Report, April, 2000

7.3.2 Machining of RDDS1 Disks

The copper disks are cut from bar-shaped raw material of Class-1 oxygen-free copper. The rough machining of RDDS1 disks and milling of HOM manifolds and slots was done by contractors who delivered their own QC report on the mechanical dimensions along with the disks. The turning was done with carbide and polycrystalline diamond tools. At that point, the disks contained remaining overstock material of $\sim 40\mu$m. Milling of the slots and HOM manifolds to the final dimensions was done with polycrystalline diamond tools. The contractor also carved the rotational alignment marks and engraved the disk identification numbers on the OD surface.

The reliability of the QC report from the contractor was confirmed by cross-checking their earlier results with a set of independent measurements using the CMM facility at KEK. This made it possible to rely on the QC results from the contractor during regular production of the rough machining, without conducting separate QC measurements within KEK prior to subsequent machining. The rough-machined disks were annealed in a vacuum environment for two hours at 500°C to release any remaining stress. The disks were then hand-lapped on one side to remove scratches using #800 sandpaper on an optical flat.

The intermediate turning which leaves a 10 μm stock removal and the final machining of RDDS1 disks were done at the precision machining laboratory within KEK. An ultra high precision lathe with two-axis control was used. After completing the final diamond turning, the whole surface feature dimensions of all disks were checked at KEK. Salient features of the work environment and the machining operation are summarized as follows:

1. The lathe was set at the bottom of a HEPA-filtered air channel (1 m × 1 m) located in a temperature controlled clean room.

2. A mist of kerosene was used on the work as a coolant during diamond turning. For temperature stabilization of the system, four hours of idling time was allocated after each cold-start of the machine.

3. The positioning of the tool in the beam axis direction was ensured by frequently cutting of the face of the vacuum chuck prior to cutting of copper disks.

4. The two-axis motions of the spindle and the tool table were measured with linear gauges. In this process, the parameters for feedback operation of lathe numerical control were tuned up. Once optimized, no significant deviations of servo controls were observed.

5. In the actual machining operation, the final turning of one side of each disk was made with the *OD* oversized by 2μm. After aligning the disk center within 0.2μm, the final turning of the other side of the disk was done with the *OD* to the exact dimension.

6. Then the outer diameter of each disk was measured with ±0.2μm accuracy with respect to a reference. If necessary, the radial positioning of the tool was readjusted for subsequent fabrications based on this data. In case of each cold-start or a start-up after a break, a dummy disk

was cut and measured for the same purpose. The thickness of each disk was also measured at this time.

7. The diamond cutting tool had a radius of 0.4 mm. After delivery from the vendor, KEK determined its exact dimension to within 0.3μm by machining an aluminum test hemisphere (ϕ60 mm) and then by measuring the surface features with a roundness tester.

8. The revolution speed of the spindle of the lathe was chosen to be 2800 rpm. The typical feed speed for the very last cutting was 3 mm/min. These rather conservative choices were due to the fact that this was our first trial fabrication of RDDS disks.

At first sight, since the dimensions of primary interest are $2a$ and $2b$, the outer diameter OD may appear of secondary importance, because it only affects the relative alignment of neighboring disks when they are stacked on a V-block for assembly. The actual situation is not quite that simple. Because of the order in which the tool positions are controlled, the final dimensions a and b critically depend on the tool positioning that determines the OD. This has been a known issue and the actions 5 and 6 in the list above have been designed to address this.

While developing the procedure for final machining of the RDDS1 disks, compared to that used for the DS and DDS disks, items 4 and 7 turned out to be of particular importance. The dimension report provided by the tool vendor was usually not precise enough to be assumed correct in fabricating the RDDS disks, which demand contouring tolerance of the order of 1 μm.

Fig. 7.15 shows a contour plot of a test RDDS disk that was fabricated at KEK. The measurement was done with a CMM machine[1] at SLAC with contouring capability. The solid line shows the design shape. The black dots show the measured shape, with the deviation from the nominal shape magnified by 200 times. It shows that the machined surface matched the design to within $\pm 1\mu$m.

A few dozen disks which were fabricated with varying a and b parameters exhibited similar machining precision. This result, together with the work outlined in Section 7.2.5, was decisive in giving us confidence that the RDDS concept could be realized. It should be emphasized that technical progress in three areas – RF calculations, machining procedures, and measurements, were all required for this technological advance.

7.3.3   Dimensional Inspections of RDDS1 Disks

It has been mentioned in section 7.3.2 that parameters such as disk OD and thickness p were measured during fabrication of each disk. This section discusses other dimensional inspections applied to the RDDS1 disks.

The surface flatness of the disk is useful information for evaluating the performance of the lathe, as well as the quality of the disk itself. An interferometer system, Mark II[2] was used for this purpose.

---

[1]Leitz PMM 12106HA, manufactured by Ernst Leitz Cooperation
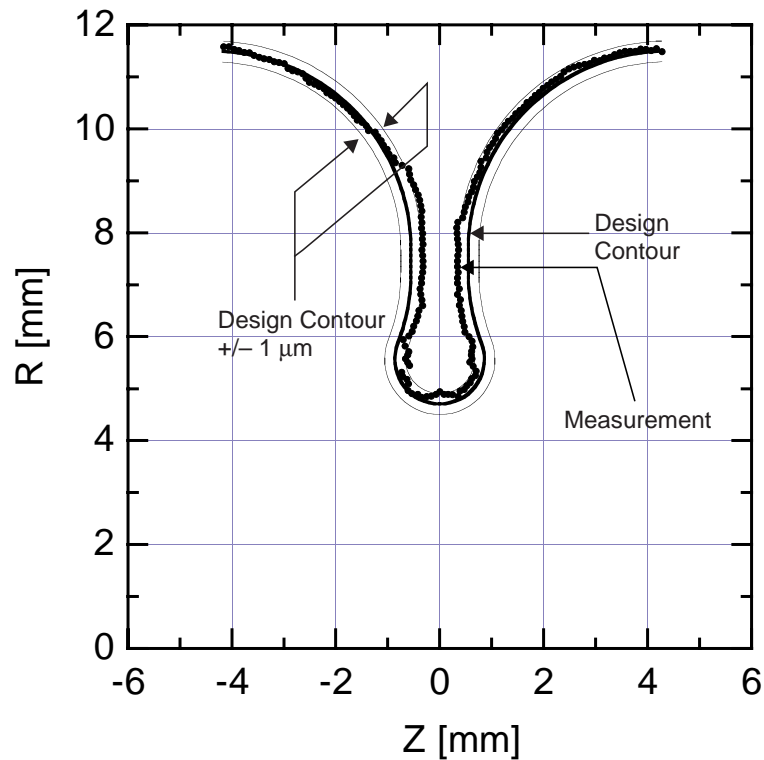
[2]Manufactured by Zygo, Co.

Figure 7.15: *Contour plot of a test RDDS disk that was measured with a CMM machine at SLAC with contouring capability.*

It could detect a surface flatness deviation in excess of 0.3μm. More than 97 % of fabricated RDDS disks showed the flatness better than 0.5 μm.

The parallelism of the two end planes of each disk was measured by using a pair of capacitive gauges which were rigidly held over a movable table supporting the disk. The disk was inserted between the gauge pair and the sum of distances between the disk surface and the gauges was recorded while the disk was moved. The accuracy of the parallelism measurement is estimated to be better than 10 μrad. The rms value of measured parallelism of RDDS1 disks was 5 μrad (the worst case value was 20 μrad).

Several measurement devices were tested for inspecting other dimensional parameters such as a, b, HOM manifold diameter, slot width, etc. Laser-servo type auto-focus microscopes use an auto-focusing laser system combined with a 3-axis moving table. They have good measurement accuracy if the surface features of the specimen are sufficiently flat. However, the models tested proved inadequate for measuring the cavity dimensions of RDDS disks, because it was difficult to determine the focusing position on the specimen surface when the slope of the surface was large with respect to the sampling plane of the apparatus. Measurement devices based on probing mechanisms using atomic forces or a stylus suffer from the same difficulty. While all these devices have an excellent measurement accuracy,
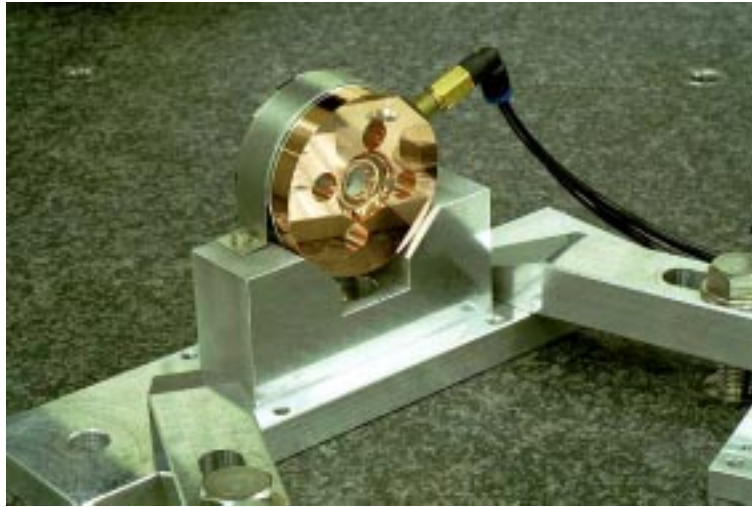
Figure 7.16: *RDDS disk in CMM setup at KEK.*

they would require the RDDS disks to be cut into segments to make the measurement. Consequently, they could not be used for a non-destructive measurement.

Thus a 3-dimensional coordinate measuring machine (CMM), CARAT 850[3] at KEK, was chosen to measure the general feature dimensions of the RDDS1 disks. The measurement mechanism was based on sensing of physical contact of a spherical probe, which was moved in 3 dimensions under computer control. The CMM at KEK has an accuracy of 0.8 μm and repeatability 0.2 μm over a small volume covering the RDDS1 disk. The temperature of the CMM inspection room is regulated at 20 ± 0.4°C. Fig. 7.16 shows an RDDS1 disk held by a fixture chuck on the CMM stage.

Fig. 7.17 (A) shows the slot width of the disks whose machining tolerance was 15 μm. As noted in 7.3.2 this part of the milling was done by the contractor during the rough machining stage. It is seen that the tolerance is well met.

Fig. 7.17 (B) shows the disk outer diameter OD. The tolerance was 1 μm. As discussed in 7.3.2, the OD of each disk was measured upon completion of machining work. Whenever the measured OD deviates from the design value by more than 0.75 μm for two disks in a row, the tool position was corrected.

Fig. 7.17 (C) and (D) show the $2a$ and $2b$ dimensions of the cavities. The measured values are systematically larger than the design by $2 \sim 3\mu$m. Inspections with a microscope indicates that the locations on the disks that were touched by the CMM probe exhibit depression marks. By measuring the diameter of these depression marks and known probe sizes, it was concluded that the systematic shifts of measured dimensions are consistent with the footprints left on the soft surface of annealed copper by the probing. Other systematic errors are excluded by fabricating two disks in identical ways, one using annealed copper, the other using non-annealed copper, and examining

---

[3]Carl Zeiss Co.
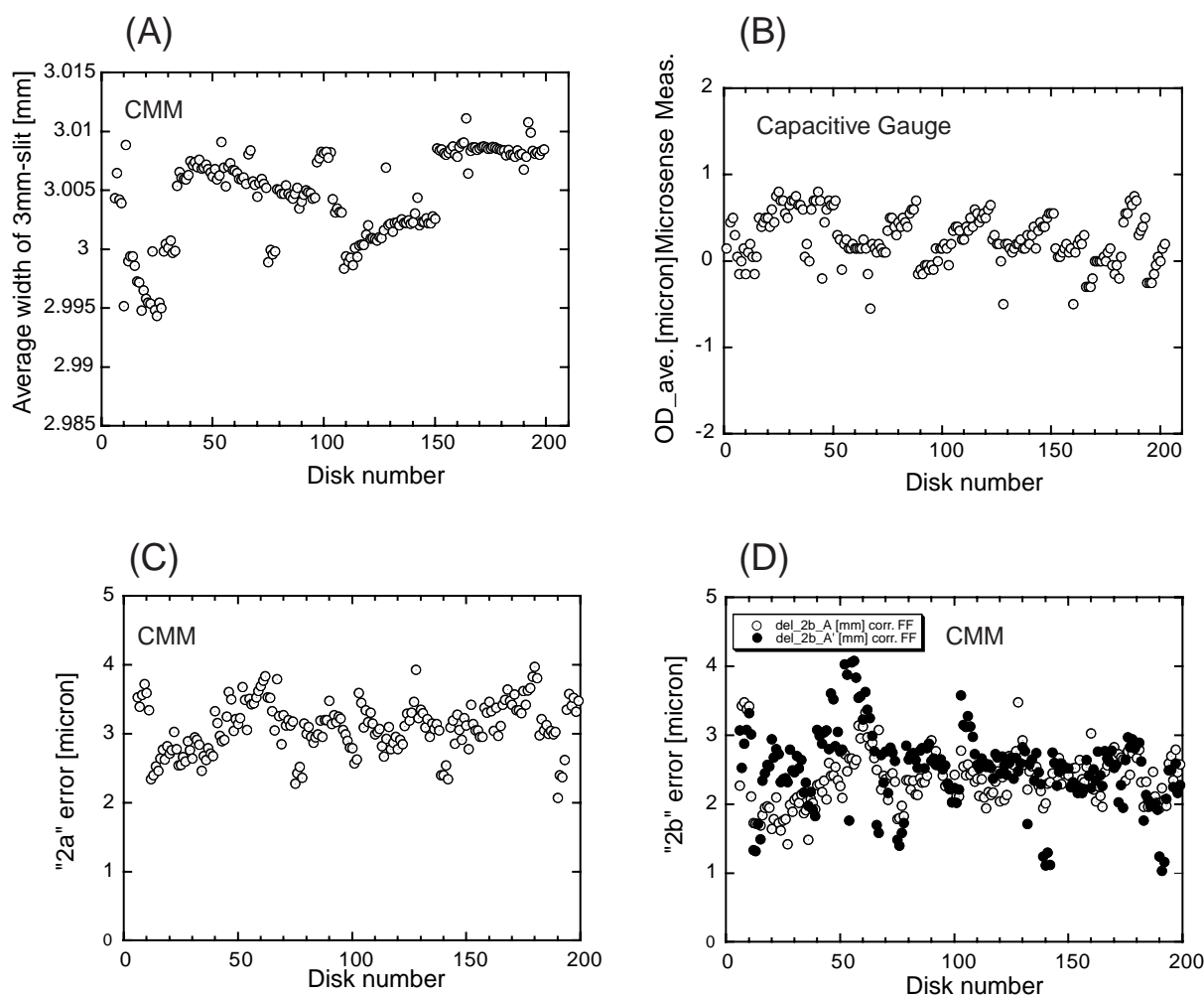
Figure 7.17: *Mechanical QC summary of fabricated RDDS1 disks, obtained from measurements with CMM and capacitive gauges at KEK. (A) the slot width of disks, whose machining tolerance was ±15μm. (B) outer diameter OD, whose machining tolerance was ±1μm. (C) 2a, aperture of the cavity. (D) 2b diameter of the cavity.*

their dimensions with the CMM. The different magnitude systematics in $2a$ and $2b$ might derive from the different local mechanical sturdiness of the material that is probed; their understanding requires further studies.

In conclusion, use of the CMM combined with other techniques provided us with suitable methods for inspecting the dimensions of machined disks with specified accuracy ($\approx 1\mu$m) in a non-destructive manner. High quality disks for RDDS1 were successfully fabricated with adequate precision. However, while it is considered acceptable at this stage of R&D, creation of depression marks and systematic effects in some aspects of the measurement with CMM indicates a need to develop a better mechanical measurement technique.

It is considered that the ultimate QC certification of disks in mass production is likely to be provided by measurements of resonant RF frequencies (see 7.3.4), in addition to measurements of key mechanical dimensions. However, it will still be necessary to go back to detailed mechanical measurements to determine the exact cause of errors, if any anomalous resonant frequencies are observed.

7.3.4   RF Measurements of RDDS1 Disks

The measurements of resonant frequencies may be considered the final verdict on the machining accuracy of the fabricated disks. This, of course, is under the assumption that the calculations of resonant frequencies are reliable enough. In practice for RDDS1, the latest calculations of the fundamental mode resonant frequency (f_0, which is canonically 11.424 GHz in our case) is considered to be good within 0.5 MHz in the absolute value. It is not, however, quite the same for the higher order modes. For instance, the absolute accuracy of present calculations on the lowest order dipole mode f_1 frequency are yet to be established.

In addition, the measurement of resonant frequencies that can be performed with individual disks during fabrication are subject to certain limitations. These are due to: (i) the difference of boundary conditions during the QC measurements and actual structure assembly, and (ii) effects of the existence of antenna probes which cause changes of the boundary conditions for the cell, and lead to a shift of the measured resonant frequencies.

In the scheme adopted for testing RDDS1 disks, the disks were stacked on a small V-block. They were sandwiched between two flat plates at the ends to electrically short the stack. Each plate contained an antenna through which the transmission characteristics, S_{21}, were measured. This allowed us to measure the resonant frequencies of the standing waves in the stacked disks. The actual measurements were done in a single disk stack setup as well as a multiple disk stack setup where typically up to six consecutive disks were used.
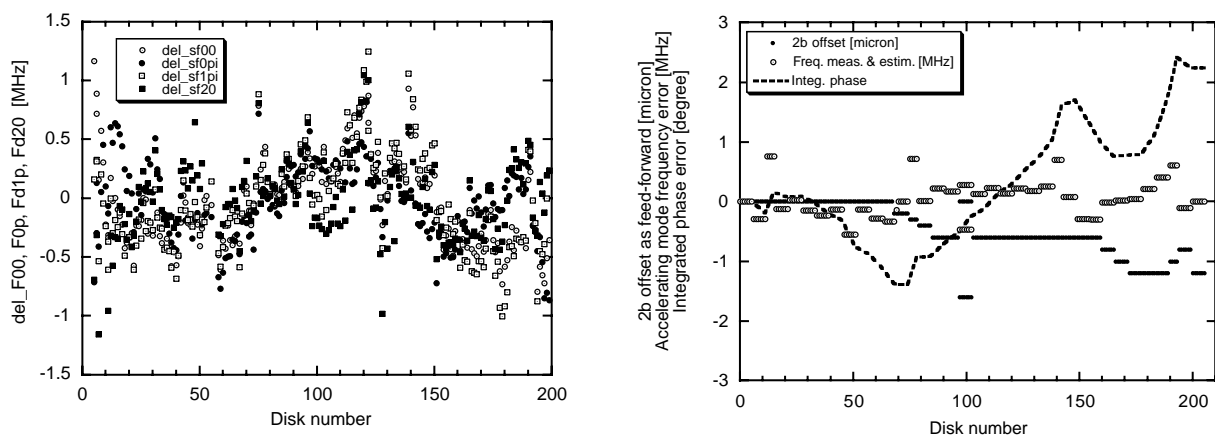
Figure 7.18: *(A) Resonance frequencies, measured in the single disk setup, of RDDS1 disks. The plot shows deviations from the 3rd order polynomial fit. (B) Fundamental mode frequencies, measured in the disk stack setup, of RDDS1 disks.*

The single disk stack setup allowed measurement of f_{00}, $f_{0\pi}$, $f_{d1\pi}$ and f_{d20} mode frequencies. Since the cell boundary conditions in this setup are quite different from the final configuration in the structure assembly, some translation is needed when interpreting the measured frequencies in an absolute sense. In practice, however, this is difficult because of numerous theoretical and experimental ambiguities.

Still, since the measured single stack resonant frequencies are expected to exhibit smoothly varying behavior as a function of disk number, the data can be examined to search for any sudden changes of resonant mode frequency which would point to an anomaly in the fabrication process. It is estimated that this method is capable of checking the smoothness of the frequency variation within ± 0.2MHz. Fig. 7.18(A) shows the measured resonant frequencies of RDDS1 disks in the single disk setup.

The multi disk stack setup allows a measurement of the accelerating mode frequency ($2\pi/3$-mode) of the chosen set of disks. It is estimated that this method has an accuracy of ± 0.2MHz (absolute value) for measuring the *average* accelerating mode frequency of the stack. Fig. 7.18(B) shows the result for RDDS1 disks.

7.3.5   Feed-forward Correction to Machining Parameters of RDDS1 Disks

While the achieved machining tolerance, as discussed in 7.3.2 and 7.3.3 is more than sufficient for the requirements on the lowest order dipole mode frequencies f_1 of the disks, this is not quite sufficient for controlling the fundamental mode frequencies f_0. This is because the performance requirement is specified in terms of the total phase slip which is an accumulation of errors in f_0, rather than the average f_0 or rms error on f_0. For instance, a systematic error of f_0 of 1 MHz, which is equivalent to roughly 1 μm errors in the a or b parameters, would result in a total phase slip error of $40°$ that the particles would see across one accelerating structure. On the other hand, demanding a tolerance on the order of 0.1 μm for a, b and other dimensions of the disks appears unrealistically difficult at this stage of fabrication technology.

Thus, some active correction for the dimensional parameters of RDDS disks is necessary during the fabrication process, based on the trend of errors in f_0.

A possible scenario is to measure the resonant frequencies f_0 and f_1 of a disk at a certain stage during the intermediate or second diamond turning, then determine the $2a$ and $2b$ parameters of this disk for final diamond turning. The drawback of this scheme is that it requires a cumbersome sequence of handling, in which a disk has to be removed from the lathe in the middle of machining and the identical machine condition, in this meanwhile, needs to be ensured. The job control task becomes very complex.

Another scenario is to complete the final diamond turning of each disk first, then measure the errors of f_0 and f_1. After this, if necessary, the same disk would be remachined and portions of the cavity carved off in a way to locally modify the $2a$ and/or $2b$ parameters. An advantage of this method is that the tolerance of this second machining is generally much looser than the first machining. Nonetheless, it is still a cumbersome procedure. In addition, since $2a$ and $2b$ can be only *increased*, the sign of the correction that can be achieved for f_0 and f_1 is limited. Depending on the magnitude and the sign of the errors, if the $2a$ and $2b$ parameters need to be substantially revised to reduce the error in f_0, excessive random fluctuations in f_1 might result.

Thus, in the case of RDDS1 disks, we decided against either interrupting the final machining or remachining each completed disk. Rather, the $2b$ parameter of subsequent disks were revised if

necessary to compensate for the history of f_0 errors of previous disks.

Some data associated with this feed-forward technique is shown in Fig. 7.18(B) that appeared in 7.3.4. The white circles show the errors in fundamental mode frequencies of the disks, obtained by multi disk measurements. Resultant phase errors are indicated with broken lines. It is seen that there is a phase slippage of about $-1.5°$ from disk 30 through disk 70. From about disk 60 on, the $2b$ parameters for final machining were slightly offset so as to make the phase slippage more positive. With this and a few other manipulations, the total phase error across ~ 200 disks was only $\sim +2°$.

One of the sources of the initial negative phase slippage (or slightly negative error in f_0) of the RDDS1 disks could come from a small systematic error in w, the width of the slots that connect the cell and HOM manifolds[4]. The vendor who was responsible for final milling of this part successfully met the specified tolerance as shown in Fig. 7.17 (A). However, that tolerance (15μm) was loose enough to allow this level of frequency errors. Fig. 7.17 (A) shows a positive error in w ($\sim 5\mu$m) from disk #30 through #100 which can cause $\delta f_0 \simeq -0.3$MHz. It also shows a step change ($\sim 6\mu$m) of w at disk #150 which can cause $\delta f_0 \simeq -0.4$ MHz. The $2b$ parameters of disks #160 and later were modified to correct the f_0 errors which could be caused by these shifts of w and other parameters.

In summary, it has been learned that it is quite possible to control the fundamental mode frequency so that the total phase error can be kept less than $5°$, by using this feed-forward technique.

---

[4]However, undetected systematic errors of $2a$ and $2b$ cannot be totally excluded, either

7.4   Assembly of Accelerating Structure

7.4.1   Introduction

The critical requirement in the assembly procedure of an accelerating structure lies in achieving sturdy and vacuum-tight junctions between neighboring copper disks. More specifically:

1. Random shifting of resonant frequency of fundamental mode due to bonding should be well below than 1 MHz.

2. The vacuum-tight bonding so that pressure level of 10^{-8} Torr or better can be maintained during beam acceleration operation.

3. The bonding must be sufficiently strong so that the accelerating structure can withstand transportation to and installation in the beam line. It has to maintain its mechanical features during the beam operation for a dozen or so years.
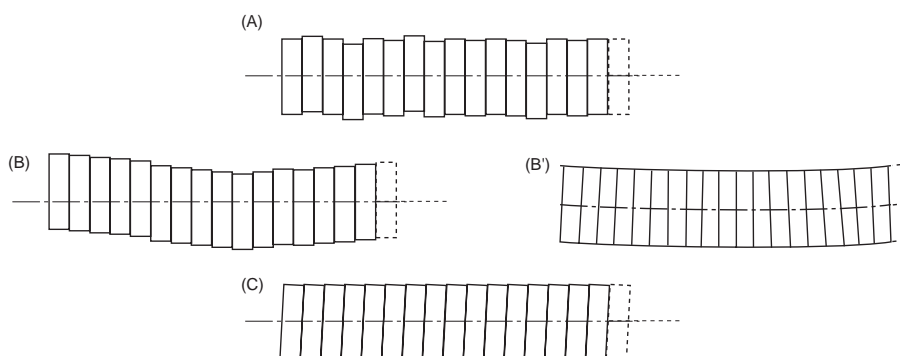
Figure 7.19: *Types of disk misalignments in the assembly of an accelerating structure: (A) Disk-to-disk transverse misalignment, (B) Bowing due to disk slips, (B') Bowing due to bending, (C) bookshelving errors.*

An estimation[17] of the effects of random transverse misalignment (Fig. 7.19(A)) of the cells along the structure gives a tolerance of about 5 μm rms for misalignments on length scales from disk-to-disk to ~10 disks. The tolerance for a longer wavelength misalignment is progressively relaxed as the characteristic length increases. Global bowing with a long wavelength (Fig. 7.19(B) and (B')) can easily be corrected through mechanical measurement and forced bending before installation. Considering these tolerances, the alignment targets for DDS and RDDS were set at (1) disk-to-disk alignment of a few μm rms and (2) global of 10 μm. "Bookshelving" is a phenomenon where a number of disks have their symmetry axis systematically tilted with respect to the overall structure axis (Fig. 7.19(C)).

The tolerance on bookshelving is quoted to be $\pm 50\mu$rad [17]. In addition, to maintain the alignment between the HOM manifolds of each disk, the rotational alignment of stacked disks around the symmetry axis should be better than $2 \sim 3$ mrad. The assembly procedure for accelerating structures must meet these requirements.

The solution adopted for DDS and RDDS prototypes was to stack the copper disks on a precision V-block, then to use diffusion bonding to form a structure body assembly. The remaining parts such as flanges, water cooling jackets, vacuum pumping ports, and waveguides for fundamental-mode and HOM power are brazed onto the structure body later. Diffusion bonding is a process where atoms in neighboring metal surfaces migrate towards each other in a high-temperature environment and form a single, bonded body. Results from extensive studies on experimental aspects of diffusion bonding and other techniques are discussed in [2] and [15].

In this section we describe some highlights of the successful assembly and bonding work that was done for DDS3 and RDDS1 prototypes, and discuss some associated issues.

7.4.2 Disk Cleaning

Removal of oil and dust from copper surfaces is necessary to establish good surface-to-surface contact of disks during diffusion bonding, as well as to ensure good surface quality for the interior of the cavity cells.

Several rinsing methods have been tested in the past at KEK to prepare the copper disks prior to diffusion bonding. Several agents have been tried including weak acid (HCl and H_2SO_4), pure water that includes ozone (O_3) gas, and acetone. While all of these rinsing methods have produced good diffusion bonding quality in the past, the acetone rinsing, when used alone, may not be sufficient to remove all unfavorable material and may leave residual carbon. While acid rinsing is effective in removing carbon, the environmental waste which results from mass production could become an issue. Thus rinsing with pure water that includes ozone gas (OPWR) has become a possible alternative.

In case of DDS3 and RDDS1[16], the disk cleaning was done in the following order: acetone rinsing in an ultra-sonic bath, pure water rinsing, OPWR rinsing, acetone rinsing, then nitrogen gas blowing and drying.

While the CuO/Cu_2O layer, which is expected to form during OPWR, is considered to protect the copper body from further oxidation, it was also feared that it might interfere with effective diffusion bonding. Experiences with DDS3 and RDDS1, where diffusion bonding was successfully performed, do not corroborate this concern. Still, more systematic studies on the effects of cleaning techniques of copper disks on diffusion bonding and high-power performance of the accelerating structure are needed in the future.

7.4.3   Disk Stacking

The machined copper disks are stacked on a precision V-block prior to diffusion bonding. Fig. 7.20 shows the cross-section of the V-block, made of Cr-plated (more than 50μm thick) S45C steel, which was used for assembling DDS3 and RDDS1 prototypes. It has a length of 2.3 m, long enough to accommodate the whole disk stack and stacking fixtures which are used at two ends of the disk stack.
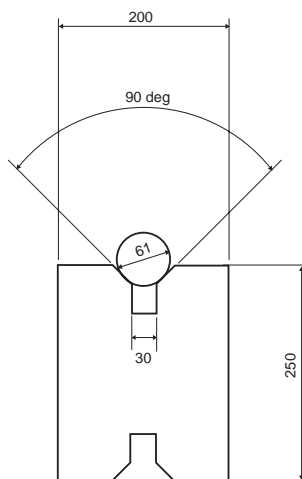

Figure 7.20: *Cross-section view of the V-block.*

The V-block is placed on, and can be screwed to, a stacking frame made of steel as shown in Fig. 7.21. The stacking frame is capable of tilting the V-block from 0 through 90° by using a hand-driven worm gear. This allows easy installation and removal of the V-block and/or the stacked copper disks. Also, it allows stacking of the copper disks while the V-block is tilted at an arbitrary angle. The DDS3 and RDDS1 disks were stacked while the V-block was tilted at 60° or 55°. This is expected to stabilize the positioning of each disk in the direction along the stack.

The stacking frame is equipped with a movable stage that supports a pair of electrical capacitive sensors[5] with a typical resolution of 0.1μm. The motion of the stage is driven by a computer-controlled stepping motor. The data from the sensors is used to estimate the transverse alignment of the disks as shown in Fig. 7.22 (A).

Near one end of the stacking frame (the right side of Fig. 7.21), there is a table where either an autocollimator and a pair of laser-interferometer assemblies can be installed. The autocollimator is used to measure the tilt angle of the end plane of each disk while stacking, and to detect the development of bookshelving errors. Bookshelving phenomena can also be detected by using the data from capacitive sensors, while moving the sensor stage in very fine steps. The laser-interferometer assembly is used, in combination with a pair of Wallaston prisms on the movable stage and a pair of mirrors on the other end of the stacking frame, for studies on the straightness of the motion of the movable stage. The movable stage also accommodates a microscope camera as shown in Fig. 7.22 (B).

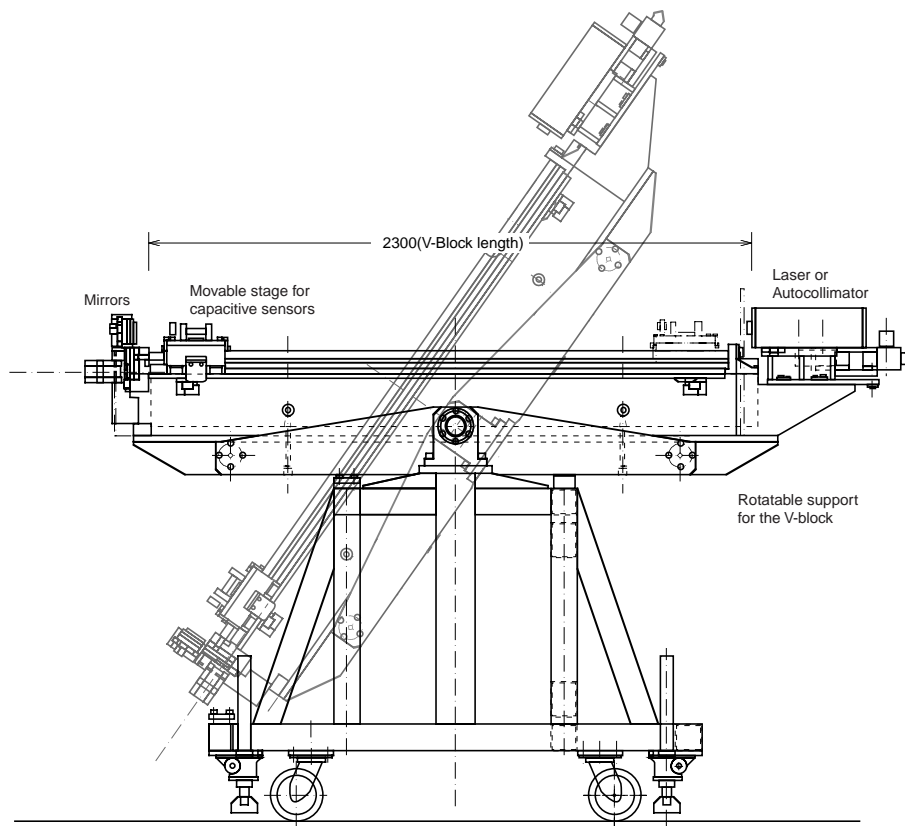---

[5] "MicroSense" from ADE Technologies, Inc.

Figure 7.21: *Stacking frame that holds the V-block and numerous equipment.*

The camera is used to check the notch marks on the OD surface of each disk to ensure the rotational alignment.

The stacking work was done in a clean room which is temperature stabilized at $(20 \pm 1)^{\circ}$C with humidity $\sim$ 70 %. The population of dust particles in this environment was about 2000 particles per cubic foot for particles larger than 0.5μm. At this stage of R&D, the stacking of copper disks was done with hand by an operator. As each disk is placed on the V-block, the rotational alignment is checked by the setup shown in Fig. 7.22(B). The inclination angle of the surface of the disk is measured with the autocollimator and recorded.

It takes typically a few minutes to place each disk on the stack. Fig. 7.23 shows a histogram of disk-to-disk alignment variation that was obtained during stacking of DDS3 disks. Stacking of RDDS1 disks has shown similar results. They indicate that, as far as hand-stacking is concerned, it is quite possible to achieve disk-to-disk misalignment of rms 1 μm or better. Automation of the stacking procedure with robotized machines is an important subject of future research.
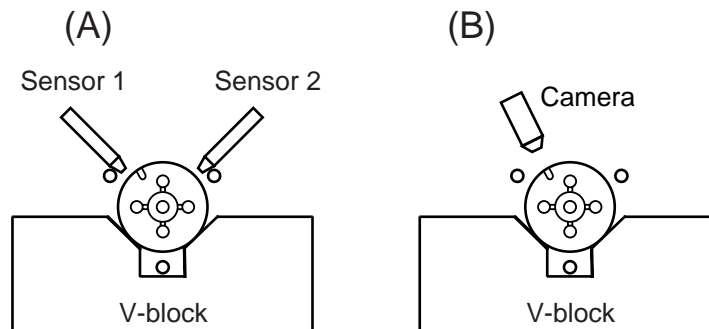
Figure 7.22: *(A) Pair of sensors used for measurement of transverse alignment of the disks on the V-block. (B) Viewing of the notch marks on the disk OD surface for rotational alignment of disks.*
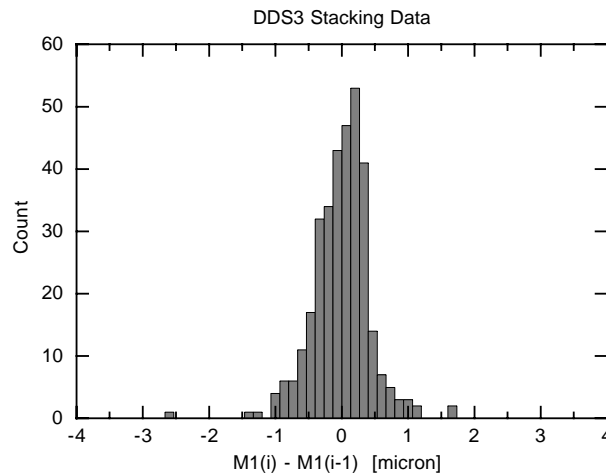
Figure 7.23: *Distribution of random disk-to-disk misalignment of DDS3 disk in a direction of one of the sensors.*

7.4.4   Diffusion Bonding

In the past several years diffusion bonding technique has been used as the primary method for forming bonded bodies of prototypes of X-band accelerating structures.

In previous prototypes, such as M2 and IH1[6][2, 15], all the disks were first stacked then bonded in a vacuum furnace as a whole body. These structures comprised of 150 pieces of copper disks with $OD = 80$mm. The total lengths of M2 and IH1 were both 1.3 m. The typical bonding condition included: vacuum level $\sim 5 \times 10^{-3}$ Pa and heat processing for 4 hours or more at temperature higher than 850°C. In the vacuum furnace, the disk stack was vertically hung, and an axially pressing force of 16 $\sim$ 40 kgf was applied at the top of the stack with a set of weight loads. In both cases, the bonding was successful, and in particular, the M2 model was tested at the ASSET facility of SLAC

---

[6]These are code-names of prototypes of detuned structure built in 1994 through 1997 by KEK.

	Temperature	Duration	Compression Pressure	Compression Force*	Configuration
Pre-bonding	150°C	24 hrs	~ 260 g/mm^2	600 kg with a steel spring	Held on a V-block, tilted at 60°
Final bonding	> 850°C	4 hrs	~ 10 g/mm^2	22 kg with metallic weight	Vertically hanging

Table 7.3: *Typical bonding conditions that were applied for assembly of DDS3 and RDDS1 prototypes. *Both prototypes had the disk OD of 61 mm.*

to show that the concept of detuned structure functions as intended[2].

When the diameter of disk is decreased to 61 mm, or when the number of disks to use is increased, concerns arise with regards to the mechanical stability of the stack during diffusion bonding. A scheme of two-step diffusion bonding was developed to address this issue[15] and was successfully tested with another prototype structure MD1. The MD1 comprised of 200 pieces of copper disks with $OD = 61$mm. In this two-step diffusion bonding scenario, the stacked disks are first "pre-bonded" in a lower temperature environment (~ 150°C) for ~ 24 hours, with a much larger axial compression force, 600 kgf. In this low temperature environment, while the copper disks are not deformed by the compression force, a substantial number of bonded spots are formed at the disk-to-disk boundaries. A test measurement showed that this pre-bonded junction could withstand a sheer force of 20 kgf.

After some studies and testing this two-step diffusion bonding technique was adopted for assembling DDS3[16] and RDDS1 prototypes, both of which have a 61mm OD and ~ 1.8 m length. The heat processing used to bond DDS3 and RDDS1 had very similar parameters. They are summarized in Table 7.3.

Pre-bonding was performed while the disk set is held on the V-block which was used for disk stacking. To prevent the disks from moving transversely when the large axial compression force is applied, the disk stacks were firmly pressed onto the V-block via three sets of viton pieces which were secured by a series of U-shaped stainless steel clamps. These devices were attached on the V-block while the disks are being stacked on the frame as shown in Fig. 7.21. The axial force was applied by using a steel spring, which was compressed by an hydraulic jack at the top of the stack. Then the V-block was removed from the stacking frame and placed on another support frame dedicated for pre-bonding. Fig. 7.24 shows the support frame for the V-block during pre-bonding. This support frame can be tilted from the horizontal up to 60°. Attaching and detaching the V-block is done while the frame is set horizontal, while pre-bonding is done with the frame tilted at 60° so as to fit inside the furnace.

After completing the pre-bonding, the disk stack is removed from the V-block and suspended vertically from another support frame, made of stainless steel. Fig. 7.25 shows a schematic diagram of the support frame and the disk stack in a set in the final diffusion bonding.

Special attentions were paid to clean all fixture components (almost all of them made of stainless steel) to keep the clean conditions in the furnace. All components were pre-baked prior to diffusion bonding.
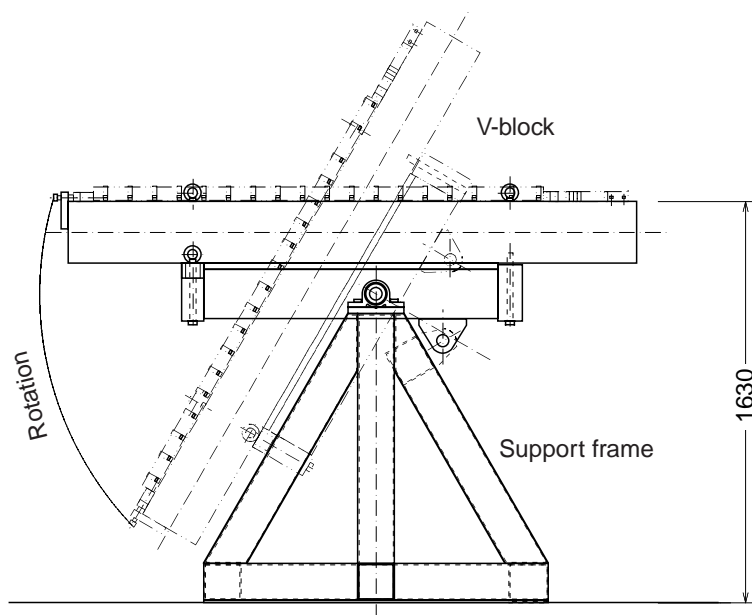
Figure 7.24: *Support frame for the V-block during pre-bonding. It is made of stainless steel to withstand the vacuum environment under temperature up to* $\sim 200°C$.

For the final bonding, a boron nitride chemical was applied to the metal-to-metal junctions, wherever it was necessary to prevent accidental diffusion bonding between fixture components. Cylindrical ceramic pieces were used between the copper disk stack and fixture components.

Fig. 7.26 shows the disk alignment of RDDS1 stack after completing the final bonding. An excellent disk-to-disk alignment of the order of 1 μm has been achieved. However, a substantial bowing of the order of $200 \sim 300 \mu$m had developed. Similar bowing also occurred with DDS3. The exact cause of the bowing is not completely understood yet. Fortunately this smooth bowing is relatively easily corrected to the level of 10 μm by applying corrective transverse forces, since the copper material is very soft due to annealing effects of diffusion bonding. While this is a welcome feature, it also means that care must be taken to protect the structure from unwanted forces during and after installation on the beamline.

While the two-step diffusion bonding procedure worked well for DDS3, the mechanical measurement at SLAC uncovered the presence of large bookshelving errors (Fig. 7.19(C)). Later investigation revealed that evidence of this bookshelving had actually been observed during the disk stacking process. Fig. 7.27 shows the inclination angle (tilt of the symmetry axis with respect to the V-block) of each disk, when it was placed in the V-block during stacking. The measurement was done with a single-axis autocollimator for DDS3 (black circle). Large bookshelving errors up to 1 mrad is seen, consistent with SLAC measurements. This error was so large that it was assumed to be some instrumentation problem, and no corrective action was attempted before proceeding with bonding.

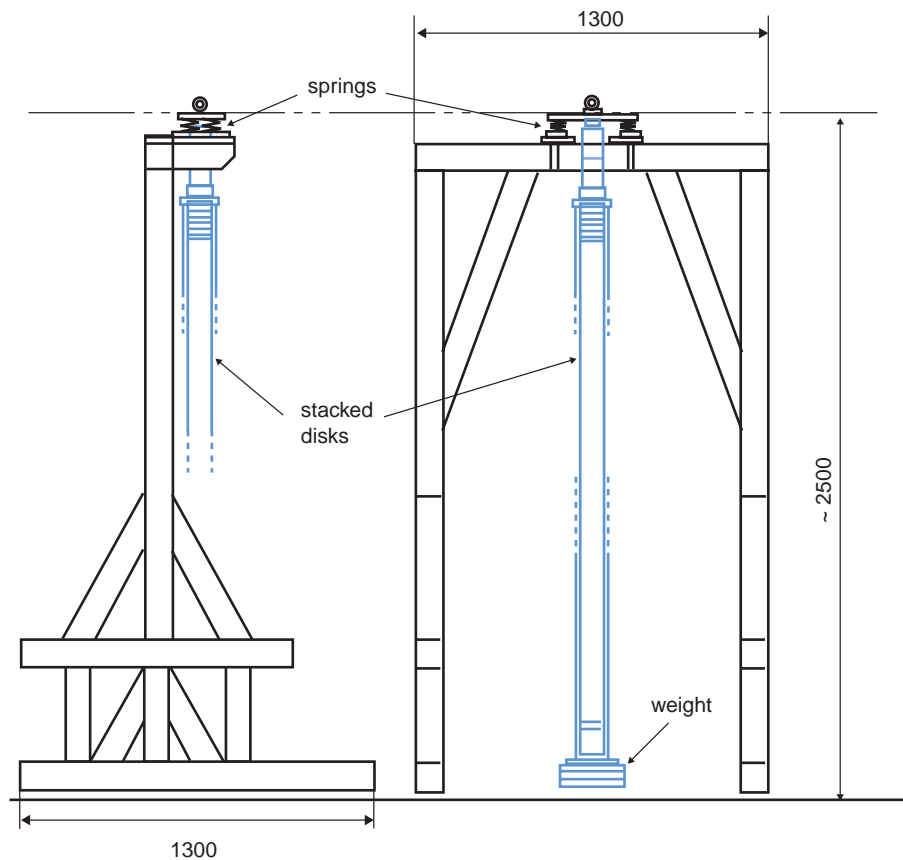Before stacking RDDS1 disks, some studies were done to understand how bookshelving errors to occur

Figure 7.25: *Support frame for the final diffusion bonding.*

during disk stacking. A new, two-axis autocollimator was introduced to provide better analysis of disk inclination angles. Dummy copper disks, mimicking the features of RDDS disks, were fabricated and used in stacking experiments. In the initial tests, the development of bookshelving errors appeared quite reproducible, as long as the same disk stacking order was maintained. This is indicative that the bookshelving originates from small errors in the parallelism of each disk or from surface defects. However, it is difficult to draw firm conclusions at this point, since the pattern of bookshelving errors became rather unpredictable after several trials.

As an interim solution for the stacking of RDDS1 disks, the operator was instructed to hand-press the end planes of each disk to keep the error in the disk inclination angles below $\sim 100\mu$rad. This worked well. The resultant inclination angle errors of stacked disks, measured with autocollimator during stacking, are displayed in Fig. 7.28, which shows a vast improvement over Fig. 7.27.

Another issue which was observed with DDS3, but in this case not quite solved with RDDS1, is transverse deformation of copper disks near the top and bottom ends. Apparently a metal-to-ceramics bonding develops at the two ends during the diffusion bonding at a temperature of $\sim 900°$C where the copper diameter is heat-expanded by $\sim 500\mu$m. When the temperature is later lowered, the disks in
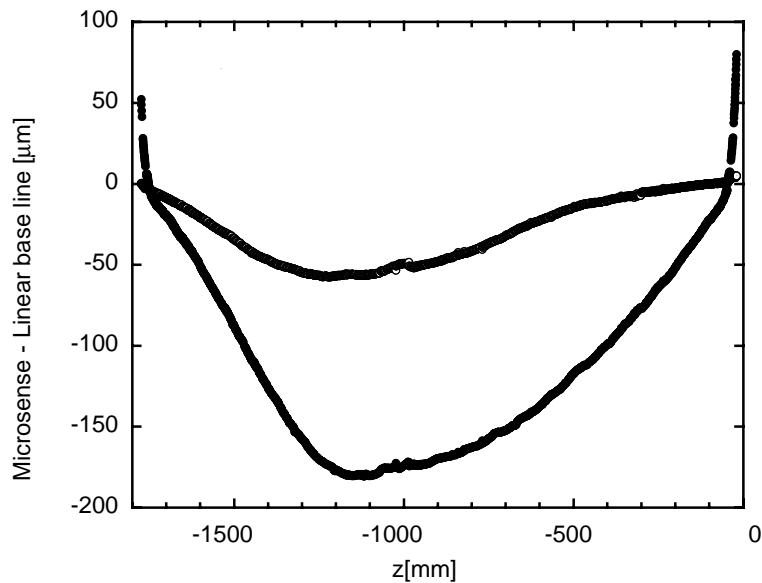
Figure 7.26: *Transverse disk alignment of RDDS1 stack after completing the diffusion bonding process.*

the mid-portion of the stack shrinks accordingly, while the end disks cannot, because of the bond with the ceramics which has a much smaller heat expansion coefficient. Consequently a gradual increase of *OD* near the stack end takes place. While it appears possible to correct this dimensional error after diffusion bonding, its recurrence should certainly be prevented. Development of its solution in the diffusion bonding process is one of the important tasks for the next RDDS prototype.

Fig. 7.29 shows a picture of the completed RDDS1 disk stack after diffusion bonding. The disk stack was then shipped to SLAC and preparation work towards its testing of wakefield characteristics at ASSET facility is presently under way.

In conclusion, the two-step bonding process was successfully applied for DDS3 and RDDS1 and it produced good bonding with excellent disk-to-disk alignment. Incidences of global bowing and deformation of end disks will be addressed with the construction of the next prototypes. In addition, a critical study item for the future is the development of a mass production scenario.
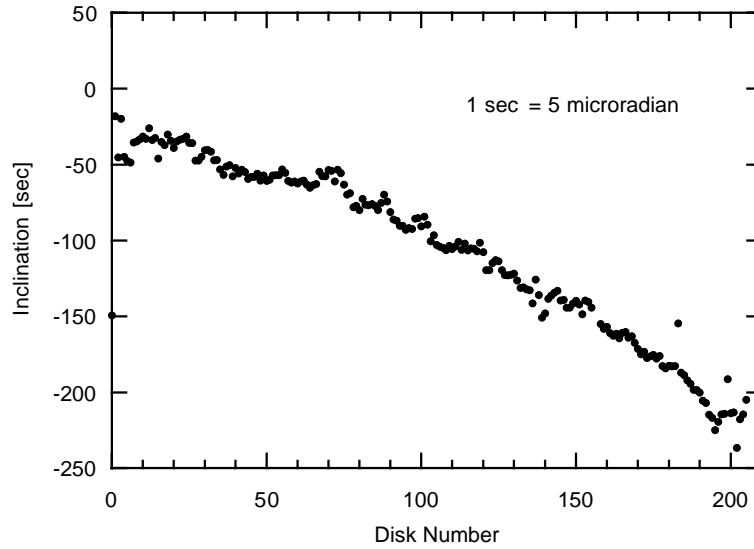
Figure 7.27: *Measured inclination of the top most disk during stacking work of DDS3. Measurements were done by using a single-axis autocollimator.*
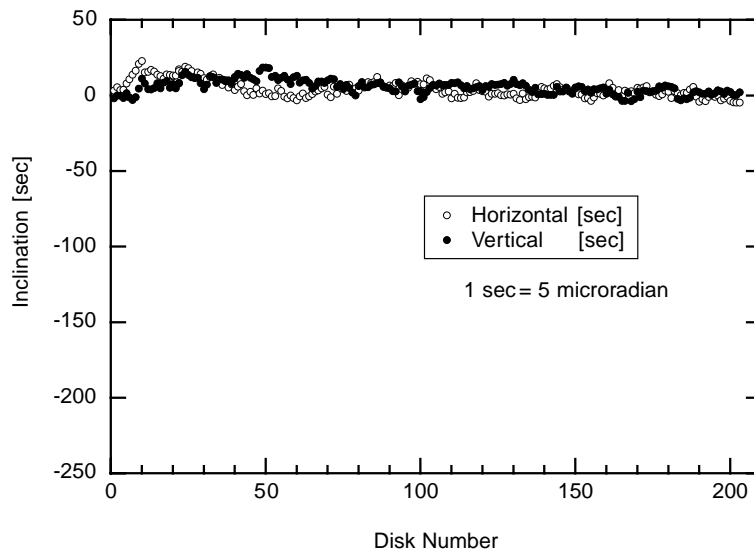

Figure 7.28: *Measured inclination of the top most disk during stacking work of RDDS1. Measurements were done by using a 2-axis autocollimator.*

Figure 7.29: *Completed RDDS1 disk stack after diffusion bonding.*

7.5   Measurement of Wakefield Characteristics

7.5.1   Introduction

The damped and detuned accelerating structures were designed using an equivalent circuit model to obtain their dipole mode characteristics[7]. Although this model is quite complex, it still contains approximations, and it models only the lowest two bands of dipole modes. For these reasons, it was considered necessary to measure the structure wakefields to check the accuracy and completeness of the model. In addition, it was important to assess the effect of cell fabrication errors on the wakefields, since these cannot be readily modeled because the errors are not known in detail. This led SLAC to build the Accelerating Structure Setup (ASSET) facility which was installed in the upstream end of the SLAC Linac, just after the electron and positron bunches are injected from the damping rings.

Fig. 7.30 shows a plan view sketch of ASSET with a DDS structure installed. To measure the transverse wakefield of the structure, the positron bunch served as the drive bunch and was extracted from the South Damping Ring and injected into the main linac via the South-Ring-To-Linac (SRTL) transport line. In the linac, this bunch passed through the structure and was then steered onto a dump. The magnet used for this purpose is also the first bend of a chicane which transported electrons back onto the linac axis. The electron bunch served as the witness bunch, and was extracted from the North Damping Ring at a later time and injected on axis into the linac via the North-Ring-To-Linac(NRTL) transport line. When traversing the structure, the witness bunch was deflected by the wakefield generated by the drive bunch. The witness bunch then passed though the chicane and into the linac where its trajectory was recorded by beam position monitors (BPMs) located in each of the quadrupole magnets. By changing the transverse position of the drive bunch in the structure and measuring the resulting changes to the witness bunch deflection, the transverse wakefield was determined.
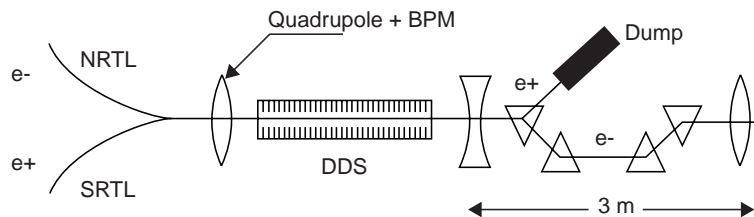

Figure 7.30: *Layout of the ASSET Facility*

The wakefields of two of the damped and detuned structures, DDS1[18] and DDS3[19], have been measured to date. During the measurements, the structures were maintained at their nominal operating temperature, and their input and output RF couplers were terminated with matched loads. The manifold ports were connected via Heliax cables to processing electronics in the Klystron Gallery above the linac tunnel. The signals were either measured with a spectrum analyzer or down-mixed

to 310 MHz and digitized to determine their amplitude and phase. A signal from a nearby stripline BPM served as the beam phase reference.

In the following two sections, highlights from these measurements are presented.

DDS1 Measurements

DDS1 was measured in 1996 over a two day period. The relative bunch timing was stepped in 8.4 ns multiples from 0 to 150 ns, and by 1.4 ns multiples in regions of interest. At each setting, a continuous bunch timing control was used to locally map the wakefield at 31 points in a $\sim$ 190 ps range. For each of these measurements, the drive beam was moved transversely relative to the structure in 2 mm increments from -2 mm to +2 mm using dipole corrector magnets in the SRTL. The measured witness bunch deflections and drive bunch intensities were then used in a straight line fit to extract the wakefield strength.

Fig. 7.31 shows two examples of the local wakefield mapping, one near the bunch crossing (t = 0), and one where the bunches were about 118 ns apart. The solid line in Fig. 7.31a is a fit to the data. The fit function is a prediction for the short-range wakefield of a point charge that was obtained by summing the synchronous mode contributions from a periodic structure with an iris radius equal to that of the middle cell in DDS1. Here the damping and detuning are ignored since their effect is small on this time scale. The fit allows for a scale factor, which has been applied to the prediction, and a relative time shift, which has been applied to the data. Also, the prediction was smeared assuming longitudinal Gaussian bunch profiles with a sigma equal to 470 μm, a value obtained from a fit to just the $t < 10$ ps data in which the bunch length was allowed to vary as well. This result, which has error of 50 μm, is consistent with the value of 550 μm expected from SLC bunch length measurements. However, the resulting scale factor of 85 % is not consistent with unity. The cause of this disagreement is not understood.

Fig. 7.31b is typical of the measurements at later times in that there are no apparent contributions from higher frequency dipole bands. One exception occurs at 25.2 ns where the data show a 25 GHz oscillation which likely originates from modes in the third dipole band. The solid line in the figure is a fit to the data of a sine function with a 15.1 GHz frequency, the mean value for the first dipole band. In some data sets, one sees a variation of the oscillation amplitude which can be as large as 50 % over a few periods. This beating effect is an expected result of the mode detuning.

From the oscillation fit, which averages over any beating, a wakefield amplitude was obtained for each local mapping. At most time settings, at least two measurements were made of the vertical amplitude and one of the horizontal. The averaged vertical results are shown in Fig. 7.32 together with the prediction from the equivalent circuit model of the structure. One sees that the data agree reasonably well with the theory although the recoherence point around 120 ns is about 10 % later than predicted. The horizontal results show a similar agreement and in most cases are consistent with the vertical results within the measurement errors.
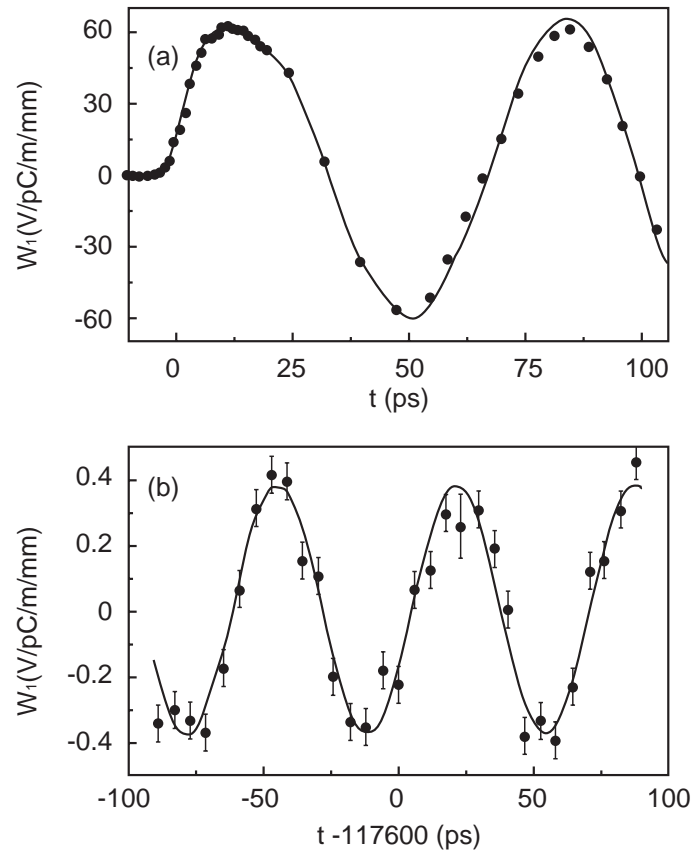
ISG Progress Report, April, 2000

Figure 7.31: *Dipole wakefield which was measured (a) near the bunch crossing, and (b) at a bunch separation of about 118 ns. The measurement errors in (a) are less than the size of the data point plot symbols. The solid lines are described in the text.*

DDS3 Measurements

In 1998, the wakefield of DDS3 was measured in a similar manner to DDS1. The data are shown Fig. 7.33 where they are plotted as a function of the square root of the relative beam time so values at short times are more discernible.

Although the initial falloff of the wakefield is large, it was expected to stay below about 0.5 V/pC/m/mm out to 20 ns, instead of rising to values near 4 V/pC/m/mm as was observed. This difference is likely the result of the cell fabrication errors being larger than the design tolerances. The effect of such errors are included in the predictions in Fig. 7.33. In the top plot, the errors are based on limited cell QC measurements made prior to the structure assembly. They are essentially equivalent to random cell-to-cell 5 MHz rms Gaussian frequency errors, and are larger than the ~ 2 MHz rms design tolerance. In the bottom plot, the errors were increased to best match the wakefield measurements, which required 12 MHz rms values. Thus, the actual cell errors may be larger than the QC results indicated or more systematic in nature, which can enhance their effect.
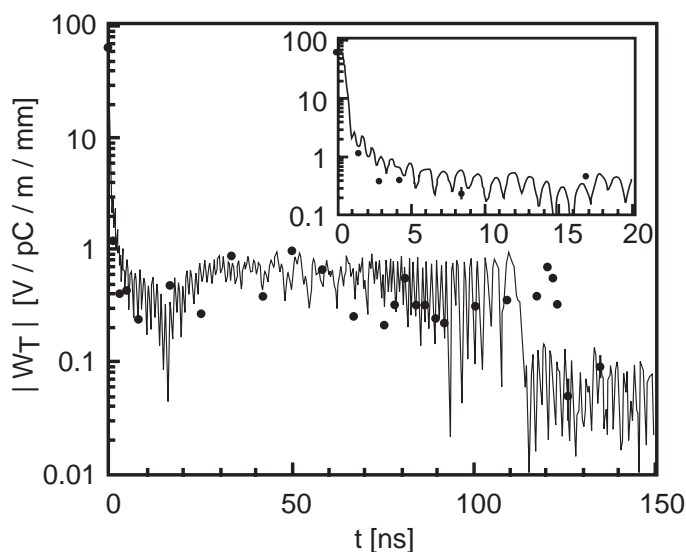
Figure 7.32: *Vertical wakefield amplitude measurements (data points) and prediction (solid line).*
The insert shows an expanded view of the first 20 ns.

Besides measuring the wakefield of DDS3, beam centering tests were done using the dipole mode
signals from the damping manifolds to measure the transverse position of the beam in the structure.
Since the beam coupling to the modes is fairly localized (2 to 10 cells) the signals were filtered by
frequency to yield the beam offset at a particular location along the structure. The NLC/JLC goal is
to use such signal information to keep the beams centered in the structures to about $\pm$ 20 μm.

As a test, data were taken in which the beam was stepped transversely across the structure while the
signal from a 15 MHz slice of the 14∼16 GHz dipole spectrum was processed. Fig. 7.34 shows data
taken at 15.0 GHz. As expected, a 180 degree phase transition occurs when the signal power goes
through a minimum. The solid lines in the plots are fits to the data: a parabola to the power and an
arctan function to the phase. In each case, a fit parameter was included to account for the addition of
an out-of-phase signal component. The size of this component is conveniently expressed in terms of
an equivalent beam offset, that is, the beam displacement relative to its position at minimum power
that increases the dipole power by an amount equal to the out-of-phase power. The phase data yields
the best measure of this offset, 5 ± 2 μm. However, values as large as 100 μm were initially observed.
After some study, it was realized that an X-Z correlation along the bunch (σ_Z =3D 0.7 mm) was
the likely source. This correlation was reduced by tuning the dispersive properties of the beamline
to decrease the horizontal bunch width. Thereafter, the measured offsets were generally smaller than
the NLC beam centering tolerance, which is desirable since it will simplify signal processing in the
JLC/NLC.

Another parameter obtained from the fits to the dipole signal data is the beam position at the minimum
signal power. These values provide a measure of the structure straightness when plotted versus the
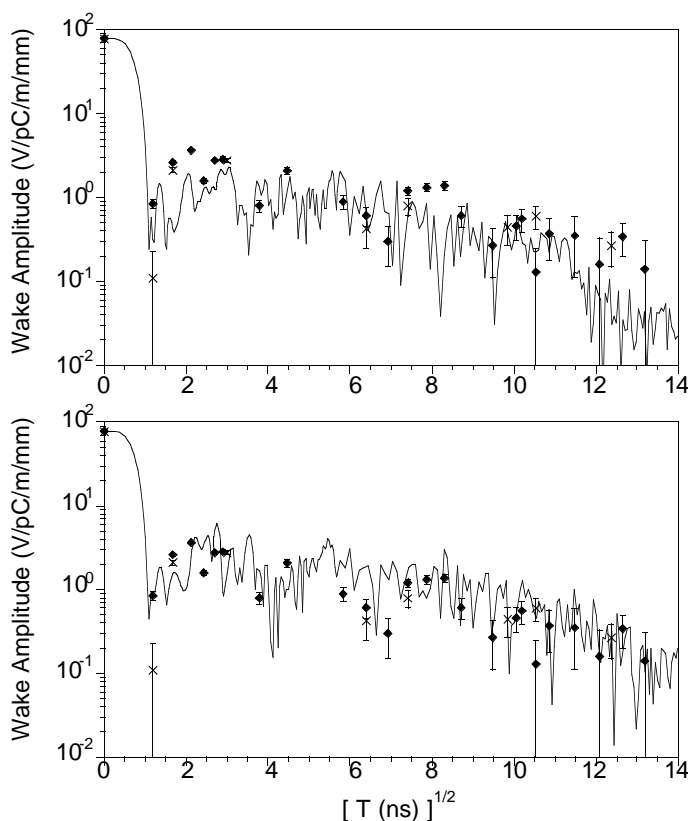corresponding point of origin of the signal (on average) along the structure.

Figure 7.33: *Horizontal (crosses) and vertical (diamonds) wakefield measurements and predictions (solid lines) including 5 MHz rms cell frequency errors (top) and 12 MHz rms frequency errors (bottom).*

Fig.7.35 shows the horizontal straightness results that were derived using the frequency to cell mapping obtained from the equivalent circuit model of the structure. Also shown are straightness results from a pre-installation survey of the outer surfaces of the cells (30.5 mm radii) that was done with a Coordinate Measuring Machine (CMM). The good agreement between these measurements, and the μm level local straightness of the structure, attest to the high precision with which the cells were fabricated and assembled. The vertical CMM and beam-based results agree less well, although a post-run survey of the structure indicates that it had vertically distorted by about 30 μm after the initial survey.

7.5.2 Measurement Summary

From the DDS1 results, we have shown that the basic approach of damping and detuning works and that we can model the wakefields reasonably well. The DDS3 beam centering results demonstrate our ability to produce a straight structure and to determine the beam position within it to high precision. For our next structure, RDDS1, the cell fabrication errors are much smaller than in DDS3,
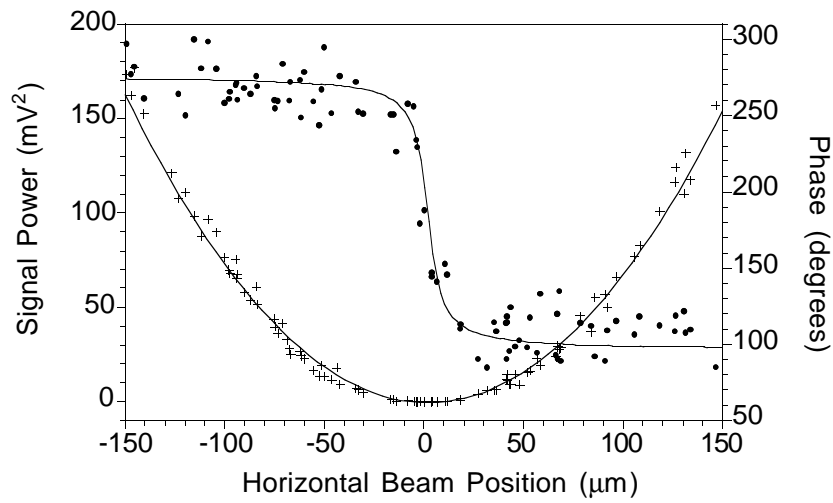
Figure 7.34: *15 GHz dipole signal power (pluses) and phase (circles) versus beam position. The fit to the data (solid lines) are described in the text.*
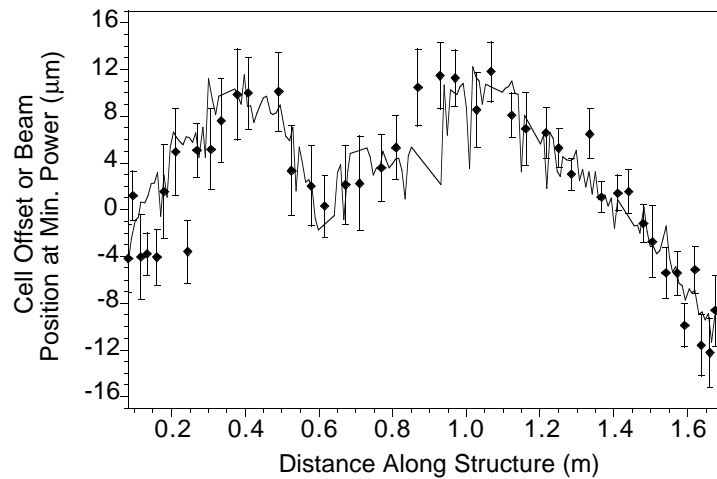

Figure 7.35: *Horizontal structure straightness measured with a beam (diamonds) and a CMM (solid line).*

and the damping and detuning are better optimized than in DDS1, so the ASSET measurements should demonstrate an even lower wakefield than for the earlier structures.

7.6 High-Power Testing of Accelerating Structures

7.6.1 Introduction

The basic requirement of the NLC/JLC structures is to accelerate the beams at an unloaded gradient of 72 MV/m. To reach such a gradient, however, we have found that it takes several hundred hours of conditioning during which the input power is limited due to RF breakdown in the structure. At present, the ultimate gradient that can be achieved with our current structure design is not clear. Early tests on short structures offered hope that gradients of over 100 MV/m are attainable. Testing longer structures that better represent the current design parameters, however, has demonstrated that pushing gradients past 80 MV/m is quite difficult.

One of the limiting factors is the surface damage to the cell irises caused by RF breakdown. If it is severe enough, it will alter the RF performance. In addition, dark currents may limit operational gradients since the currents absorb RF energy, decreasing the accelerator gradient. Otherwise, the dark currents are not a big problem since they are dispersed by the quadrupole magnets between the structures.

The electrical and physical properties of the cell may include many factors that both affect the rate of processing as well as limit the maximum achievable gradient. Such factors include circuit parameters (such as energy storage per cell), surface quality (machining finish, contaminants), and vacuum quality (pumping speed). Unfortunately, there is currently no physical theory of RF breakdown that predicts performance as a function of these parameters.

Several early SLAC 1.8m structures have been tested to accelerating gradients of 68 MV/m and were limited by available power. They were not manufactured, however, with the cleanliness and precision used in recent structures. The latest tests[21] of the KEK M2 structure offer a closer comparison to current structure design. Lastly, the results are not altogether definitive but serve as a guide to future experimental investigations.

7.6.2 Experiment

In 1996, KEK built a 150 cell, 1.3 m long structure (referred to as M2) to test the effect of detuning on the long-range transverse wakefield. After its wakefield was measured in ASSET it was kept in vacuum of 10^{-9} Torr level for two years. Just before the high power testing it was baked in situ at 250°C for two days. It was then processed to high power in the Accelerating Structure Test Area (ASTA) at SLAC. The setup and results are described below.

Setup

Two 50 MW X-band klystrons operating at 11.424 GHz and 1 μs pulse width combine in a magic tee to feed a SLED-II pulse compression system. The output 150 ns RF pulse then feeds the accelerator structure test area (ASTA). All system components before the accelerating structure were previously tested to more than 300 MW at this pulse width at a repetition rate of 60 Hz. At this power, the average accelerating field in the M2 structure would be well over 100 MV/m. Pairs of vacuum pumps located near the input and output couplers monitor gas activity. Since there is no pumping in the structure cells, these pumps, along with the beam line pump, supply a limited pumping speed for the bulk of the structure.

SLED and structure input powers are measured with a HP peak power meter. A crystal detector measuring reflected power is interlocked to remove triggers to the low-level drive of the klystrons for reflected peak power exceeding 5 MW. This interlock is meant to protect the klystron windows but it also prevents large gas bursts in the accelerating structure caused by multiple arcing. One downstream Faraday cup measures dark current and another off-axis Faraday cup measures the dark current energy spectrum using a spectrometer. Radiation levels are monitored with 3 scintillators along the structure and a calibrated radiation meter measures contact levels at the input or output ends.

Over the several week test, the high voltage running time meter logged more than 560 hours of which an estimated 440 hours can be considered as active processing. At the 60 Hz repetition rate, this time gives approximately 1×10^8 total pulses, a factor of 4∼5 greater than the number of pulses used in previous structure tests at SLAC.

7.6.3   Results

A PC system running LabVIEW handled the majority of processing by adjusting power levels based on structure vacuum and reflected arc interlock trips. Details of the algorithm are beyond the scope of this paper but the overall strategy for conditioning remained consistent between operator and computer control. The first 100 hours were mainly processed by hand to the 60 MV/m level. During this time, as indicated in Fig. 7.36, the SLED compression was not phased for maximal gain in order to allow average power heating to help out-gas the structure.

Even at a conservative pace, only 20 hours were required to reach 50 MV/m average gradient and the structure suffered only a handful of reflected power trips due to RF breakdown. At higher power, once arcing started, gas bursts and vacuum recovery limited progress. After the first 150∼200 hours, gas activity associated with breakdown became quite negligible and the only problem was reflected power trips. Although progress slowed dramatically, continued processing still seemed to increase the achievable peak power. Reversing the axes of the previous plot reveals an exponential behavior.

At the end of testing, the average gradient reached 85 MV/m and was sustainable for ∼10 seconds before arcing. At 75 MV/m, however, the structure ran for one hour without any arc trips. Previous
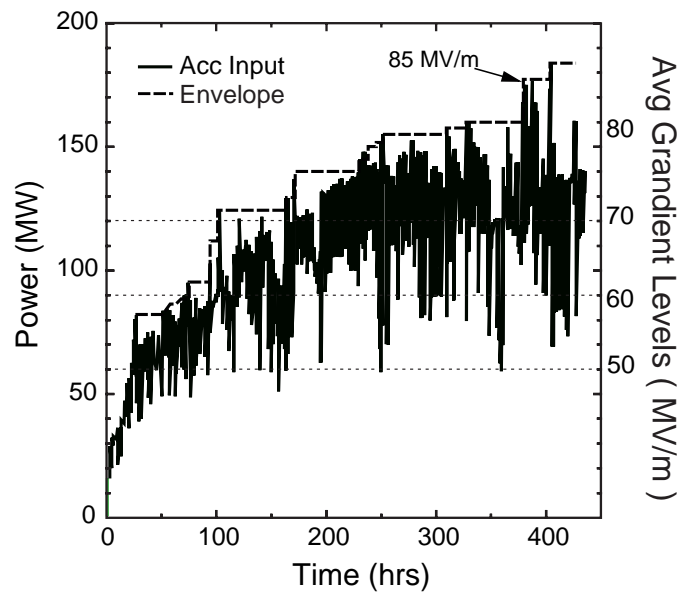
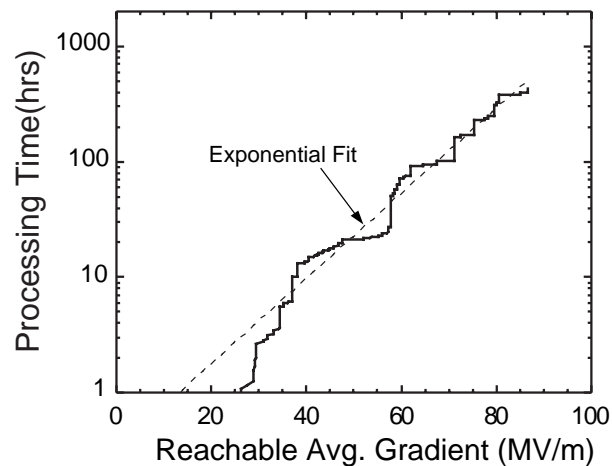**Figure 7.36:** *M2 active processing history.*

Figure 7.37: *Time required to reach desired gradient using monotonic envelope from Fig. 7.36.*

tests of the SLAC 1.8m DS1 structure reached gradients of only 68 MV/m and were limited by available power. Both structures showed similar patterns in processing difficulty, dark current emission, and dark current energy spectrum. Fig. 7.38 shows the peak dark current readings from the downstream Faraday cup for M2, and also for DS1. It should be noted that the amount of the dark current depends on the structure length, beam hole diameter, cutoff beam pipe diameter and its length. We consider that apparent differences between M2 and DS1 are likely to be due to their effects. The dark current measured at a particular gradient did not steadily improve during processing as had happened in the
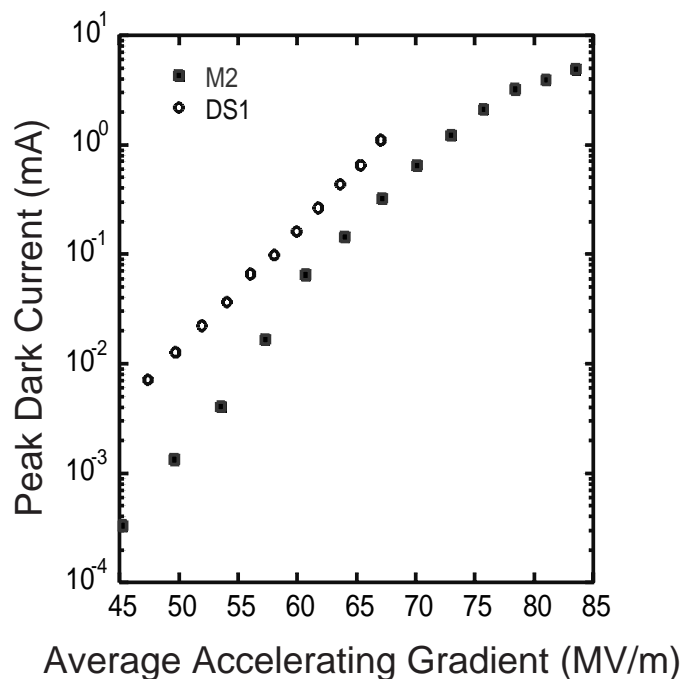
DS1 tests.

Figure 7.38: Measured dark current with M2 and DS1.

A conservative estimate of 3000 arcs occurred at average gradients over 50 MV/m. Once the high power test finished, the structure was visually inspected with a boroscope to evaluate the extent of damage to the cells. The output end showed no discernible damage to the cells; the copper still had a diamond-turned surface with grain boundaries easily identified. In marked contrast, the input cells were heavily damaged (but only the first 30 cells could be viewed); the cell irises were completely pitted with no sign of the original machined surface finish remaining. Both ends of the structure reached equivalent average gradients, but the dynamics of RF breakdown seem to protect the downstream cells from arcing at the expense of the upstream cells.

Conclusions

In summary, the M2 structure test achieved several milestones. With the aid of computer assisted processing, the total number of integrated pulses in conditioning approached 1×10^8. Stable and achievable gradients of 75 MV/m were demonstrated in a usable accelerating structure. The effects of intensive conditioning were also easily seen and quantified. As a result, tests are underway at SLAC to better understand arc formation and the mechanism of RF breakdown, particularly in long structures.

ISG Progress Report, April, 2000

7.7 Conclusions and Future Prospects

The ISG collaboration has been extremely productive and expedited the development efforts on X-band accelerating structure for JLC/NLC. Measurements of wakefield characteristics of earlier proto-type structures showed good agreement with the modeling calculation, giving very encouraging results for the real-life implementation of the Damped-Detuned structure concept at NLC/JLC. A major progress has been made in development of the new Rounded Damped-Detuned structure, where the elaborated procedure for the disk electrical designs was established in tight combination with the solid advancement of fabrication, assembly and numerous quality assurance techniques. In parallel to these, a number of R&D issues have been identified for the near-future efforts:

1. Re-evaluation of numerous types of acceptable fabrication and assembly errors is required for beam operating conditions that are simulated as realistic as possible. Some tolerances may turn out looser than what are conceived now, some other may go the opposite. The findings will undoubtedly provide important pointers to fabrication and assembly QA/QC issues to be emphasized or deemphasized in the near future.

2. Re-evaluation of the f_1 distribution to use, the arrangement of HOM extraction to implement, and other aspects of electrical design are needed to further improve the expected performance of the accelerating structure, both in terms of beam acceleration and HOM reduction control. Estimation of dipole modes higher than the second order is also required.

3. A large class of issues associated with mass fabrication and assembly of required copper disks, automation of the production line, QA/QC techniques are required to be studied. Their study is still at its infancy at this moment.

4. While the prototype accelerating structures demonstrated good conditioning performance up to 50 MV/m in high-power testing, steady operation at the target value of unloaded gradient 75 MV/m is yet to be firmly established. At the same time, the vacuum level inside the structure during high-power operation needs to be established and confirmed.

5. Complete engineering design of the total linac system, including the support and alignment mechanism, accelerating structures, waveguides, power distribution systems, klystron, modulator and associated control and instrumentation electronics, needs to be established. Demonstration of a "string test" of such a system will be a major R&D agenda in the coming several years.

The ISG group has already started addressing some of these issues by the efforts towards the second RDDS prototype, RDDS2. Given the achievement made in the past two years, it is expected that the ISG collaboration, if continued, should be able to play leading roles in addressing other remaining issues as well.

References for Chapter 7

[1] Zeroth-Order Design Report for the NLC, 1996, SLAC-PUB-5214.

[2] JLC Design Study; KEK report 97-1, April 1997. p.335.

[3] 55 MV/m is the loaded gradient, while 70 MV/m is the unloaded gradient that is expected at JLC/NLC.

[4] H. Deruyter et al., Proc. EPAC90, June 1990, SLAC-PUB-5214.

[5] R.H. Miller et al.,"A Damped Detuned Structure for the Next Linear Collider," SLAC-PUB-7288, LINAC 96, Geneva, 26-30 Aug., 1996.

[6] "MAFIA User's Guide," CST GmbH, Darmstadt, Germany.

[7] R.M. Jones, K. Ko, N.M. Kroll, R.H. Miller, "A Spectrum Function Method Applied to the Calculations of the Wake Function for the NLCTA," SLAC-PUB-7287, LINAC 96, Geneva, 26-30 Aug., 1996.

[8] Z. Li et al., "RDDS Cell Design and Optimization for the Linear Collider Linacs," SLAC-PUB-8224, PAC99, New York City, March 29 - April 2, 1999.

[9] G. Bowden et al., "A Compact RF Power Coupler for the NLC," SLAC-PUB-8395, PAC 99, New York City, March 29 - April 2, 1999.

[10] J.W. Wang et al., PAC91, SLAC-PUB-5498.

[11] T. Higo et al., Proc. APAC98, March 1998, Tsukuba, Japan.

[12] J. Klingmann et al., "Fabrication of DDS-3, an 11.4 GHz Damped-Detuned Structure," PAC99, New York, 1999.

[13] Y. Higashi et al., "Studies on High-Precision Machining of Accelerator Disks of X-band Structure for Linear Collider," KEK Report 2000-1, April, 2000.

[14] T. Higo et al., "Feasibility Study of 2-D Machining of RDDS1 Disks," LCC note, in preparation, April, 2000.

[15] Y. Higashi et al., "Study on High-Precision Diffusion Bonding for X-band Accelerating Structure," KEK Report 2000-2, April, 2000.

[16] T. Higo et al., "Studies which Resulted in Successful Main-Body Bonding of DDS3 Structure.", LCC note, in preparation, April, 2000.

[17] G. Stupakov, presentation at ISG3, SLAC, Jan., 1999.

[18] C. Adolphsen et al., SLAC-PUB-7519, May, 1997.

[19] C. Adolphsen et al., SLAC-PUB-8174, Sep, 1999.

[20] M. Seidel, SLAC-PUB-7557, June, 1997.

[21] R. Loewen et al., "SLAC High Gradient Testing Of A KEK X-Band Accelerating Structure" SLAC-PUB-8399, 1999.

Authors and Major Contributors of Chapter 7

- C. Adolphsen
- K. Asano
- G. Bowden
- Y. Funahashi
- Y. Higashi
- T. Higo
- N. Hitomi
- R. Jones
- J. Klingmann
- N. Kroll
- Z. Li
- R. Loewen
- R. Miller
- C. Ng
- C. Pearson
- R. Ruth
- Toshikazu Suzuki
- T. Takatomi
- N. Toge
- J.W. Wang
- Y. Watanabe

CHAPTER 8

Collimation, Final Focus and Interaction Region

Contents

8.1   Introduction

8.1.1   Description of Beam Delivery System and Interaction Region

The Beam Delivery System is a sequence of beam lines which prepare the beam produced by the main linac for collision at the Interaction Point (IP). While the acceleration technologies adopted by different linear collider designs for their main linacs vary considerably, all designs have beam delivery systems which contain approximately the same subsystems in the same order:

- A collimation system which removes particles at large amplitudes in position, angle, or energy; such particles would otherwise generate backgrounds and/or radiation; either by synchrotron emission in magnets or by impacting the vacuum chamber of the accelerator and producing an electromagnetic shower

- An achromatic arc which permits the beams to collide with a small horizontal angle, and which provides additional protection against muons for the detector

- A final focus system which performs the demagnification of the beams down to the small sizes required for luminosity production, and which uses sextupoles in a dispersive region to cancel the large chromaticity of the demagnifying final lenses

- An extraction line which transports the spent beams and collision debris (pairs and beam-strahlung photons) to high-power dumps some distance from the detector.

8.1.2   Performance Requirements

At the end of the linac, the high energy beam has transverse dimensions of 10-μm by 1-μm in x and y, respectively. The energy density of the compact beam can destroy most materials in a single pulse. The Gaussian core of the beam may be accompanied by a distribution of particles, commonly referred to as the beam halo, which are at large amplitudes compared to the beam core. The halo particles can cause backgrounds in the particle detector as they hit nearby apertures or radiate synchrotron photons in the strong fields of the final focusing magnets. The focusing properties of the beam delivery system are a strong function of energy, and, therefore, particles which are different in energy from the design by more than a few percent also pose a risk of backgrounds.

The collimation section of the accelerator must remove all particles which are likely to generate backgrounds, either by virtue of their amplitudes or their energies. Typically this is done by inserting a metallic scraping element close to the beam, although non-linear magnetic elements are also being considered. The interaction of the halo with the collimator material produces muons; the overall system must be designed so that these particles do not themselves form an important background

for the detector. At the linear collider, building a collimation system is made difficult because of the energy density of the beam and because the collimator may induce wakefields that can amplify beam jitter, increase emittance, and enlarge the final beam spot size.

In addition to protecting the detector from backgrounds caused by particles which are far from the design orbit or energy, the collimation system protects the detector and the final focus from being damaged by full bunch trains which are outside the collimation envelope. Klystron misfires and other hardware failures may make this a relatively frequent occurrence.

In order to maximize efficiency, each pulse of the linac accelerates a train of approximately 90 bunches which are separated by 2.8 nanoseconds (84 centimeters). Maximum luminosity and stable operation are achieved if each bunch collides with one and only one bunch of the opposing beam. This is accomplished by colliding the beams at a shallow horizontal crossing angle (anywhere from 4 to 30 milliradians). The crossing angle is provided by achromatic arcs which are just downstream of the collimation systems on either side. The crossing angle also separates the disrupted (large-emittance) outgoing beam from the low-emittance incoming beam, allowing the outgoing beam to be transported in a beamline with a larger aperture. The arcs also provide additional protection for the detector from muons which are generated in the collimation system, since the detector is not on the flight path of most of the muons.

The clean beam must then be demagnified by about a factor of 40 (250) in x (y) to a transverse size of 235-nm (3.9-nm) at the interaction point (IP). Important design issues in the final focus include energy upgradability, tuning schemes, sensitivity to varying incoming beam conditions, and tolerances on alignment, vibrations, and magnetic field changes.

The interaction region (IR) design must be compatible with the detector and provide adequate masking against backgrounds. In addition, it must include a support platform for the final magnetic lenses, which must be stable with respect to each other to the nm level, and incorporate adequate instrumentation for measuring and maintaining the machine's luminosity. Detector backgrounds can arise from either the IP itself, through the fundamental electromagnetic and hadronic processes resulting from the beam-beam interaction, or from the accelerator elements. Questions of collimation depth, assumptions of beam halo production mechanisms, energy bandwidth of the extraction line, and magnet apertures and field gradients can determine the intensity and energy spectrum of charged particles, photon, and neutrons impacting near the IP.

8.1.3 Historical Background

Before the ISG was organized, both KEK[1, 3] and SLAC[2] published design reports on a future linear collider. These reports included detailed designs of final focus and collimation systems.

These designs were influenced to a great extent by the experience of running the SLC from 1989 through June 1998 to produce high luminosity interactions with sufficiently low machine backgrounds that the SLD physics detector could efficiently trigger and take data. At the SLC high luminosity was usually coupled to low backgrounds. When incoming beam jitter, energy tails, or beam halo were

large, luminosity was low and the detector's HV wire imaging systems could not stay on. The sense that a design must be stable, robust, and tunable permeated the thinking when designs for future linear colliders were considered.

In addition, an international collaboration, the Final Focus Test Beam at SLAC[4], was formed to prototype a final focus system with the same demagnification required for future linear colliders. This international effort was co-led by a Japanese - American team. SLAC was responsible for the assembly of the beamline while KEK provided, among other items, the optics and the laser interferometer which was used to measure the final beam spot size. The outstanding accomplishment of the FFTB was a demonstration of a 60 nm beam size at the Interaction Point. It is worth mentioning that the final result was realized only after several earlier runs of the experiment. The collaboration found and corrected the weak points in the setup, built additional instrumentation to monitor the beam, and ultimately achieved its goal.

8.1.4   Summary of ISG Activities on Interaction Region Issues

A working group was formed at the second ISG meeting in July, 1998 to study R&D issues for the beam delivery areas of a linear collider. As knowledgeable people who could work on the accelerator physics aspects of the collimation and final focus lattices were otherwise occupied, it was decided to initially limit the scope of the working group to items of importance in the area of the interaction region.

The general goals were as follows;

- Set a guideline for IR performance.

- Identify necessary hardware elements and their specifications.

- Identify and evaluate scientific tools available for designs of individual parts.

- Set efficient procedures for overall design.

- Identify R&D items.

The following sections describe some of the issues addressed by the working group and gives some summary of the results. Items which are still under discussion and future plans are described in the last sections.

8.2   Interaction Region Layout

Fig. 8.1 and Fig. 8.2 show the current concepts of the IR layout for the JLC and the NLC designs. In the JLC design the beams cross at 8 mrad and exit through the coil pocket of a conventional iron
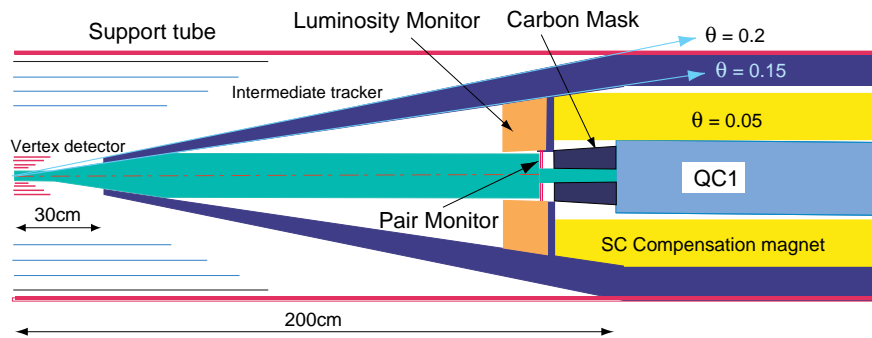
Figure 8.1: *Plan view of the currently proposed interaction region for the JLC detector.*

magnet that is shielded from the detector's solenoid field by a superconducting coil. In the NLC design the beams cross at 20 mrad, exit past the outer radius of a permanent magnet final focusing element, and are accepted by an extraction line that begins 6 m from the IP.

A critical issue is how to stabilize the beams against vertical jitter to keep them in collision. All IR designs must incorporate means to keep the relative vertical motion of the final focusing quadrupole magnets on either side of the IP to less than the design y beam spot size of 3 nm. The nanometer-scale vertical motion could be driven by naturally occurring seismic activity or by cultural sources. Cultural sources could be either self-induced (e.g. motors, compressors, or flowing cooling water) or independent of the project (e.g. nearby road traffic). Low frequency drift and jitter can be corrected for by the use of a slow feedback system that monitors the beam-beam deflection with precision Beam Position Monitors (BPMs) and controls FFTB-style movable magnet supports. Here "low frequency" and "slow feedback" refer to the maximum frequency for which the 120 Hz accelerator repetition rate can drive a correction signal; $\sim$3-5 Hz is typically taken as the frequency below which this feedback would operate effectively.

For higher frequencies, other means must be taken to protect against potential jitter. The JLC design is based on the assumption that a support tube that spans the IP and ties the focusing magnets together will suffice to lock the quadrupole magnets together. The NLC design assumes that a support tube is insufficient and that compact low mass magnets free of cooling water can be tied together by "attaching" each magnet independently to the local bedrock with active sensors that drive piezoelectric actuators. To this end, a significant amount of R&D has been done on developing a so-called "optical anchor" interferometer as a candidate for the active sensor.

There are many open questions of mutual interest that should be answered before finalizing any IR design.

- **Passive compliance and definition of vibration standards**
  What criteria (as measured by a well defined procedure using specified hardware) should be applied to site selection, equipment purchased, mounting devices and the like? How often may these criteria be violated and what is the cost in luminosity lost and what recovery procedure
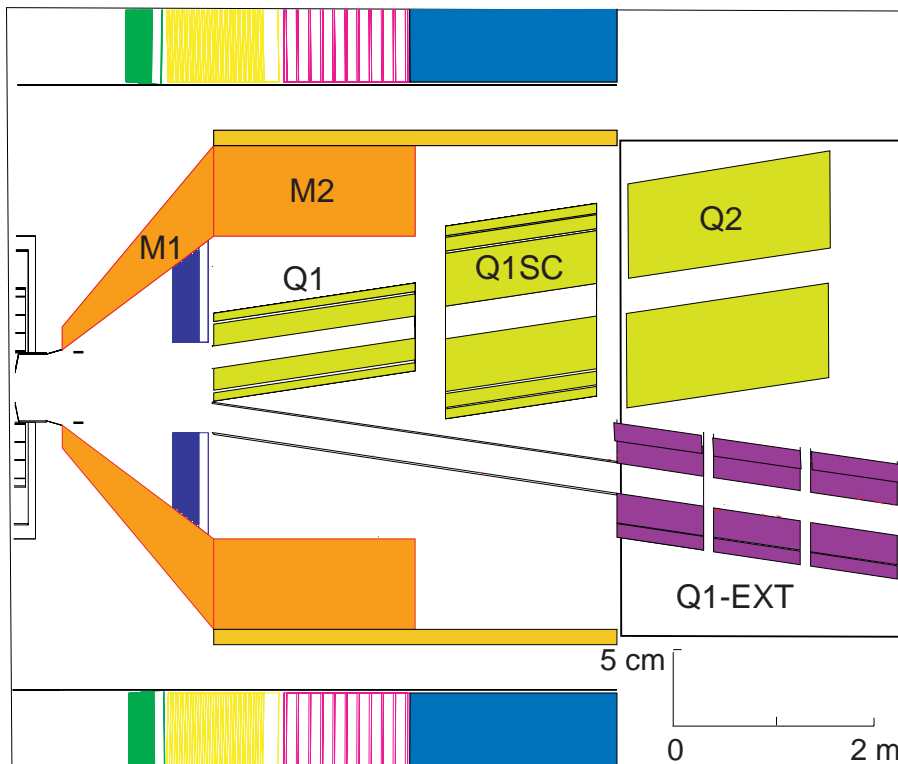
Figure 8.2: *Plan view of the currently proposed interaction region for the NLC small detector.*

is required?

- **Effectiveness of vibration suppression schemes**
  What reduction in amplitude can be expected from any proposed scheme which hopes to suppress relative jitter? How should one measure the amplitude and frequency response of these methods? What vibration suppression will beam-based feedback supply? What R&D is required to develop very low latency feedback that could correct the trailing bunches in a train after the behavior of the early bunches has been measured?

- **Utility of a support tube**
  The assumptions made in the ANSYS analysis of the JLC support tube are being independently evaluated by the SLAC engineering staff. This is occurring with the full cooperation of all parties, and with the relevant exchange of all documentation and information. We hope to have, by the next meeting of the ISG group, a more detailed understanding of what realistic suppression the tube might provide. We would like to understand the sensitivity of the result to assumptions on how the tube is supported in the detector, its construction, the size and weight of the final quadrupole magnets, and the input spectrum of ground vibration.

- **Measurement of final quadrupole vertical motion**
  Over the next few years, we plan to construct and instrument different test apparatus that will

serve to demonstrate that we can achieve the vibrational tolerances required by any design. Ideally, at the end of this effort, we will test a full mechanical mockup of the interaction region, using mechanics for the masses of the final quad magnet technology chosen within the constraints of the detector chosen. For now, the simpler set ups will tell us how easy or difficult it may be to stabilize the optical elements as a function of their size, shape, and weight. It would be useful to use a joint facility for this purpose so that the various suggestions being considered can be equally evaluated.

8.3 Detector Backgrounds

From the point of view of the experimental detector, the issue of most concern is detector backgrounds. Detector backgrounds are expected to come from the following sources:

Machine Backgrounds	IP Backgrounds
Direct beam loss	Disrupted primary beam
beam-gas scattering	Beamstrahlung photons
collimator edge scattering	e^+e^- pairs from beam-beam interactions
Synchrotron radiation	Radiative Bhabhas
Muon Production	Hadrons from $\gamma\gamma$ interactions
Neutron back-shine from Dump	
Extraction Line Loss	

Machine backgrounds
The beams must be collimated to limit the profile of synchrotron radiation through the IR. Since the beams may have long tails at 1 - 0.1% of the total intensity, a large number of $\mu^\pm$ pairs can be created at the collimators. If one wishes to limit the rate to less than one muon/pulse, these muons have to be prevented from reaching the detector by muon attenuators or spoilers. The collimation depth required is set by ℓ^* and the aperture of the final quadrupole magnets.

IP backgrounds
The $e^\pm$ pairs cause two major backgrounds in the detector.

The first is from the primary electrons and positrons. Although most of them are produced in very forward angles $\propto m_e/E_e$, they are significantly deflected by the strong magnetic field of the beam and acquire relatively large transverse momenta. They may then hit parts of the detector, in particular the vertex detector which is closest to beam line. The hit rate depends on the radial location of the vertex detector, whose minimal radius is typically 1 to 2 cm and on the strength of the detector-solenoidal magnetic field, 2 (JLC) to 6 (NLC) Tesla. Generally, physics requires the smallest radius with the strongest magnetic field for better tagging efficiency of bottom/charm quarks. However, there may be a limitation on the maximum field strength coming from the optics of the final focus system, in

particular if there is a large horizontal crossing angle as for the NLC.

The second background is due to the secondary photons and neutrons back-scattered from the beam pipe, the quadrupole magnets or the beam dump. The detectors are shielded from the photons by conical and cylindrical masks of tungsten around the final quadrupole magnets. However, soft photons with a few hundred KeV are easily produced in an electromagnetic interaction, so it is very important to have the "minimum" material near the IR. Even with this masking system, several thousand photons/pulse can be scattered into the central tracking region at $r > 30$cm. To absorb the neutrons, additional masks, e.g. made of boronated polyethylene, are necessary in front of the quadrupole magnets and the beam dump. The present estimation is $10^8 - 10^9$ neutrons/cm^2/year at the vertex detector which is well below the tolerable level for a Charge Coupled Device (CCD).

8.3.1   Background Calculations

Since the potentially most serious background is produced by e$^\pm$ pairs generated by the beam-beam interaction, we have devoted much effort to calculating this background. First, e$^\pm$ pairs are generated by a simulation of the beam-beam interaction. Then these pairs are tracked in the realistic three-dimensional detector geometry while simulating high energy interactions with the detector materials. Any particle hitting a detector component is counted as detector background. We have developed software tools to carry out the calculation, and come to a reasonable understanding of the background and the masking scheme. However, due to the differences between JLC and NLC in the machine, IR and detector designs, it is not straightforward to compare the background calculations. The process of understanding and resolving the differences has nonetheless been valuable for attaining a deeper understanding of the background issues.

To simulate the beam-beam interaction, the JLC group uses ABEL and CAIN, and the NLC group ABEL and Guinea-pig. We have compared these three programs, and found a good agreement between CAIN and Guinea-pig, although ABEL predicted 20% less e$^\pm$ pairs than the other programs. This was found to be due to a different treatment of the beam-size effect and after revision, ABEL is now consistent with CAIN and Guinea-pig.

To simulate high energy interactions, both the JLC and NLC groups use GEANT 3 which is a standard tool for high energy detector simulation. Both photons and e$^\pm$ are tracked to 10 KeV. While GEANT 3 is a reliable simulation program for photons and e$^\pm$, it does not simulate neutron production. Since GEANT 3 has a neutron transport package based on MICAP, we have written a program to simulate the giant-dipole-resonance (GDR) process which is the dominant process for low energy ($<$ 20 MeV) neutron production. However, since other processes to produce higher energy neutrons are not simulated, we may underestimate the neutron background. Because of this GEANT limitation, both the JLC and NLC groups use FLUKA 98 to calculate the neutron background.

The e$^\pm$ hit density in the CCD vertex detector appears to be different for JLC and NLC. However, when the differences in the solenoid field strength and the machine energy are taken into account, the two numbers are consistent. We have a consensus that the e$^\pm$ hit density can be reduced to an

acceptable level for the vertex detector either by using a strong solenoidal field (6 Tesla vs. 2 Tesla) or by increasing the vertex detector radius (2.5 cm vs. 1.2 cm).

There is at least a factor of five difference in the number of photons hitting the central tracking chamber for the two designs. Since the NLC detector uses either a Silicon tracker (Small detector) or TPC (Large detector), the low energy photons are not a problem. The JLC detector, on the other hand, plans to use a drift chamber and the photon background becomes very important. We have spent a significant effort to understand the difference between the two calculations. The complete history of those background photons is followed to identify which part of the detector has produced the photons. The background photons reaching the tracking chamber at large radius come from low energy secondary $e^{\pm}$ that are produced in the final doublet and then come back to the IP following the solenoid field lines to interact with the beam-pipe and vertex detector materials. The detailed differences in the magnet geometries and beamline setups produce the different estimates of photon backgrounds.

Some difference is also seen in the neutron background calculations. While both groups use FLUKA 98 to calculate the neutron background, the neutron hit density in the vertex detector is estimated to be $7 \times 10^7/\text{cm}^2/\text{year}$ for JLC, and $2 \times 10^9/\text{cm}^2/\text{year}$ for NLC. The geometry difference and machine energy difference (500 GeV in JLC and 1 TeV in NLC) seem to explain this difference. However, there is a difference in the source of neutron background. QC1 is identified as a dominant contributor for JLC, while the majority of neutrons are produced in M1 for NLC. Further investigation is required.

8.3.2   Machine Backgrounds

Machine backgrounds not discussed in the previous section include muon production, synchrotron radiation, and lost particles arising from beam gas scattering. Discussions on how to estimate the level and distribution of halo outside the beam core have only just begun. The beam halo controls the depth to which the beam must be collimated to limit synchrotron radiation and the number of muons produced in the collimation system. Beam vacuum requirements have not been discussed at all. The sensitivity of the detectors to beam loss as a function of position should be calculated for each of the final focus and collimation designs currently being considered.

Muon Backgrounds

To suppress the muon background the JLC design incorporates two concentric oppositely magnetized steel toroids around some length of the beamline downstream of the collimation region. The NLC design includes some number of 9 m long tunnel filling dipole magnets. We are still discussing the effectiveness of each of these two approaches.

8.3.3   Future Work on Background Calculations

We have found that the calculations can be highly sensitive to the assumptions used in the calculational model. There will continue to be an ongoing effort to reconcile any discrepancies between calculations as they arise, such as the current differences in muon and neutron background estimates.

8.4   Collimation, Final Focus, and Extraction Line Lattices

The current versions of the JLC and the NLC incorporate different schemes for the collimation system, the final focus, and the extraction line. While work on a common lattice was not explicitly a goal for the ISG, for completeness of this report we briefly describe below the designs being considered.

As was stated in the introduction, only time and available manpower have kept us from comparing the pros and cons of each other's designs. The lattices currently being used should be considered as working prototypes, good for engineering studies and cost estimates. The parameter space of potential solutions is vast and certainly best explored in a collaborative manner. We expect the time scale of this work to be set by design deadlines imposed by the relevant international or national organizations.

8.4.1   The JLC Beam Delivery System

The JLC Beam Delivery System [3] design contains:

- An energy collimation system, 400 m in length, which eliminates particles which differ from the design energy by more than 2%

- A betatron collimation system, 800 m in length, which performs combined collimation in x, x', y, and y', two collimation iterations per degree of freedom, and uses nonlinear elements to enlarge the beam halo at the collimators relative to the core; the collimation amplitudes are $\pm 6\sigma_x$ and $\pm 40\sigma_y$

- An 7.5 mrad arc composed of combined-function bending/focusing magnets, 200 m in length; in order to allow 2 interaction regions, each side of the Beam Delivery System contains 2 such arcs in sequence, and one or the other arc is deactivated to deliver beam to each IP

- A final focus system which provides the final demagnification required to achieve the design luminosity, 1600 m in length; the final focus uses an "asymmetric dispersion" chromatic correction scheme [12] and incorporates a 3.5 mrad reverse-bend arc, to provide a final total crossing-angle of 8 mrad.
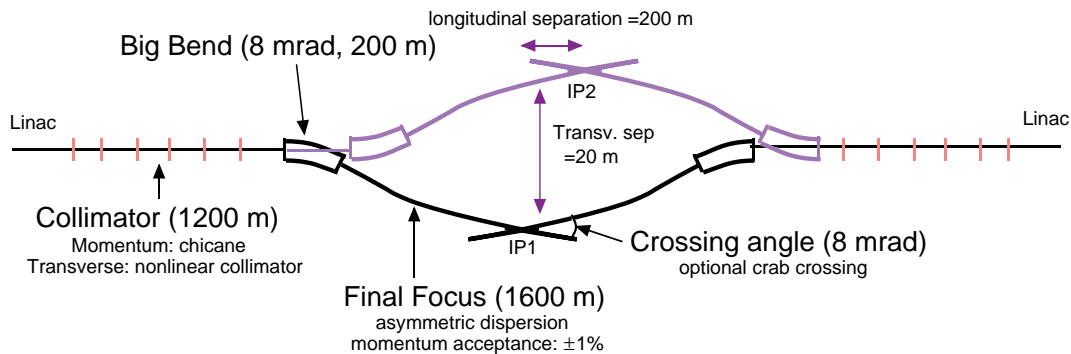
Figure 8.3: *Schematic layout of the beam delivery system at JLC (JLC Design Study, April 1997).*

8.4.2 The NLC Beam Delivery System

The NLC Beam Delivery System described in the ZDR contains:

- A combined energy/betatron collimation system, 2500 m in length, which collimates x/x' at $\pm 5\sigma$, y/y' at $\pm 35\sigma$, and δ at $\pm 4\%$, two collimation iterations per degree of freedom, and provides passive protection against large energy or betatron errors arising in the main linac; only linear elements are used to enlarge the beam and halo

- A 10 mrad arc of separated-function magnets, 400 m in length, which is subdivided into a 1 mrad "IP Switch" followed by a pair of side-by-side 9 mrad arcs which bend in opposite directions; by reversing the bend polarity of the switch, the beam may be directed into either of 2 interaction regions

- An optical module for correction of xy coupling followed by a 4-dimensional emittance diagnostic module, with a combined length of 350 m

- A final focus system, 1800 m in length, which uses the conventional chromatic correction optics of the Final Focus Test Beam [13] to achieve the demagnification and chromatic correction required; the total crossing angle is 20 mrad.

Present thinking on the NLC Beam Delivery System incorporates a number of changes from the design described in the ZDR. The collimation system will be divided into an energy collimation lattice which incorporates passive protection against large single-pulse energy errors, followed by a betatron collimation lattice which does not provide passive protection of collimators but instead incorporates "consumable" or "renewable" collimators; the total collimation system lattice will be on the order of 1.2 km in length. The lattice of the 10 mrad arc will be converted to combined-function magnets to
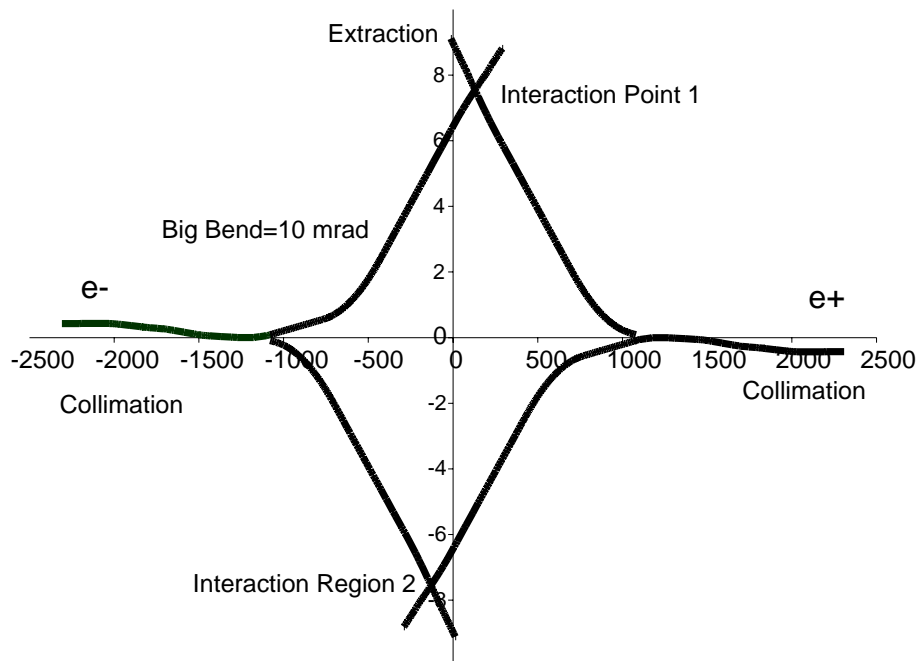
Figure 8.4: *Schematic layout of the beam delivery system at the NLC.*

permit a reduced length (200 m instead of 400 m) and reduced SR emittance dilution (12% at 1.5 TeV CM). The optical module for coupling correction and emittance diagnostics will be reduced in length to 240 m by increasing the strength of the quadrupole magnets in the system. Finally the final focus length will be reduced to approximately 850 meters by reoptimizing the bend magnets for 1 TeV CM instead of 1.5 TeV CM; the performance at 1.5 TeV CM will still be acceptable for the shorter system, although some small modifications in the magnet positioning will be required.

8.4.3   Technology Choices

Complementing the lattice design effort is an R&D program on various accelerator components that are common to any machine design. This program includes work in the following areas.

- **Collimators:**   There is an active program to design and prototype collimators that would not need to be replaced if they were to be damaged by the beam. A damaged collimator surface would cause a wakefield that could increase the beam emittance to unacceptable levels. One line of engineering develops collimators based on rotating wheels or moving metal tapes that may be moved to a fresh position if damaged. Another R&D effort investigates the feasibility of using a continuously regenerated metal surface by refreezing a liquid metal on a drum of an appropriate material. The tolerances that can be achieved by such systems will influence the collimation lattice design.

- **Permanent Magnets:** Improvements in cost, reliability, tolerances, or complexity may be achieved by replacing appropriate electromagnets in the beam delivery lattice with permanent magnets. The field quality, strength, variability, temperature sensitivity, radiation resistance, and magnetic rigidity in an external field are being investigated for a variety of permanent magnet designs.

- **Instrumentation:** Simulations and engineering prototypes are beginning on the beam position monitors, kicker, and associated electronics that would use the variation of beam-beam deflection angle to correct the offset of the colliding beams after only a small fraction of a bunch train has gone by. If successful, the tolerances for the vibration stability of the final quadrupole magnet mounts would be relaxed.

  It has been suggested that the energy distribution of the beam-beam pairs be used as a luminosity monitor. R&D on an appropriate pixelated device is beginning.

8.5 Summary and Conclusions

IR issues are listed together with JLC and NLC status, tools and planned R&D in Table 8.1,8.2.

In formulating the designs for the beam delivery, we have tried to learn from the experience of SLC and FFTB. While reaching design beam energy was never a problem at the SLC, the luminosity achievable was often limited by problems with high backgrounds and unstable operation. It is important not to underestimate the difficulty of reliably delivering good beam as we enter a new regime of beam size, roughly 1000 times smaller than ever attempted. The JLC/NLC will also have to deal with very high beam intensity, where new physical processes begin to become important sources of background particles which could be very detrimental to the physics program. Both JLC and NLC have emphasized conservative designs which can accommodate larger backgrounds than expected and which have flexibility to respond to unforseen optics limitations.

As outlined in this chapter, there remains a considerable amount of work to do in the final focus, collimation, and interaction region areas to solidify our understanding. The different approaches to each issue currently advocated by the JLC and NLC groups should be considered more as possible points in the space of all solutions than as well studied optimal solutions. The most efficient way to attack these challenging problems will be to continue to collaborate in a coherent manner in the allocation of new resources and in the frank examination of all conclusions reached.

Item	JLC	NLC	tools and R&D etc.
collimation	nonlinear, ellipse	linear, rectangular	SAD,EGS
	1.2km/1.5TeV	2.4km/1.5TeV	wakefield meaurement
	$6\sigma_x \times 40\sigma_y$	$7\sigma_x \times 35\sigma_y$	detail tunnel geometry
			shorter collimation
			exotics: laser,liquid metal ?
muon-background	6 iron cylinders	4 spoilers	MUCARLO
	$0.6\phi \times 120$m	$3 \times 3 \times 9$m^3	radio-activation in tunnel
			optimization with two schemes
crossing angle	8 mrad or smaller	20 mrad or larger	ABEL,CAIN,Guinea-Pig
	SR backgrounds	"6 Tesla"	tolerance for crab cavity
	option (L 40% up)	must	requires 0.2^o phase stability
	higher luminosity	easier extraction	needs prototype cavity
	w/o crab cavity	of disrupted beam	
FF Q magnet	warm magnet	2 permanet mag.	warm magnet: water
	(2.2m)	(1m)+Q1SC(0.5m)	cooling w/0 vibration
	inner r=6.85mm	inner r= 7, 8mm	permanent magnet: no beam-
		outer r= 2, 2.5cm	based alignment
		PEP-II experinece	SC magnet: how to extract
	$\ell^* = 2$m	$\ell^* = 2$m	beam?
SC shielding mag.	must	no at least	thinner cryostat for
		for small detector	smaller dead cone
detector solenoid	2 Tesla	6 Tesla	GEANT
			optimization with
			calorimeter performance
support of FF-Q	support tube with	optical anchor	ANSYS
	active alignment	no support tube	analysis with measured
			ground motion
feedback	slow (< 10Hz)	slow (< 10Hz)	SAD, TURTLE, MERLIN
	O(nm) ground motion	fast feedbak(2.8ns,	CAIN
	at > 10Hz causes	< 200Hz)	BPM:10-100nm resolution
	5% L loss.		

Table 8.1: *IR issues.*

Item	JLC	NLC	tools and R&D etc.
SR background	no problem with collimation/mask	same as JLC	SQRAD,MQRAD,GEANT SLD experiences; large fluctuation of SR background in CDC.
$e^{\pm}$ pairs	1 hit/mm^2/train at r=2.4cm(B=2T) 10,000γ in CDC for $\sqrt{s}$ =500GeV	10 hits/mm^2/train at 1.2cm(B=6T) 120,000γ in CDC for $\sqrt{s}$ =1 TeV	ABEL,CAIN,Guinea-Pig GEANT detailed geometry at IP tolerable hit rates ?
neutrons	10^7 n/cm^2/year giant resonances	2$\times$10^9 n/cm^2/year with high energy n	GEANT,FLUKA98 depend on detailed geometry CCD/VTX:$<$10^{10}n/cm^2/year
pair monitor	double discs of CCD		ABEL,CAIN,Guinea-Pig GEANT, dE/dX measurement
Shintake mon.			laser optics close to IP?
IP-BPM			O(10nm) resolution
L measurement	acollinearity angle of Bhabha scattering		L within a 1% beam energy spread ?
beam dump line		a chicane to separate electrons and photons with a commom dump	ABEL,CAIN,Guinea-Pig SAD,GEANT,FLUKA98 to measure E, ΔE, P etc.

Table 8.2: *IR issues (continued).*

References for Chapter 8

[1] JLC-I, KEK Report 92-16, December, 1992.

[2] Zeroth-Order Design Report for the Next Linear Collider, LBNL-PUB-5424, also SLAC Report 474 or UCRL-ID-124161, May 1996.

[3] JLC Design Study, KEK Report 97-1, April 1997.

[4] V. Balakin *et al.*,*Phys. Rev. Lett.* **74**, 2479 (1995).

[5] T.Tauchi, K.Yokoya and P.Chen, *Part. Accel.* **41**, 29 (1993).

[6] SAD (Strategic Accelerator Design) is a computer program complex for accelerator design which has been developet at KEK since 1996. See `http://www-acc-theory.kek.jp/SAD/sad.html` for resources.

[7] GEANT3.21-Detector Description and Simulation Tool, Application Software Group, computing and networks division, CERN, CERN Program Library Long Writeup W5013, March 1994.

[8] T.Tauchi and K.Yokoya, *Phys. Rev.* E **51**, 6119 (1995).

[9] M.N. Frary, D.J. Miller, in: e^+e^- collisions at 500 GeV: the physics potential, ed.by P. Zerwas, DESY report 92-123A, 1992,p.379.

[10] P. Chen, G. Horton-Smith, T. Ohgaki, A.W. Weidemann, K. Yokoya, Nucl. Instr. and Meth. **A355** (1995) 107.

[11] N. Toomi et al., in preparation.

[12] K. Oide, "Final Focus System with Odd-Dispersion Scheme," Proceedings of the 15 International Conference on High Energy Accelerators (Hamburg, 1992), pages 861 – 863.

[13] K. Oide, "Design of Optics for the Final Focus Test Beam at SLAC," in Proceedings of the 1989 IEEE Particle Accelerator Conference, pages 1319 – 1321.

Authors and Major Contributors of Chapter 9

- Eric Doyle

- Josef Frisch

- Jeff Gronberg

- Stan Hertzbach

- Lew Keller

- Thomas W. Markiewicz

- Takashi Maruyama

- Akiya Miyamoto

- Yoshihito Namito

- Tor Raubenheimer

- Andrew Ringwall

- Knut Skarpaas, VIII

- Yasuhiro Sugimoto

- Toshiaki Tauchi

- Peter Tenenbaum

- Hiroshi Yamaoka

- Mike Woods